

Steam Generator Inspection Reliability Assessments on Primary Side Cracking in U-Bends

International Steam Generator Tube Integrity
Program—Assessment of SG Inspection
Techniques and Reliability

Date Published: August 2023

Prepared by:
S. Bakhtiari
T. Elmer
Z. Zeng
C. B. Bahn
S. Majumdar

Argonne National Laboratory
9700 South Cass Avenue
Lemont, IL 60439

Patrick Purtscher, NRC Project Manager

Disclaimer

Legally binding regulatory requirements are stated only in laws, NRC regulations, licenses, including technical specifications, or orders; not in Research Information Letters (RILs). A RIL is not regulatory guidance, although NRC's regulatory offices may consider the information in a RIL to determine whether any regulatory actions are warranted.

ABSTRACT

Cracking that initiates from both the inside and outside surface has been observed in the U-bend region of steam generator (SG) tubes. Based on the past operating experience with Alloy 600 tubing materials, cracking can initiate anywhere along the U-bend including the tangent regions. The ability to detect and size cracks in that region, and the ability to assess their significance (i.e., size) are important for ensuring tube integrity. Research was conducted at Argonne National Laboratory (Argonne) to assess the ability of conventional eddy current (EC) inspection techniques to detect and size primary water stress corrosion cracks (PWSCCs) in the U-bend region of SG tubes. In comparison with other locations in the SG tube bundle the higher level of noise associated with tube geometry and dimensional variations at U-bends, commonly referred to as tube ovalization, can result in a greater degradation of signal-to-noise ratio (S/N) and consequently diminish the utility of nondestructive examination (NDE) techniques in those regions.

Assessing the reliability of EC inservice inspection (ISI) techniques in application to U-bend regions of SG tubing that exhibit a high degree of tube deformation is directly related to the structural integrity of tubes. To that end, a library of representative U-bend specimens was assembled at Argonne under the International Steam Generator Tube Integrity Program (ISG-TIP). A facility was set up to induce stress corrosion cracking (SCC) in U-bend tubes with two different radii of curvature. The focus of the efforts in this work to manufacture flaws was on PWSCC at U-bend regions, which are more challenging to produce in comparison with laboratory-produced flaws in straight tubes or at the U-bend outside diameter (OD). Eddy current inspections were performed on the U-bend specimens at different stages of the flaw manufacturing process. Supplementary inspections were also carried out on the entire set of tubes before they were subjected to pressurization tests, which were performed in connection with evaluations of tube structural integrity. The EC inspection data were analyzed at different stages of the pre- and post-crack manufacturing process using both conventional and alternative data analysis methods.

A study was initially carried out in an effort to identify the primary sources of background interference in EC rotating probe data in small radius U-bends. As part of the initial investigations, we also evaluated different methods for suppression of unwanted signals at U-bend regions.

Two separate studies were subsequently conducted to assess the viability of correlations between various NDE parameters, obtained through analyses of EC inspection data, and structural parameters, obtained through destructive examination (DE) of the specimens. Only data from 57-mm-radius U-bend specimens were included in those assessments. The first study revolved around evaluating the degree of indirect correlation between the NDE parameters, obtained using conventional analysis of EC data, and tube structural integrity. The dataset used in those evaluations was thus limited to flaws that failed during pressure testing of the tubes. Based on the results of the first study, we identified a subset of the NDE parameters, among those examined, consisting of the more viable indicators of tube structural integrity. Following the completion of destructive examinations, a second study was conducted to assess the viability of both direct and indirect correlations between NDE parameters and structural parameters associated with tube integrity. The DE results obtained by fractography served as the ground truth for flaw size. The NDE estimates of flaw size used in the second study included those obtained using both conventional and alternative data analysis methods.

This report presents the results of inspection reliability assessments on primary side cracking in the U-bend region of SG tubes with small bend radii. Initially, the report describes production of PWSCCs in a set of representative U-bend specimens assembled for this purpose. Next, we present eddy current examination results based on conventional and alternative analyses of data

acquired using a +Point™ rotating probe. Subsequently, the results are discussed of investigations on the source of strong background interference in small-radius U-bends and the signal processing methods evaluated for optimal suppression of such unwanted signals. Finally, the results are presented from two separate studies on correlations between various NDE parameters and structural parameters obtained by DE, as well as tube structural integrity, as determined by the measured failure pressure.

TABLE OF CONTENTS

Abstract	iii
Table of Contents	v
List of Figures	vii
List of Tables	xvi
Executive Summary	xvii
Acknowledgments	xxi
Abbreviations and Acronyms	xxii
1 Introduction	1-1
2 Production of Cracks in U-bend Specimens	2-1
2.1 U-bend Specifications	2-1
2.2 U-bend Inspection and Data Verification	2-4
2.2.1 Verification of Dimensional Specifications	2-5
2.2.2 Characterization of U-bends	2-7
2.3 Manufacturing of U-bend SCC	2-12
2.3.1 Procedure for Axial PWSCC throughout the 57-mm-Radius U-bend Region.....	2-12
2.3.2 Procedure for Axial PWSCC at Tangential Regions of 57-mm-Radius U-bends	2-14
2.3.3 Procedure for Circumferential PWSCC throughout the 152-mm-Radius U-bend Region	2-14
3 Eddy Current Examination of U-bend Tubes	3-1
3.1 Eddy Current Examination Technique	3-1
3.2 Post-Cracking Inspection of U-bend Specimens	3-3
3.3 Effect of U-bend Geometry on Eddy Current Probe Response	3-13
3.4 Suppression of U-bend Noise in Rotating Probe Data	3-22
4 Assessment of Correlations Between NDE and DE Structural Parameters	4-1
4.1 Assessment of Indirect Correlations	4-1
4.2 Evaluation of NDE Sizing Accuracy for PWSCC at U-Bends	4-6
4.3 Assessment of Direct and Indirect Correlations	4-12
5 Summary and Conclusions	5-1
6 References	6-1
APPENDIX A – Timeline for Various Research Activities Associated with U-bend Specimens	A-1
APPENDIX B – Eddy Current Inspection Results for 57-mm-Radius U-bend Specimens	B-1

APPENDIX C – Eddy Current Inspection Results for 152-mm-Radius U-bend Specimens.....	C-1
APPENDIX D – Eddy Current and Visual Inspection Data for 57-mm-Radius U-bend Specimens.....	D-1
APPENDIX E – Eddy Current and Visual Inspection Data for 152-mm-Radius U-bend Specimens.....	E-1
APPENDIX F – NDE Depth Profiles for CraCks in 57-mm-Radius U-bend Specimens.....	F-1
APPENDIX G – NDE and DE Depth Profiles for PWSCC in 152-mm-Radius U-bend Specimens.....	G-1

LIST OF FIGURES

Figure 2-1.	Schematic of U-bend tubing showing the locations of extrados, intrados, flank, apex, and tangent.	2-2
Figure 2-2.	U-bend specimens with 19.1-mm (0.75-in.) OD and with two different bend radii of 57 mm (inner tube) and 152 mm (outer tube).....	2-5
Figure 2-3.	Distributions of (a) the wall thickness reduction at the extrados apex and (b) the ovality for 19.1-mm OD and 57-mm bend radius U-bend specimens, using data reported by Valinox.....	2-6
Figure 2-4.	Distributions of (a) the wall thickness reduction at the extrados apex and (b) the ovality for 19.1-mm OD and 152-mm bend radius U-bend specimens, using data reported by Valinox.	2-6
Figure 2-5.	Photographs showing sections of a representative 19.1-mm OD U-bend tube near (a) 0deg and (b) 180deg tangents. Visible in the photo of the 180deg tangent are light dent at the extrados and bulge at the intrados.....	2-7
Figure 2-6.	Measured wall thickness variation of 19.1-mm OD U-bends at (a) "0deg" tangent, (b) 45°, and (c) 90° for (left) 57-mm bend radius and (right) 152-mm bend radius.....	2-8
Figure 2-7.	Wall thickness profiles of 19.1-mm OD and 57-mm bend radius U-bends (1100-10) along the angle of U-bend axis.	2-9
Figure 2-8.	OD reduction along the extrados/intrados and the flanks of Argonne U-bends with 19.1-mm OD with (a) 57-mm and (b) 152-mm bend radii.....	2-11
Figure 2-9.	Measured ovality profiles of 19.1-mm OD and 57-mm bend radius U-bends along the angle of U-bend axis.	2-11
Figure 2-10.	Schematic of displacing U-bend legs with clamps and the location of chemical exposure area.	2-13
Figure 2-11.	Photos of a 57-mm bend radius U-bend tube with clamps (a) before and (b) after the leg displacement. Note that the ruler in photos is 300 mm long.....	2-13
Figure 2-12.	U-bend tangential region compressed by stainless steel clamps to generate tensile hoop stress at the tube ID.....	2-14
Figure 2-13.	152-mm bend radius U-bend with clamps (a) before and (b) after the inward leg displacement. Note that the ruler in the photos is 300 mm long.	2-15
Figure 2-14.	Photographs showing (a) the Teflon insert with O-ring, (b) U-bend with the inserted Teflon insert, and (c) the Teflon insert and rod placed with the U-bend to show the approximate location of the Teflon plug in the U-bend after the insertion. (Note that the ruler is 300 mm long.)	2-16
Figure 3-1.	Photographs of detachable flexible rotating probe with a mid-range +Pt coil, placed along the intrados of (a) a 57-mm and (b) a 152-mm radius U-bend tube specimen at Argonne.	3-1
Figure 3-2.	Drawing for EDM notch standard tube used for calibration of rotating probe data. The tube has 18 notches of OD and ID origin with axial and circumferential orientation.	3-3

Figure 3-3.	Representative +Pt probe data for a 57-mm-radius U-bend specimen 890-12 (a) before and (b) after the chemical exposure process.....	3-5
Figure 3-4.	Representative +Pt probe data for 57-mm-radius U-bend specimen 920-19 (a) before, (b) midway through, and (c) after the chemical exposure process.	3-6
Figure 3-5.	Maximum signal amplitude for axial PWSCCs in U-bend specimens, with and without the clamps, as a function of maximum depth estimated using data from +Pt probe examinations.	3-8
Figure 3-6.	Isometric plots of rotating +Pt probe data showing the axial PWSCCs in U-bend specimens (a) 890-08, (b) 890-20, (c) 1180-11, and (d) 920-19.....	3-8
Figure 3-7.	Representative baseline data for 57-mm-radius U-bend specimen 890-08 before chemical exposure of tangent regions.....	3-9
Figure 3-8.	Representative data for 57-mm-radius U-bend specimens with axial PWSCC at tangent regions.	3-10
Figure 3-9.	Representative data for a 152-mm-radius U-bend specimen with circumferential PWSCC throughout the U-bend region.....	3-12
Figure 3-10.	Isometric plots of rotating probe data showing circumferential PWSCCs throughout 152-mm-radius U-bends.....	3-13
Figure 3-11.	Cross-sectional view of U-bend specimen 890-12 cut at 45° and at 90° bend locations as denoted in the figure. The top of each cross-section is extrados and the bottom is intrados. Also shown in the figure is the configuration of test setup for EC inspection of the U-bend section, which includes an in-line calibration standard with a 270° TSP collar.	3-15
Figure 3-12.	Polar plots of the ID radius along the circumference of U-bend 890-12 with two different radius scales showing (a) actual and (b) exaggerated profiles.	3-15
Figure 3-13.	Linear plot of the radius profile along the circumference of U-bend specimen 890-12.....	3-16
Figure 3-14.	Wall thickness variation of U-bend specimen 890-12 along the circumference (a) at 45° and 90° bend locations and (b) remeasurement at apex.	3-16
Figure 3-15.	Image and cross-sectional terrain profiles of +Pt rotating probe data at 300 kHz for the U-bend specimen 1180-13 collected (a, b) on the “push” and (c, d) on the “pull.”	3-18
Figure 3-16.	Image and terrain profiles showing +Pt data at 300 kHz for the U-bend section of the tube with three sets of markers at the tangent point, 45°, and 90° positions.	3-18
Figure 3-17.	Filtered image and terrain profiles (after suppression of baseline signal) at (a) 300 kHz and (b) 50 kHz showing the alignment of the markers more clearly along the U-bend of specimen 1180-13.....	3-19
Figure 3-18.	Isometric display of the vertical component (V-comp) and horizontal component (H-comp) of rotating probe data collected with (a, b) an HF-PC probe at 600 kHz and (c, d) a +Pt probe at 300 kHz on a 57-mm-radius U-bend.	3-20

Figure 3-19.	Cross-sectional plots of rotating probe data collected with HF-PC and mid-range +Pt probe at (a) 90° section and (b) 45° section of a 57-mm-radius U-bend tube.....	3-21
Figure 3-20.	Field data acquired during the 2003 ISI with a +Pt rotating probe from a small-radius U-bend tube. The tube had a PWSCC just above the tangent. Shown above are (a) pre- and (b) post-processed data at 300 kHz showing good suppression of the background noise using spatial domain filtering.....	3-23
Figure 3-21.	(a) Pre- and (b) post-processed +Pt data at 300 kHz for the U-bend section of the tube in Figure 3-20. The same PWSCC signal is superimposed at three locations along the U-bend. Also shown are (c) the estimated depth profiles of the crack at the three locations.	3-24
Figure 4-1.	(a) Correlation plot of failure pressure vs. NDE signal amplitude for axial PWSCC in 57-mm-radius U-bends and (b) the same plot as (a) with the added points (circles) for the predicted flaw to fail based on the NDE parameter.	4-4
Figure 4-2.	(a) Correlation plot of failure pressure vs. NDE length for axial PWSCC in 57-mm-radius U-bends and (b) the same plot as (a) with the added points (circles) for the predicted flaw to fail based on the NDE parameter.....	4-4
Figure 4-3.	(a) Correlation plot of failure pressure vs. NDE maximum depth for axial PWSCC in 57-mm-radius U-bends and (b) the same plot as (a) with the added points (circles) for the predicted flaw to fail based on the NDE parameter.	4-5
Figure 4-4.	(a) Correlation plot of failure pressure vs. NDE crack area (depth * length) for axial PWSCC in 57-mm-radius U-bends and (b) the same plot as (a) with the added points (circles) for the predicted flaw to fail based on the NDE parameter.....	4-5
Figure 4-5.	Comparison of depth profiling results by (a) NDE and (b) fractography for an axial PWSCC in U-bend specimen 890-16. Also displayed in various formats is (c) the EC data segment encompassing the flaw signal.	4-7
Figure 4-6.	Comparison of depth profiling results by (a) NDE and (b) fractography for an axial PWSCC in U-bend specimen 1180-11. Also displayed in various formats is (c) the EC data segment encompassing the flaw signal and videoscope image of the PWSCCs after pressure testing of the tube.....	4-8
Figure 4-7.	Comparison of depth profiling results by (a) NDE and (b) fractography for an axial PWSCC in U-bend specimen 920-19. Also displayed in various formats is (c) the EC data segment encompassing the flaw signal and photo of multiple PWSCCs after pressure testing of the tube.	4-9
Figure 4-8.	Comparison of depth profiling results by (a) NDE and (b) fractography for an axial PWSCC in U-bend specimen 1180-20. Also displayed in various formats is (c) the EC data segment encompassing the flaw signal.	4-10
Figure 4-9.	Comparison of NDE and DE sizing results for axial PWSCCs in U-bend specimen 1180-20 located at the tangent (left column) and at the apex (right column) regions of the tube.....	4-11

Figure 4-10.	(a) Correlation plot of DE vs. NDE crack length with a single line fitted to all data points and (b) the same plot as in (a) with separate lines fitted to tangent and U-bend (above tangent) data points.	4-13
Figure 4-11.	(a) Correlation plot of DE vs. NDE maximum depth with a single line fitted to all data points and (b) the same plot as in (a) with separate lines fitted to tangent and U-bend (above tangent) data.	4-14
Figure 4-12.	(a) Correlation plot of DE vs. NDE crack area (depth * length) with a single line fitted to all data points and (b) the same plot as in (a) with separate lines fitted to tangent and U-bend (above tangent) data points.	4-14
Figure 4-13.	(a) Correlation plot of DE length vs. NDE signal amplitude with a single line fitted to all data points and (b) the same plot as in (a) with separate lines fitted to tangent and U-bend (above tangent) data points.	4-15
Figure 4-14.	(a) Correlation plot of DE maximum depth vs. NDE signal amplitude with a single line fitted to all data points and (b) the same plot as in (a) with separate lines fitted to tangent and U-bend (above tangent) data points.	4-15
Figure 4-15.	(a) Correlation plot of DE crack area vs. NDE signal amplitude with a single line fitted to all data points and (b) the same plot as in (a) with separate lines fitted to tangent and U-bend (above tangent) data points.	4-16
Figure 4-16.	(a) Correlation plot of failure pressure vs. NDE crack length obtained from NDE depth profile and (b) the same plot as in (a) with the added points (circles) for the predicted flaw to fail based on the NDE parameter.	4-19
Figure 4-17.	(a) Correlation plot of failure pressure vs. NDE crack area (depth * length) obtained from ERC depth profile and (b) the same plot as in (a) with the added points (circles) for the predicted flaw to fail based on the NDE parameter.	4-19
Figure 4-18.	(a) Correlation plot of failure pressure vs. NDE crack area (depth * length) with maximum depth obtained from NDE depth profile and length obtained from ERC profile and (b) the same plot as in (a) with the added points (circles) for the predicted flaw to fail based on the NDE parameter.	4-20
Figure 4-19.	(a) Correlation plot of measured failure pressure vs. NDE-based failure pressure (ligament rupture) using ERC profile and (b) the same plot as in (a) with the added points (circles) for the predicted flaw to fail based on the NDE parameter.	4-20
Figure 4-20.	(a) Correlation plot of measured failure pressure vs. NDE-based failure pressure (burst) using ERC profile and (b) the same plot as in (a) with the added points (circles) for the predicted flaw to fail based on the NDE parameter.	4-21
Figure 4-21.	(a) Correlation plot of measured failure pressure vs. NDE-based failure pressure (lower value of ligament or rupture burst) using ERC profile and (b) the same plot as in (a) with the added points (circles) for the predicted flaw to fail based on the NDE parameter.	4-21
Figure F-1.	Data analysis results for an axial PWSCC in specimen 1100-06 showing (a) EC (dashed line) and ERC (solid line) depth profiles and (b) output of the ERC tool using the Argonne data analysis software.	F-2

Figure F-2.	Data analysis results for an axial PWSCC in specimen 1100-07 showing (a) EC (dashed line) and ERC (solid line) depth profiles and (b) output of the ERC tool using the Argonne data analysis software.	F-2
Figure F-3.	Data analysis results for an axial PWSCC at 90° in specimen 1100-08 showing (a) EC (dashed line) and ERC (solid line) depth profiles and (b) output of the ERC tool using the Argonne data analysis software.	F-3
Figure F-4.	Data analysis results for an axial PWSCC at 90° in specimen 1100-14 showing (a) EC (dashed line) and ERC (solid line) depth profiles and (b) output of the ERC tool using the Argonne data analysis software.	F-3
Figure F-5.	Data analysis results for an axial PWSCC at 90° in specimen 1100-15 showing (a) EC (dashed line) and ERC (solid line) depth profiles and (b) output of the ERC tool using the Argonne data analysis software.	F-4
Figure F-6.	Data analysis results for an axial PWSCC at 90° in specimen 1100-18 showing (a) EC (dashed line) and ERC (solid line) depth profiles and (b) output of the ERC tool using the Argonne data analysis software.	F-4
Figure F-7.	Data analysis results for an axial PWSCC at 0° intrados in specimen 1100-19 showing (a) EC (dashed line) and ERC (solid line) depth profiles and (b) output of the ERC tool using the Argonne data analysis software.	F-5
Figure F-8.	Data analysis results for an axial PWSCC at 90° in specimen 1180-02 showing (a) EC (dashed line) and ERC (solid line) depth profiles and (b) output of the ERC tool using the Argonne data analysis software.	F-5
Figure F-9.	Data analysis results for an axial PWSCC at 0° extrados in specimen 1180-11 showing (a) EC (dashed line) and ERC (solid line) depth profiles and (b) output of the ERC tool using the Argonne data analysis software.	F-6
Figure F-10.	Data analysis results for an axial PWSCC at 45° in specimen 1180-11 showing (a) EC (dashed line) and ERC (solid line) depth profiles and (b) output of the ERC tool using the Argonne data analysis software.	F-6
Figure F-11.	Data analysis results for an axial PWSCC at 90° in specimen 1180-14 showing (a) EC (dashed line) and ERC (solid line) depth profiles and (b) output of the ERC tool using the Argonne data analysis software.	F-7
Figure F-12.	Data analysis results for an axial PWSCC at 180° extrados in specimen 1180-15 showing (a) EC (dashed line) and ERC (solid line) depth profiles and (b) output of the ERC tool using the Argonne data analysis software.	F-7
Figure F-13.	Data analysis results for an axial PWSCC at 0° extrados in specimen 1180-16 showing (a) EC (dashed line) and ERC (solid line) depth profiles and (b) output of the ERC tool using the Argonne data analysis software.	F-8
Figure F-14.	Data analysis results for an axial PWSCC at 90° in specimen 1180-18 showing (a) EC (dashed line) and ERC (solid line) depth profiles and (b) output of the ERC tool using the Argonne data analysis software.	F-8
Figure F-15.	Data analysis results for an axial PWSCC at 0° extrados in specimen 1180-20 showing (a) EC (dashed line) and ERC (solid line) depth profiles and (b) output of the ERC tool using the Argonne data analysis software.	F-9

Figure F-16.	Data analysis results for an axial PWSCC at 90° in specimen 1180-21 showing (a) EC (dashed line) and ERC (solid line) depth profiles and (b) output of the ERC tool using the Argonne data analysis software.	F-9
Figure F-17.	Data analysis results for an axial PWSCC at 180° extrados in specimen 1180-22 showing (a) EC (dashed line) and ERC (solid line) depth profiles and (b) output of the ERC tool using the Argonne data analysis software.	F-10
Figure F-18.	Data analysis results for an axial PWSCC at 90° extrados in specimen 1180-22 showing (a) EC (dashed line) and ERC (solid line) depth profiles and (b) output of the ERC tool using the Argonne data analysis software.	F-10
Figure F-19.	Data analysis results for an axial PWSCC at 0° extrados in specimen 1180-23 showing (a) EC (dashed line) and ERC (solid line) depth profiles and (b) output of the ERC tool using the Argonne data analysis software.	F-11
Figure F-20.	Data analysis results for an axial PWSCC at 90° extrados in specimen 1180-23 showing (a) EC (dashed line) and ERC (solid line) depth profiles and (b) output of the ERC tool using the Argonne data analysis software.	F-11
Figure F-21.	Data analysis results for an axial PWSCC at 90° in specimen 890-01 showing (a) EC (dashed line) and ERC (solid line) depth profiles and (b) output of the ERC tool using the Argonne data analysis software.	F-12
Figure F-22.	Data analysis results for an axial PWSCC at 0° extrados in specimen 890-03 showing (a) EC (dashed line) and ERC (solid line) depth profiles and (b) output of the ERC tool using the Argonne data analysis software.	F-12
Figure F-23.	Data analysis results for an axial PWSCC at 180° flank in specimen 890-04 showing (a) EC (dashed line) and ERC (solid line) depth profiles and (b) output of the ERC tool using the Argonne data analysis software.	F-13
Figure F-24.	Data analysis results for an axial PWSCC at 90° in specimen 890-04 showing (a) EC (dashed line) and ERC (solid line) depth profiles and (b) output of the ERC tool using the Argonne data analysis software.	F-13
Figure F-25.	Data analysis results for an axial PWSCC in specimen 890-07 showing (a) EC (dashed line) and ERC (solid line) depth profiles and (b) output of the ERC tool using the Argonne data analysis software.	F-14
Figure F-26.	Data analysis results for an axial PWSCC at 180° (flaw #3) in specimen 890-08 showing (a) EC (dashed line) and ERC (solid line) depth profiles and (b) output of the ERC tool using the Argonne data analysis software.	F-14
Figure F-27.	Data analysis results for an axial PWSCC at 180° (B1) in specimen 890-08 showing (a) EC (dashed line) and ERC (solid line) depth profiles and (b) output of the ERC tool using the Argonne data analysis software.	F-15
Figure F-28.	Data analysis results for an axial PWSCC at 180° in specimen 890-08 showing (a) EC (dashed line) and ERC (solid line) depth profiles and (b) output of the ERC tool using the Argonne data analysis software.	F-15
Figure F-29.	Data analysis results for an axial PWSCC at 90° in specimen 890-08 showing (a) EC (dashed line) and ERC (solid line) depth profiles and (b) output of the ERC tool using the Argonne data analysis software.	F-16

Figure F-30.	Data analysis results for an axial PWSCC at 180° in specimen 890-15 showing (a) EC (dashed line) and ERC (solid line) depth profiles and (b) output of the ERC tool using the Argonne data analysis software.	F-16
Figure F-31.	Data analysis results for an axial PWSCC at 0° extrados in specimen 890-16 showing (a) EC (dashed line) and ERC (solid line) depth profiles and (b) output of the ERC tool using the Argonne data analysis software.	F-17
Figure F-32.	Data analysis results for an axial PWSCC at 0° intrados in specimen 920-08 showing (a) EC (dashed line) and ERC (solid line) depth profiles and (b) output of the ERC tool using the Argonne data analysis software.	F-17
Figure F-33.	Data analysis results for an axial PWSCC at 90° extrados in specimen 920-08 showing (a) EC (dashed line) and ERC (solid line) depth profiles and (b) output of the ERC tool using the Argonne data analysis software.	F-18
Figure F-34.	Data analysis results for an axial PWSCC in specimen 920-10 showing (a) EC (dashed line) and ERC (solid line) depth profiles and (b) output of the ERC tool using the Argonne data analysis software.	F-18
Figure F-35.	Data analysis results for an axial PWSCC at 0° extrados in specimen 920-12 showing (a) EC (dashed line) and ERC (solid line) depth profiles and (b) output of the ERC tool using the Argonne data analysis software.	F-19
Figure F-36.	Data analysis results for an axial PWSCC at 80° extrados in specimen 920-12 showing (a) EC (dashed line) and ERC (solid line) depth profiles and (b) output of the ERC tool using the Argonne data analysis software.	F-19
Figure F-37.	Data analysis results for an axial PWSCC at 90° extrados in specimen 920-12 showing (a) EC (dashed line) and ERC (solid line) depth profiles and (b) output of the ERC tool using the Argonne data analysis software.	F-20
Figure F-38.	Data analysis results for an axial PWSCC at 180° extrados in specimen 920-15 showing (a) EC (dashed line) and ERC (solid line) depth profiles and (b) output of the ERC tool using the Argonne data analysis software.	F-20
Figure F-39.	Data analysis results for an axial PWSCC at 90° extrados in specimen 920-15 showing (a) EC (dashed line) and ERC (solid line) depth profiles and (b) output of the ERC tool using the Argonne data analysis software.	F-21
Figure F-40.	Data analysis results for an axial PWSCC at 45° in specimen 920-15 showing (a) EC (dashed line) and ERC (solid line) depth profiles and (b) output of the ERC tool using the Argonne data analysis software.	F-21
Figure G-1.	NDE and DE results for a PWSCC at location F in specimen 07-02. Shown here are (a) the estimated EC depth profile based on +Pt data at 300 kHz, (b) DE depth profile with and without RA filter, and (c) SEM image of crack surface.	G-2
Figure G-2.	NDE and DE results for the PWSCC at location B in specimen 07-02. Shown here are (a) the estimated EC depth profile based on +Pt data at 300 kHz, (b) DE depth profile with and without RA filter, and (c) SEM image of crack surface.	G-3
Figure G-3.	NDE and DE results for a PWSCC at location E in specimen 07-03. Shown here are (a) the estimated EC depth profile based on +Pt data at 300 kHz, (b) DE depth profile with and without RA filter, and (c) SEM image of crack surface.	G-4

Figure G-4.	NDE and DE results for a PWSCC at location F in specimen 07-03. Shown here are (a) the estimated EC depth profile based on +Pt data at 300 kHz, (b) DE depth profile with and without RA filter, and (c) SEM image of crack surface.	G-5
Figure G-5.	NDE and DE results for a PWSCC at location E in specimen 14-01. Shown here are (a) the estimated EC depth profile based on +Pt data at 300 kHz, (b) DE depth profile with and without RA filter, and (c) SEM image of crack surface.	G-6
Figure G-6.	NDE and DE results for a PWSCC at location G in specimen 14-01. Shown here are (a) the estimated EC depth profile based on +Pt data at 300 kHz, (b) DE depth profile with and without RA filter, and (c) SEM image of crack surface.	G-7
Figure G-7.	NDE and DE results for a PWSCC at location B in specimen 14-01. Shown here are (a) the estimated EC depth profile based on +Pt data at 300 kHz, (b) DE depth profile with and without RA filter, and (c) SEM image of crack surface.	G-8
Figure G-8.	NDE and DE results for a PWSCC at location F in specimen 15-02. Shown here are (a) the estimated EC depth profile based on +Pt data at 300 kHz, (b) DE depth profile with and without RA filter, and (c) SEM image of crack surface.	G-9
Figure G-9.	NDE and DE results for two PWSCCs at location F in specimen 15-02. Shown here are (a) the estimated EC depth profile based on +Pt data at 300 kHz, (b) DE depth profile with and without RA filter, and (c) SEM image of crack surface.	G-10
Figure G-10.	NDE and DE results for a PWSCC at location D in specimen 20-01. Shown here are (a) the estimated EC depth profile based on +Pt data at 300 kHz, (b) DE depth profile with and without RA filter, and (c) SEM image of crack surface.	G-11
Figure G-11.	NDE and DE results for a PWSCC above the 180° tangent in specimen 22-01. Shown here are (a) the estimated EC depth profile based on +Pt data at 300 kHz, (b) DE depth profile with and without RA filter, and (c) SEM image of crack surface.	G-12
Figure G-12.	NDE and DE results for a PWSCC at location A in specimen 23-01. Shown here are (a) the estimated EC depth profile based on +Pt data at 300 kHz, (b) DE depth profile with and without RA filter, and (c) SEM image of crack surface.	G-13
Figure G-13.	NDE and DE results for a PWSCC at location D in specimen 23-01. Shown here are (a) the estimated EC depth profile based on +Pt data at 300 kHz, (b) DE depth profile with and without RA filter, and (c) SEM image of crack surface.	G-14
Figure G-14.	NDE and DE results for a PWSCC at location D in specimen 25-01. Shown here are (a) the estimated EC depth profile based on +Pt data at 300 kHz, (b) DE depth profile with and without RA filter, and (c) SEM image of crack surface.	G-15
Figure G-15.	NDE and DE results for a PWSCC at location D in specimen 29-01. Shown here are (a) the estimated EC depth profile based on +Pt data at 300 kHz,	

	(b) DE depth profile with and without RA filter, and (c) SEM image of crack surface.	G-16
Figure G-16.	NDE and DE results for a PWSCC at location D in specimen 31-01. Shown here are (a) the estimated EC depth profile based on +Pt data at 300 kHz, (b) DE depth profile with and without RA filter, and (c) SEM image of crack surface.	G-17
Figure G-17.	NDE and DE results for a PWSCC at location D in specimen 52-01. Shown here are (a) the estimated EC depth profile based on +Pt data at 300 kHz, (b) DE depth profile with and without RA filter, and (c) SEM image of crack surface.	G-18

LIST OF TABLES

Table 2-1.	Comparison of U-bend tubing specifications described in EPRI Guidelines [4] and ASME Code [5].....	2-3
Table 2-2.	Mill annealing conditions and mechanical properties of Alloy 600 tubing used for U-bend specimens.	2-4
Table 2-3.	Number of U-bend specimens for each heat.	2-4
Table 2-4.	Chemical compositions (wt%) of Alloy 600 tubes used in the bending.	2-5
Table 4-1.	Summary of correlation method along with the standard deviation of the fit and number of alternate selections based on the NDE parameter.	4-22
Table 4-2.	Summary of least squares fits to the data discussed in Sections 4-1 and 4-3.	4-23
Table A-1.	Timeline for production of PWSCC in U-bend tube specimens.	A-2
Table A-2.	Timeline for various research activities in connection with U-bend tube specimens.	A-2
Table B-1.	Eddy current examination results for specimens with predominantly axial PWSCC throughout the bend region of 57-mm-radius U-bends.	B-2
Table B-2.	Eddy current examination results for specimens with predominantly axial PWSCC at tangential regions of 57-mm-radius U-bends.	B-5
Table C-1.	Eddy current examination results for specimens with predominantly circumferential PWSCC throughout the bend region of 152-mm-radius U-bends.	C-2
Table D-1.	Eddy current and visual (videoscope) data for PWSCCs in 57-mm-radius U-bend tube specimens.	D-2
Table D-2.	Pre- and post-pressure test NDE and DE data for PWSCCs in 57-mm-radius U-bend tube specimens.	D-27
Table E-1.	Eddy current and visual (videoscope) data for PWSCCs in 152-mm-radius U-bend tube specimens.	E-2
Table E-2.	Pre- and Post-pressure test NDE and DE data for PWSCCs in 152-mm-radius U-bend tube specimens.	E-12

EXECUTIVE SUMMARY

Research was conducted to assess the ability of conventional eddy current (EC) inspection techniques to detect and size primary water stress corrosion cracks (PWSCCs) in the U-bend region of steam generator (SG) tubes with small-bend radii. In comparison with other regions of the SG tube bundle, the higher level of interference associated with tube geometry and dimensional variations at small radius U-bends, commonly referred to as tube ovalization, can degrade the signal-to-noise ratio (S/N) and diminish the utility of nondestructive examination (NDE) techniques in those regions. Assessing the reliability of EC in-service inspection (ISI) techniques in application to U-bend regions that exhibit a high degree of tube deformation is important from the standpoint of structural integrity.

The uncertainties associated with any particular NDE technique need to be determined in advance so they can be factored into engineering assessments of tube integrity. To that end, a library of tube specimens was assembled at Argonne National Laboratory (Argonne) under the International Steam Generator Tube Integrity Program (ISG-TIP). Representative U-bends were fabricated by one of the primary SG tube manufacturers in accordance with the specifications identified in industry guidelines and American Society of Mechanical Engineers (ASME) codes. A facility was set up to induce stress corrosion cracking (SCC) in U-bend tubes with two different radii of curvature. The focus of the flaw manufacturing efforts in this work was on PWSCCs at U-bend regions, which are more challenging to produce than cracks in straight tubes or at locations that do not pose major access limitations. The NDE and destructive examination (DE) data obtained in this work thus complement other databases of U-bend cracking, which mostly include data obtained from specimens with machined notches or laboratory-produced cracks that originate from the tube's secondary side.

The EC inspection data were analyzed at different stages of the pre- and post-crack manufacturing process using both conventional and alternative data analysis methods. Eddy current examinations included a number of different techniques that utilize bobbin, rotating, and array probes. The results of research activities presented in this report, however, pertain only to data collected with one particular type of rotating probe. That probe is routinely used in the United States for inspecting the U-bend regions of the first few rows of tubes within the SG tube bundle and any other potential flaw indications found by bobbin inspections.

A study was initially conducted to identify the primary sources of background interference in EC rotating probe data in small radius U-bends. It was determined that the combined effect of tube dimensional and geometry variations, introduced by the bending process, produces a complex probe response at U-bends. This undulating probe response, commonly referred to as U-bend noise, is attributed to the change in conductivity caused by non-uniformity of tube wall thickness and variations in probe alignment and lift-off associated with tube ovalization. The U-bend noise exhibits an increasing trend in amplitude, starting just above the tangents and reaching a maximum at the apex. The characteristic probe response at U-bend regions was found to be fairly consistent in EC data from tube specimens with the same bend radius. In addition, a comparable rotating probe response at U-bends was observed in a limited set of field data examined in this study. The amplitude of the background noise is largest in U-bends with the smallest bend radius and drops rapidly for bend radii greater than 152 mm. As the bend radii increase, the level of background noise at U-bend regions becomes comparable to that of straight sections of SG tubing.

The pseudo-periodic rotating probe response at U-bends can interfere both constructively and destructively with flaw signals. Thus, the ability to detect and size the same SCC signal at different

locations within the U-bend region can be affected by its axial and circumferential position along that section of the tube. Because of the difficulty in separating potential flaw signals, particularly those with a low amplitude, from the more dominant background noise, the measurement of signals at U-bend regions becomes more subjective as a direct consequence of diminished S/N. This subjectivity, in turn, can lead to a higher degree of uncertainty in data analysis results. An important observation made based on the results of the initial investigations was that improper measurement of signals for historical comparison of EC data could lead to underestimation of growth in crack signals at U-bends. To compare EC data from different inspections using conventional data analysis methods, the measurement window should enclose the component of signal principally associated with the flaw. In the presence of a strong background interference, inclusion of the entire composite signal (i.e., the combined probe response from background and flaw) within the measurement window can lead to underestimation of the percentage change in amplitude of the flaw signal.

As part of the studies on the source of U-bend noise, we also evaluated different methods to suppress unwanted signals in rotating probe data. Among a number of signal processing techniques evaluated for this purpose, bidirectional statistical filters were found to be best suited for improving S/N at U-bends while minimally affecting the signals associated with cracks. The use of signal processing algorithms evaluated in this work generally resulted in enhanced detection capability for crack-like signals at U-bends. However, such tools should be used with caution and in a consistent manner because arbitrary application of filters intended for optimal suppression of unwanted signals could also result in inadvertent suppression of potentially consequential signals.

Two separate studies were subsequently conducted to assess the viability of correlations between various NDE parameters, obtained through analyses of EC inspection data, and structural parameters associated with tube integrity, obtained by DE. Only data from 57-mm-radius U-bend specimens were included in those assessments.

The first study was conducted immediately after pressure testing of the U-bend specimens but before the completion of destructive examinations. It revolved around assessing the degree of indirect correlation between the NDE parameters, obtained using conventional analysis of EC inspection data (i.e., NDE parameters indicative of flaw size), and tube structural integrity, as determined by the measured failure pressure. The dataset used in those evaluations was thus limited to cracks that failed during pressure testing of the tubes. Based on the results of the first study, we identified a subset of the NDE parameters, among those examined, consisting of the more viable indicators of tube structural integrity.

Following the completion of destructive examinations, a second study was conducted to assess the viability of both direct and indirect correlations between NDE parameters and destructively measured structural parameters. The DE results obtained by fractography served as the ground truth for flaw size. The NDE estimates of flaw size used in the second study included those obtained using both conventional and alternative data analysis methods. The later analyses were performed using the EC inspection data acquired with a +Point™ (+Pt) probe shortly before the U-bend tube specimens were subjected to pressurization. The NDE depth profiles for cracks were all generated by using Argonne's computer-aided data analysis tool.

Among various NDE parameters evaluated in this study, the EC signal amplitude (voltage) and the crack area, estimated based on analyses of +Pt probe data, were found to be the more viable indicators of tube structural integrity associated with PWSCCs at the U-bend region. The results were consistent for NDE sizing results obtained using conventional and alternative data analysis

methods. The maximum amplitude (voltage) of PWSCC signal provided the highest degree of correlation with tube failure pressure. This implicit relationship can be explained by the underlying principle that, for a given type of flaw and in the absence of different contributing factors, the EC probe response is more closely associated with the flaw volume than with any linear dimension of the flaw. By itself, the NDE estimate of maximum depth of the crack provided a notably lower degree of correlation with DE structural parameters than crack length. However, the maximum depth of a crack may be of greater relevance from the leakage integrity standpoint. Another observation from the studies was lower scatter in correlation plots of NDE versus DE structural parameters when using the equivalent rectangular crack (ERC) dimensions, generally referred to as structural length and depth, instead of the actual crack dimensions. Validation of the ERC model for cracks at U-bends is reported elsewhere. In general, direct correlations between NDE and DE structural parameters produced larger standard deviations than those based on indirect correlations (i.e., tube failure pressure as a function of EC estimates of crack size).

From a statistical analysis standpoint, the performance indicator used in correlation analyses in this work is the regression error rather than the correlation coefficient. Therefore, the results are more indicative of viable trends in the data rather than the prediction accuracy of the correlation functions. It is worth noting that for engineering assessments, systematic under- or over-estimation of any particular structural parameter could, in principle, be accounted for once the NDE uncertainties and trends have been determined in advance. In all of the cases examined, a lower standard deviation was obtained when separate regression lines were fitted to the data for cracks at tangents and cracks at other regions of the U-bend (above tangents). This is plausibly associated with the difference in fracture mechanics behavior of cracks at those locations in U-bend tubes with a smaller bend radii.

As noted previously, the inspection reliability assessments in this work are all based on the NDE results obtained using one particular EC rotating probe examination technique. Therefore, the viability of such correlations between structural parameters and NDE parameters for other inspection techniques and for other flaw types needs to be evaluated independently. It is also worth noting that the assessments are based, in part, on the analysis of EC inspection data with prior knowledge about the location and history of the laboratory produced flaws in the U-bend specimens. Because the potential variabilities associated with field analyses of ISI data are not factored into analyses of EC examination data from laboratory specimens, the results presented in this report may be treated as the upper limit of the NDE technique's detection capability and sizing accuracy. In principle, ISI reliability could be further improved through comparative assessments of NDE data acquired with multiple probe types and analyzed using alternative data analysis methods. Finally, based on the results of this research, it can be stated that the level of confidence in engineering assessments could be increased by considering a larger number of NDE parameters that are viable indicators of SG tube structural integrity.

The following suggestions are made regarding follow-on research efforts on inspection reliability for U-bends. The results presented in this report are based on characterization of the dominant PWSCC in each U-bend specimen and a small subset of secondary cracks. The available database could be augmented with data from a larger number of small cracks by conducting additional destructive examinations of the existing specimens. Furthermore, analyses of the available EC examination data collected with different probe types could help improve SG tube inspection reliability through comparative assessments of NDE techniques. For example, limited studies conducted to date indicate that improved detection and sizing of shallow primary side flaws could be achieved by using a high-frequency rotating pancake probe. Evaluation of alternative sizing methods based on analysis of the available data from U-bend specimens could help toward implementation of more accurate sizing techniques. Future research on this subject

can further leverage the available NDE and DE data assembled as a result of this work. Another area of research with a broad range of applications is the use of signal superposition to augment the existing database of PWSCCs at U-bends. This approach could help significantly reduce the cost associated with experimental evaluations. Finally, assessing the viability of correlations between NDE parameters and structural parameters for challenging flaw types in other regions of SG tube bundle warrants further investigation.

ACKNOWLEDGMENTS

The authors wish to acknowledge C. W. Vulyak, E. R. Koehl, and E. J. Listwan for their assistance with experimental activities. The authors also thank K. Karwoski, E. Murphy, C. Harris, M. Baquera, P. Klein, A. Johnson, and P. Purtscher for their useful guidance in the performance of this work. Use of the Center for Nanoscale Materials, an Office of Science user facility, was supported by the U.S. Department of Energy, Office of Science, Office of Basic Energy Sciences, under Contract No. DE-AC02-06CH11357.

ABBREVIATIONS AND ACRONYMS

Argonne	Argonne National Laboratory
ASME	American Society of Mechanical Engineers
DE	Destructive Examination
EC	Eddy Current
ECT	Eddy Current Testing
EDM	Electro-Discharge Machined
EPRI	Electric Power Research Institute
ERC	Equivalent Rectangular Crack
ETSS	Examination Technique Specification Sheet
FEA	Finite Element Analysis
HF-PC	High-Frequency Pancake Coil
ID	Inside Diameter, Identification
IRSN	Institut de Radioprotection et de Sûreté Nucléaire
ISG-TIP	International Steam Generator Tube Integrity Program
ISI	In-service Inspection
LS	Least Squares
NDD	No Detectable Degradation
NDE	Nondestructive Examination
NRC	U.S. Nuclear Regulatory Commission
OD	Outside Diameter
+Pt	+Point™
PDA	Percent Degraded Area
PWR	Pressurized Water Reactor
PWSCC	Primary Water Stress Corrosion Crack(s)/Cracking
RA	Running Average
RSG	Recirculating Steam Generator
S/N	Signal-to-Noise Ratio
SCC	Stress Corrosion Cracking
SEM	Scanning Electron Microscopy
SG	Steam Generator
SS	Stainless Steel
TSP	Tube Support Plate
TT	Thermally Treated
TW	Through Wall
VT	Visual Testing

1 INTRODUCTION

Stress corrosion cracking (SCC) in Steam Generator (SG) tube U-bend regions has been reported for many years, and a number of documents summarizing the experience with that mode of degradation have been published. During the 1970s, axial primary water stress corrosion cracking (PWSCC) occurred at the apex and at the hot leg tangent regions. In the past, U-bends were not stress-relieved after the bending process. Metal ball mandrels, inserted during the bending process, caused an irregular tangent region with high residual stress, which, in turn, resulted in cracking. The bending process has since been modified, and a stress-relieving heat treatment is performed for low-row U-bends to reduce the potential for cracking. Based on the evidence of past occurrences, cracking can initiate anywhere along the U-bend, including in the tangent regions. Crack morphology can be axially and circumferentially oriented, and cracks can initiate from both the inside diameter (ID) and the outside diameter (OD) of a tube. Primary side cracking, however, has been more dominant than secondary side cracking at U-bends.

A scoping study was conducted early in this work to evaluate past experiences with U-bend cracking in SG tubes. That information was used to determine the morphology (shape, orientation, location, etc.) of laboratory-produced cracks in the specimens made for inspection reliability studies at Argonne National Laboratory (Argonne). Three types of cracking were selected and produced: axial PWSCC throughout the bend region, axial PWSCC at the tangent region, and circumferential PWSCC throughout the bend region. It is worth noting that, among the crack types, axial PWSCC was the most challenging to produce.

The laboratory-produced PWSCCs were initially compared with field-induced cracks to determine whether they are representative [1, 2]. The Electric Power Research Institute (EPRI) guidelines provide a procedure for such comparative evaluations [3]. While the procedure has various requirements, it basically consists of comparing the nondestructive examination (NDE) and destructive examination (DE) data generated from the laboratory specimens with the field data. However, little information is available on the morphology of field cracks in U-bends. Therefore, the evaluations in this work relied mainly on comparison of NDE parameters between the laboratory and field data. Based on these evaluations, it was determined that the eddy current (EC) probe response associated with laboratory cracks are generally comparable to those from U-bend cracks found in the field [1, 2]. However, further verification studies may be needed, especially concerning the uncertainties in measuring crack-like EC signals in small-radius U-bends.

Research activities were carried out to assess the ability of conventional EC inspection techniques to detect and size flaws in the U-bend region of SG tubes. In comparison with other SG elevations, the higher level of noise associated with tube geometry and dimensional variations at small-radius U-bends, generally referred to as tube ovalization, can result in a greater degradation of signal-to-noise ratio (S/N) and, in turn, diminish the utility of NDE techniques in those regions. Assessing the reliability of EC in-service inspection (ISI) techniques in application to U-bend regions that exhibit a high degree of tube deformation is important from the standpoint of structural integrity. The uncertainties associated with any particular NDE technique need to be determined in advance so they can be factored into engineering assessments of tube integrity. To this end, a library of representative specimens was assembled at Argonne for EC inspection reliability studies. A facility was set up to induce SCC in U-bend tubes with two different radii of curvature. The focus of flaw manufacturing efforts in this work is on PWSCC, which is more challenging to produce at U-bends in comparison with laboratory-produced flaws at other locations along SG tubing. The data reported here thus complements other databases of U-bend cracking, which mostly consist of data from tubes with secondary side manufactured flaws.

Eddy current inspections were performed on U-bend specimens at different stages of the flaw manufacturing process. The data were then analyzed using both conventional and alternative data analysis methods. The timeline for various research activities carried out in connection with the U-bend specimens is provided in Appendix A. The results presented in this report pertain only to data collected with a flexible +Point™ (+Pt) rotating probe that is more commonly used in the U.S. for inspection of low-row U-bend regions of the SG tube bundle.

Two separate studies were conducted, before and after DE of the U-bend specimens, to assess potential correlations between NDE parameters and structural parameters. The initial study, conducted immediately after pressure testing of all specimens, assessed the correlations between various NDE parameters (i.e., EC estimates of flaw size) and tube structural integrity (i.e., failure pressure). Therefore, the dataset was limited to flaws that failed during pressure testing of the tubes. The flaw sizing results used in the first study were based on conventional manual analysis of EC inspection data in accordance with a generic examination technique specification sheet (ETSS). Following the completion of destructive examinations of the specimens, a second study was conducted to assess the viability of indirect and direct correlations between NDE parameters and structural parameters. The NDE estimates of flaw size used in the second study included those obtained using conventional as well as alternative EC data analysis methods. Alternative analyses of EC data, discussed later in this report, were performed using the latest version of the data analysis software implemented at Argonne.

In the following sections, results are reported from the two inspection reliability studies on small-radius U-bends with primary side cracking. The organization of the report aligns with the sequence in which the research activities were conducted. The flaw manufacturing process is briefly described in Section 2. Tables in that section show the inventory of U-bend tubes and the locations of laboratory-produced cracks for a subset of those tubes used for NDE-related studies. Eddy current inspections are discussed in Section 3, along with post-cracking inspections of the specimens and the effect of U-bend geometry on EC probe response. In Section 4, the results of two separate analyses are presented on correlation of NDE parameters with tube structural integrity. Section 4 also compares NDE and destructive examination results. Finally, Section 5 provides concluding remarks on the results of studies performed in this work. Suggestions are also provided in that section regarding follow-on research efforts on inspection reliability for U-bends that can leverage the available database of NDE and DE data assembled as a result of this work.

2 PRODUCTION OF CRACKS IN U-BEND SPECIMENS

The following sections describe the manufacturing specifications of the U-bend tubes (acquired from Valinox), the inspection results, and the laboratory procedures developed and used for manufacturing the three types of PWSCC in U-bend tubes.

2.1 U-bend Specifications

The contract for bending straight mill-annealed Alloy 600 tubes was awarded to Valinox, France. Valinox is one of the SG tube manufacturers for nuclear power plants. The nominal tube diameter and wall thickness used for manufacturing the U-bends was 19.1 mm (0.75 in.) and 1.09 mm (0.043 in.), respectively. The selected bend radii were 57 mm (2.25 in.) and 152 mm (6.0 in.), representing the first row and a higher row (possibly a third or fourth row) U-bends of recirculating SGs (RSGs), respectively. The U-bends were not heat treated after bending. The specifications are described for the bending processes and geometrical dimensions of U-bends in the following.

There are two sources available for the specifications on manufacturing U-bends:

- EPRI guidelines [4] and
- American Society of Mechanical Engineers (ASME) Boiler & Pressure Vessel Code Section II, SB-163 [5].

Figure 2-1 shows a schematic of U-bend tubing and the locations of extrados, intrados, flank, apex, and tangent. As illustrated in the cross-sectional view of Figure 2-1, the wall thickness varies due to the tube bending process; the wall thickness is reduced along the extrados and increased along the intrados. The thickness along the flank is similar to what it is prior to bending. In reference to the inset drawing in Figure 2-1, the minimum wall thickness of the U-bend is usually at the apex extrados region. For the wall thickness reduction, the allowable limits from the two sources are different. The EPRI guidelines say that the wall thickness reduction at the apex extrados shall not exceed 12% of the initial value. The ASME code specifies that the wall thickness at the apex of the U-bend section shall not be less than the value determined by the equation provided in Table 2-1. The variables in the ASME equation include the minimum wall thickness, bend radius, and tube OD. For comparison, the allowable wall thickness was calculated using that equation. The estimated minimum wall thickness of 19.1 mm OD tubing is around 0.99 mm (0.039 in.), assuming a design pressure of 17.3 MPa (2,500 psig) at 350°C, which is a conservative assumption. The ASME allowable wall thicknesses after bending become 0.86 and 0.94 mm (0.034 and 0.037 in.) for 57- and 152-mm bend radii, respectively. These wall thickness reductions are equivalent to 21% and 14% reduction with respect to the nominal thickness (1.09 mm). Therefore, the ASME code is less restrictive on the wall thickness reduction than the EPRI guidelines.

A straight tube becomes oval shaped after bending, as illustrated in the cross-sectional view of Figure 2-1. EPRI guidelines suggest that the ovality, which is determined as the ratio of the difference between maximum and minimum outside diameters to the nominal diameter, shall not exceed 3%, except for specimens of 22.2-mm (0.875-in.) OD tubing with a 57-mm bend radius, where it shall not exceed 4.5%. The ASME code states that neither the major nor the minor outside diameter of the tube at any one cross-section included within the points of tangency of the bend shall deviate from the nominal diameter prior to bending by more than 10%, which is much less restrictive than the EPRI guidelines.

Buckling, which is specified only in the EPRI guidelines and is determined as the difference between outside diameter at the largest crest and the outside diameter at the adjacent valley, shall not exceed 3% of the nominal outside diameter, as specified by those guidelines. The ASME code specifies that the leg spacing, determined by the distance between the points of tangency of the bend to the legs, shall not vary from the $2R$ ($=2 \times \text{Bend Radius}$) by more than 1.6 mm (1/16 in.) when the centerline bend radius is equal to or less than 460 mm (18 in.).

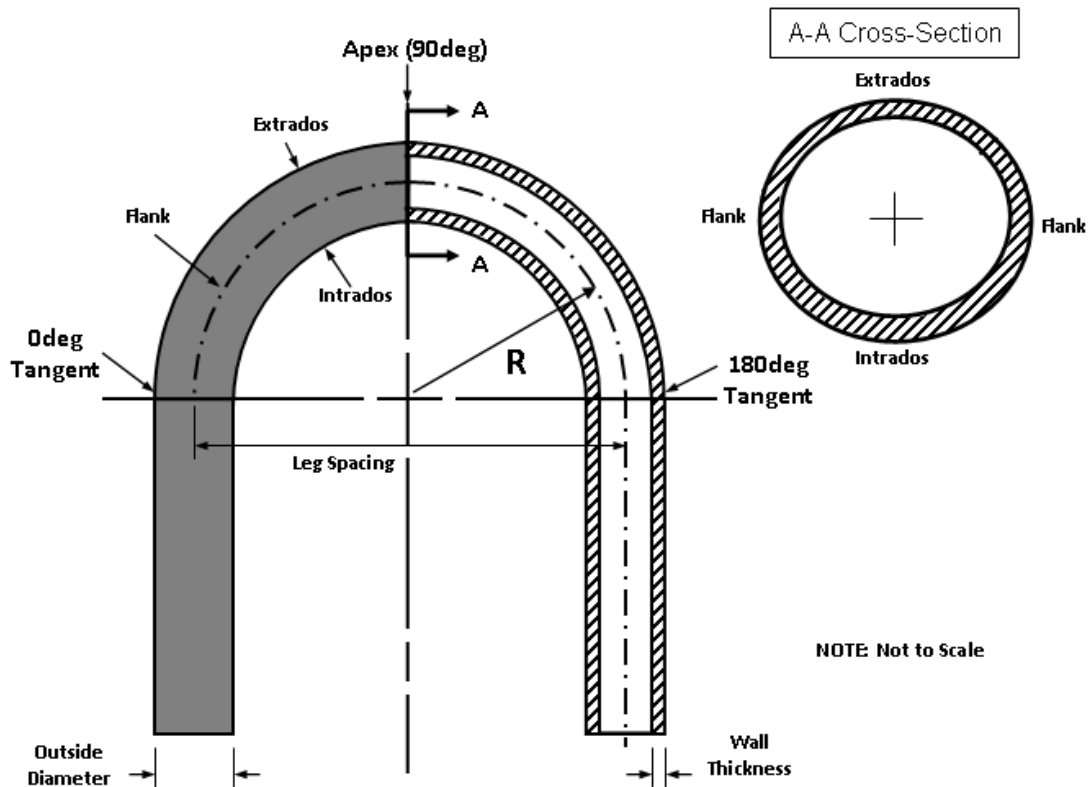


Figure 2-1. Schematic of U-bend tubing showing the locations of extrados, intrados, flank, apex, and tangent.

Table 2-1 compares the EPRI and the ASME specifications. It is noted that there are some other requirements not included in Table 2-1, such as hydrostatic testing or leg length difference. The bending method and buckling limitations are specified only in the EPRI guidelines, which recommend bending the tubing without an internal mandrel; but if needed, a plastic (usually Nylon) cylindrical mandrel can be used for smaller bend radius U-bends. Neither specification discusses requirements for the bending die or tools.

Table 2-1. Comparison of U-bend tubing specifications described in EPRI Guidelines [4] and ASME Code [5].

#	Specification Description	EPRI Guidelines	ASME Code Section II, SB-163
1	Bending Method	Without internal mandrel or using an internal plastic cylindrical mandrel; no metal ball mandrel.	Not specified.
2	Wall Thickness Reduction	Shall not exceed 12% of the initial value.	At the apex of the U-bend section; shall be not less than the value determined by the following Eq.: $TF = T(2R) / (2R + D)$ where: TF=thickness after bending, T=min. permissible thickness of tube wall prior to bending, R=centerline bend radius, D=nominal outside diameter of the tube.
3	Buckling	Shall not exceed 3% of the nominal OD. Determined by the difference between outside diameter at the largest crest and the outside diameter at the adjacent valley.	Not specified.
4	Ovality	Shall not exceed 3%, except for inner two rows of 22.2-mm (7/8-in.) OD tubing: then shall not exceed 4.5%. Determined by the ratio of the difference between maximum and minimum outside diameters to the nominal diameter: $Ovality = (D_{max} - D_{min}) / D_{nom}$	Shall not deviate from the nominal OD prior to bending by more than 10%.
5	Leg Spacing	Not specified.	Shall not vary from the 2R by more than 1.6 mm (1/16 in.) when the centerline bend radius is equal to or less than 460 mm (18 in.). Determined by the distance between the points of tangency of the bend to the legs.

2.2 U-bend Inspection and Data Verification

A total of 156 U-bend specimens with 19.1 mm OD were manufactured by Valinox. Table 2-2 shows the heat treatment conditions and the mechanical properties of various heats used for U-bend specimens. The U-bends are composed of two different heats and three different lots. The heat NX8524 has two lots, which are identified as “NX8524LT” and “NX8524HT” in this report. Table 2-3 shows the specimen numbers for each heat. The U-bends with smaller bend radius are mostly made out of NX8524LT heat, whereas the larger-radius U-bends show four different heat treatment conditions. Table 2-4 shows the chemical compositions of the three Alloy 600 tube heats used for the U-bend specimens.

The U-bend specimens and a data package provided by Valinox were inspected to determine whether they met the specifications. Argonne provided the U-bend specifications according to the EPRI guidelines, except for the leg spacing, which followed the ASME code. Figure 2-2 shows the as-received representative 19.1-mm-OD U-bends with bend radii of 57 mm and 152 mm. Based on the data package, all specimens met the specifications regarding wall thickness reduction, ovality, buckling, and leg spacing, except one U-bend specimen. To confirm that the data reported in the data package meets the specification the wall thicknesses and ovalities of specimens were measured at Argonne.

Table 2-2. Mill annealing conditions and mechanical properties of Alloy 600 tubing used for U-bend specimens.

Tube OD (mm)	Heat #	Carbon Content	Final Mill Annealing Condition	Mechanical Properties			
				0.2% YS @RT (MPa)	UTS @RT (MPa)	0.2% YS @350°C (MPa)	UTS @350°C (MPa)
19.1	NX8524LT	0.022–0.023	@950°C for 5 min. 30.sec	310	679	233	630
19.1	NX8524HT	0.022–0.023	@1024°C for 3 min.	241	662	No data	No data
19.1	NX8520	0.022	@1024°C for 3 min.	261	612	No data	No data

Table 2-3. Number of U-bend specimens for each heat.

Bend Radius	NX8524LT	NX8524HT	NX8520
57 mm	90	1	0
152 mm	27	7	31

Table 2-4. Chemical compositions (wt%) of Alloy 600 tubes used in the bending.

Heat #	C	Mn	Fe	S	Si	Cu	Ni	Cr	Al	Ti	Co	P	B	N
NX8524 LT/HT	0.022- 0.023	0.20	9.11- 9.16	<0.001	0.17- 0.20	<0.01	74.66- 74.95	14.94- 15.21	0.22- 0.24	0.29- 0.35	0.01- 0.02	0.003- 0.005	0.002- 0.004	<0.01
NX8520	0.022	0.19	7.96- 8.03	<0.001	0.18- 0.21	0.02	75.63- 75.77	15.28- 15.40	0.21	0.26- 0.34	0.02	0.004	0.002- 0.004	<0.01

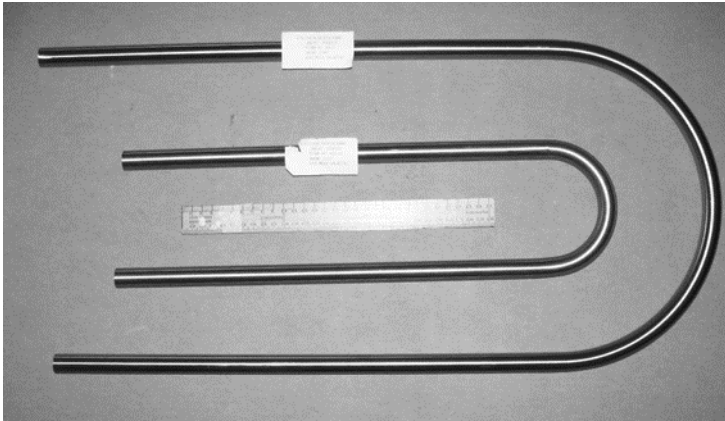


Figure 2-2. U-bend specimens with 19.1-mm (0.75-in.) OD and with two different bend radii of 57 mm (inner tube) and 152 mm (outer tube).

2.2.1 Verification of Dimensional Specifications

Dimensional measurements were performed at Argonne to independently verify that the specimens meet the specified tolerances. Figure 2-3 shows the distributions of the wall thickness reduction and the ovality for 19.1-mm OD tubes with 57-mm-bend-radius U-bends. The data indicate that they all meet the EPRI specification limits for the wall thickness reduction (< 12%) and ovality (< 3%). However, specimens closest to the limits were measured for the purpose of confirmation. Figure 2-4 shows the distributions of wall thickness reduction and ovality for 19.1-mm OD tubes with 152-mm-bend-radius U-bends. As compared with the data in Figure 2-3, the wall thickness reduction and ovality are lower, which is consistent with a general trend that as the bend radius becomes larger, the wall thickness reduction and ovality become smaller.

To verify data provided by Valinox on ovality and wall thickness reduction, ovality and wall thickness reduction were measured for selected U-bend specimens at the apex and $\pm 45^\circ$ away from the apex region. A micrometer was used for ovality measurements. The micrometer was calibrated using a standard metal block before measuring tube OD. For 19.1-mm OD U-bends, the measurements made by Argonne and Valinox were consistent with each other, with only a relatively small discrepancy observed between the two.

The wall thickness of U-bends was measured by an ultrasonic thickness meter (NOVA 900, NDT Systems). Because the sound velocity varies with materials, a piece of Alloy 600 tube cut from a U-bend leg was used as a calibration block. Although the measurements of wall thickness made by Valinox and Argonne showed some discrepancies, all wall thickness measurements made by both parties were lower than the specification limit of 12%. For the entire set of 19.1-mm OD

tubing, the measured wall thickness reduction at the apex varied between 7% and 11% for the 57-mm bend radius and between 2% to 6% for the 152-mm bend radius.

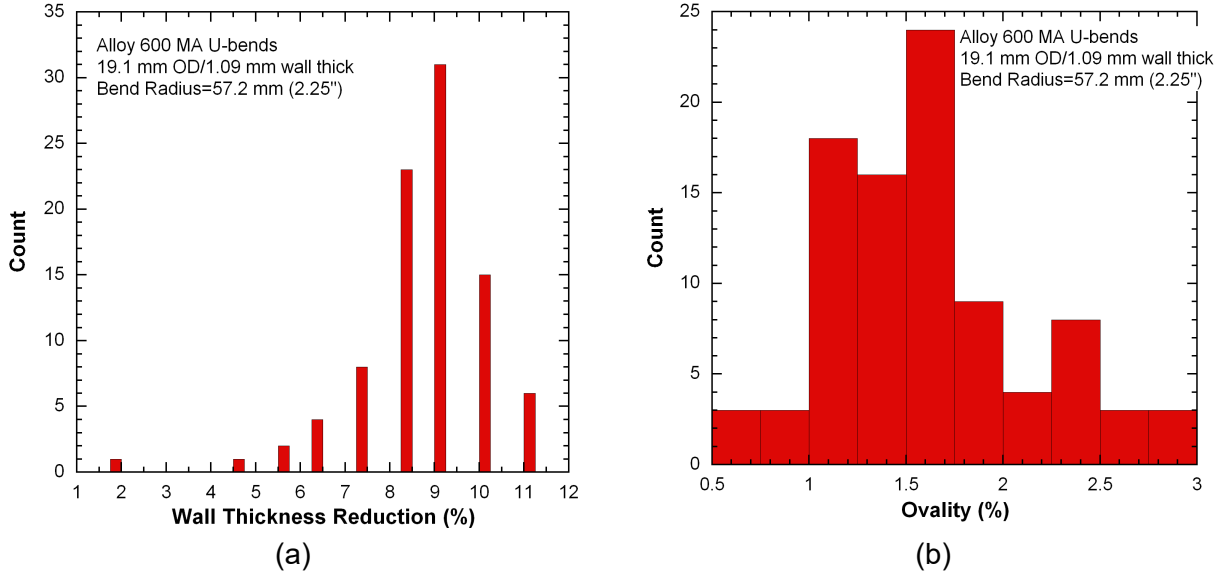


Figure 2-3. Distributions of (a) the wall thickness reduction at the extrados apex and (b) the ovality for 19.1-mm OD and 57-mm bend radius U-bend specimens, using data reported by Valinox.

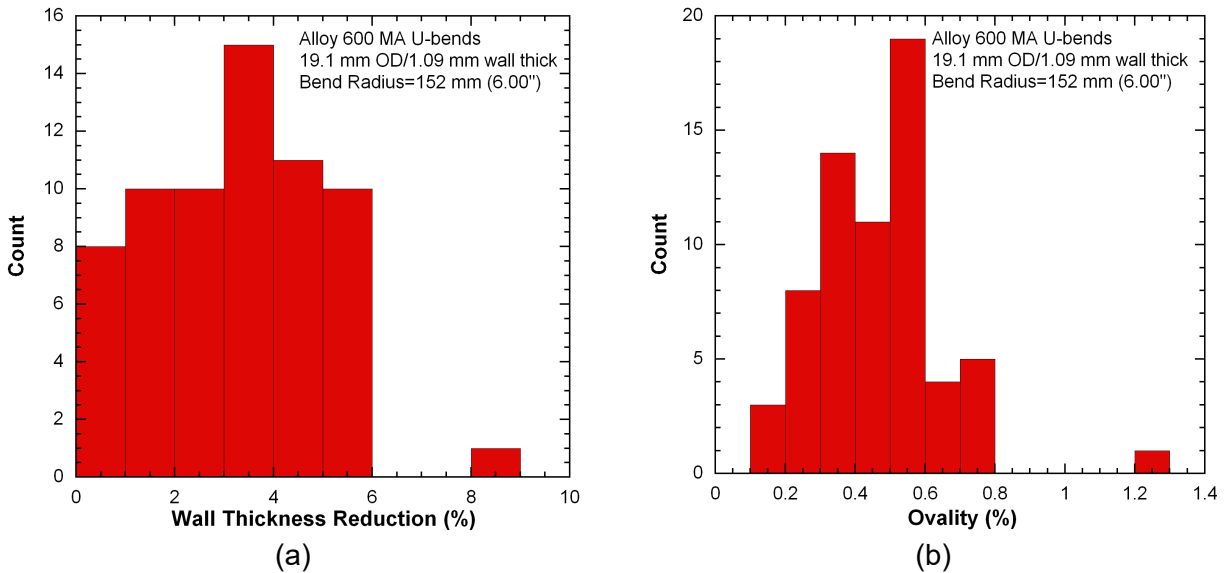


Figure 2-4. Distributions of (a) the wall thickness reduction at the extrados apex and (b) the ovality for 19.1-mm OD and 152-mm bend radius U-bend specimens, using data reported by Valinox.

2.2.2 Characterization of U-bends

Figure 2-5 shows photos of the U-bend regions near “0deg” and “180deg” tangents for a 19.1-mm OD tube. One tangent identified as “0deg” throughout this report has a well-defined tangential point, whereas the other tangent identified as “180deg” shows no definite point of the tangency. The “180deg” tangent area shows a slight dent at the extrados and a bulge at the intrados, although they may not be visually discernible in the photos. This observation suggests that there are irregular shapes at one tangent zone. Based on the information provided by the vendor, this phenomenon is rather typical in U-bends with a small bend radius, suggesting that low-row U-bends in actual SGs would also have this geometric irregularity.

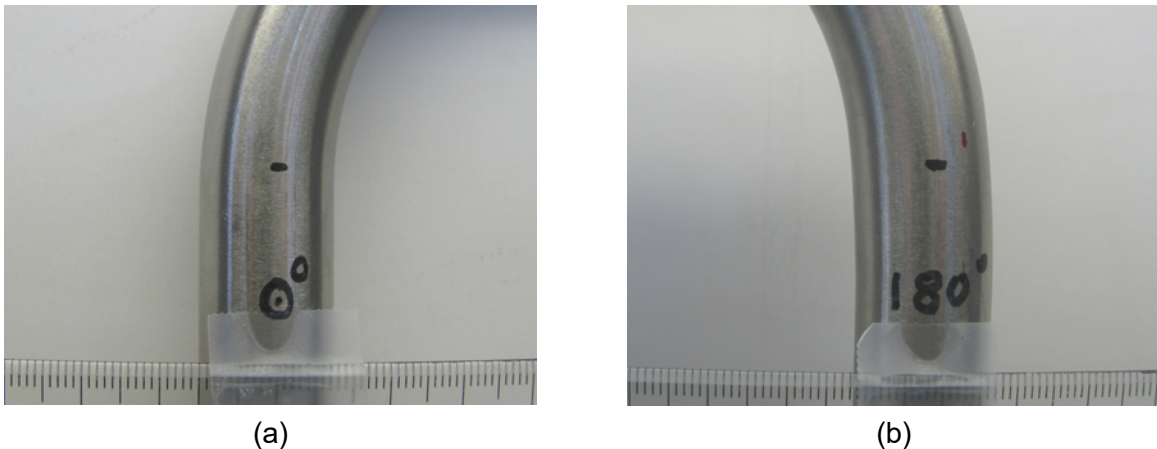
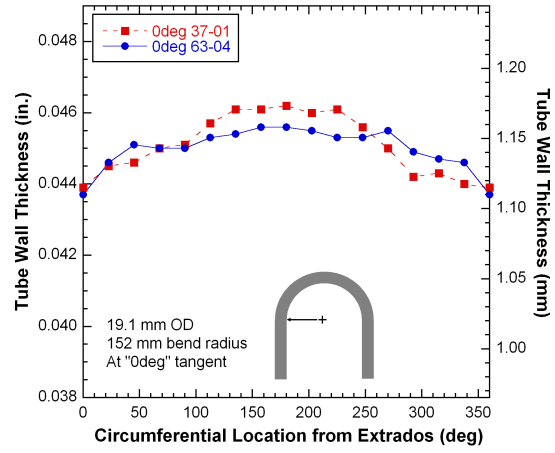
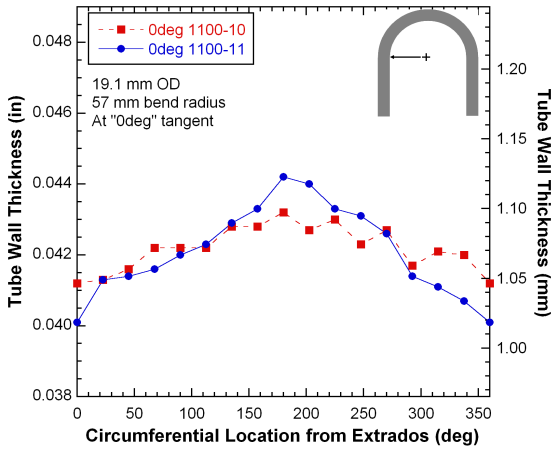


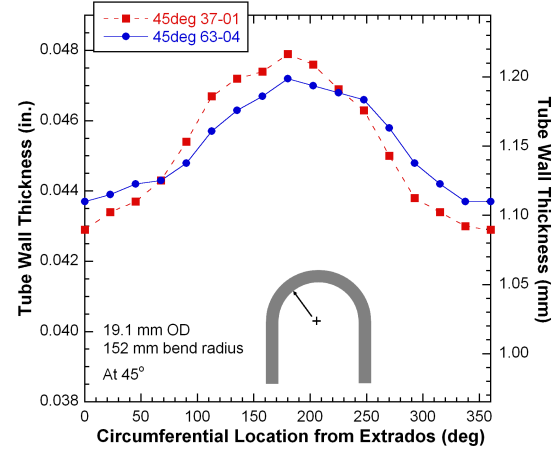
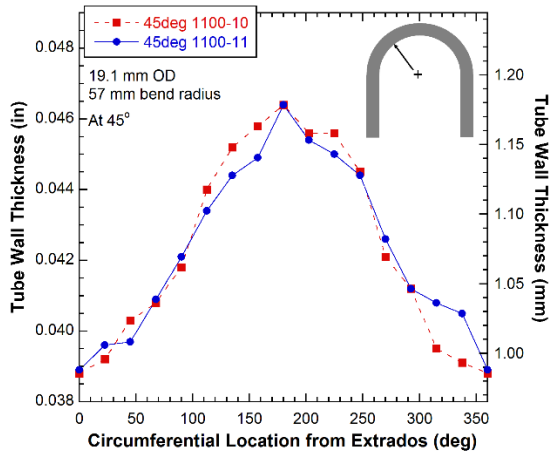
Figure 2-5. Photographs showing sections of a representative 19.1-mm OD U-bend tube near (a) 0deg and (b) 180deg tangents. Visible in the photo of the 180deg tangent are light dent at the extrados and bulge at the intrados.

Wall thicknesses of U-bend specimens were measured at various locations by using the ultrasonic thickness gauge noted in the previous section. Figure 2-6 shows the measured wall thickness variations of representative 19.1-mm OD U-bends along the circumference at three locations: “0deg” tangent, 45°, and 90° (apex). Two U-bend tubes for each bend radius were selected to estimate the tube-to-tube variation. As expected, the wall thickness becomes thicker at the intrados and thinner at the extrados because of the bending process, although the extent of wall thickness variation was not significant at the tangential point. The wall thickness profiles along the circumference were quite similar at the 45° and the 90° locations. The specimen-to-specimen variation was not noticeable in those cases. However, the true variation can only be determined by using a larger number of data points (refer to Figures 2-3 and 2-4). The wall thickness variation was more pronounced in tubes with a smaller bend radius than those with a larger bend radius.

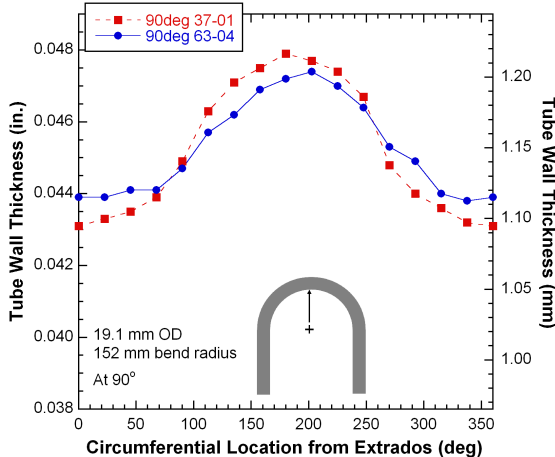
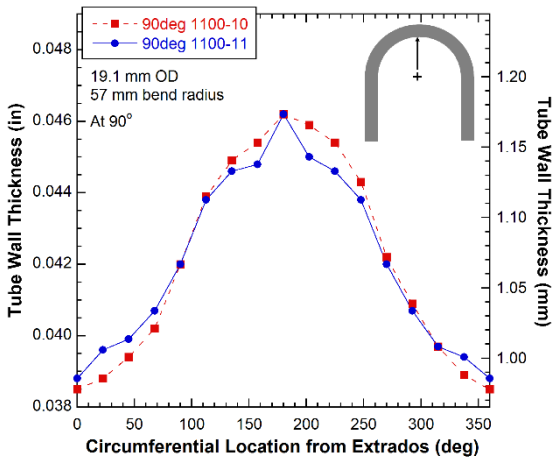
To obtain additional baseline data, wall thickness profiles along the U-bend axis were also measured using an ultrasonic thickness gauge. Figure 2-7 shows the thickness profiles for a 19.1-mm OD U-bend with a 57-mm bend radius measured along the angle of U-bend axis. As expected, the tube wall at U-bend extrados became thinner and at the intrados became thicker as a result of the bending process. There is no significant change in the wall thickness at the flank region except for the area near the 0° tangent. The wall thickness at both the extrados and the intrados was quite uniform along the angle of U-bend axis. Therefore, it was decided that it is not necessary to modify a common industry practice, which is to find the maximum wall thickness reduction, where the wall thickness is measured at the apex.



(a)



(b)



(c)

Figure 2-6. Measured wall thickness variation of 19.1-mm OD U-bends at (a) “0deg” tangent, (b) 45°, and (c) 90° for (left) 57-mm bend radius and (right) 152-mm bend radius.

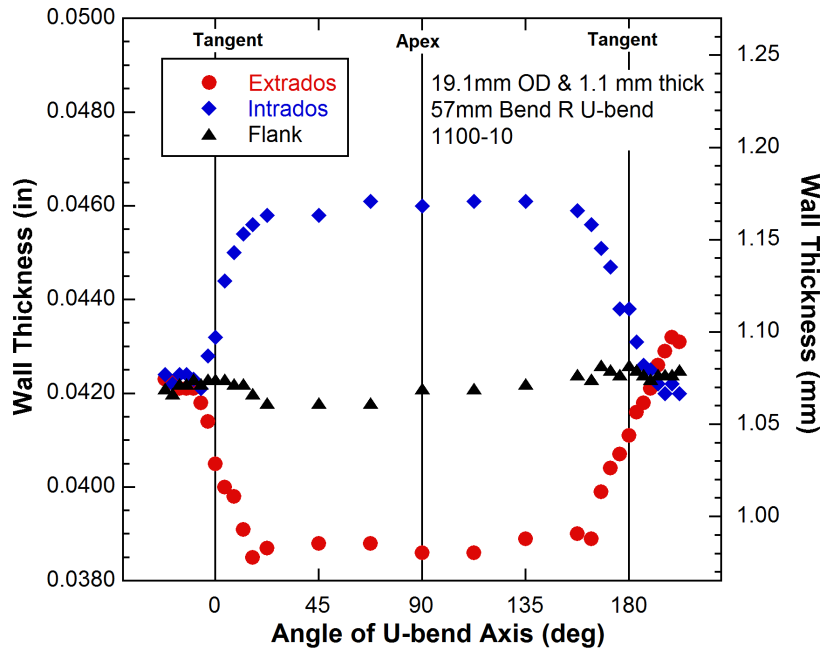


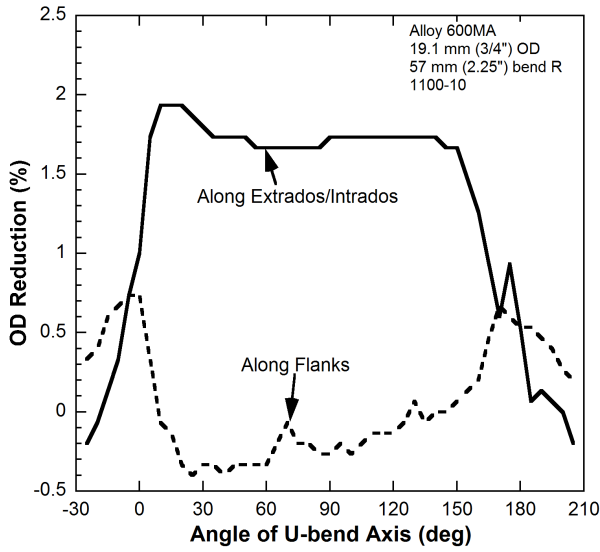
Figure 2-7. Wall thickness profiles of 19.1-mm OD and 57-mm bend radius U-bends (1100-10) along the angle of U-bend axis.

Ovality profiles of U-bends were measured using a caliper to acquire baseline data. Because earlier literature [6–8] mentioned the unique ovality profile observed in U-bends, it was decided to compare the ovality of Argonne U-bends with those reported in the literature. Yashima et al. [6] measured the OD reduction profiles of the U-bends with a variation of bending methods: using a metal ball mandrel or a plastic cylindrical mandrel. The OD reduction profile of the pulled U-bend tubes bent using the ball mandrel showed the peak near the 0 deg tangent (i.e., smooth transition) and a gradual decrease along the U-bend axis. The minimum OD reduction was observed near the 180° tangent (i.e., irregular transition). However, the OD reduction increased at the 180° tangent, that is, a “valley point” was observed near the 180° tangent. This irregular OD reduction at the valley point caused higher residual stress and eventually earlier initiation of SCC. A laboratory specimen using the cylindrical mandrel was produced, and its OD reduction profile was measured for comparison with the available data. The peak was still observed near the 0 deg tangent, but the profile was quite uniform without a large variation as observed with the pulled-out U-bend. It should be noted, however, that the valley point was still noticeable near the 180° tangent although the magnitude was smaller. Therefore, the comparison confirmed that the use of the cylindrical mandrel improved the tube OD reduction profile and possibly reduced the residual stresses. The OD reduction profiles of Argonne U-bend tubes were measured to determine whether the valley point was noticeable. The U-bend has a bend radius of 57 mm, which is similar to that of the row 1 U-bend. The OD reduction profile of Argonne U-bend tubes along the extrados/intrados showed a good agreement with that of the laboratory specimen except in the areas near both tangential points. The valley point was not observed near the 180° tangent. This could be attributed to the difference in the bending method, although both methods used a plastic cylindrical mandrel. Because the valley point resulted in a PWSCC initiation site at U-bends, the absence of the valley point in the Argonne U-bend tubes may be a result of improvement in the bending technique.

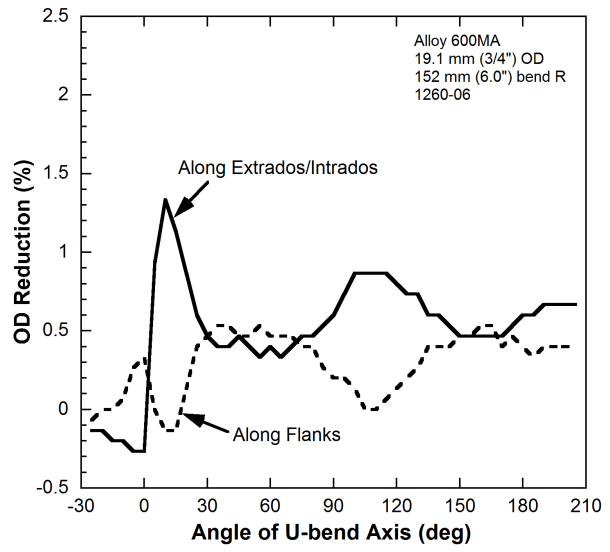
The OD reduction profiles of Argonne U-bend tubes were also measured to determine whether the valley point is present near the 180° tangent of the 19.1-mm OD U-bend tubes. Figure 2-8 shows the OD reduction profile along two flanks and along the extrados/intrados of two different

U-bends. The negative OD reduction denotes the increase in the OD between the flanks and the positive OD reduction denotes the decrease in the OD between the extrados and intrados. It should be noted that the 19.1-mm OD U-bends with 57-mm bend radius showed the valley point in the ovality along the extrados/intrados near the 180° tangent. Based on the data, one can speculate that the residual stress level and the possibility of crack initiation at the valley point might be lower for the 19.1-mm OD U-bend than that for larger diameter tubes. The maximum percentage of OD reduction (both increase and decrease) occurs on the U-bend axis between 20° and 30°, regardless of the bend radius. The EPRI guideline [4] specified the limit on U-bend ovality; however, it did not specify where the ovality measurements should be made. The wall thickness is specified to be measured in the tangent and the apex regions. Valinox measured the ovality at 45-, 90-, and 135-deg locations, which appears to be a common industry practice. Based on the ovality profiles shown in Figure 2-8, the common practice for the ovality measurements may need to be revised to determine the true maximum ovality.

The OD reduction profiles were converted to the ovality profiles according to the definition in the EPRI guideline [4]. Figure 2-9 shows the ovality profiles of four 19.1-mm OD U-bend tubes (with a 57-mm bend radius) along the angle of U-bend axis. The 0° tangent is defined as a smooth transition, whereas the 180° tangent is defined as an irregular transition where a tangential point is not well-defined. More than one U-bend was measured to evaluate the specimen-to-specimen variation. The measurements show that the maximum ovality was located at 20–30° of the U-bend axis. It appears that the specimen-to-specimen variation is not significant for the Argonne U-bend specimens. Valinox measured the ovality at the U-bend apex and $\pm 45^\circ$ away from the apex. If this is a common industry practice, the true maximum ovality of U bends might be missed. The ovality dip (or valley point) is observed near the 180° tangent of 19.1-mm OD U-bends where the tangential point is not well defined. In reference to field experience at Vogtle, because U-bend cracking occurred slightly above the tangent [9], that cracking might be related to the ovality dip, and possibly higher residual stress, even though the U-bends had been stress-relieved. Therefore, from an ISI perspective, it would be sensible to pay particular attention to examination of the tangential regions of the low-row U-bends.



(a)



(b)

Figure 2-8. OD reduction along the extrados/intrados and the flanks of Argonne U-bends with 19.1-mm OD with (a) 57-mm and (b) 152-mm bend radii.

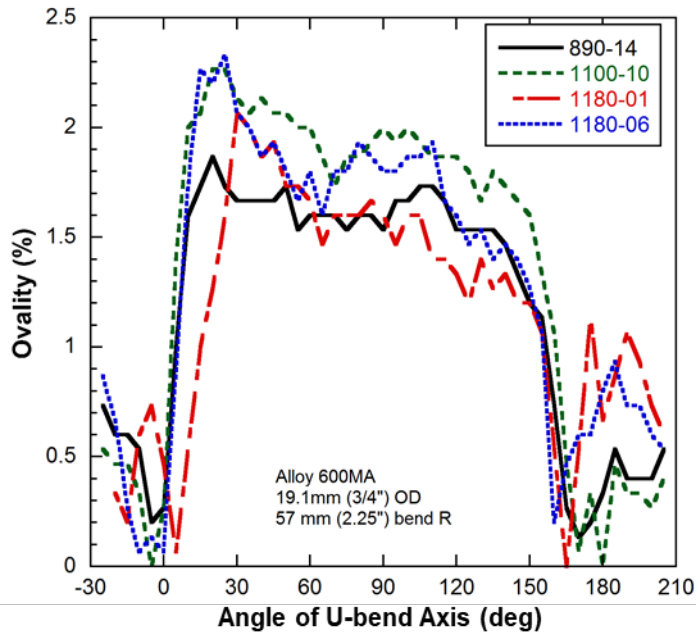


Figure 2-9. Measured ovality profiles of 19.1-mm OD and 57-mm bend radius U-bends along the angle of U-bend axis.

2.3 Manufacturing of U-bend SCC

2.3.1 Procedure for Axial PWSCC throughout the 57-mm-Radius U-bend Region

A method of manufacturing SCC specimens at ambient condition was developed by Argonne in the 1990s [1]. Previously, this method has been used to produce mainly straight tubes and mechanically expanded transition specimens [1, 2]. In the current work, the method was applied to generate cracks in U-bend specimens. To experimentally induce SCC in the U-bends, sensitized microstructure, corrosive chemicals, and tensile stress are needed. As-received U-bend specimens with a 57-mm bend radius (Heat # NX8524LT) were heat treated in a vacuum furnace at 650°C for 6 h to sensitize the grain boundaries. An initial trial test revealed that the heat treatment turned out to be necessary not only for the sensitization but also for the residual stress/strain relief. As corrosive chemicals, 0.1 to 1.0 M sodium tetrathionate ($\text{Na}_2\text{S}_4\text{O}_6$) aqueous solutions were used. Samans was the first to report the intergranular cracking of Alloy 600 in a polythionic acid solution at room temperature after being sensitized at 650°C for 4 h [1]. To apply tensile stress in the cracking region, U-bend legs were displaced. The method of displacing legs inward was applied to induce the hoop stress at the inner surface of the apex region in the 57-mm bend radius U-bend based on the earlier field cracking experiences [1] and laboratory testing [1, 2, 7]. In the area of the flow slots where the structural resistance is low enough, deformation of a tube support plate (TSP) can occur because of corrosion products buildup in the gap between tube and the uppermost TSP [1]. If this deformation occurs on both sides of the flow slot, the sides of the flow slot are forced inward at the middle, causing the previously rectangular-shaped flow opening to develop the shape of an hourglass, referred to as hourglassing. In the low-row U-bends, PWSCC is significantly more likely to occur if hourglassing forces the tube legs closer together, given that a small movement of the tube legs will concentrate sufficient tensile stress at the apex of the U-bend.

Figure 2-10 shows a schematic of the apparatus for displacing U-bend legs with clamps and the location of the chemical exposure area. As illustrated in Figure 2-10, the two legs of the U-bend are displaced to an inward direction using a clamping device. This procedure can produce the tensile hoop stress at the inner surface of the apex extrados region that is necessary to grow axial PWSCC. Total leg displacement was around 5.1 mm (0.2 in.), that is, 2.5 mm (0.1 in.) per leg when growing cracks at the apex. The total leg displacement was increased to 7.6 mm (0.3 in.) when growing cracks between the tangent and the apex. Figure 2-11 shows a 57-mm bend radius U-bend with clamps on before and after displacing the legs. A baseline EC scan of the U-bend with clamps on was obtained before introducing any chemicals. A small amount of the test solution (~1.0–0.5 mL volume), just enough to wet the apex region, was then introduced inside the U-bend specimen by using a long plastic tubing and a syringe. When it is necessary to grow cracks between the tangent and the apex, the U-bend with clamps was tilted accordingly (usually ~45°) so that the wetting area (i.e., chemical exposure area) was placed between the tangent and the apex. After a certain exposure time, the specimen was removed for EC examination to determine whether there was any cracking. When a crack-like indication was barely detectable, the EC data were compared with the baseline scan to ensure that the crack-like indication was not part of the background noise. This process turned out to be essential for U-bend specimens because the background noise level was significantly higher than that of a straight section and varied with the location along the U-bend region. The chemical exposure and EC examination were repeated until detectable cracks were grown. To monitor crack initiation/growth in U-bends, acoustic emission (AE) sensors were applied. The AE method, however, did not perform reliably for monitoring crack growth at U-bends. Once crack-like indications were detected by EC examination, the possible cracking area was inspected with a borescope. It should be noted that short and shallow cracks were not detectable by visual testing (VT) using a borescope. However,

axial PWSCCs were detectable by VT once they reached a certain size. The actual size of the cracks in the U-bend specimens were ultimately determined by destructive examination (DE). The tubes were first burst-tested, and then burst fractography was performed using scanning electron microscopy (SEM).

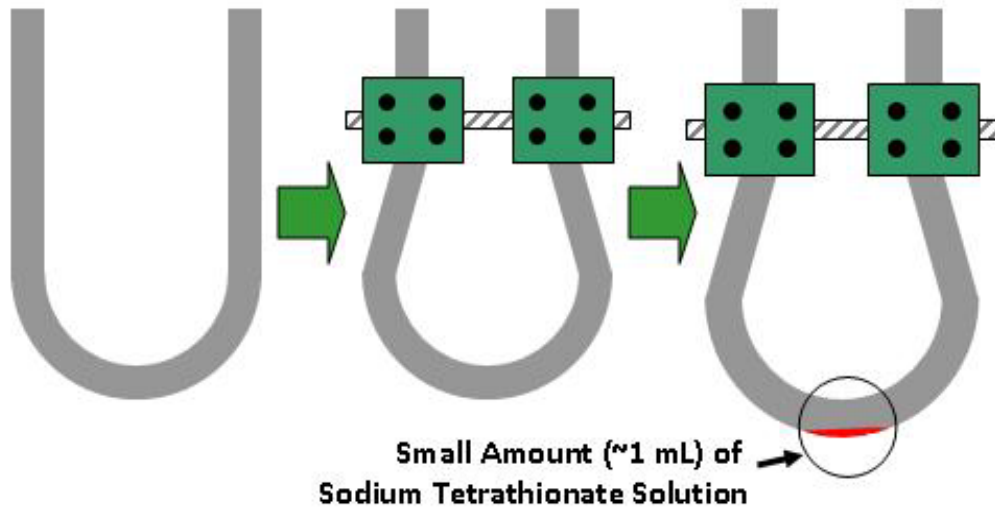


Figure 2-10. Schematic of displacing U-bend legs with clamps and the location of chemical exposure area.

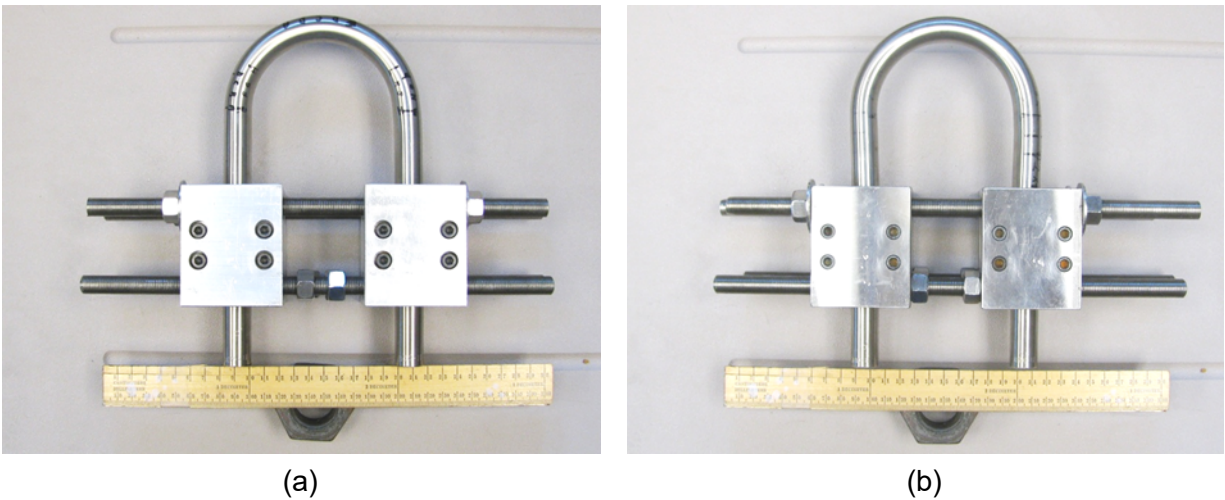


Figure 2-11. Photos of a 57-mm bend radius U-bend tube with clamps (a) before and (b) after the leg displacement. Note that the ruler in photos is 300 mm long.

2.3.2 Procedure for Axial PWSCC at Tangential Regions of 57-mm-Radius U-bends

The crack manufacturing method for axial PWSCC at the tangential regions of U-bend specimens differs slightly from the method used for manufacturing axial PWSCC at the bend region. As-received U-bend specimens with 57-mm bend radius (Heat # NX8524LT) were heat treated in a vacuum furnace at 650°C for 6 hours to sensitize microstructure and reduce compressive residual stress/strain as was carried out on U-bends for axial PWSCC at the bend region. As a corrosive chemical, 0.1 to 1.0 M sodium tetrathionate (Na₂S₄O₆) aqueous solutions were used. To expose only the tangential region to the corrosive chemicals, a Teflon[®] rod with a Viton[®] O-ring near the rod end was inserted into either the “0deg” or “180deg” tangent leg. The top of the rod was kept at an elevation that was slightly lower than the U-bend tangential point. To grow axial PWSCC at the extrados or intrados of the tangential region, tensile hoop stress is needed at the ID surface. Figure 2-12 shows stainless steel clamps compressing the U-bend tangential region—applying this particular stress. Finite-element analysis (FEA) showed that tensile hoop stress can be produced at the ID surface of the extrados region by compressing the tube. The displacement by compression of the tube was measured by a caliper to help ensure that the maximum stress at the tube ID surface would be similar to the yield point predicted by FEA. The diametric total displacement realized by compression was between 0.15 and 0.18 mm (0.006 and 0.007 in.), except for some U-bends with larger displacements. Test solution (~1 mL volume) was then added in the U-bend using a long plastic tube with a small diameter and a syringe. The U-bend with the clamps was usually placed as shown in Figure 2-12, that is, the extrados was facing down; however, when growing cracks not only at the extrados but also at the intrados, the specimen was placed vertically with a larger test solution volume of ~3 mL. The U-bend specimens that were used for the production of axial PWSCC throughout the bend region were used once again for the production of axial PWSCC at their tangent regions. Therefore, the U-bend specimens with the 57-mm bend radius used in this work usually have axial PWSCCs not only at the tangent but also throughout the bend region.

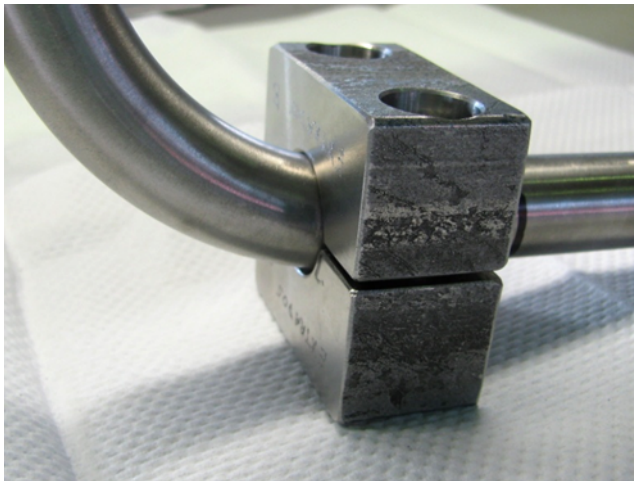


Figure 2-12. U-bend tangential region compressed by stainless steel clamps to generate tensile hoop stress at the tube ID.

2.3.3 Procedure for Circumferential PWSCC throughout the 152-mm-Radius U-bend Region

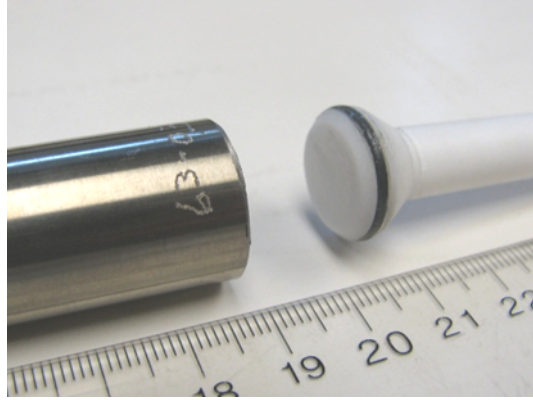
The manufacturing method for generating circumferential PWSCCs throughout the U-bend region is similar to the method used for axial PWSCCs throughout the bend region. Because

circumferential cracking was reported most often in connection with high-row U-bends, larger-bend-radius U-bends (152 mm) were used for the induction of circumferential cracking. The larger-bend-radius U-bends have a different heat (Heat # NX8520) from those with a smaller bend radius. As-received U-bend specimens were heat treated in a vacuum furnace at 650°C for 6 hours to sensitize the microstructure and reduce compressive residual stress/strain, if any. As a corrosive chemical, 0.1 to 1.0 M sodium tetrathionate ($\text{Na}_2\text{S}_4\text{O}_6$) aqueous solutions were used. To grow circumferential PWSCC, tensile axial stress is needed at the ID surface. The same leg-displacing method was applied to the larger-bend-radius U-bends as was applied to the smaller-bend-radius U-bends. Figure 2-13 shows a U-bend tube with the attached clamps before and after the leg displacement. The leg displacement could generate the tensile axial stress at the tube ID of the larger-bend-radius U-bend's apex region. To monitor crack initiation/growth in U-bends, an active crack monitoring system using piezoelectric crystals was applied to a couple of specimens. The results of that investigation, which are reported elsewhere, suggest the potential applicability of the system for the monitoring of crack initiation/growth in SG tubing under laboratory conditions. To limit the area exposed to the corrosive chemicals, a Teflon insert with a Viton O-ring near the rod end was inserted. Figure 2-14(a) shows the Teflon insert with the O-ring. Figure 2-14(b) shows the U-bend after its insertion, and Figure 2-14(c) shows the location of the Teflon insert inside the U-bend by placing the insert outside along the bend. The Teflon insert could be positioned anywhere in the bend region. Circumferential cracking was attempted throughout the bend region including at the apex.

As a first trial, as-received U-bend specimen 07-04 with a 19.1-mm OD and 152-mm bend radius was displaced with the total leg displacement of around 25 mm (1 in.), that is, 13 mm (0.5 in.) for each U-bend leg. The apex region was exposed to corrosive chemicals to induce circumferential PWSCC. After the total exposure time of 4.5 days to 1 M sodium tetrathionate ($\text{Na}_2\text{S}_4\text{O}_6$) solution, the U-bend specimen was examined with the +Pt rotating probe. However, the EC examination did not show any flaw indications. After this first trial, subsequent U-bend specimens were heat treated to sensitize their microstructure and thus, in effect, reduce their residual stress.



Figure 2-13. 152-mm bend radius U-bend with clamps (a) before and (b) after the inward leg displacement. Note that the ruler in the photos is 300 mm long.



(a)



(a)



(b)

Figure 2-14. Photographs showing (a) the Teflon insert with O-ring, (b) U-bend with the inserted Teflon insert, and (c) the Teflon insert and rod placed with the U-bend to show the approximate location of the Teflon plug in the U-bend after the insertion. (Note that the ruler is 300 mm long.)

3 EDDY CURRENT EXAMINATION OF U-BEND TUBES

Eddy current inspection of U-bend specimens is discussed in the following subsections. Section 3.1 provides a brief description of the generic EC examination technique used for inspection of all the tube specimens. Data analysis results are presented in Section 3.2 for representative flaws at different regions of U-bends following termination of the crack manufacturing process. Flaw sizing results in that section are based on conventional analysis of EC data. The results of studies on identifying the source of large background interference associated with probe response at U-bends are discussed in Section 3.3. Finally, in Section 3.4, data analysis results are presented in connection with depth profiling of cracks using EC inspection data acquired prior to pressure testing of the U-bend tubes.

3.1 Eddy Current Examination Technique

Eddy current examinations were performed on all U-bend specimens during the crack production process. The NDE method served both as a means to guide the crack manufacturing process and for sizing of cracks afterwards. Although a number of different EC examination techniques—including those that employ bobbin, rotating, and array probes—were implemented to acquire data on U-bend specimens, the results presented in this report pertain only to data acquired with a flexible +Pt rotating probe manufactured by Zetec, Inc. Results of analyses associated with the other EC examination techniques will be the subject of future studies. The main components of the inspection system used in this work include a MIZ-85iD-1 remote eddy current testing instrument, a 10D4 pusher, and EC probe. Probe motion control and data acquisition are implemented under the EddyNet™ software environment. Data collected earlier in this work were obtained using a MIZ-30 eddy current testing instrument. The flexible +Pt probe is designed to traverse the smallest-radius U-bends, which are the innermost (i.e., lowest row number) tubes within the tube bundle of a recirculating SG. Figure 3-1 shows photos of the flexible rotating probe used for inspection of U-bend tubes at Argonne. The probe head houses a single mid-range +Pt coil.

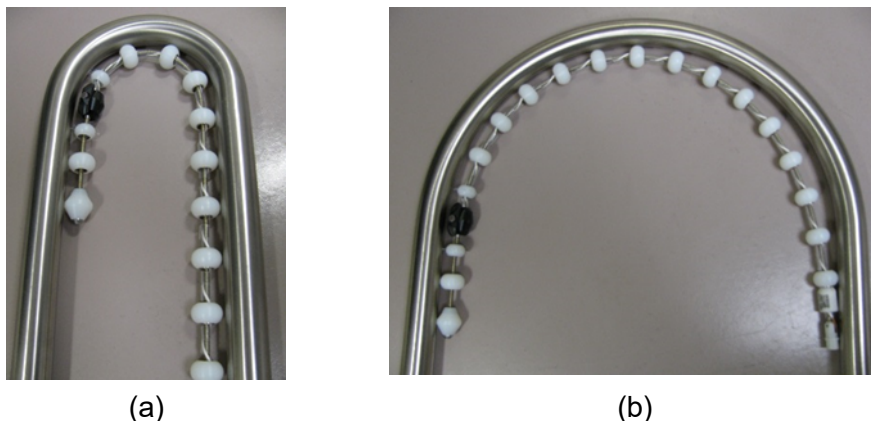


Figure 3-1. Photographs of detachable flexible rotating probe with a mid-range +Pt coil, placed along the intrados of (a) a 57-mm and (b) a 152-mm radius U-bend tube specimen at Argonne.

A generic +Pt rotating probe EC examination technique was implemented for acquisition of data on the U-bend tube specimens. The acquisition setup used here is in line with those defined in qualified ETSSs for detection of axial and circumferential PWSCC at small-radius (“low-row”) U-bend regions of SGs with Alloy 600 tubing with 19.1-mm (0.75-in.) OD and 1.09-mm (0.043-in.) wall thickness. It is worth noting that the existing techniques are not generally qualified for sizing of PWSCC at U-bend regions of SGs. The acquisition setup for inspection of U-bend specimens at Argonne included the ETSS-prescribed frequency channels of 400 kHz, 300 kHz, 200 kHz, and 100 kHz. For the purpose of evaluating alternative data analysis methods, additional frequency channels outside those specified in the ETSS were also included in the acquisition setup. Results reported in accordance with conventional data analysis procedures, however, are all based on measurements made from the primary 300-kHz frequency channel. Manual analyses of EC data acquired during the crack manufacturing process were carried out using the EddyNetSuite™ software (Zetec, Inc.).

Calibration of +Pt probe data was performed in accordance with the procedure defined in generic ETSSs for detection of PWSCC in U-bend regions [10]. Figure 3-2 shows a drawing of the electro-discharged machined (EDM) notch standard tube used at Argonne for calibration of rotating probe data. The 0.75-in. OD tube is made of Alloy 600 material and contains a total of 18 EDM notches of OD and ID origin with axial and circumferential orientation. The notches are 0.375-in. long and vary in depth from 20% to 100% through wall (TW). The calibration standard tube is fitted with a removable TSP collar, which simulates the probe response from SG support structures.

Calibration of data for all the channels is performed by normalizing the signal amplitude and adjusting the phase angle of each channel with respect to the signals from the 100%TW and the 40%TW ID notch, respectively. The amplitude is normalized such that the peak-to-peak amplitude (V_{pp}) of the 100%TW notch is approximately 20 v. The phase angle is adjusted so that the 40%TW ID notch forms an angle of approximately 15° , which by convention is measured clockwise from the horizontal axis in the second quadrant. Separate process channels are created to analyze data associated with circumferential indications. The probe response for those channels is adjusted such that circumferentially oriented flaws produce a signal with a positive vertical component. To allow measurement of the axial extent of signals, the data are axially scaled based on the position of known indications on the calibration standard tube. Circumferential positional information, displayed in degrees, is based on the trigger channel data, which is supplied by the rotating probe motor unit.

Crack depth is estimated by applying a phase-based calibration curve that is generated using signals from ID-originated EDM notches on the calibration standard tube and includes data points for 0% and 100%TW depths. Separate calibration curves are generated for the axially and the circumferentially oriented flaws. The phase-based calibration curve for the axial channel is generated in the main analysis window. The calibration curve for the circumferential channel is generated using the circumferential lissajous from the C-scan analysis window. While all of the analysis channels are independently calibrated, the flaw sizing results reported here are all based on data from the 300-kHz channel. The estimates of flaw depth represent the depth measured at or near the maximum amplitude of flaw signal.

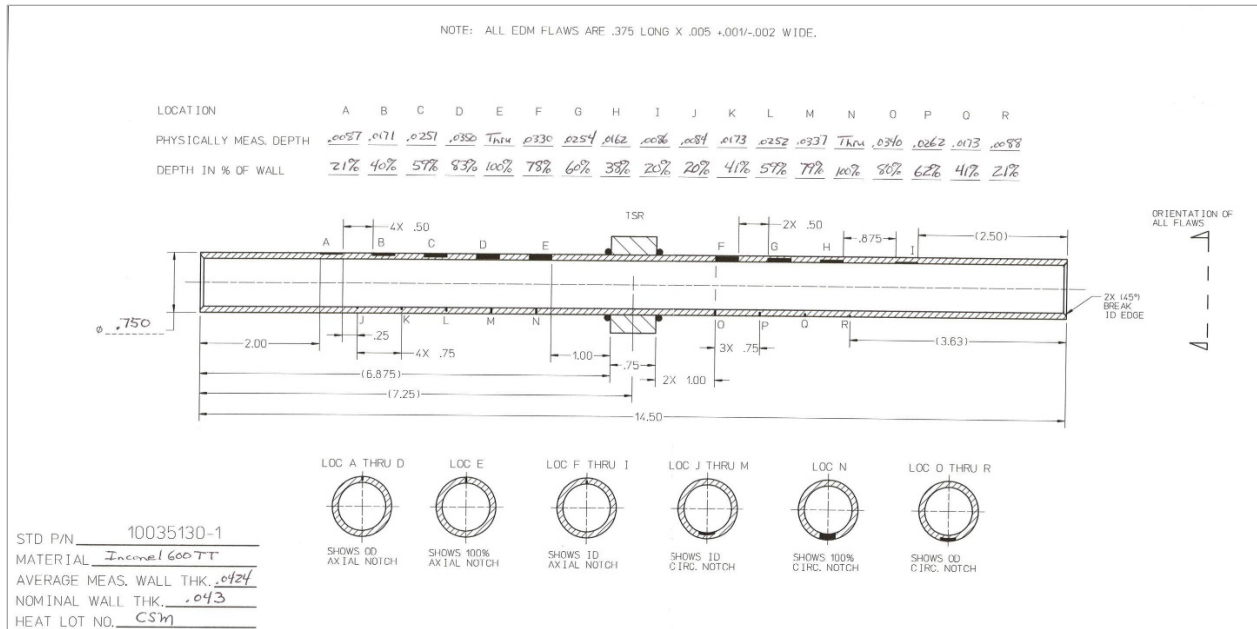


Figure 3-2. Drawing for EDM notch standard tube used for calibration of rotating probe data. The tube has 18 notches of OD and ID origin with axial and circumferential orientation.

3.2 Post-Cracking Inspection of U-bend Specimens

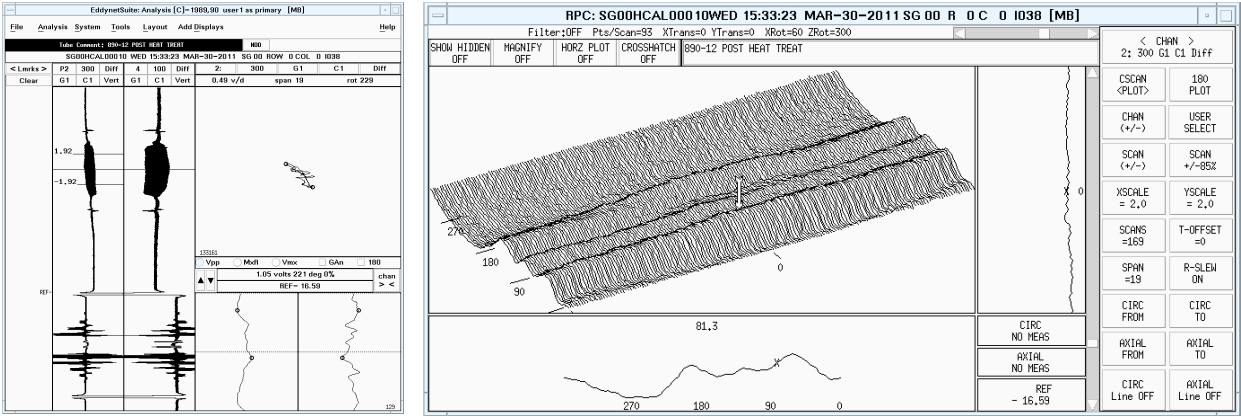
Inspection was also performed immediately after termination of the manufacturing process for each laboratory-produced PWSCC. Eddy current data acquired at each stage of the process were analyzed, and the results were reported after the final stage of the flaw manufacturing process. Data analysis results are presented next for representative cracks produced at various regions of the U-bend specimens. The NDE results for all the SCCs, categorized on the basis of flaw type and location along the U-bend, are provided in separate tables in the appendices. They include axial PWSCC throughout the U-bend region, axial PWSCC at tangent regions, and circumferential PWSCC throughout the U-bend region. The information provided in each table includes the specimen identification number, test conditions, location of flaw in U-bend, and the NDE estimates of flaw size.

Detectable signals indicative of axial PWSCC initiation were observed in EC inspection data from the U-bend apex region within a three-day exposure time for the majority of laboratory-produced cracks. Indications of cracking in most of those specimens were detectable within one day of exposure time. The criterion for detection was based on the presence of a discernible change in +Pt probe signal from indications with crack-like signal characteristics. Analyses of data during the crack manufacturing process included comparison of the signals between the current and previous scans of the same tube. As such, the ability to detect flaw signals at an early stage in this study may not be readily extended to other detection scenarios for which prior knowledge about flaws is not available. This finding holds particularly true for detection of small signals in SG tube elevations, such as small-radius U-bend and expansion transition regions, where large background interference from variations in tube geometry makes detection of flaw signals more challenging. This topic is discussed in greater detail in the next section.

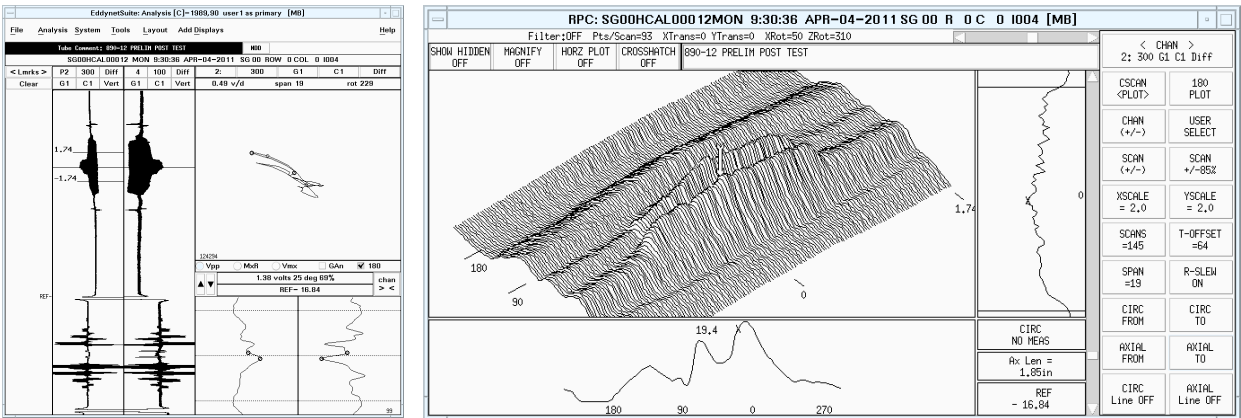
Figure 3-3 shows screen captures of representative data analysis results for a 57-mm-radius U-bend specimen, 890-12, both before and after chemical exposure. Comparison of pre- and post-exposure EC signals at the intended crack initiation location indicates the post-exposure presence of two major axial PWSCCs near the apex region. The characteristic probe response along the U-bend is clearly visible in Figure 3-3(a), which is the baseline data collected on the clean tube. This rather significant source of signal interference, in the form of ridges, is present throughout the bend region and is more pronounced for smaller-radius bends. The maximum +Pt signal amplitude and depth of cracks in 890-12 are 1.38 v and 69%TW, respectively. In reference to Figure 3-3(b), the two parallel axial cracks are located along the peak of the axially aligned ridges. As noted earlier, the noise level in the bend region is significantly higher than that found in the straight section of SG tubes. This rather deterministic source of background interference is associated with large geometrical and dimensional changes along the U-bend, which gives rise to a large probe response in that region. The source of excessive EC noise in the U-bend region is discussed in some detail in the next section.

As another example, EC inspection data are shown in Figure 3-4 for a 57-mm-radius U-bend specimen, 920-19, with axial PWSCC produced in its apex region. In this case, screen captures of data analysis windows are shown before, midway through, and after the crack manufacturing process. The post heat treatment data are displayed in Figure 3-4(a), which shows no detectable indication of cracking. Once again, the large characteristic probe response at U-bend is clearly visible in the baseline data. Figure 3-4(b) shows the EC data for roughly the same region of the tube after the second exposure with leg displacement clamps in place. The large probe responses from clamps are the dominant signals in the trace corresponding to the lower frequency channel. In reference to Figure 3-4(b), although the signal from PWSCC was detectable after the second exposure, the low amplitude of the signal did not allow for reliable estimation of crack length. The low amplitude of the signal can be attributed to the tightness of crack at that stage of the exposure process. As Figure 3-4(c) shows, the length of the crack was measurable with reasonable accuracy after another stage of chemical exposure.

Eddy current examination results for all of the specimens with predominantly axial PWSCC throughout the bent section of 57-mm-radius U-bends are listed in Table B-1. As described previously, estimated flaw sizes are based on manual analysis of data acquired with +Pt probe after termination of the crack manufacturing process. Most of the specimens listed in Table B-1 have multiple cracking locations. As shown on the drawing at the bottom of that table, three area indications are used in Table B-1 and in the text thereafter, denoted 45°, 90°, and 135°. The notation "45°" indicates that the axial PWSCC is located between "0deg" tangent and the apex. The "0deg" tangent represents a tangential area where the transition point from straight to bending is clearly defined. It should be noted that the crack is not always located exactly at the 45° location. The notation "90°" indicates that the crack is located near the apex extrados. The notation "135°" indicates that the crack is located between the apex and 180° tangent. This report provides additional examples of results using EC data analysis on the sizing of PWSCC in various locations along the U-bend in connection with correlations between NDE and structural parameters.



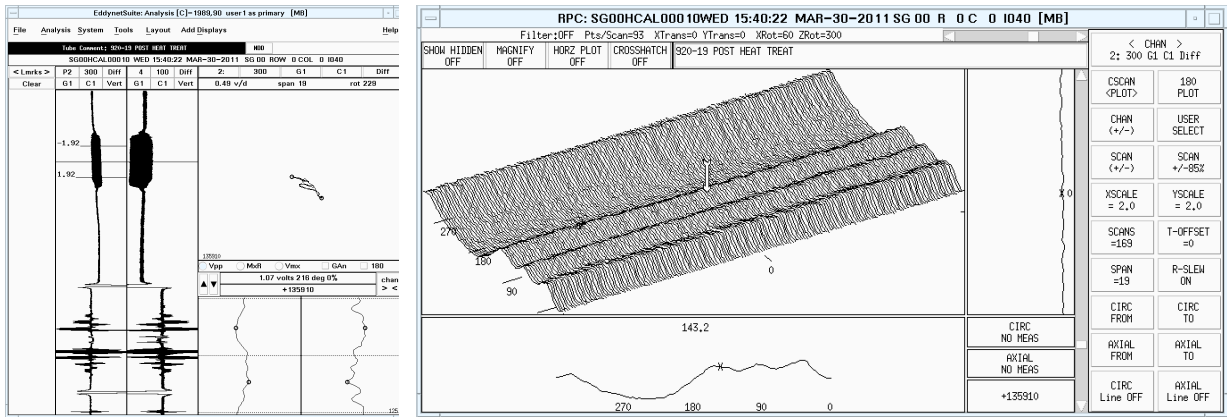
(a)



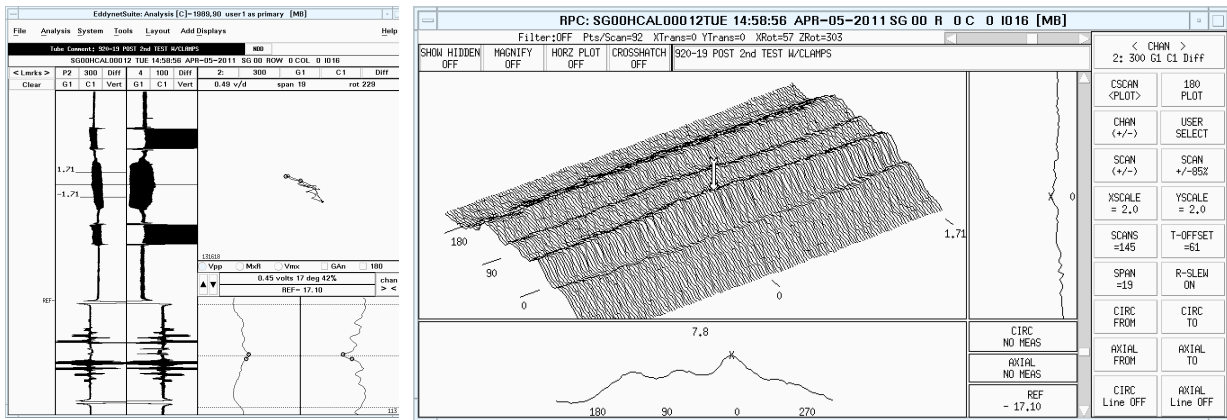
(b)

Note: Multiple axial cracking was generated at the apex region of the tube. Displayed in each case are the stripchart (left) and isometric plot (right) of the data within the measurement window.

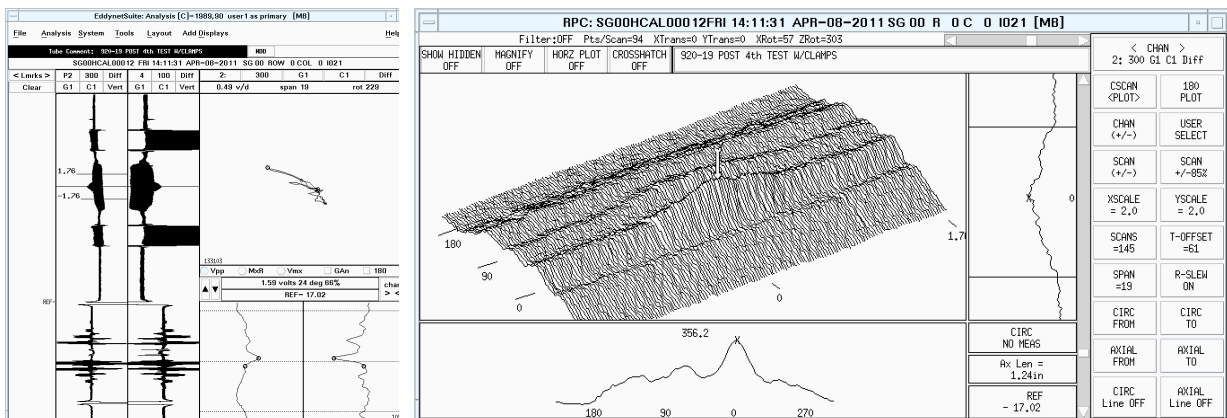
Figure 3-3. Representative +Pt probe data for a 57-mm-radius U-bend specimen 890-12 (a) before and (b) after the chemical exposure process.



(a)



(b)



(c)

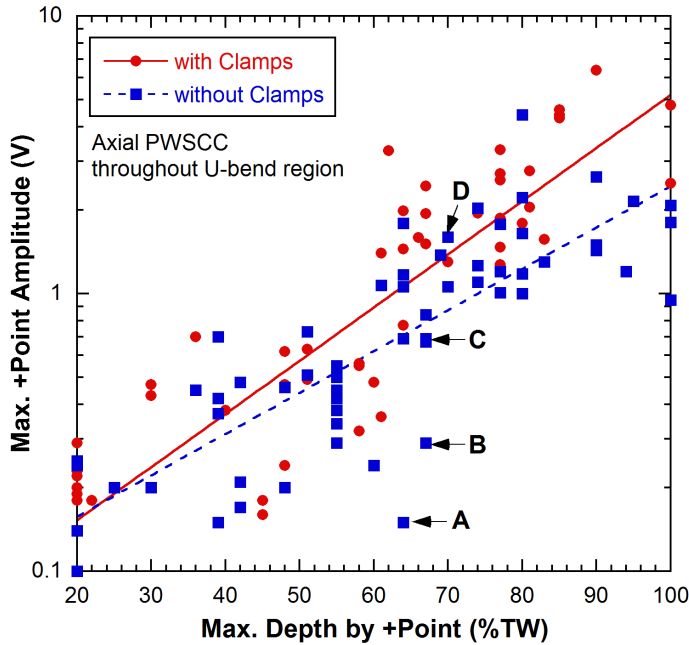
Note: Multiple axial cracking was generated at the apex region of the tube. Displayed in each case are the stripchart (left) and isometric plot (right) of the data within the measurement window.

Figure 3-4. Representative +Pt probe data for 57-mm-radius U-bend specimen 920-19 (a) before, (b) midway through, and (c) after the chemical exposure process.

Eddy current inspection data were collected both with and without the leg displacement clamps in place on nearly all of the U-bend specimens with axial PWSCC. For baseline EC inspections, each U-bend tube was scanned with the +Pt probe before the chemical exposure and with the clamp attached. If measurable crack-like signals were detected, the U-bend was then re-inspected with and without the clamps. If cracking occurs due to the hourglassing effect in the field, the U-bend legs would be slightly displaced inwardly. From that perspective, the EC inspection data set collected on the specimens with clamps could be considered more representative of field data. However, because the cracking due to the hourglassing effect is not common in the field, one must assume that the EC inspection data set collected on U-bend specimens without the clamps would, in general, be more representative of field data. It was noted early in this work that the U-bends were permanently deformed after removing the clamps, even with application of a leg displacement as small as 5.1 mm. Therefore, to some extent, all U-bend specimens have permanent deformation caused by the leg displacement process.

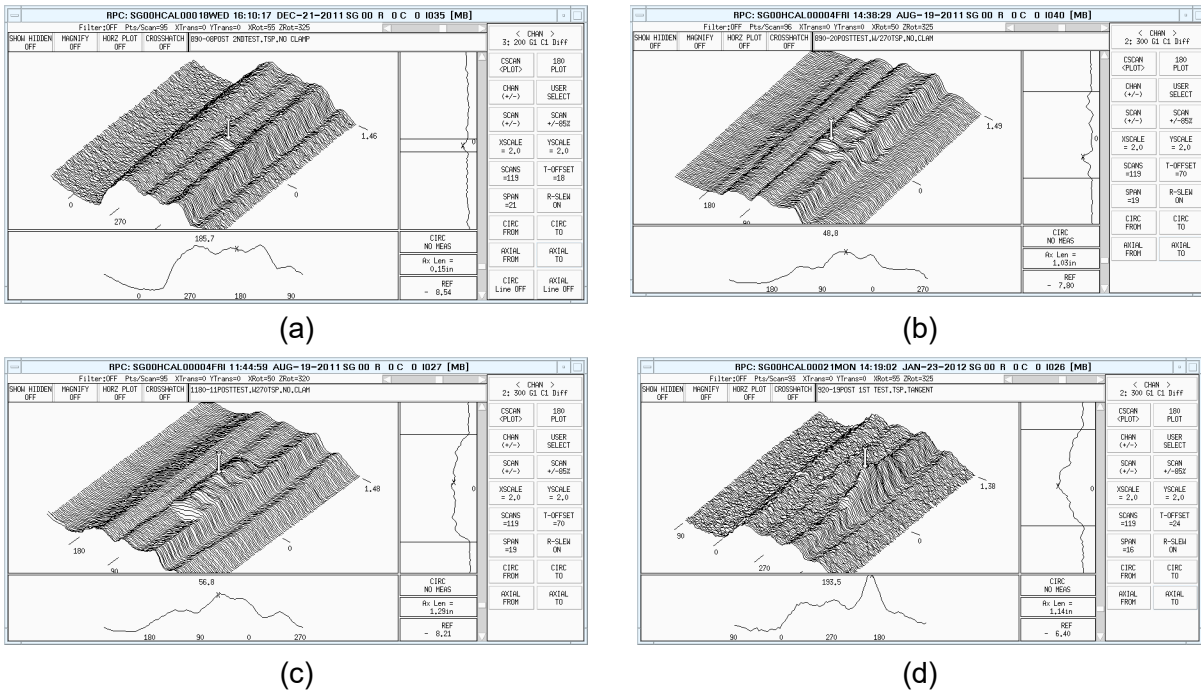
Figure 3-5 shows a plot of the maximum signal amplitude for axial PWSCC in the bent section as a function of the maximum crack depth. The two data sets (i.e., with and without the clamps) show a noticeable difference in distribution of the measured signals. As indicated by the regression lines, the +Pt signal amplitude for the PWSCC in U-bends with clamps in place is higher than that without the clamps. This finding suggests that, for a given crack length, as the leg is inwardly displaced, the existing axial crack opening becomes larger, which, in turn, results in a higher EC signal amplitude. In reference to Figure 3-5, the estimated maximum depth of cracks ranges from 20%TW to 100%TW and is distributed uniformly over that entire range.

At a given crack depth, the measured signal amplitude based on +Pt data in some cases shows significant variability. To further evaluate the range of variability in signal amplitude, four axial PWSCCs at U-bends were selected for that purpose. The data points for those cracks are denoted by the symbols A through D in Figure 3-5. The cracks all had comparable NDE depth estimates (64–70%TW) but varied significantly in their signal amplitude (0.15–1.5 v). Figure 3-6 shows the isometric plot of rotating probe data for the four axial cracks in the U-bend region. The data were collected after the clamps were removed. Because of its low S/N, PWSCC A was barely detectable, and the estimated length of the crack was ~4 mm (0.15 in.). The PWSCC B was composed of multiple short crack segments, and the longest segment was greater than 4 mm. The PWSCC C appeared to be composed of multiple axial cracks; however, the EC signals from the crack segments could not be clearly resolved because of the limited spatial resolution of the probe. The proximity of the cracks can be observed from the axial cross-section of the isometric plot shown in Figure 3-5(c). The EC signal from PWSCC D, which was relatively large, suggests the presence of a single crack longer than 25 mm (1 in.). It is apparent that the crack length affects the signal amplitude at the given crack depth. However, based on the data from the four axial PWSCCs examined here, no simple correlation exists between the crack length and the signal amplitude when dealing with complex forms of cracking. It should be noted that the crack depths in Figure 3-5 were estimated based on analysis of EC data. However, a more reliable assessment of NDE sizing capability should be based on the actual crack depths determined by DE. To that end, Section 4 presents the results on the correlation of flaw size estimated by NDE with that obtained by DE.



Note: Data points A, B, C, and D denote the four axial PWSCCs selected for evaluating the range of variability in signal amplitude.

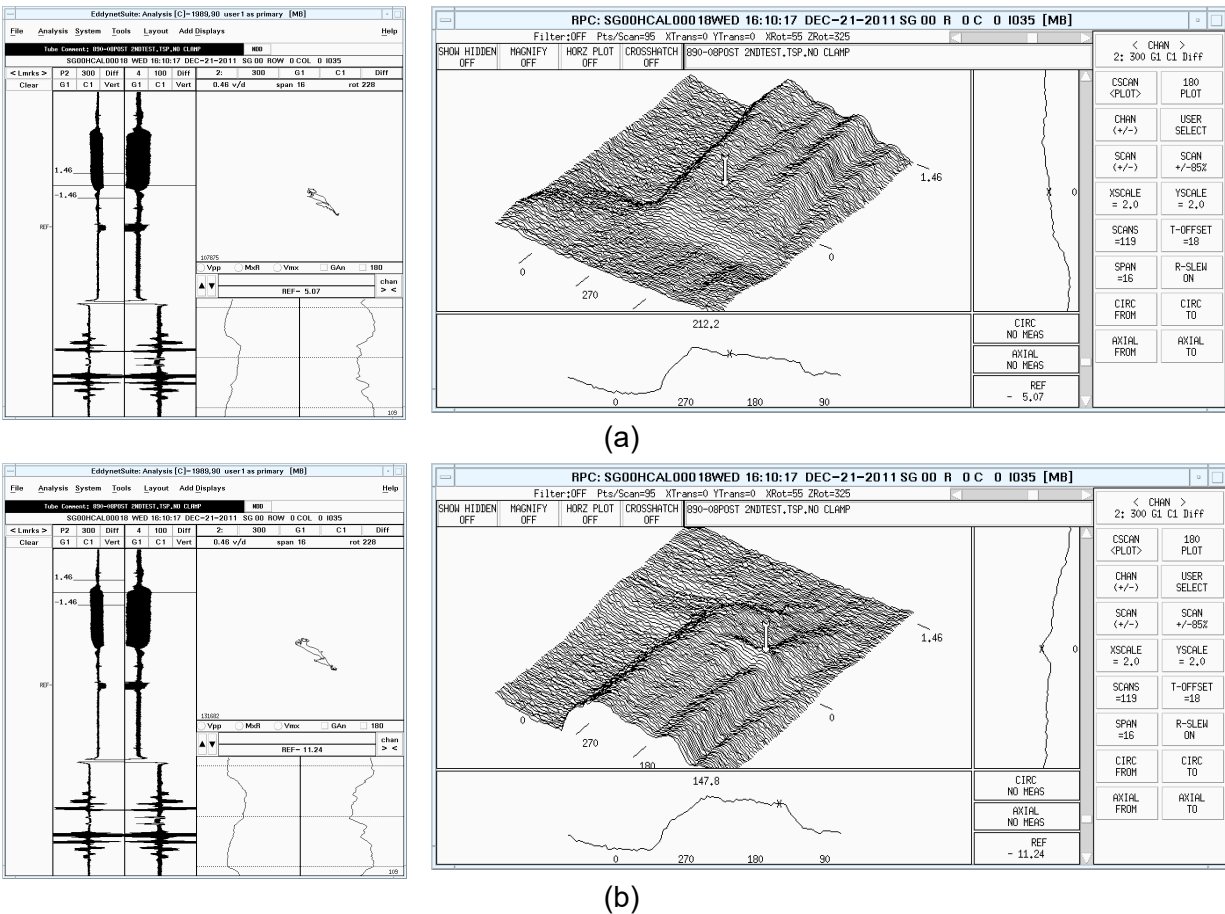
Figure 3-5. Maximum signal amplitude for axial PWSCCs in U-bend specimens, with and without the clamps, as a function of maximum depth estimated using data from +Pt probe examinations.



Note: The data points associated with EC estimates of crack size in these tubes are marked by symbols A, B, C, and D in Figure 3-5, respectively.

Figure 3-6. Isometric plots of rotating +Pt probe data showing the axial PWSCCs in U-bend specimens (a) 890-08, (b) 890-20, (c) 1180-11, and (d) 920-19.

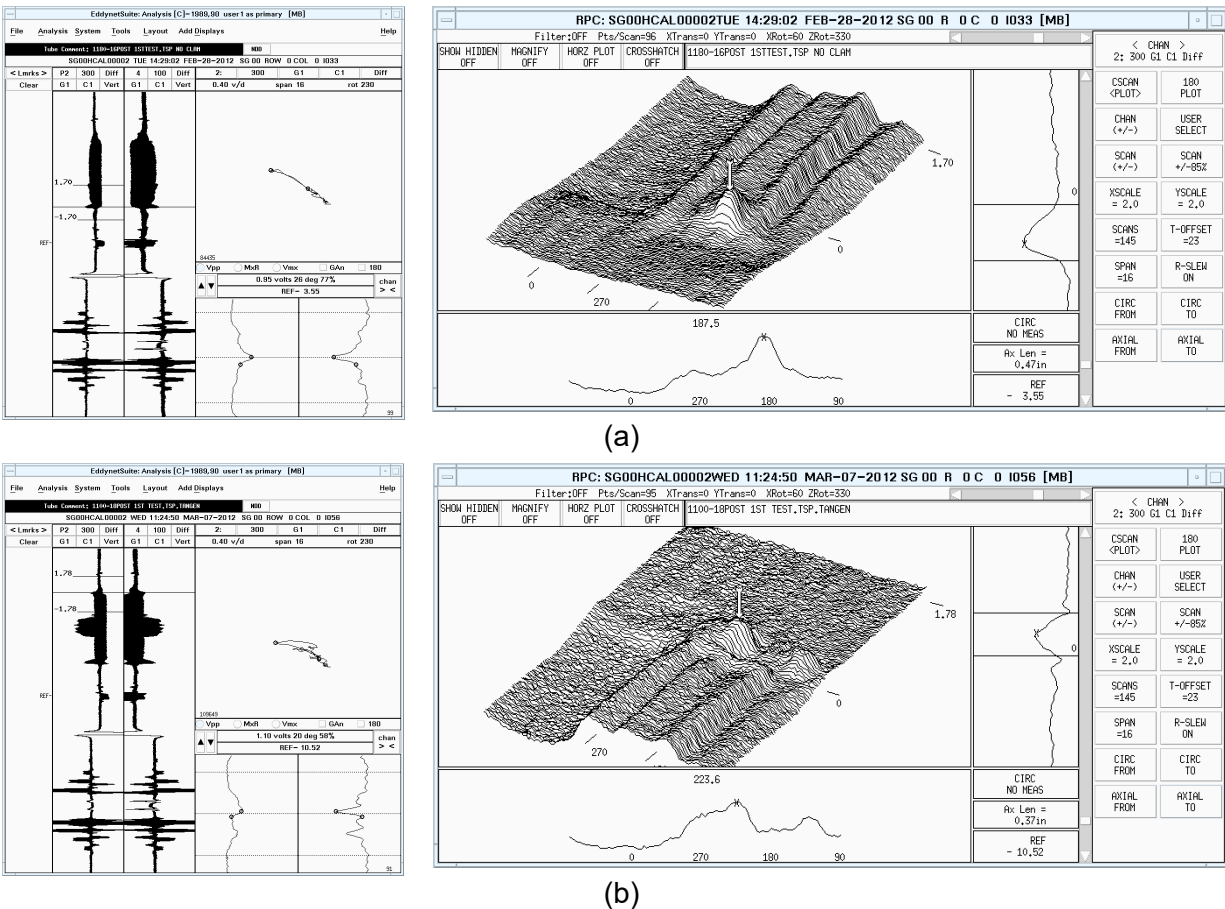
Baseline EC inspections were performed on U-bend specimens before chemical exposure of the tangent regions. Figure 3-7 shows representative data acquired with a rotating +Pt on a 57-mm-radius U-bend specimen, 890-08. Screen captures of both the main analysis window (strip chart and lissajous plots) and the C-scan window (isometric plot) are shown in Figure 3-7(a) and (b) with the data screening window displaying the region encompassing the “0deg” and the “180deg” tangent, respectively. As evidenced in previous examples, both the stripchart and the isometric plots clearly show that the characteristic background noise is present throughout the bend region, starting from the tangential point. Note that the probe does not exhibit an identical response at the two tangents. In reference to the isometric plot in Figure 3.7(b), a circumferentially oriented flaw-like signal is observable within the “180deg” tangent region, where the amplitude of the characteristic probe response at U-bend begins to taper down. All of the U-bend tubes with a 57-mm bend radius showed a similar flaw-like signal before any chemical exposure was introduced. It was postulated that the signal is caused by the local geometric effects. This topic was discussed in a previous section.



Note: Shown above are the stripchart (left) and isometric plot (right) of the +Pt rotating probe data with the measurement window displaying the region encompassing the (a) “0deg” and (b) “180deg” tangent.

Figure 3-7. Representative baseline data for 57-mm-radius U-bend specimen 890-08 before chemical exposure of tangent regions.

Axial PWSCC detectable by EC rotating probe examination was developed at the tangential regions of 57-mm-radius U-bends by following the method described earlier. Table B-2 provides a list of all axial PWSCCs produced at U-bend tangents, along with the associated NDE results. In most cases, axial cracking developed within two days, and the crack varied in length from 3 mm to 20 mm. Except for a few cases, the cracks at the tangential regions could not be detected by borescope examination, presumably because the cracks were shorter and tighter than those produced at the apex region. Cracking at the “180deg” tangent was notably different from that at the “0deg” tangent. The ones at “0deg” tangent mostly consisted of a single axial crack at the extrados, whereas those at the “180deg” tangent consisted mostly of two parallel axial cracks separated by $\sim 90^\circ$, centered at the extrados. A few of the cracks at the “180deg” tangents, however, were single axial cracks. Figure 3-8(a) and (b) show screen captures of the data analysis windows for two representative U-bend specimens after cracking was produced at the “0deg” and the “180deg” tangent, respectively. Time to cracking was comparable at both tangents, although the geometric shapes of the cracks were different. This result suggests that the stress at



Note: Shown above are the stripchart (left) and isometric plot (right) of the +Pt probe data with the measurement window displaying the region encompassing the (a) “0deg” and (b) “180deg” tangent.

Figure 3-8. Representative data for 57-mm-radius U-bend specimens with axial PWSCC at tangent regions.

the tangents was mainly controlled by the diametric compression rather than the residual stress. The sensitization heat treatment could reduce any residual stresses at the tangent. It appears that the discrepancy between the cracking behavior at the two tangents is also related to the local geometric irregularity at the “180deg” tangent.

The brief discussion that follows provides information on post-cracking inspection of 152-mm-radius U-bend specimens containing predominantly circumferential PWSSC throughout the bend region. Although EC examinations were performed on all of these tubes, the data were not included in the follow-on studies on correlations between NDE and DE structural parameters. Eddy current inspection results for all of the U-bend specimens with a bend radius of 152 mm are provided in Appendix C. Representative EC data from these tubes, presented below, serve primarily to illustrate the effect of bend radius, and hence the level of noise associated with tube geometry variations, on detection of cracks in small-radius U-bends.

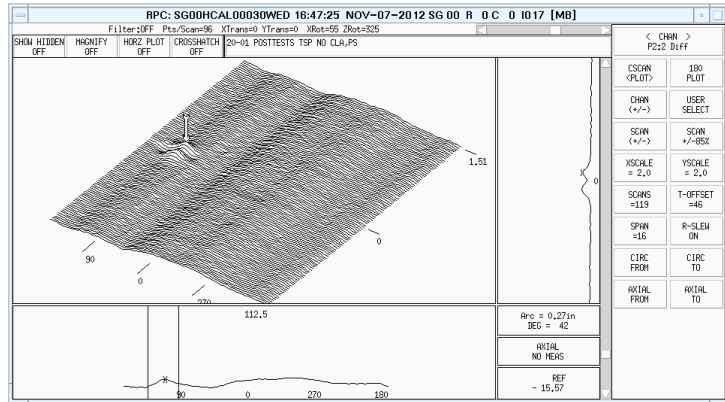
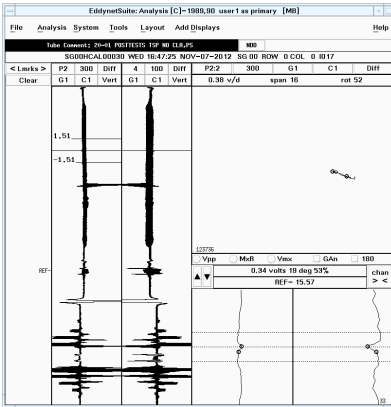
Circumferential PWSSC that is detectable by +Pt probe examination was generated throughout the bend region within three days of exposure time. Most cracks exhibited a discernible signal within one day of exposure time. The outward leg displacement was applied to most of the U-bend tubes while the inward leg displacement was applied to a fewer number of tubes. When the legs were displaced outward, that is, away from each other, circumferential cracks were usually grown at intrados or between the flank and intrados. The inward leg displacement produced circumferential cracks at the extrados or between the flank and extrados.

Eddy current inspection results for all 152-mm-radius U-bend specimens are provided in Table C-1. As listed in that table, the majority of specimens have multiple cracking locations. Seven area indications — marked as A through G around the U-bend — are identified in Table C-1 with those locations shown in a schematic diagram included at the bottom of that table. The D location indicates that the crack is located near the apex. The A and the G markings indicate that the crack is located near the 45° and the 135° angles along the U bend axis, respectively.

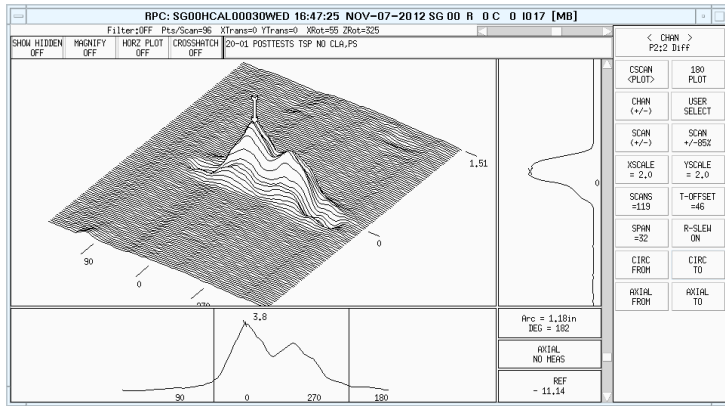
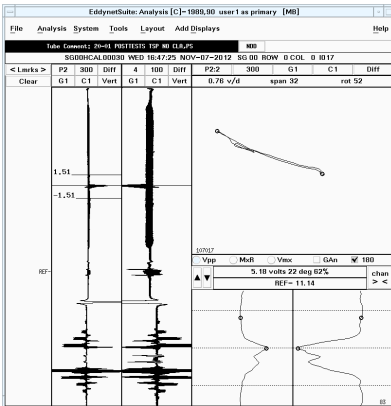
Representative screen captures of data analysis results are shown in Figure 3-9. Once again, displayed in that figure are the main analysis window and the C-scan window showing the data segment encompassing the circumferential PWSSCs in U-bend specimen 20-01. Similar to smaller-radius bends, the characteristic background noise (i.e., ridges) is present throughout the bend region. The noise level in the bend region of this tube, however, is much lower than that associated with U-bend tubes with smaller bend radius. The lower level of noise in larger-radius U-bends is because of the lesser degree of tube deformation caused by the bending process. In reference to Figure 3-9(b), the influence of noise on EC probe response in larger-radius bends becomes negligible as the crack signal becomes larger.

Results of data analysis for another set of representative circumferential cracks located throughout the bend region are shown in Figure 3-10. Although these cracks were all estimated, on the basis of phase angle information from rotating probe data, to have a similar depth (50–55%TW), the amplitudes of the signals for these four cracks range from 0.1 v to 4 v. Figure 3-10 shows the isometric plots of the four circumferential PWSSCs. While crack A has the smallest circumferential extent, cracks A through C all have a similar extent based on EC estimate of flaw size. Crack D has a significantly larger extent than the other three SCCs. As in the previous case, no simple relationship could be observed between the signal amplitude and the crack depth in this case. Once again, it is apparent that for complex forms of cracking, multiple variables including the crack length, depth, and opening affect the EC signal. More detailed analysis of correlations

between NDE estimates of flaw size and actual flaw size based on fractographic examinations are presented in Section 4.0 of this report.



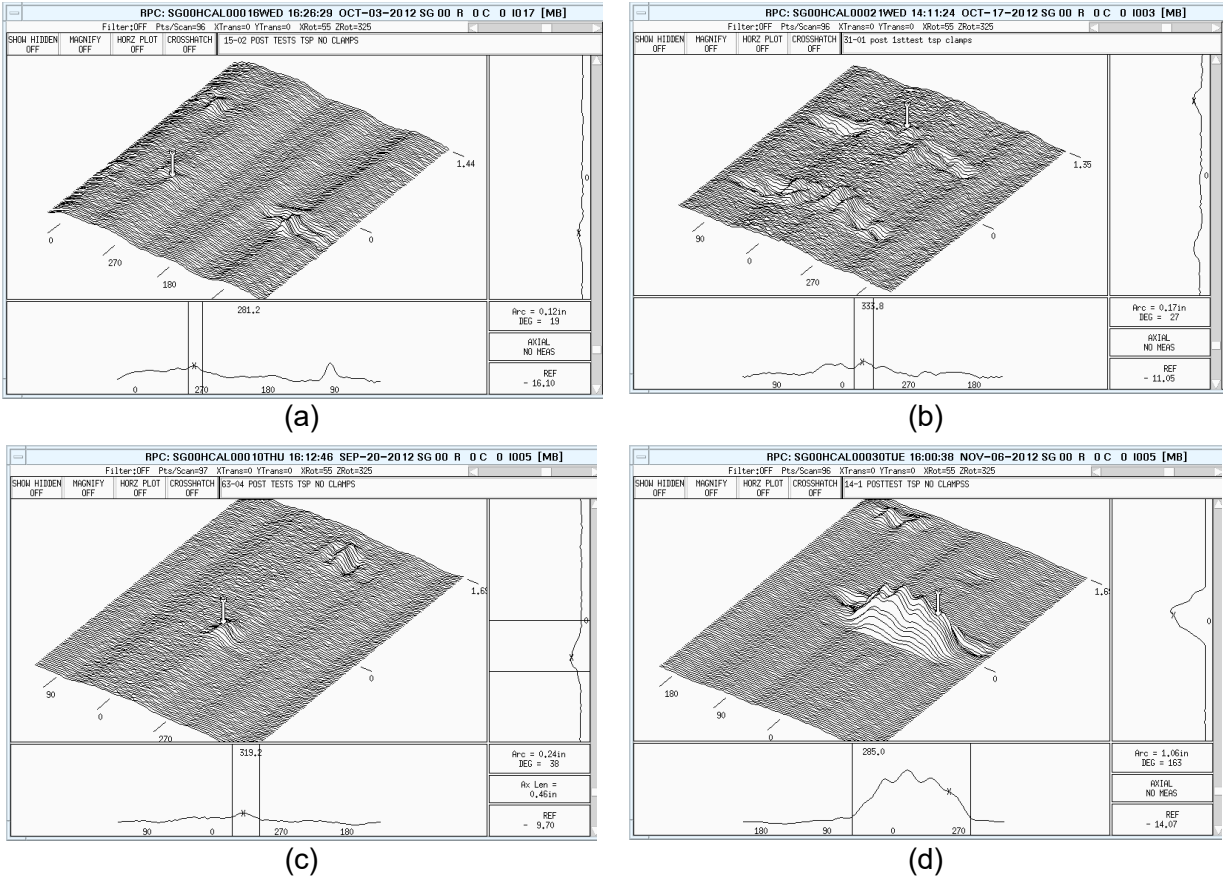
(a)



(b)

Note: Shown above are the stripchart (left) and isometric plot (right) of the +Pt probe data for (a) a small and (b) a large crack in specimen 20-01.

Figure 3-9. Representative data for a 152-mm-radius U-bend specimen with circumferential PWSCC throughout the U-bend region.



Note: The crack signals are (a) at location E in specimen 15-02, (b) at location B in specimen 31-01, (c) at location A in specimen 63-04, and (d) at location E in specimen 14-01.

Figure 3-10. Isometric plots of rotating probe data showing circumferential PWSCCs throughout 152-mm-radius U-bends.

3.3 Effect of U-bend Geometry on Eddy Current Probe Response

The large characteristic response of EC probes at small-radius U-bends can adversely affect detection, characterization, and sizing of flaws that might be present anywhere along the bend region. This is particularly true for small-amplitude signals (i.e., low S/N), which could be masked by the larger background signal at U-bends. The deterministic source of noise at small-radius bends exhibits itself as transverse ripples in EC rotating probe data with the features resembling deep flaw-like indications of ID origin. This unwanted background signal, referred to here as U bend noise, is not truly periodic and can interfere either constructively or destructively with consequential signals associated with cracking. Because of the difficulty in separating potential flaw signals from the more dominant noise, measurement of signals at U-bend regions could become ambiguous. For that same reason, measuring the change in signals through conventional historical comparison of EC inspection data from small-radius U-bends can become subjective and thus lead to a higher level of uncertainty in data analysis results.

Initial evaluations carried out in this work indicated that the level of coherent and deterministic U-bend noise present in EC inspection data from the Argonne specimens was comparable to

those obtained from other sources, which included the EPRI database of outside diameter stress corrosion cracking (ODSCC) at U-bends and a limited set of field data. In an attempt to better determine the source of characteristic EC rotating probe response in data from small-radius U-bends, we sectioned one specimen, 890-12, at 45° and at 90° bend locations. Figure 3-11 shows the cross-sectional views of the two cut sections of the tube. Also shown in the figure is the schematic of the test setup for EC inspection of the U-bend tube. It includes an in-line calibration standard with a 270° TSP collar, which is also used as a circumferential position marker. In the figure, the top side of the section is the extrados and the bottom side is the intrados. As the photos in Figure 3-11 show, the change in ovality at the 90° section is higher than that at the 45° section because of the leg displacement induced during the crack production process.

To measure the radius variation along the circumference, a coordinate measuring machine was used. Figure 3-12 shows the polar plots of the inside radius profile along the circumference of the U-bend section. The actual radius profiles are displayed in Figure 3-12(a). Figure 3-12(b) displays an exaggerated (i.e., difference-enhanced) version of the radius profile of the plot in Figure 3-12(a).

A linear plot of the radius profile is shown in Figure 3-13. The radius has its minima near the extrados and the intrados. This is expected because the tube cross-section is squeezed by the bending process and by the leg displacement. The radius profile at the 90° section is closer to a sinusoidal shape than that at the 45° section.

The wall thickness variation along the circumference was also measured by using an ultrasonic thickness gauge, as shown in Figure 3-14(a). As expected, the wall thickness has its minimum value at the extrados and its maximum value at the intrados. There is a negligible difference between wall thickness profiles at the 45° and at 90° sections. Wall thickness variation of specimen 890-12 along the circumference at the apex was remeasured using an ultrasonic thickness probe. Given that two main axial cracks were produced in that specimen by that point, the wall thickness was remeasured to determine whether there are any local changes in proximity to the cracking regions, near the extrados. The two sets of measurements of the wall thickness are plotted in Figure 3-14(b). The second measurement was relatively consistent with the first one, although it showed a slight local variation in the data. Near the main axial cracking regions, as indicated by arrows in Figure 3-14(b), a slight local wall thickness variation can be observed, which exhibits a rather irregular shape. A similar local thickness variation is also evident near the intrados region.

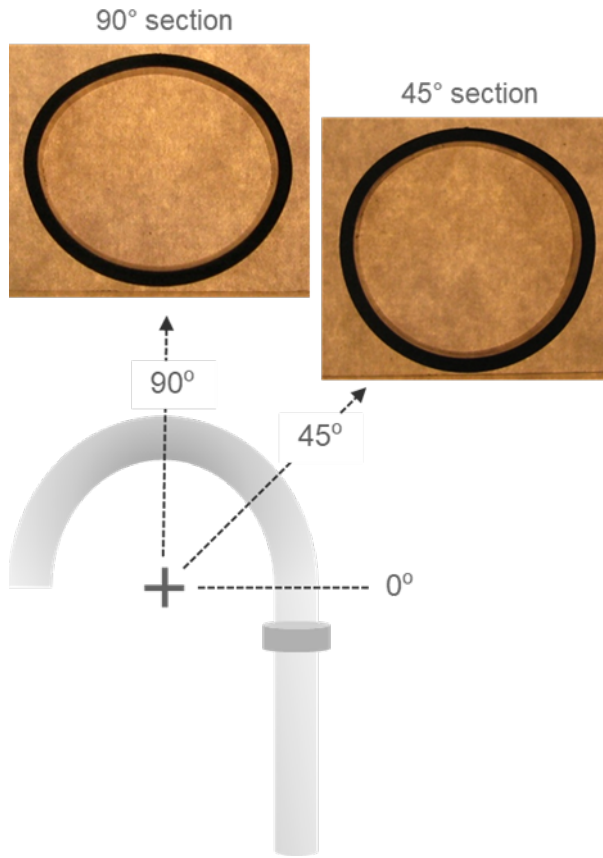


Figure 3-11. Cross-sectional view of U-bend specimen 890-12 cut at 45° and at 90° bend locations as denoted in the figure. The top of each cross-section is extrados and the bottom is intrados. Also shown in the figure is the configuration of test setup for EC inspection of the U-bend section, which includes an in-line calibration standard with a 270° TSP collar.

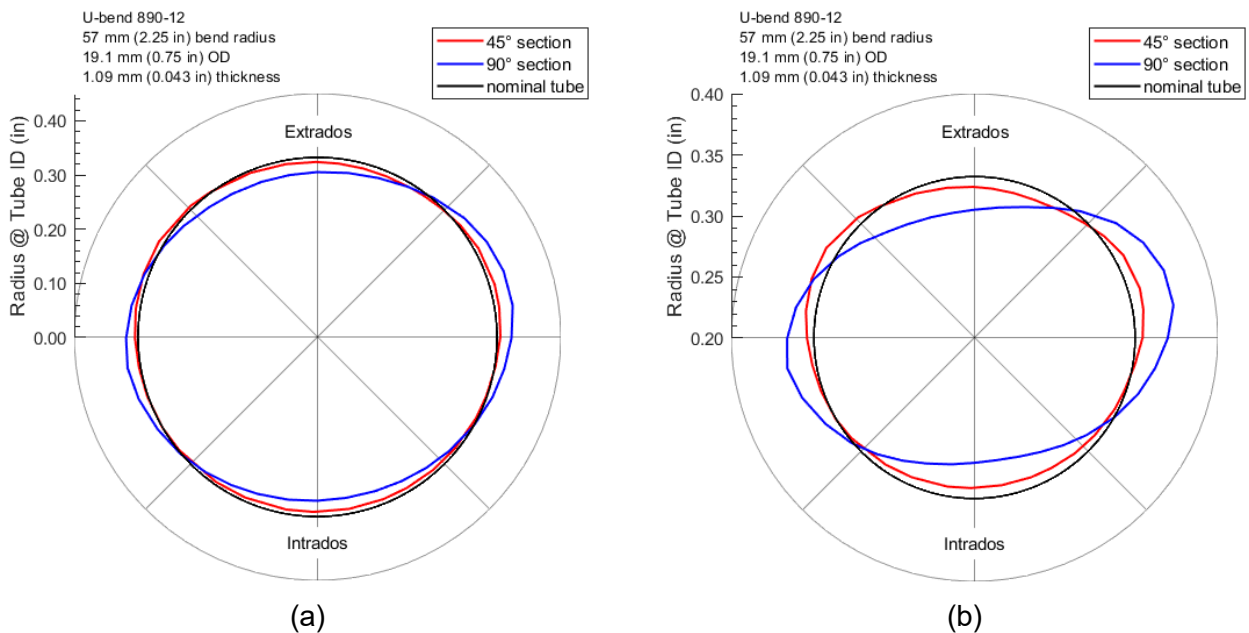


Figure 3-12. Polar plots of the ID radius along the circumference of U-bend 890-12 with two different radius scales showing (a) actual and (b) exaggerated profiles.

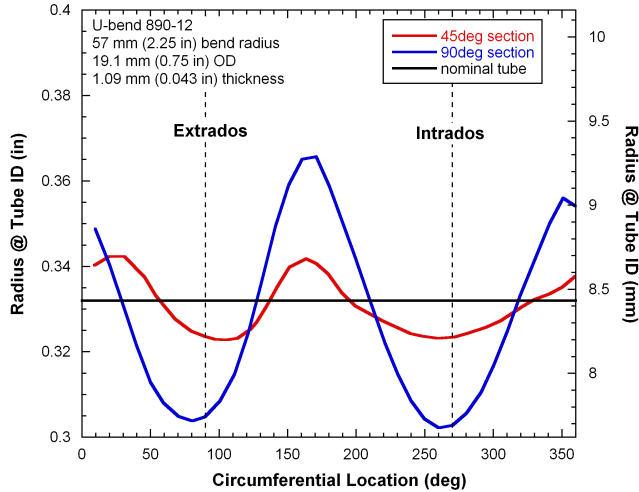
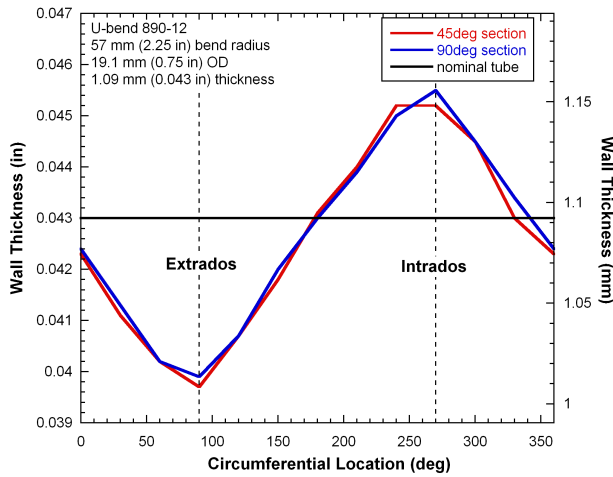
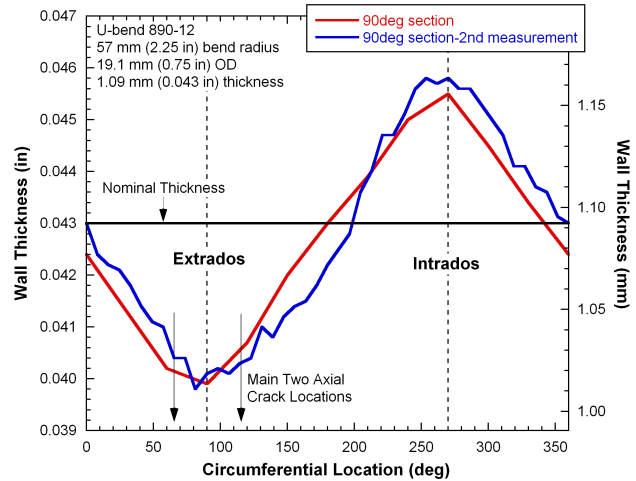


Figure 3-13. Linear plot of the radius profile along the circumference of U-bend specimen 890-12.



(a)



(b)

Figure 3-14. Wall thickness variation of U-bend specimen 890-12 along the circumference (a) at 45° and 90° bend locations and (b) remeasurement at apex.

To identify the locations of the ripples in EC rotating probe response, U-bend specimen 1180-13 with a 19.1-mm OD and 57-mm bend radius was scanned with a 270° TSP collar and carbon steel wire-markers placed on the OD of the tube. In reference to Figure 3-11, the middle of the 90° open section of the TSP collar is aligned with the U-bend intrados. The carbon steel wire-markers are placed at the 0° (tangent point), 45°, and 90° positions along the U-bend. At each position, four wire-markers are placed symmetrically (i.e., 90° apart) around the tube circumference. The rotating probe data were examined using Argonne’s computer-aided data analysis software.

As shown in Figure 3-15, comparison of +Pt rotating probe data for U-bend specimen 1180-13 collected on the “push” and on the “pull” showed no significant difference between the two cases. The results suggest that the alignment of probe and direction of motion do not contribute

significantly to the large baseline signal. This test further suggests that probe wobble inside small-radius U-bends is not the only source of noise in that region.

Figure 3-16 shows the image and the isometric (“terrain”) plot of the calibrated +Pt probe data at 300 kHz encompassing the U-bend section of the tube. The three sets of markers placed at the tangent, 45°, and 90° positions are visible in the data displayed in that figure. The missing section of the TSP collar is aligned with the intrados. The length of U-bend (tangent-to-tangent) was estimated based on axially scaled EC data to be ~185 mm (~7.3 in.).

Figure 3-17 displays the image and isometric plot of the filtered data (after suppression of unwanted background signal) at 300 kHz and at 50 kHz, showing more clearly the alignment of the markers along the U-bend region of specimen 1180-13. While the intensity of the marker signals in Figure 3-16 vary significantly with their circumferential position along the U-bend, the same signals in Figure 3-17 exhibit a relatively uniform intensity once the U-bend noise is suppressed.

To further examine the source of U-bend noise, comparisons were made between the EC inspection data collected with different rotating probes. Isometric plots of data acquired with a high-frequency pancake coil (HF-PC) probe and a mid-range +Pt probe are shown in Figure 3-18. Also shown in those figures are the cross-sectional traces for a single axial location at the apex. In accordance with conventional data analysis procedures, data are calibrated so that flaw-like signals produce a positive vertical component. Comparison of the data in Figure 3-18 for the two probes shows similar trends in variation of both the vertical and the horizontal signal components. The maximum and the minimum values of the vertical signal components of the circumferential trace at the apex appear near the intrados and the extrados, respectively. The horizontal components of the circumferential traces at the apex for the two probes exhibit a similar overall shape with a more abrupt change in probe response being present around the extrados.

Comparisons of the circumferential traces of EC rotating probe data at the 90° and the 45° locations are shown in Figure 3-19. In each case the data for both the +Pt and the HF-PC are plotted on the same graph. Also shown at the top of Figure 3-19(a) and 3-19(b) are plots of the measured ID radius and wall thickness of the tube at the two locations along the U-bend. In general, the data shown in Figure 3-19 indicate that the probe responses at 90° and the 45° zones are rather similar and exhibit a comparable overall complexity. The cross-correlated horizontal signal components, which are more closely related to probe lift-off/wobble, for both the HF-PC and the +Pt probe have similar shapes. Variation of the vertical components of signals exhibits a better correlation to change in wall thickness. The higher frequency variations of the signal components in data from both probes are more likely associated with non-uniform probe motion and misalignment. An important observation based on the data shown in Figure 3-19 is that the dimensional (i.e., wall thickness) and geometry (ID radius) variations of the tube are out-of-phase, which give rise to independent responses of the EC probe in the U-bend. Both the change in conductivity due to wall thickness variations and the change in probe alignment and lift-off due to the change in ID radius of the tube can produce large fluctuations in the EC probe response. In combination, the two effects can produce a complex response by the probe as observed in EC inspection data from small-radius bends.

In summary, the results of these tests indicate that the characteristic probe response in U-bends is the combined effect of tube deformation and change in wall thickness of small-radius bends. The ovalized shape of the tube cross-section at smaller-radius U-bends also leads to a higher level of probe wobble in that region of SG tubing.

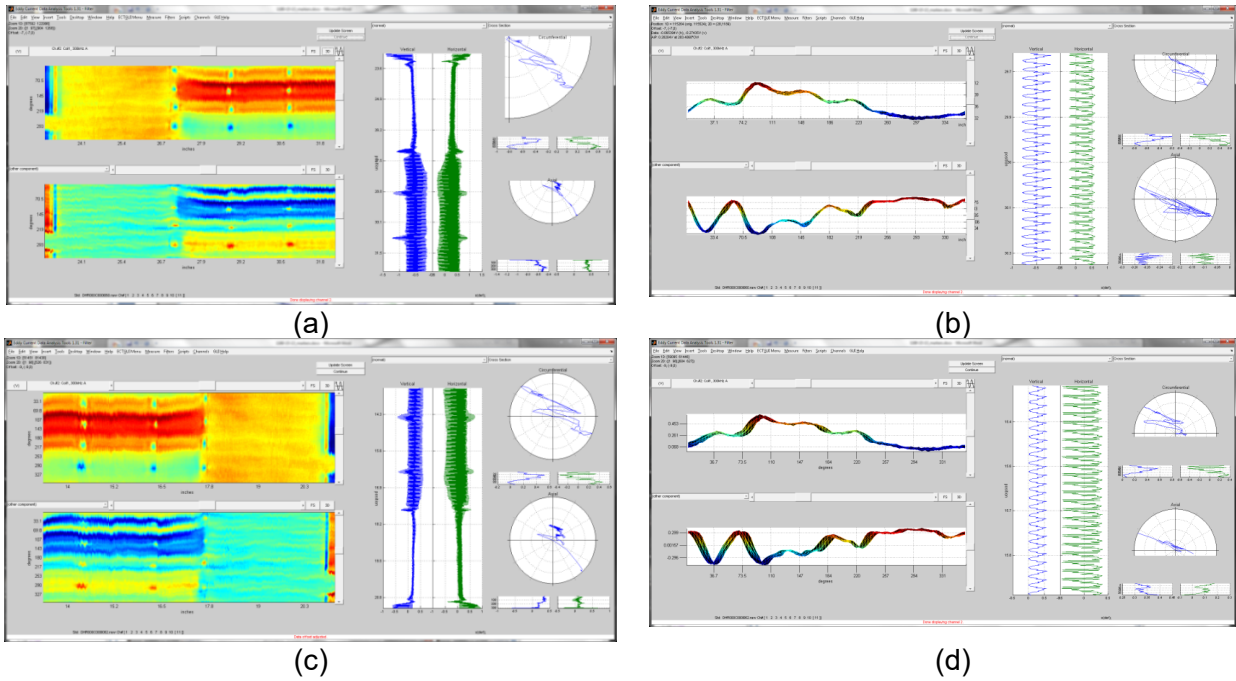


Figure 3-15. Image and cross-sectional terrain profiles of +Pt rotating probe data at 300 kHz for the U-bend specimen 1180-13 collected (a, b) on the “push” and (c, d) on the “pull.”

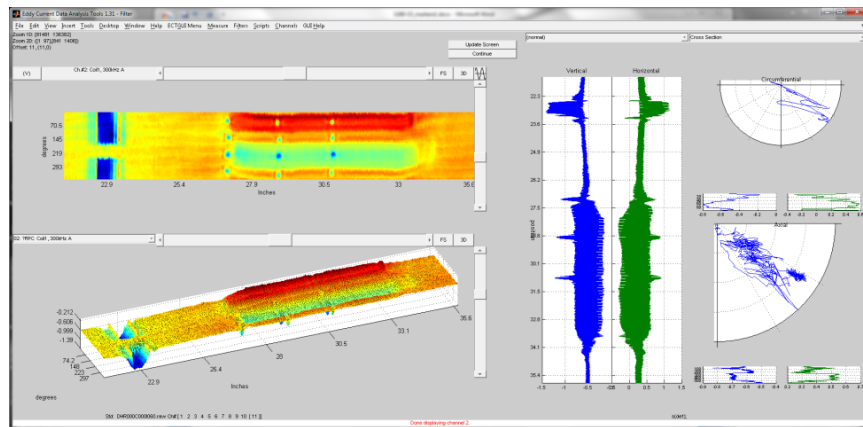
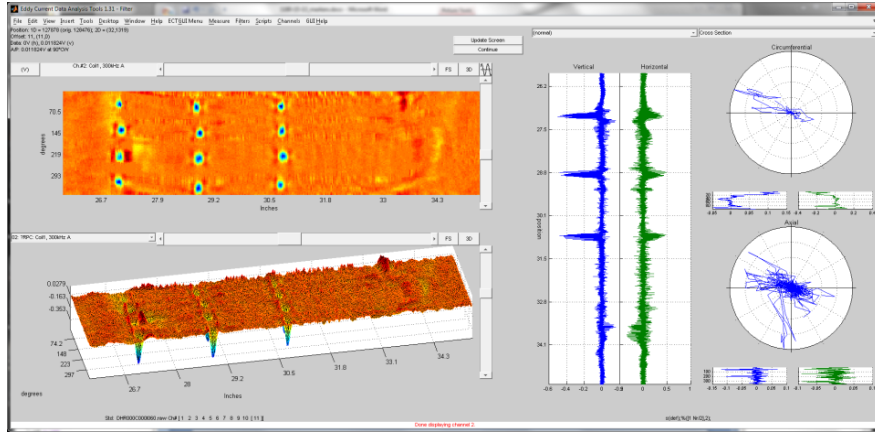
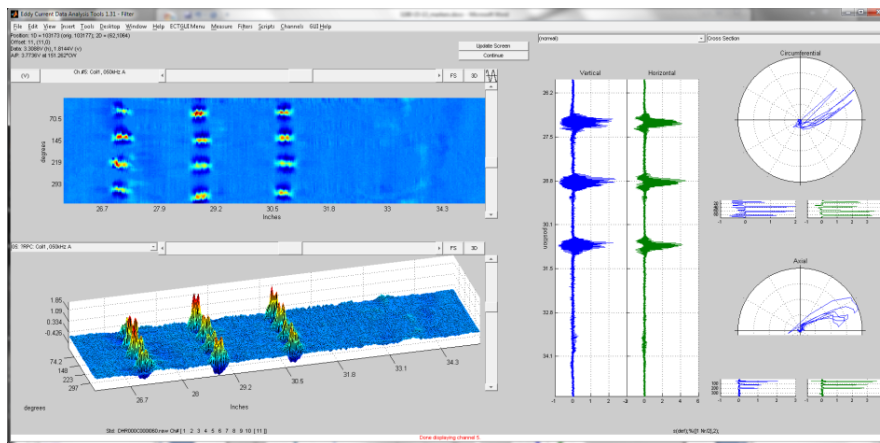


Figure 3-16. Image and terrain profiles showing +Pt data at 300 kHz for the U-bend section of the tube with three sets of markers at the tangent point, 45°, and 90° positions.

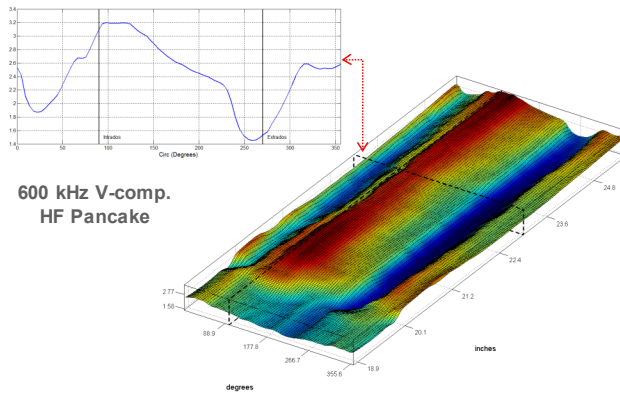


(a)



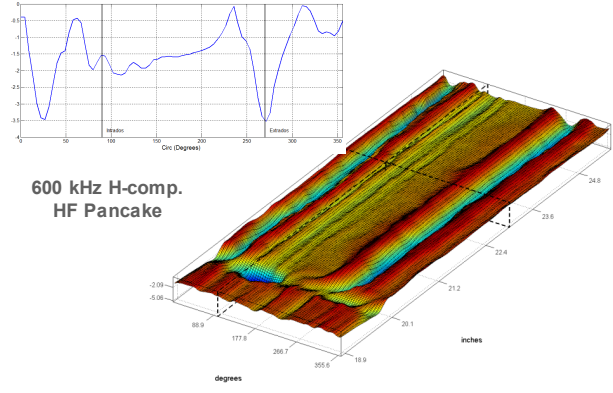
(b)

Figure 3-17. Filtered image and terrain profiles (after suppression of baseline signal) at (a) 300 kHz and (b) 50 kHz showing the alignment of the markers more clearly along the U-bend of specimen 1180-13.



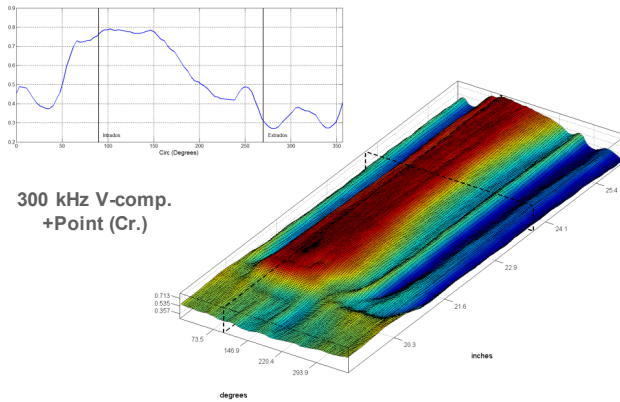
600 kHz V-comp.
HF Pancake

(a)



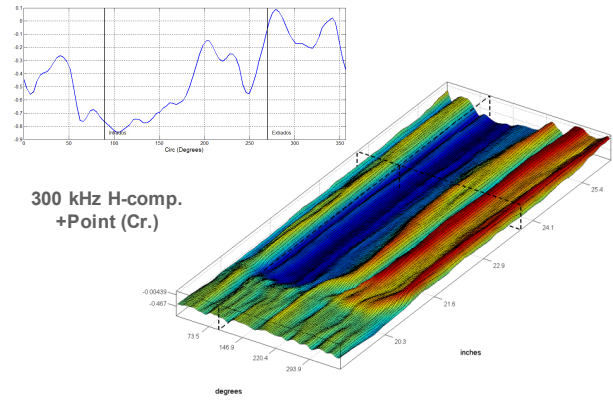
600 kHz H-comp.
HF Pancake

(b)



300 kHz V-comp.
+Point (Cr.)

(c)



300 kHz H-comp.
+Point (Cr.)

(d)

Note: Shown in each case are the circumferential cross-section of data at the apex with the position of intrados and the extrados marked by vertical lines.

Figure 3-18. Isometric display of the vertical component (V-comp) and horizontal component (H-comp) of rotating probe data collected with (a, b) an HF-PC probe at 600 kHz and (c, d) a +Pt probe at 300 kHz on a 57-mm-radius U-bend.

HF-PC +Pt. (Cr.)

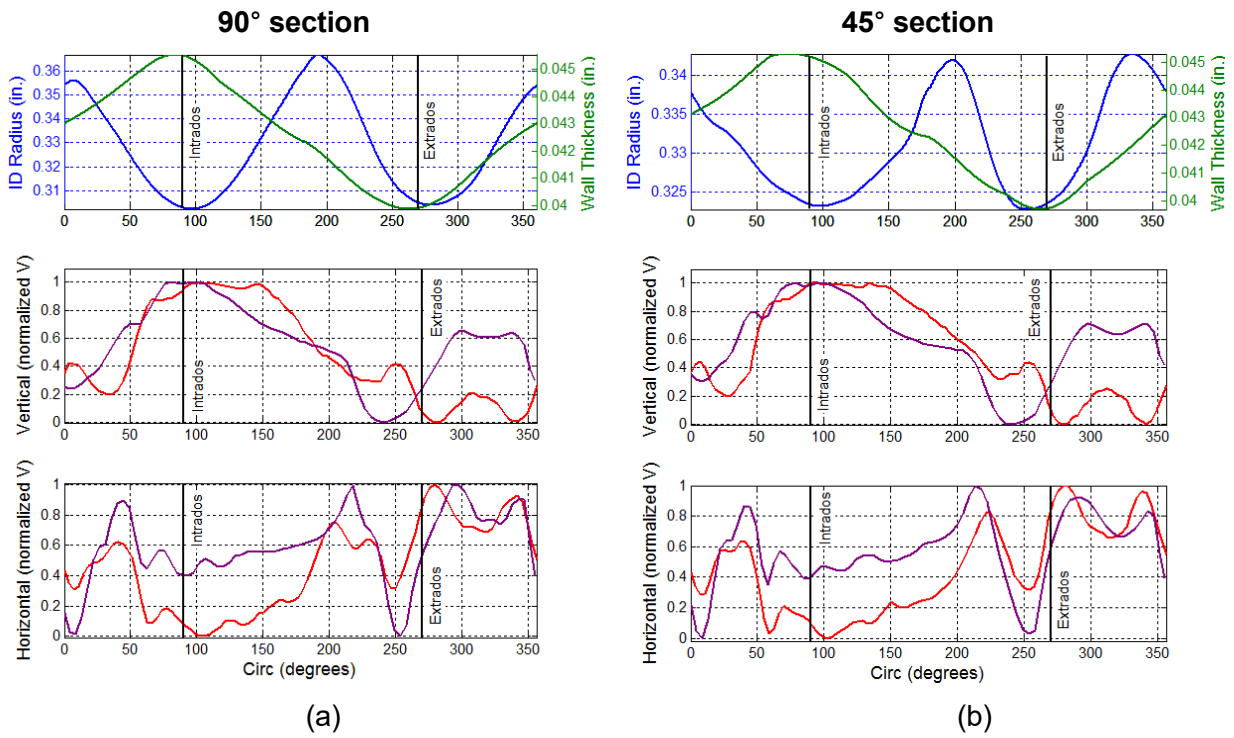


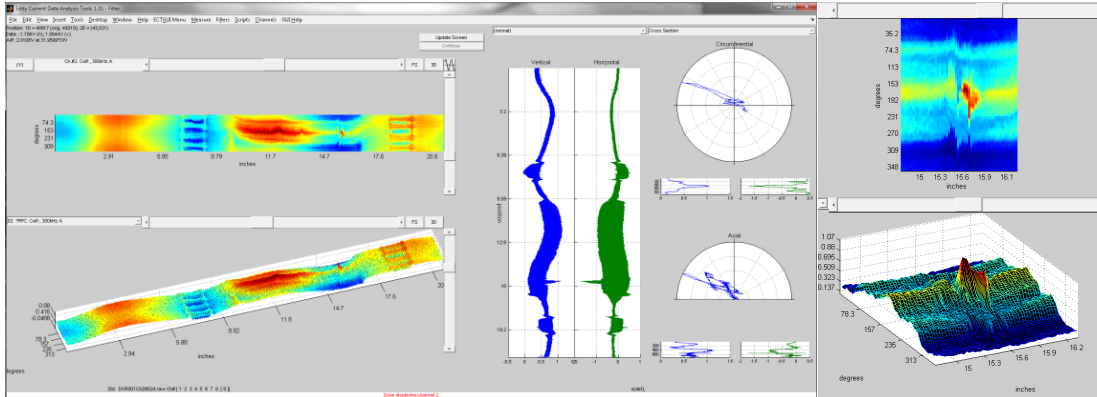
Figure 3-19. Cross-sectional plots of rotating probe data collected with HF-PC and mid-range +Pt probe at (a) 90° section and (b) 45° section of a 57-mm-radius U-bend tube.

3.4 Suppression of U-bend Noise in Rotating Probe Data

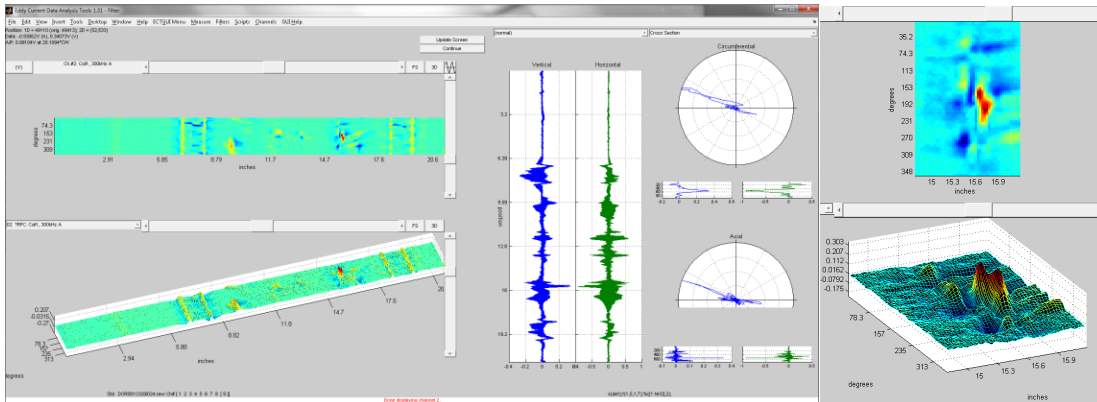
Application of frequency domain filters for suppression of U-bend noise has been shown to be rather ineffective because of the aperiodic nature of such noise in EC rotating probe data. The results of studies here indicate that case-specific spatial domain filtering methods for background suppression are more effective in reducing the influence of the characteristic probe response at U-bends. Among a number of signal processing techniques evaluated for this purpose, bidirectional statistical filters were found to be best suited for improving S/N at U-bends while minimally affecting the signals associated with cracks. However, filters in general should be used with caution and in a consistent manner. This is because arbitrary application of digital filters for removal of unwanted signals can potentially result in inadvertent suppression of consequential signals. Some examples of background suppression schemes in application to EC inspection data from U-bend regions are provided below. A description of the signal processing algorithms used here are provided in other Argonne reports [11, 12].

Representative test cases are shown next that demonstrate the utility of spatial domain filtering schemes implemented at Argonne for suppression of unwanted background signals in the U-bend regions. The examples pertain to analysis of field data for PWSCC at a small-radius-U-bend. The ISI data were collected in 2003 and 2009. The crack signal went undetected — reported as no detectable degradation (NDD) — during the 2003 scheduled shutdown. The signal was detected during the 2009 ISI with an estimated length of >0.5 in. and a maximum depth of 100%TW based on post-ISI analysis of EC inspection data. Based on the EC examination data, the PWSCC was located at approximately 3 inches above the seventh TSP on the hot leg side, which places it slightly above the tangent point in the U-bend. The RSG tubing material was Alloy 600TT with 0.688-in. OD and 0.040 in. nominal wall thickness. The TSPs were a quatrefoil design made of Type 405 SS material. Figure 3-20 displays the pre- and post-processed EC inspection data acquired during the 2003 ISI using a +Pt probe. The data were reanalyzed using the Argonne computer-aided data analysis tool. Based on the data shown in Figure 3-20(a), the crack signal is located at the extrados. The processed data from the 300-kHz channel shown in Figure 3-20(b) indicates good suppression of the background using a spatial domain filter. Comparison of the flaw and the background signals in Figure 3-20(a) and 3-20(b) clearly shows a significant improvement in the S/N of the crack signal.

A second test case on the application of spatial domain digital filters for suppression of background interference is shown in Figure 3-21. In this case, the PWSCC signal extracted from 2009 ISI data was superimposed at three different locations on the data from the U-bend section of the same tube shown in Figure 3-20. The crack signal was amplitude-scaled and phase-rotated to resemble a shallower ID crack before insertion into the host data from 2003. The pre- and post-processed +Pt data at 300 kHz are shown in Figure 3-21(a) and 3-21(b), respectively. Comparison of the data in those figures shows good suppression of the background after the application of a spatial domain filter. The locations of injected signals are marked by arrows in the pre- and post-processed data. Depth profiles of cracks generated automatically using a phased-based sizing method are shown in Figure 3-21(c). The EC flaw sizing results show some difference among the estimated depth profiles of the same superimposed crack at the three locations. This result is attributed to the difference in the level of unwanted residual signals at those U-bend locations following the background suppression process. It is worth noting that the signal processing algorithms evaluated in this study are applicable to suppression of a wide range of background interference in various SG tubing locations.



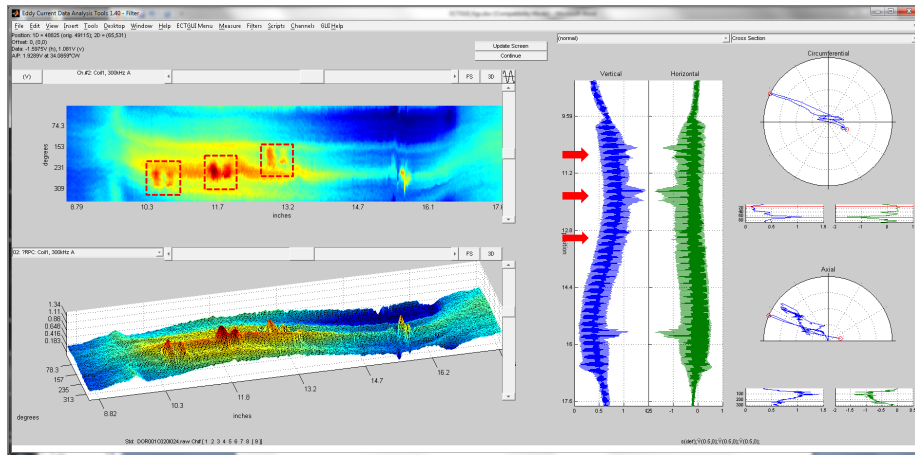
(a)



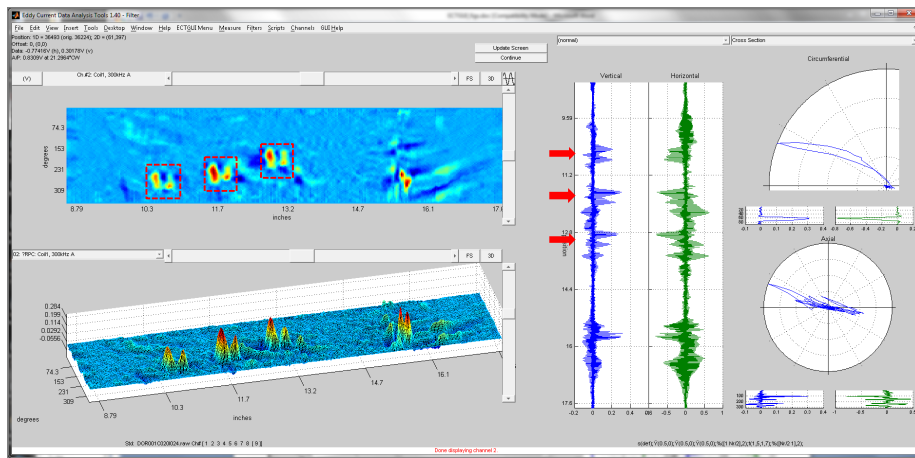
(b)

Note: The data displayed on the right side of each analysis window are the expanded views of a small section of the tube encompassing the PWSCC signal.

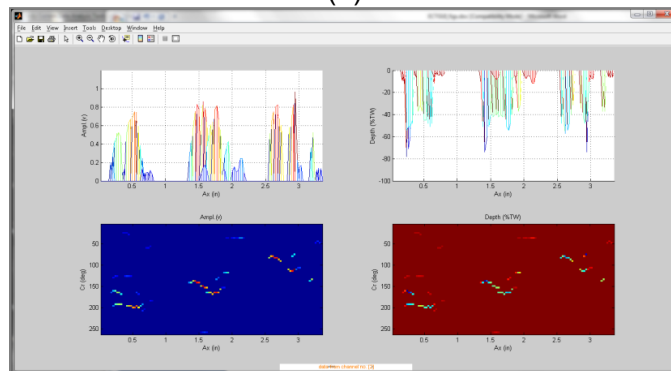
Figure 3-20. Field data acquired during the 2003 ISI with a +Pt rotating probe from a small-radius U-bend tube. The tube had a PWSCC just above the tangent. Shown above are (a) pre- and (b) post-processed data at 300 kHz showing good suppression of the background noise using spatial domain filtering.



(a)



(b)



(c)

Figure 3-21. (a) Pre- and (b) post-processed +Pt data at 300 kHz for the U-bend section of the tube in Figure 3-20. The same PWSCC signal is superimposed at three locations along the U-bend. Also shown are (c) the estimated depth profiles of the crack at the three locations.

4 ASSESSMENT OF CORRELATIONS BETWEEN NDE AND DE STRUCTURAL PARAMETERS

Two separate studies were conducted, before and after destructive examination of flaws in the U bend specimens used in this work to assess potential correlations between NDE parameters and structural parameters. The initial study, which was conducted immediately after pressure testing of all specimens, revolved around assessment of correlations between various NDE parameters obtained from analysis of EC inspection data (i.e., NDE estimates of flaw size described in Section 3.2) and tube structural integrity (i.e., failure pressure). Therefore, the dataset was limited to flaws in 57-mm-radius U-bends that failed during pressure testing of the tubes. The flaw sizing results, provided in Appendix B, in the first study were based on conventional analysis of EC inspection data.

Following the completion of destructive examinations, a second study was conducted to assess the viability of indirect as well as direct correlations between NDE and structural parameters. The NDE estimates of flaw size used in the second study further included the sizing results obtained using alternative analysis of EC inspection data collected shortly before pressurization of the tubes (Section 3.2).

In the following sections, the results are reported from inspection reliability assessments on 57-mm radius U-bends with primary side cracking. First, the results of initial analyses are presented on assessing the viability of indirect correlations between NDE parameters with tube structural integrity. Next, the results of evaluations on NDE sizing accuracy through comparison with DE results for U-bend specimens are presented. Last, the results of a second study are discussed on correlation of NDE parameters with structural parameters obtained from the DE data.

4.1 Assessment of Indirect Correlations

Following the completion of pressure tests for all U-bend specimens at Argonne, studies were conducted to assess potential correlations between NDE and tube structural integrity. The pressure test results for a subset of flaws in 57-mm-radius U-bend tubes and the associated NDE results are provided in Appendix D. Although not used in these studies, the corresponding DE and NDE results for 152-mm-radius U-bend specimens are provided in Appendix E. Eddy current and visual examination (videoscope) data for the cracks in 57-mm- and 152-mm-radius U-bend tubes are provided in Table D-1 and Table E-1, respectively. The pre- and post-pressure NDE and DE results for the cracks in 57-mm- and the 152-mm-radius U-bend tubes are provided in Table D-2 and Table E-2, respectively. The tables also list the failure pressure data for the dominant flaw in each tube that ruptured during the test. It is notable that only a subset of tubes failed when tested up to maximum pressure of the facility (~7.5 KSI).

A study was conducted to assess indirect correlations between various NDE parameters obtained from conventional analysis of EC inspection data (i.e., NDE parameters indicative of flaw size) with tube structural integrity (i.e., measured failure pressures). Only data from U-bend tubes with a 57-mm radius were included in this study. Exclusion of data associated with 152-mm-radius U-bends was based on several factors. Those included the availability of a lower number of specimens, difference in flaw type — that is, PWSCCs in 152-mm-radius bends are primarily circumferential whereas those in 57-mm-radius bends are primarily axial — and the unreliability of the measured failure pressure data (i.e., a number of specimens had an excessively deep flaw). The dataset used in this study is thus limited to PWSCCs in 57-mm-radius U-bends that failed

during pressure testing of the U-bend tubes. Furthermore, the EC inspection data were collected with the U-bend leg displacement clamps in place. The difference between the EC signal amplitude from PWSCCs at U-bends both with and without the presence of leg displacement clamps was discussed in Section 3.2.

Correlation plots were generated for tube failure pressure versus different NDE sizing parameters obtained through conventional analysis of EC inspection data acquired with a +Pt rotating probe. Different symbols are used to distinguish between the data points associated with the flaws at tangents and the flaws at other locations along the U-bend (i.e., above the tangent regions). A linear least squares (LS) regression line was fitted to the data points, which are displayed on a log-linear plot of the dependent variable (i.e., on a linear scale) versus the independent variable on a logarithmic scale. The logarithm of the independent variable was used in LS regression calculation in order to allow fitting a straight line through the data. The performance indicator used in the correlation analyses is the regression error defined in terms of the standard deviation of the fitted data. The first set of independent variables included estimates of maximum signal amplitude (voltage), maximum crack depth, crack length, and crack area (depth * length). The depth here refers to the EC estimate of crack depth, using a phase-based calibration curve, at or near the maximum signal amplitude (i.e., depth at maximum voltage). Different criteria were then used in selecting the candidate dominant flaw in each tube. With most tubes containing multiple flaws, different NDE parameters were evaluated as predictors of the most likely flaw to fail. The results presented here, however, pertain to the selection criteria based on the same NDE parameter used to generate the correlation plot. On each plot, the alternative flaws that were predicted to fail are represented by a different symbol (circles), with a horizontal line connecting the predicted data point to the data point for the flaw that ultimately failed. Table 4-1 includes a summary of the correlation methods used in this section along with the standard deviation of the regression and the number of alternate selections based on the NDE parameter. A summary of LS regression equations describing the fits to the data used in this study is included in Table 4-2.

Figure 4-1(a) shows a plot of the observed failure pressure versus the NDE signal amplitude for axial PWSCCs at 57-mm-radius U-bends. Also drawn on the figure is the regression line fitted to all of the data points. The data in Figure 4-1(a) show a generally good correlation between the EC signal amplitude and the observed tube failure pressure. Figure 4-1(b) has the same plot as Figure 4-1(a), except for the added data points for the predicted alternate flaw to fail in the same tube based on EC signal amplitude as the selection parameter. The predicted failure pressure of alternate flaws in nearly all of the cases here is on the conservative side — the predicted failure pressure of alternate PWSCC is lower than the observed failure pressure of the crack that failed.

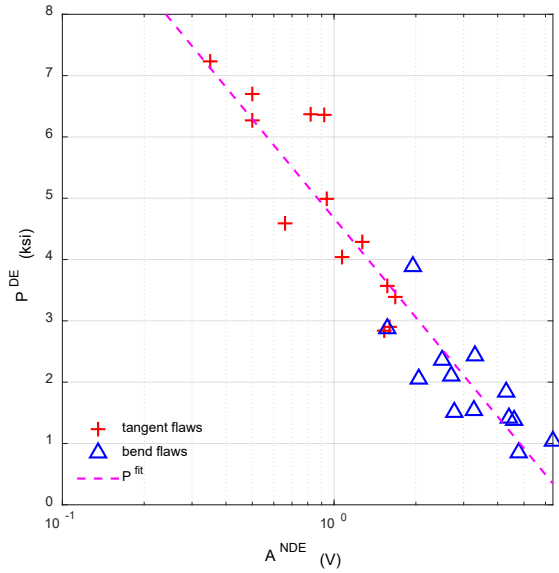
Figure 4-2(a) shows a plot of the observed failure pressure versus the NDE estimate of length for axial PWSCCs at 57-mm-radius U-bends. The data in Figure 4-2(a) show a generally good correlation between the EC estimate of crack length and the tube failure pressure. Figure 4-2(b) has the same plot as Figure 4-2(a), except for the added data points for the predicted alternate flaw to fail in the same tube based on NDE estimate of flaw length as the selection parameter. Once again, the predicted failure pressure of alternate flaws in nearly all of the cases here is on the conservative side. In comparison with the plot shown in Figure 4-1(b), the number of alternate flaws, which were falsely predicted to fail, is larger in Figure 4-2(b).

Figure 4-3(a) shows a plot of the observed failure pressure versus the NDE estimate of maximum depth for axial PWSCCs at 57-mm-radius U-bends. As expected, as the NDE parameter, the maximum depth of a crack alone is not a robust indicator of tube failure pressure. It is also worth noting that the inaccuracy in estimating the depth of cracks, although dependent on various test parameters including the inspection technique, is in general larger than other NDE sizing

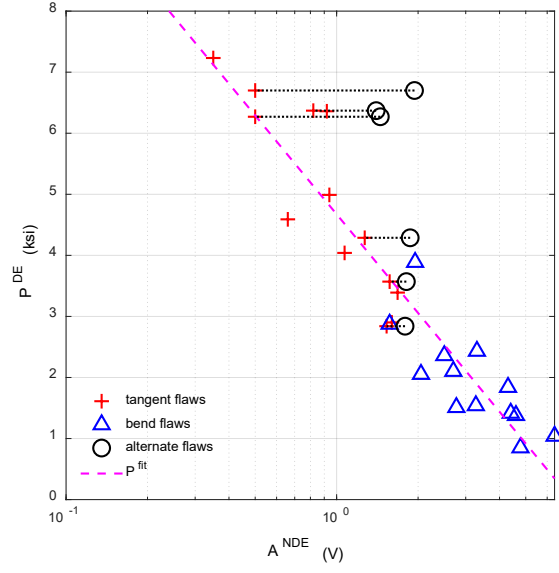
parameters. The challenge in part can be attributed to the complexity of crack morphology. While the flaw depth may be an important parameter from the leakage integrity standpoint, by itself the depth may not be closely associated with the overall size of a crack. Figure 4-3(b) has the same plot as Figure 4-3(a), except for the added data points for the predicted alternate flaw to fail in the same tube based on the NDE estimate of maximum depth as the selection parameter. Figure 4-3(b) shows the added data points for the predicted alternate flaw to fail in the same tube based on NDE maximum crack depth as the selection parameter. As in previous cases, in comparison with the observed failure pressure, the predicted failure pressure of alternate flaws in this case is also on the conservative side.

Finally, Figure 4-4(a) shows a plot of the observed failure pressure versus the NDE estimate of crack area for axial PWSCCs at 57-mm-radius U-bends. The data in Figure 4-4(a) show a generally good correlation between the NDE estimate of crack area and the tube failure pressure. Figure 4-4(b) has the same plot as Figure 4-4(a), except for the added data points for the predicted alternate flaw to fail in the same tube based on the NDE estimate of crack area as the selection parameter. Once again, predicted failure pressure of alternate flaws in nearly all of the cases here is on the conservative side. In comparison with the plot shown in Figure 4-1(b), the number of alternate flaws, which were falsely predicted to fail, is somewhat larger in Figure 4-4(b).

Among the NDE parameters examined above, the EC signal amplitude (V_{pp}) and the crack area (depth * length) exhibited a high degree of correlation with the tube failure pressure. The +Pt signal amplitude, as the NDE parameter, produced the highest degree of correlation with the tube failure pressure. This implicit relationship can be explained by the underlying principle that, for a given flaw type and in the absence of different contributing factors, the EC probe response is more closely associated with the volume than any linear dimension of the flaw. Slightly better prediction results were also obtained in nearly all of the cases examined here when the signal amplitude was used as the selection parameter for prediction of alternative flaw to fail. As noted above, analyses performed separately on the data used in this study indicate that a smaller standard deviation is obtained by fitting separate regression lines to the data for cracks at tangents and cracks at other regions of the U-bend (above tangents). It is worth noting that the distributions of crack sizes at tangents and at other regions of the U-bend are not uniform in the dataset used in this study. Also, EC probe response from failed cracks at the tangent regions are generally smaller than that of cracks in other regions, which could bias the results of correlation analyses. Finally, in some cases, a smaller flaw (based on signal amplitude) in the tangent regions failed before a larger flaw at the apex region. No visible difference was found between flaw morphologies in those regions, as discussed in the next section.

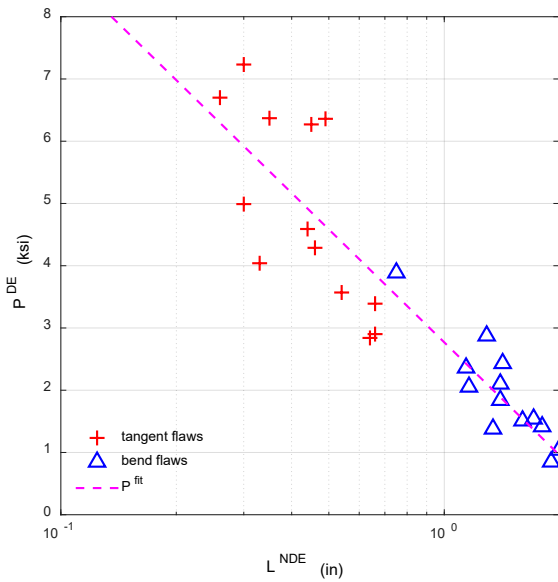


(a)

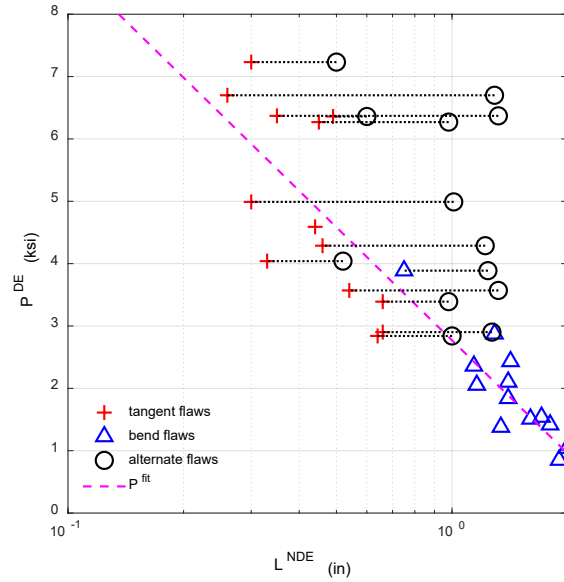


(b)

Figure 4-1. (a) Correlation plot of failure pressure vs. NDE signal amplitude for axial PWSCC in 57-mm-radius U-bends and (b) the same plot as (a) with the added points (circles) for the predicted flaw to fail based on the NDE parameter.



(a)



(b)

Figure 4-2. (a) Correlation plot of failure pressure vs. NDE length for axial PWSCC in 57-mm-radius U-bends and (b) the same plot as (a) with the added points (circles) for the predicted flaw to fail based on the NDE parameter.

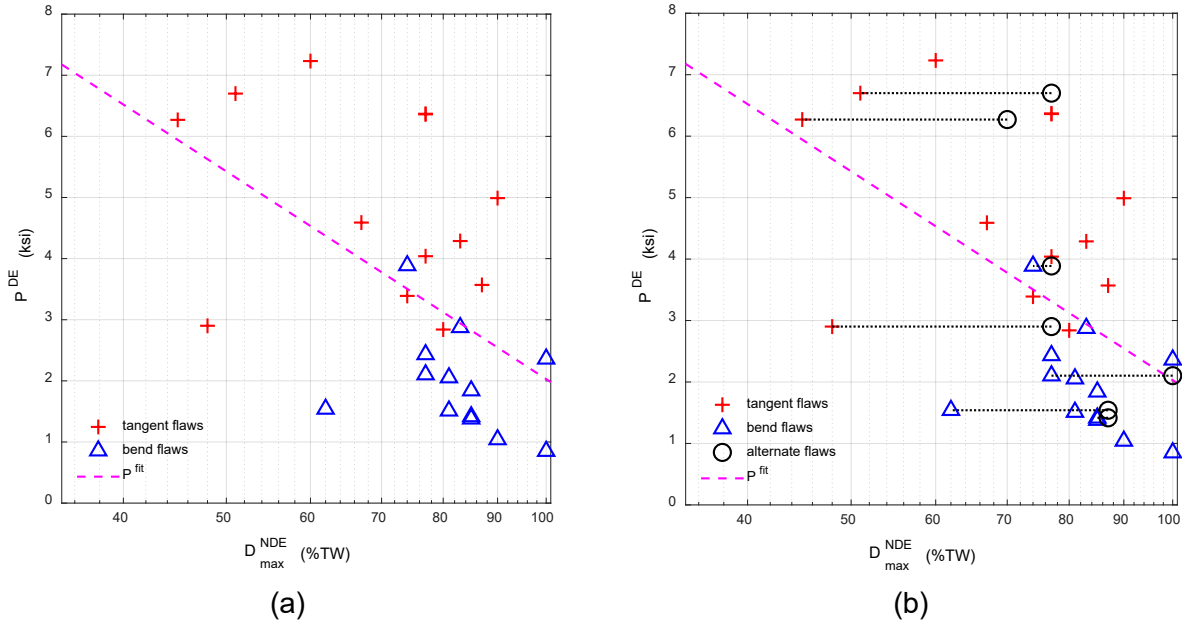


Figure 4-3. (a) Correlation plot of failure pressure vs. NDE maximum depth for axial PWSCC in 57-mm-radius U-bends and (b) the same plot as (a) with the added points (circles) for the predicted flaw to fail based on the NDE parameter.

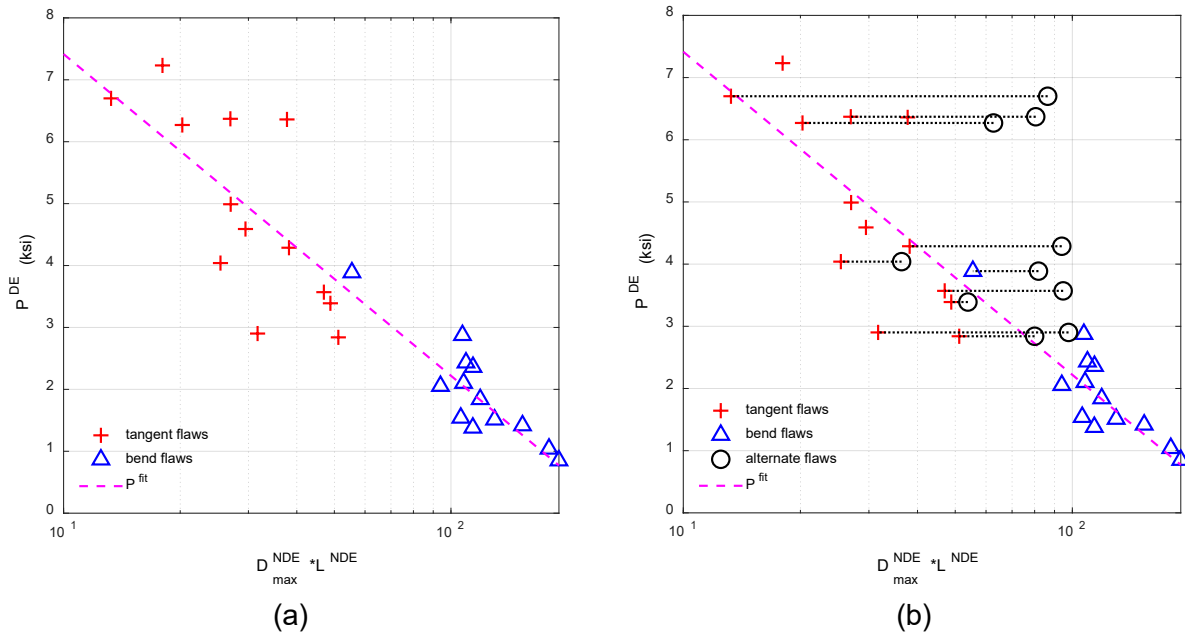


Figure 4-4. (a) Correlation plot of failure pressure vs. NDE crack area (depth * length) for axial PWSCC in 57-mm-radius U-bends and (b) the same plot as (a) with the added points (circles) for the predicted flaw to fail based on the NDE parameter.

4.2 Evaluation of NDE Sizing Accuracy for PWSCC at U-Bends

Following pressure testing of all U-bend tube specimens, fractography was performed on each specimen using SEM. The destructive examination results obtained in this manner served as the ground truth data for the evaluation of NDE estimates of flaw size. Depth profiling based on EC inspection data was performed on all of the primary PWSCCs, as well as on a subset of secondary cracks in each tube section. The analyses were carried out using the computer-aided data analysis tool implemented at Argonne. Comparison of NDE and DE profiles for selected cracks in 57-mm-radius U-bends is provided below. The NDE depth profiles for all PWSCCs in 57-mm-radius U-bends used for correlation analyses are provided in Appendix F. For completeness, depth profiles for a subset of PWSCCs in 152-mm-radius U-bends on which DE was performed are provided in Appendix G.

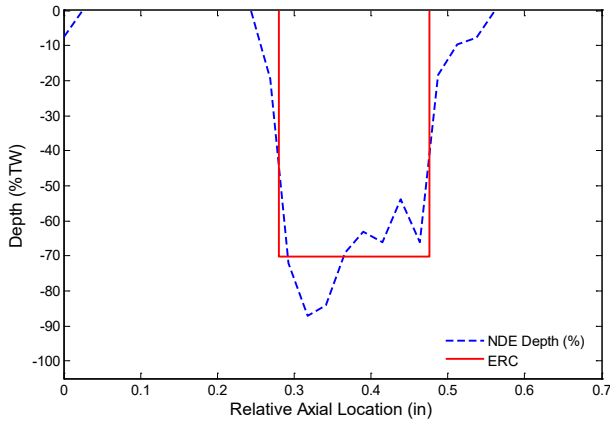
Selected examples are presented on comparison of NDE and DE depth profiles for PWSCCs at U-bends. The EC depth profiles were generated based on analysis of +Pt probe data at 300 kHz. Figure 4-5 shows the flaw sizing results for an axial PWSCC in U-bend specimen 890-16. The tube was pressure tested to failure at 7.14 KSI. The estimated NDE depth profile along with the ERC profile, calculated from NDE data, are shown in Figure 4-5(a). The measured depth profile by fractography is shown in Figure 4-5(b). Figure 4-5(c) displays the EC data segment encompassing the flaw signal in various formats. The results in this case indicate reasonable agreement between DE and NDE estimate of flaw size.

Figure 4-6 shows the flaw sizing results for multiple axial PWSCCs in U-bend specimen 1180-11. The tube was pressure tested to failure at 3.56 KSI. The estimated NDE depth profile along with the ERC profile, calculated from NDE data, are shown in Figure 4-6(a). The measured depth profile by fractography is shown in Figure 4-6(b). Figure 4-6(c) displays the EC data segment encompassing the flaw signal in various formats. Also included in that figure is the videoscope image of the cracks after pressure testing of the tube. The results in this case indicate underestimation of flaw size by NDE. Comparison of the NDE and DE data in this case further demonstrates the challenge associated with resolving closely spaced flaws by EC examination. This outcome is attributed to the limited spatial resolution of the probe, which is dictated by the EC probe's field spread over the conducting surface.

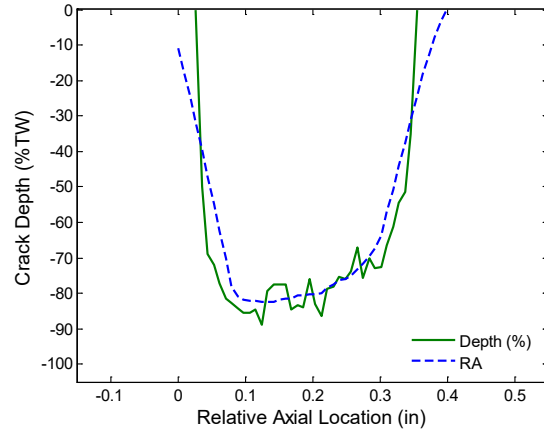
Figure 4-7(a) and (b), respectively, show the depth profiling results by NDE and by fractography for an axial PWSCC in U-bend specimen 920-19. Figure 4-7(c) displays in various formats the EC data segment encompassing the flaw signal. Also provided in that figure is a photo of the cracking region after pressure testing of the tube, showing the presence of multiple PWSCCs separated by ligaments. The results in this case indicate an overall underestimation of flaw size by NDE and the inability of the EC technique to spatially resolve ligaments along the crack length. Figure 4-8 shows another example of depth profiling results for an axial PWSCC in U-bend specimen 1180-20. The NDE and DE depth profiles are shown in Figure 4-8(a) and (b), respectively, and the EC data segment encompassing the flaw signal is shown in Figure 4-8(c). In addition to underestimation of flaw size by NDE, the results once again indicate the inability of the EC inspection technique to resolve crack ligaments. The presence of ligaments can lead to reduction of the EC signal amplitude by providing a conducting path for current flow.

Finally, comparison of NDE and DE sizing results are presented in Figure 4-9 for two axial PWSCCs in U-bend specimen 1180-20. The cracks are located at the tangent and at the apex region of the tube. The EC signal amplitude profiles of the two PWSCCs are shown in Figure 4-9(a) and (b). The NDE depth profiles are shown in Figure 4-9(c) and (d), and the fractography depth profiles are shown in Figure 4-9(e) and (f) for the crack at the tangent and at

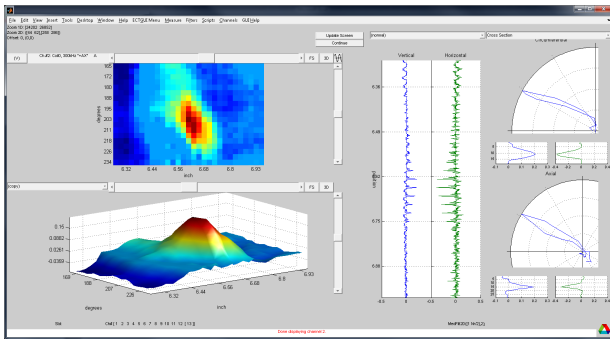
the apex region, respectively. In this case, the crack located at the tangent with the smaller signal amplitude failed before the one with the larger signal amplitude located at the apex. This phenomenon was observed in a few other cases in which a smaller flaw, based on EC signal amplitude, at the tangent failed before a larger flaw at the apex in the same U-bend tube. In all those cases, no visible difference was observed between the morphologies of cracks at those two locations. The initial investigations have pointed to the effect of cold work at the apex, resulting in increased yield strength, as the plausible cause of this phenomenon. Nevertheless, further investigations may be warranted to help gain a better understanding of this phenomenon.



(a)

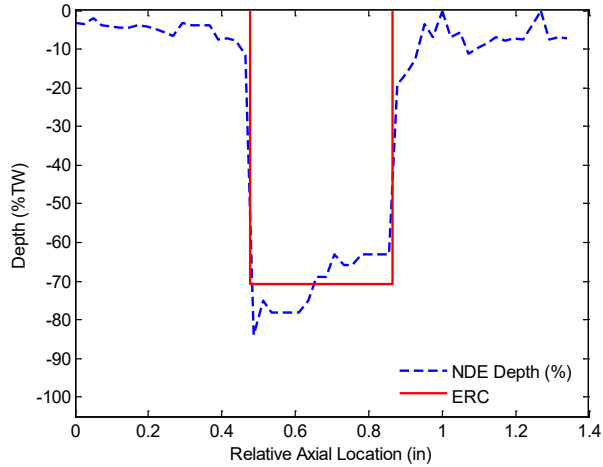


(b)

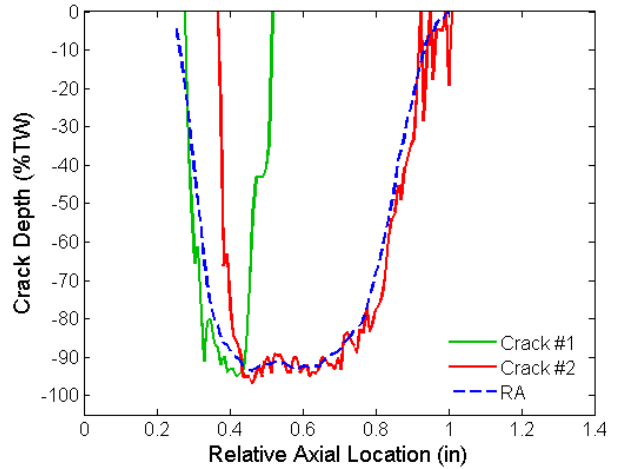


(c)

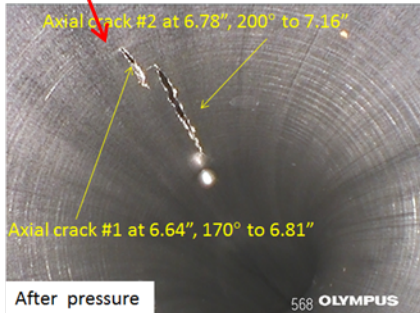
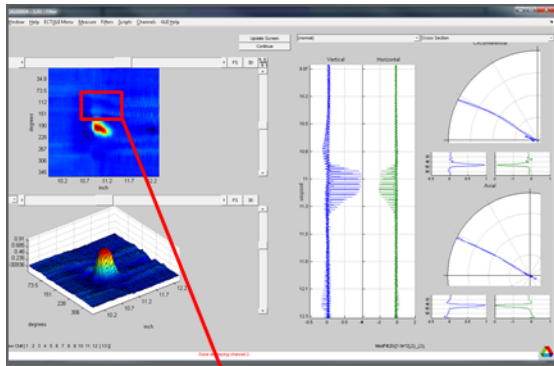
Figure 4-5. Comparison of depth profiling results by (a) NDE and (b) fractography for an axial PWSCC in U-bend specimen 890-16. Also displayed in various formats is (c) the EC data segment encompassing the flaw signal.



(a)

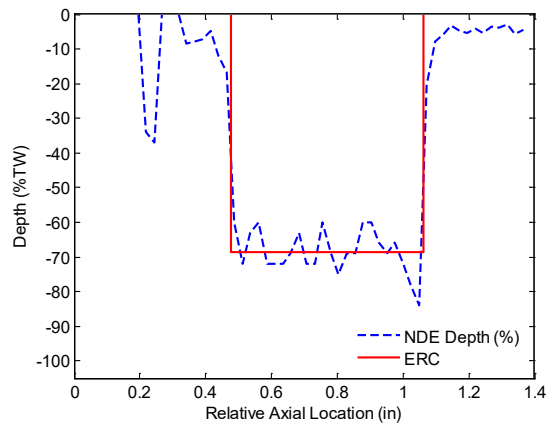


(b)

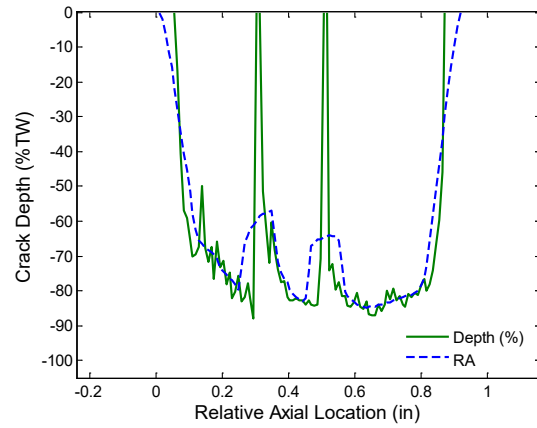


(c)

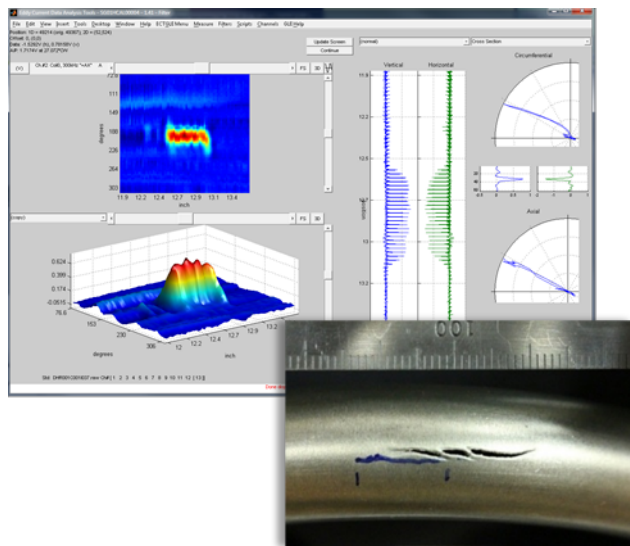
Figure 4-6. Comparison of depth profiling results by (a) NDE and (b) fractography for an axial PWSCC in U-bend specimen 1180-11. Also displayed in various formats is (c) the EC data segment encompassing the flaw signal and videoscope image of the PWSCCs after pressure testing of the tube.



(a)

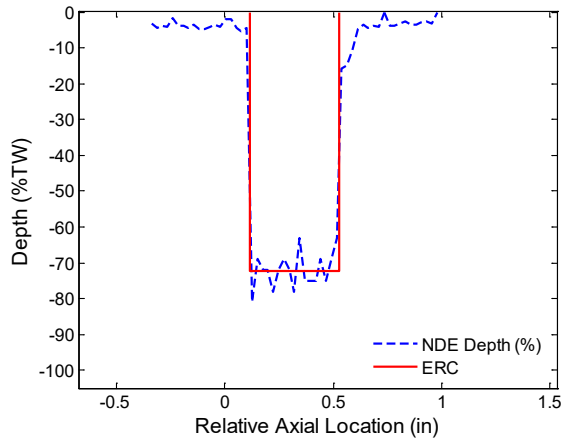


(b)

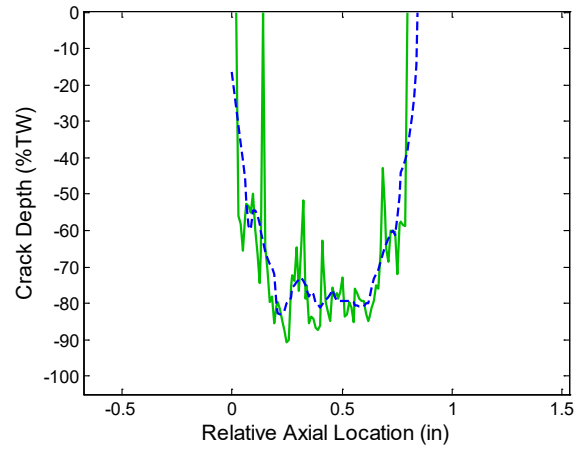


(c)

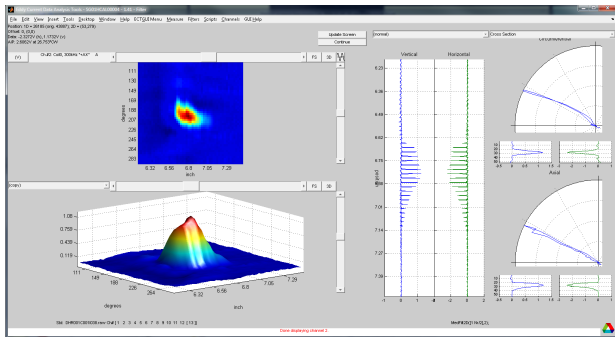
Figure 4-7. Comparison of depth profiling results by (a) NDE and (b) fractography for an axial PWSCC in U-bend specimen 920-19. Also displayed in various formats is (c) the EC data segment encompassing the flaw signal and photo of multiple PWSCCs after pressure testing of the tube.



(a)

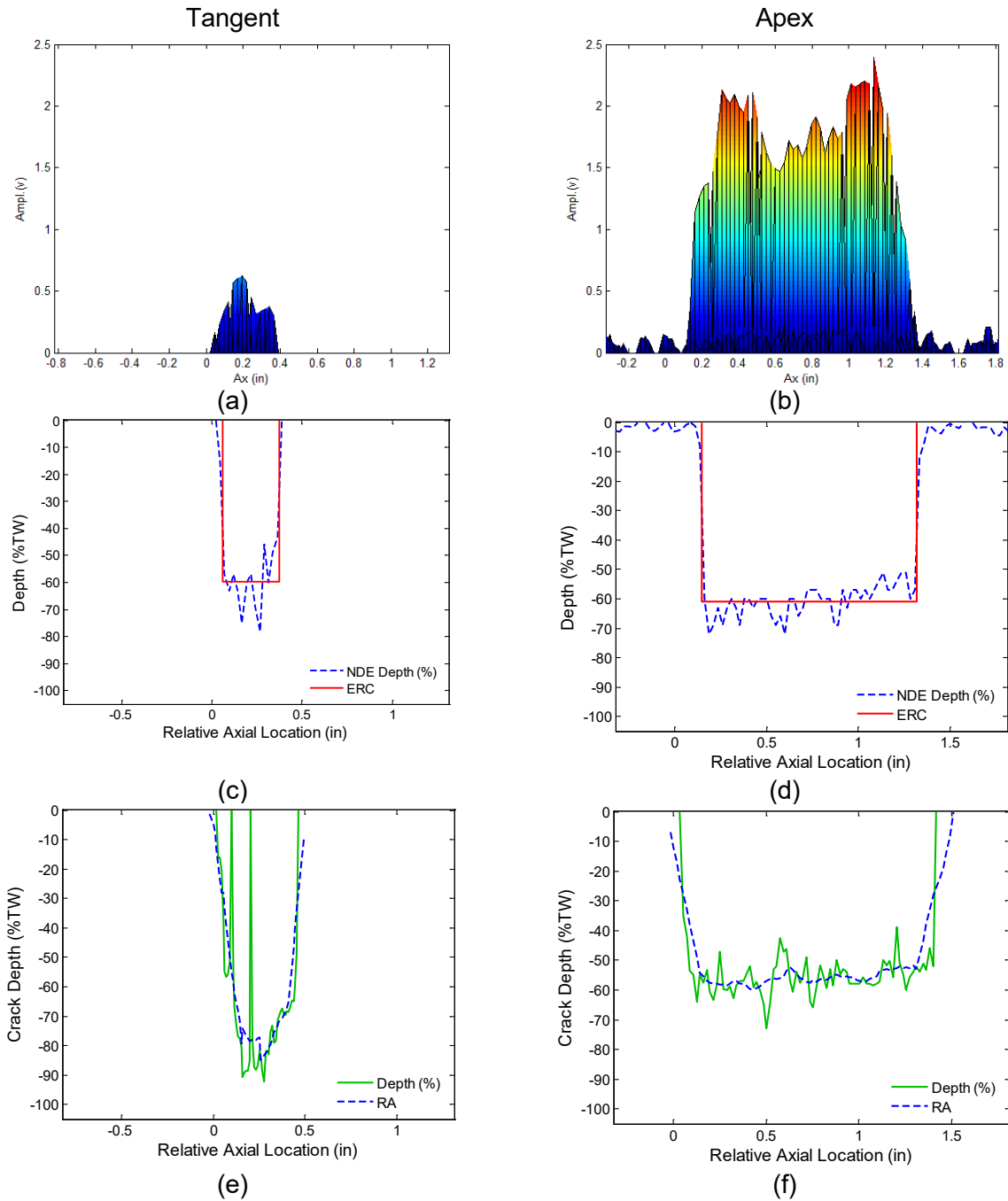


(b)



(c)

Figure 4-8. Comparison of depth profiling results by (a) NDE and (b) fractography for an axial PWSCC in U-bend specimen 1180-20. Also displayed in various formats is (c) the EC data segment encompassing the flaw signal.



Note: Shown above are (a, b) EC signal amplitude profiles, (c, d) NDE depth profiles, and (e, f) fractography depth profiles for the crack at the tangent and at the apex, respectively. The crack at the tangent failed before the one at the apex.

Figure 4-9. Comparison of NDE and DE sizing results for axial PWSCCs in U-bend specimen 1180-20 located at the tangent (left column) and at the apex (right column) regions of the tube.

4.3 Assessment of Direct and Indirect Correlations

Following the completion of destructive examinations, a second study was conducted to assess the viability of both direct and indirect correlations between NDE and DE structural parameters. The DE results obtained by fractography served as the ground truth for the actual flaw size. The NDE estimates of flaw size used in the second study included those obtained using both conventional and alternative data analysis methods. The later analyses were performed using the EC inspection data acquired shortly before the U-bend tube specimens were subjected to pressurization. The results of those analyses were discussed in Section 4.2. A description of the correlation methods used in this study was provided in Section 4.1. In all of the plots shown here, different legends are used for data points associated with axial PWSCCs at the tangent region and those associated with cracks everywhere else along the U-bend (i.e., above the tangent region). A subset of plots includes separate regression lines for the data associated with PWSCCs at tangents and for those at the U-bend region. As described in Section 4.1, Table 4-1 includes a summary of the correlation methods used in this study, along with the standard deviation of the regression and the number of alternate selections based on the NDE parameter. A summary of LS regression equations describing the fits to the data used in this study is included in Table 4-2.

Figure 4-10(a) shows a plot of the measured, by DE, versus the estimated, by NDE, crack lengths for the axial PWSCCs in 57-mm-radius U-bend specimens. The NDE crack lengths were measured using conventional analysis of EC inspection data. Also drawn on Figure 4-10(a) is the regression line fitted to all of the data points, as well as a 45° line representing a perfect positive correlation. Figure 4-10(b) is the same plot as Figure 4-10(a) except that in this case, separate lines are fitted to the data points associated with flaws at tangents and to those associated with the other regions along the U-bend. The data in those figures show an overall good correlation between the NDE and the corresponding structural parameter. The fitted lines in Figure 4-10(b), however, resulted in smaller regression errors when the data points from the tangents and the other locations along U-bend are treated independently.

Figure 4-11(a) shows a plot of the measured, by DE, versus the estimated, by NDE, maximum crack depth for the axial PWSCCs in 57-mm-radius U-bend specimens. The NDE depth in this case is the depth at or near the maximum signal amplitude, which was estimated using conventional analysis of EC inspection data. Also shown in Figure 4-11(a) is the regression line fitted to all of the data points, as well as a 45° line representing a perfect positive correlation. Figure 4-11(b) is the same plot as Figure 4-11(a) except that in this case, separate lines are fitted to the data associated with flaws at tangents and to those associated with the other regions along the U-bend. The data in those figures show a relatively weaker correlation between the NDE and the corresponding structural parameter in comparison to the other parameters examined in this study. Once again, the fitted lines in Figure 4-11(b) resulted in smaller regression errors when the data points from the tangents and the other locations along the U-bend are treated independently.

Figure 4-12(a) shows a plot of the measured, by DE, versus the estimated, by NDE, crack area (depth * length) for the axial PWSCCs in 57-mm-radius U-bend specimens. The flaw size in this case was estimated using conventional analysis of EC inspection data, with the NDE depth representing the depth at or near the maximum signal amplitude. Also shown in Figure 4-12(a) is the regression line fitted to all of the data points, as well as a 45° line representing a perfect positive correlation. Figure 4-12(b) is the same plot as Figure 4-12(a) except that in this case, separate lines are fitted to the data associated with flaws at tangents and to those associated with the other regions along the U-bend. The data in both figures show a reasonable correlation between the NDE and the corresponding structural parameter. As in previous cases, the fitted

lines in Figure 4-12(b) resulted in smaller regression errors when the data points from the tangents and the other locations along U-bend are treated independently.

Figures 4-13 to 4-15 show a series of graphs associated with correlation of the measured flaw size, by DE, with NDE signal amplitude for the axial PWSCCs in 57-mm-radius U-bend specimens. Figure 4-13(a) is a plot of the measured crack length versus the EC signal amplitude, along with a regression line fitted to all the data points. Figure 4-13(b) is the same plot as Figure 4-13(a) except that in this case, separate lines are fitted to the data-associated flaws at tangents and to those associated with the other regions along the U-bend. The standard deviation of regression was lower for the tangent flaws than the U-bend flaws when separate lines were fitted to data for these two regions. In both cases, the data in Figure 4-13 show a good correlation between the NDE and the corresponding structural parameter. Figures 4-14(a) and (b) are plots of the measured crack depth versus the EC signal amplitude. The independent variable in this case is plotted on a logarithmic scale so that the data exhibit a linear trend. Finally, Figure 4-15(a) and (b) show plots of the measured crack area (depth * length) versus EC signal amplitude. The standard deviations of regression in the plots shown in Figure 4-15 are comparable to those in Figure 4-13. Also, similar to the data in Figure 4-13, there is a good correlation between the NDE and the corresponding structural parameter in Figure 4-15.

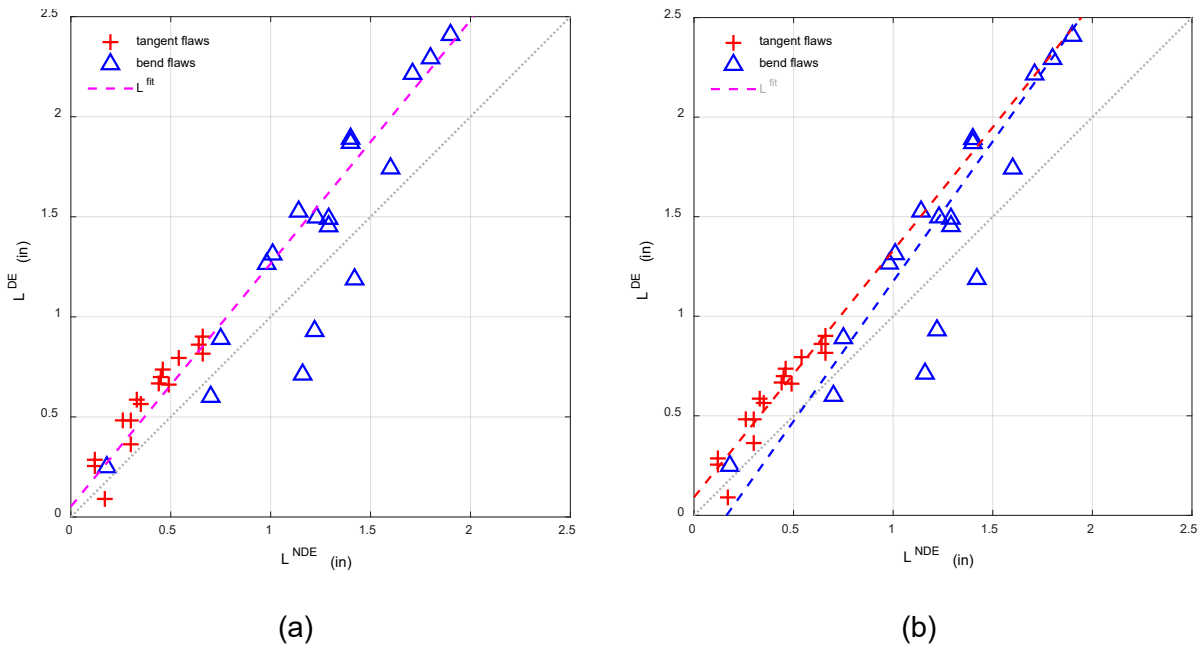
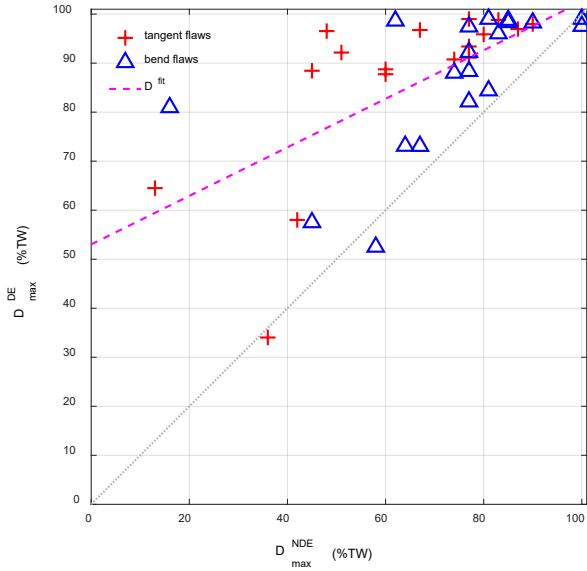
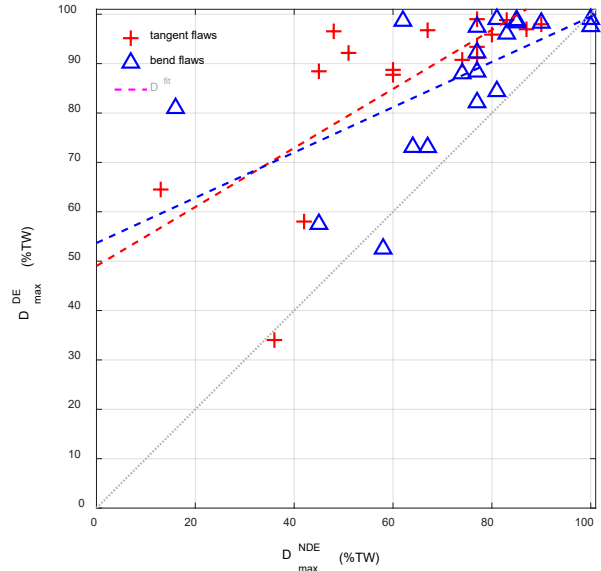


Figure 4-10. (a) Correlation plot of DE vs. NDE crack length with a single line fitted to all data points and (b) the same plot as in (a) with separate lines fitted to tangent and U-bend (above tangent) data points.

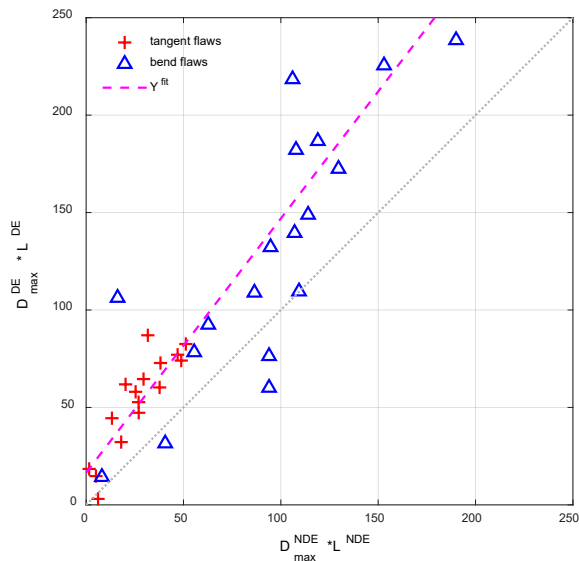


(a)

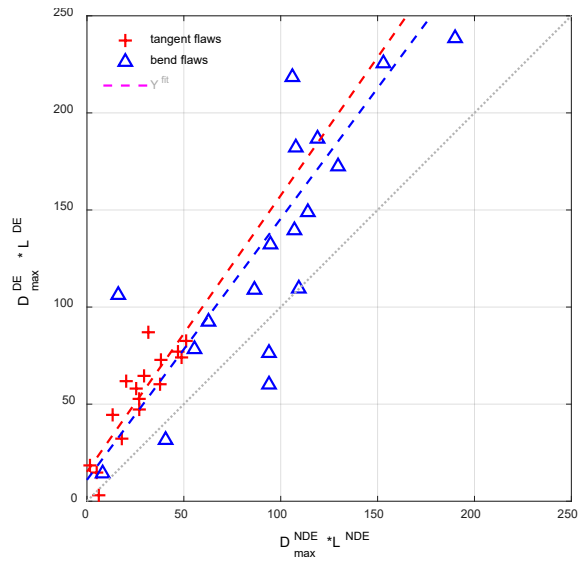


(b)

Figure 4-11. (a) Correlation plot of DE vs. NDE maximum depth with a single line fitted to all data points and (b) the same plot as in (a) with separate lines fitted to tangent and U-bend (above tangent) data.

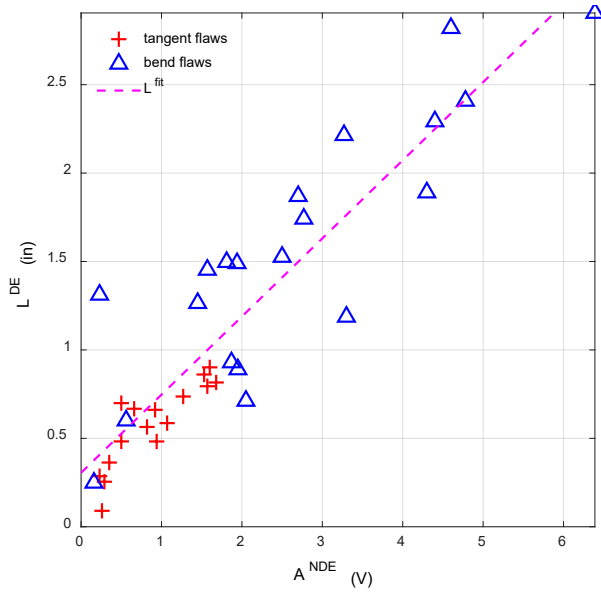


(a)

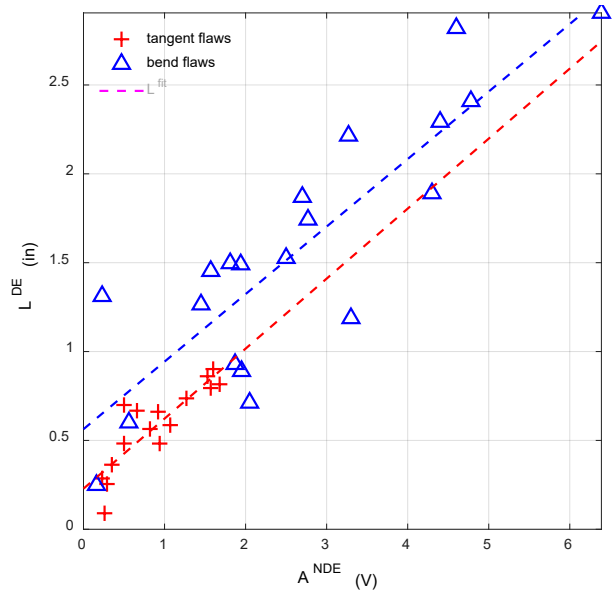


(b)

Figure 4-12. (a) Correlation plot of DE vs. NDE crack area (depth * length) with a single line fitted to all data points and (b) the same plot as in (a) with separate lines fitted to tangent and U-bend (above tangent) data points.

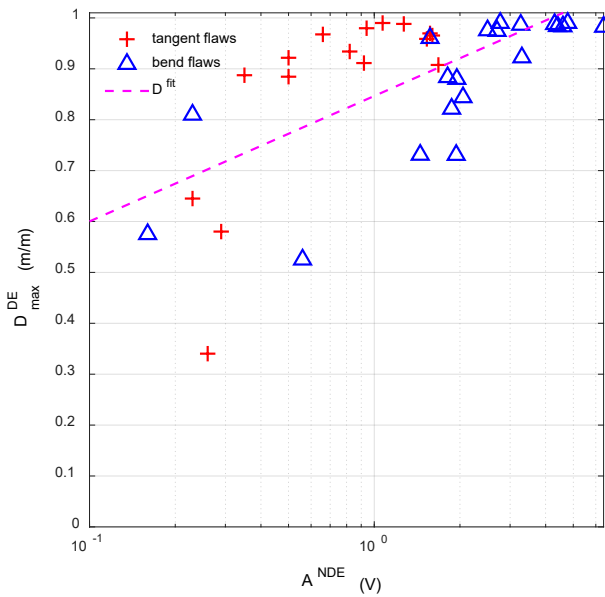


(a)

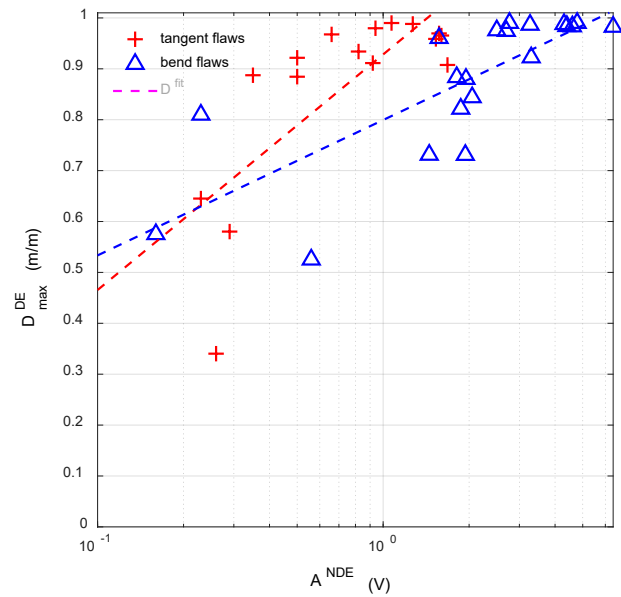


(b)

Figure 4-13. (a) Correlation plot of DE length vs. NDE signal amplitude with a single line fitted to all data points and (b) the same plot as in (a) with separate lines fitted to tangent and U-bend (above tangent) data points.



(a)



(b)

Figure 4-14. (a) Correlation plot of DE maximum depth vs. NDE signal amplitude with a single line fitted to all data points and (b) the same plot as in (a) with separate lines fitted to tangent and U-bend (above tangent) data points.

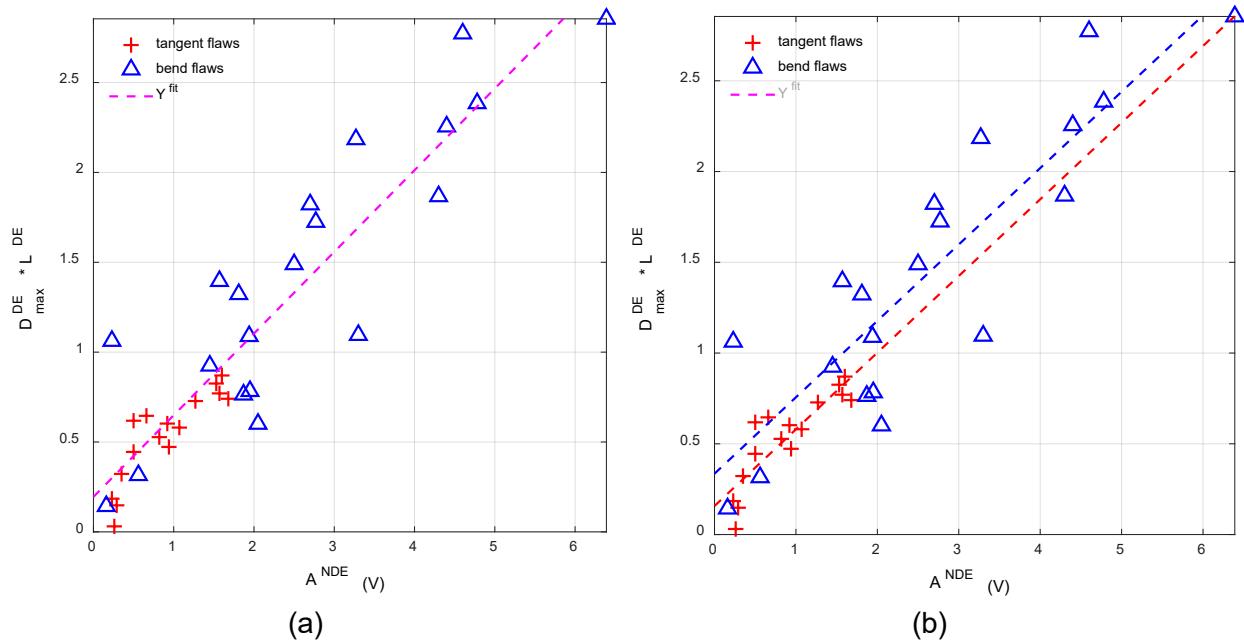


Figure 4-15. (a) Correlation plot of DE crack area vs. NDE signal amplitude with a single line fitted to all data points and (b) the same plot as in (a) with separate lines fitted to tangent and U-bend (above tangent) data points.

The results of evaluations are presented next on the correlation between various NDE and DE structural parameters. The NDE estimates of crack size were obtained through alternative analysis of EC inspection data acquired with a +Pt rotating probe. Depth profiling of PWSCCs was performed using Argonne’s computer-aided data analysis tool, which applies multiple processing stages to the EC data and provides point-by-point estimates of depth along the crack axis. In what follows, the NDE parameters obtained in this manner are denoted by the superscript PRF. Different symbols are used on the graphs shown next to distinguish between the data points associated with the flaws at tangents and the flaws at other locations along the U-bend (i.e., above the tangent regions). A linear LS regression line was fitted to the data points for assessing the degree of correlation between different variables. As noted before, Table 4-1 includes a summary of the correlation methods used in this section, along with the standard deviation of the regression and the number of alternate selections based on the NDE parameter. Table 4-2 contains a summary of LS regression equations describing the fits to the data used in this study.

Figure 4-16(a) shows a plot of the observed failure pressure versus the NDE estimate of length, on a logarithmic scale, for axial PWSCCs in 57-mm-radius U-bends. In this case, the ERC length was used as the NDE parameter. The data in Figure 4-16(a) show a generally good correlation between the EC estimate of crack length and the tube failure pressure. Figure 4-16(b) is the same plot as found in Figure 4-16(a), except for the added data points for the predicted alternate flaw to fail in the same tube based on NDE estimate of flaw length as the selection parameter. The predicted failure pressure of alternate flaws in all of the cases here is on the conservative side. In comparison with the correlation plot shown in Figure 4-2(b), a smaller number of alternative flaws were selected for the data shown in Figure 4-16(b).

Figure 4-17(a) shows a plot of the observed failure pressure versus the NDE estimate of crack area (depth * length), on a logarithmic scale, for axial PWSCCs in 57-mm-radius U-bends. In this

case, the ERC depth and length were used to calculate the NDE parameter. The data in Figure 4-17(a) show a generally good correlation between the EC estimate of crack area and the tube failure pressure. Figure 4-17(b) is the same plot as found in Figure 4-17(a), except for the added data points for the predicted alternate flaw to fail in the same tube based on NDE estimate of flaw size as the selection parameter. The predicted failure pressure of alternate flaws in all the cases here is on the conservative side. In comparison with the correlation plot shown in Figure 4-16(b), the same number of alternative flaws were selected for the data shown in Figure 4-17(b).

Figure 4-18(a) shows a plot of the observed failure pressure versus the NDE estimate of crack area (depth * length), on a logarithmic scale, for axial PWSCCs in 57-mm-radius U-bends. In this case, the length and the maximum value from the moving average depth profile were used to calculate the NDE parameter. The data in Figure 4-18(a) show a generally good correlation between the EC estimate of crack area and the tube failure pressure. Figure 4-18(b) is the same plot as found in Figure 4-18(a), except for the added data points for the predicted alternate flaw to fail in the same tube based on NDE estimate of flaw size as the selection parameter. The predicted failure pressure of alternate flaws in all of the cases here is on the conservative side. In comparison to the previous two correlation plots, the same number of alternative flaws were selected for the data shown in Figure 4-18(b).

Figure 4-19(a) shows a plot of the observed failure pressure versus the predicted ligament rupture pressure (P_{sc}) by NDE for axial PWSCCs in 57-mm-radius U-bends. In this case, the ERC depth and length were used to calculate the NDE parameter. Calculation of the ERC-based failure pressure, P_{sc} , was based on using the same model parameters as those used for a straight tube. Except for one outlier point, the data in Figure 4-19(a) show a generally good correlation between the measured and the predicted failure pressure. Figure 4-19(b) is the same plot as found in Figure 4-19(a), except for the added data points for the predicted alternate flaw to fail in the same tube based on NDE estimate of flaw size as the selection parameter. The predicted failure pressure of alternate flaws in all the cases here is on the conservative side. In comparison to the previous correlation plots, the same number of alternative flaws were selected for the data shown in Figure 4-19(b).

Figure 4-20(a) shows a plot of the observed failure pressure versus the predicted critical pressure (P_{CR}) by NDE for axial PWSCCs in 57-mm-radius U-bends. In this case, the ERC depth and length were used to calculate the NDE parameter. The data in Figure 4-20(a) show a generally good correlation between the measured and the predicted pressure. Figure 4-20(b) is the same plot as found in Figure 4-20(a), except for the added data points for the predicted alternate flaw to fail in the same tube based on NDE estimate of flaw size as the selection parameter. The predicted failure pressure of alternate flaws in all of the cases here is on the conservative side. In comparison to the previous correlation plots, nearly the same number of alternative flaws were selected for the data shown in Figure 4-20(b).

Figure 4-21(a) shows a plot of the observed failure pressure versus the predicted failure pressure by NDE for axial PWSCCs in 57-mm-radius U-bends. In this case, the ERC depth and length were used to calculate the NDE parameter. In reference to Figures 4-19 and 4-20, the predicted failure pressure was taken as the minimum value of the P_{CR} and the P_{sc} . In comparison with the previous two figures, data in Figure 4-21(a) show a smaller standard deviation, and the regression line forms a smaller angle with the 45° line, indicating a higher degree of correlation between the observed and predicted values. Figure 4-21(b) is the same plot as found in Figure 4-21(a), except for the added data points for the predicted alternate flaw to fail in the same tube based on NDE estimate of flaw size as the selection parameter. The predicted failure pressure of alternate flaws in all the cases here is on the conservative side. In comparison to the previous correlation plots,

the data show that nearly the same number of alternative flaws were also selected in this case. Based on the results of analyses presented above, the NDE-based ERC size of PWSCC is a viable indicator of tube structural integrity.

Some general remarks could be made based on the results of correlation analyses presented above. From a statistical analysis standpoint, the performance indicator used in correlation studies here is the regression error rather than the correlation coefficient. Therefore, the results are more indicative of viable trends in the data rather than the prediction accuracy of the correlation functions. It is worth noting that for engineering assessments, systematic under- or over-estimation of any particular structural parameter could in principle be accounted for once the NDE uncertainties and biases have been determined in advance. Among the NDE parameters evaluated in this study, the EC signal amplitude and the crack area, which were estimated based on analysis of +Pt probe data, showed a higher degree of correlation with tube structural integrity associated with PWSCC at the U-bend region. The results were consistent for NDE sizing results obtained using conventional and alternative data analysis methods. In general, better correlations were observed between NDE parameters and tube failure pressure (i.e., indirect correlation) than direct correlations between NDE and DE parameters. By itself, the NDE estimate of crack maximum depth provided a notably lower degree of correlation with DE structural parameters than crack length. It was also observed that the use of ERC dimensions, instead of actual crack dimensions, leads to smaller standard deviations in correlations between structural and NDE parameters. In all the cases examined in this study, a lower standard deviation was obtained when separate regression lines were fitted to the data for cracks at tangents and cracks at other regions of the U-bend (above tangents). As noted previously, this is plausibly associated with the difference in fracture mechanics behavior of cracks at those locations in U-bend tubes with small bend radius.

It should be noted that the observations discussed above are based on the analysis of EC inspection data with prior knowledge about the location and the history of laboratory-produced flaws in the U-bend specimens. Because the potential variables associated with field analyses of ISI data are not factored into analyses of EC examination data from laboratory specimens, the results presented in this report may be treated as the upper limit of the NDE technique's capability. Accordingly, the applicability of the correlation functions established in this work to EC data analysis results from field examinations or to other SG tube flaw types and locations needs to be independently demonstrated.

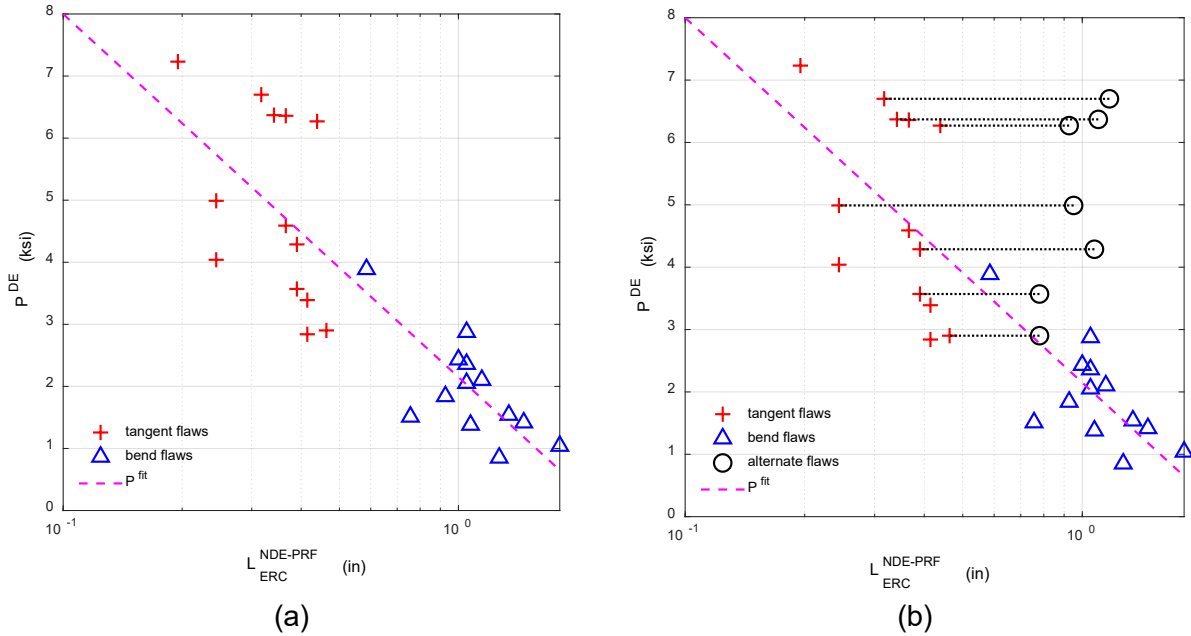


Figure 4-16. (a) Correlation plot of failure pressure vs. NDE crack length obtained from NDE depth profile and (b) the same plot as in (a) with the added points (circles) for the predicted flaw to fail based on the NDE parameter.

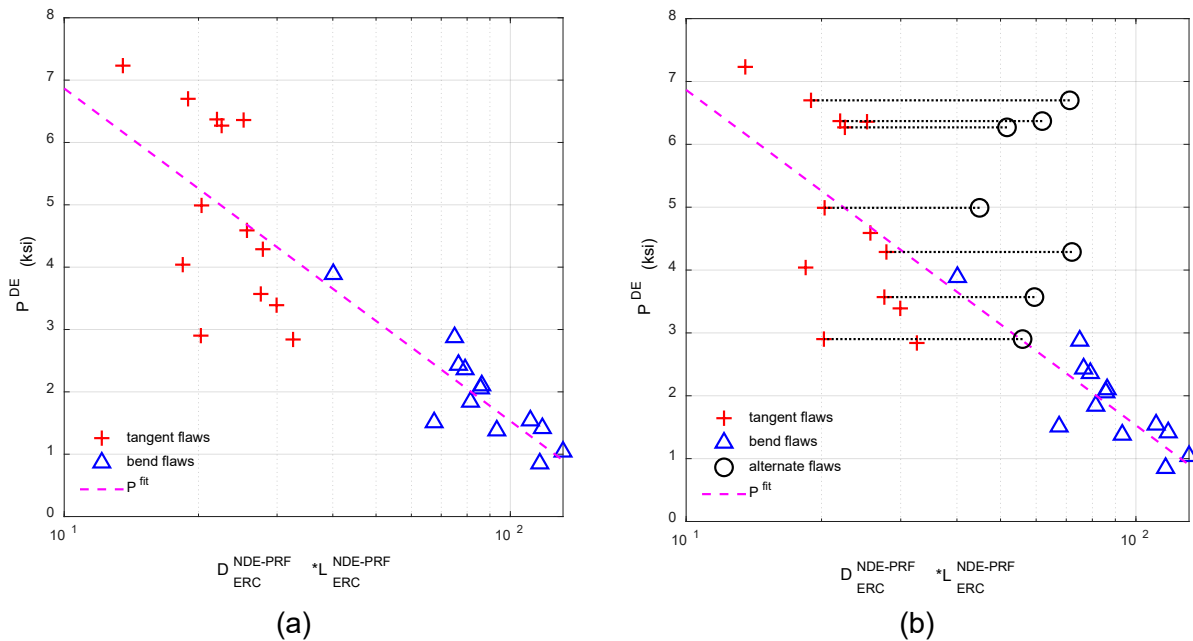


Figure 4-17. (a) Correlation plot of failure pressure vs. NDE crack area (depth * length) obtained from ERC depth profile and (b) the same plot as in (a) with the added points (circles) for the predicted flaw to fail based on the NDE parameter.

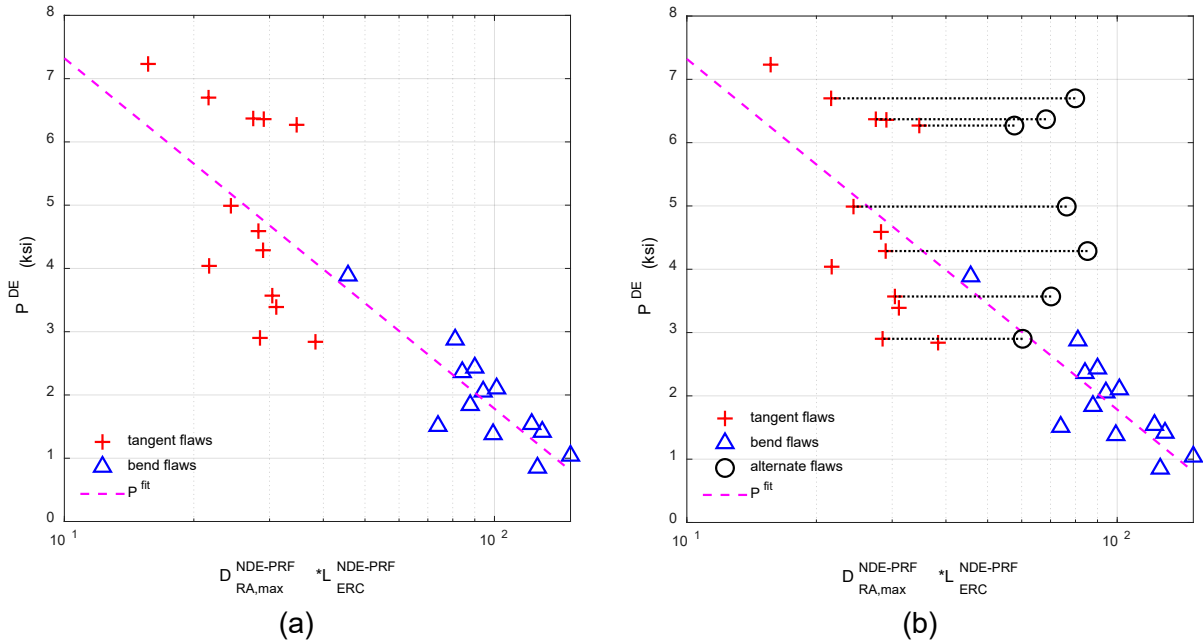


Figure 4-18. (a) Correlation plot of failure pressure vs. NDE crack area (depth * length) with maximum depth obtained from NDE depth profile and length obtained from ERC profile and (b) the same plot as in (a) with the added points (circles) for the predicted flaw to fail based on the NDE parameter.

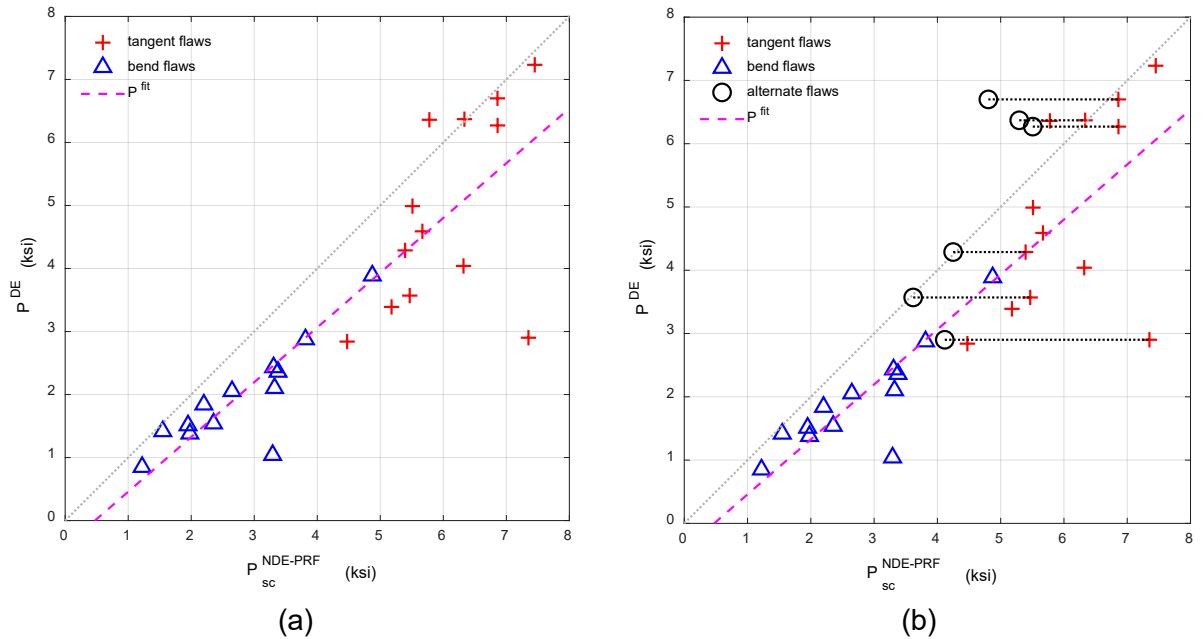


Figure 4-19. (a) Correlation plot of measured failure pressure vs. NDE-based failure pressure (ligament rupture) using ERC profile and (b) the same plot as in (a) with the added points (circles) for the predicted flaw to fail based on the NDE parameter.

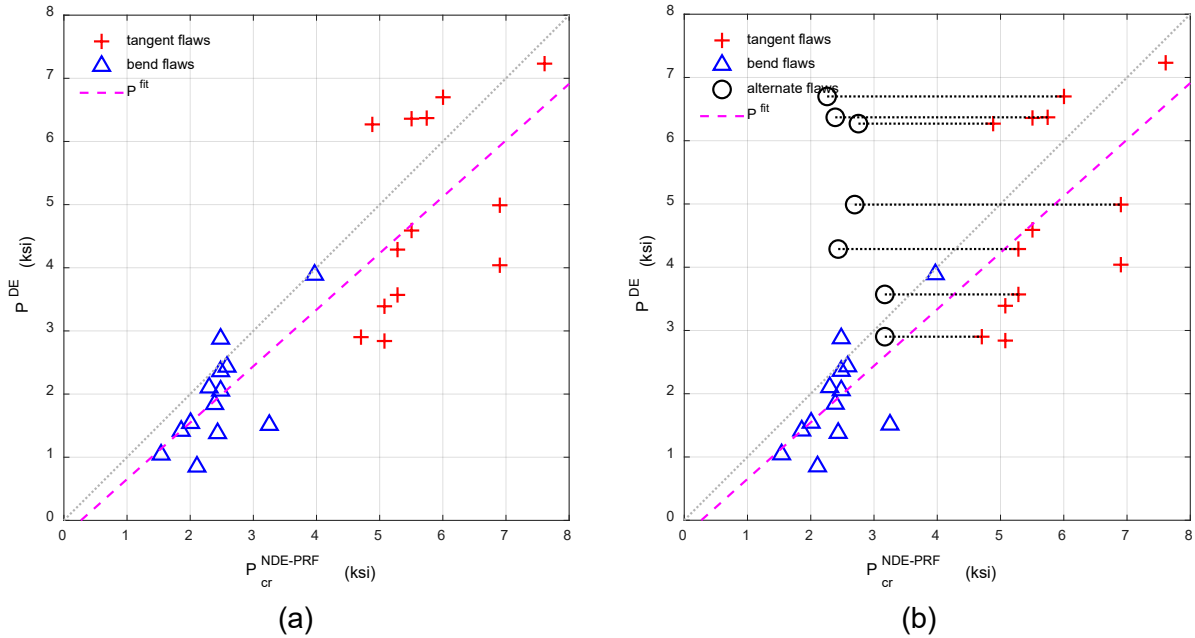


Figure 4-20. (a) Correlation plot of measured failure pressure vs. NDE-based failure pressure (burst) using ERC profile and (b) the same plot as in (a) with the added points (circles) for the predicted flaw to fail based on the NDE parameter.

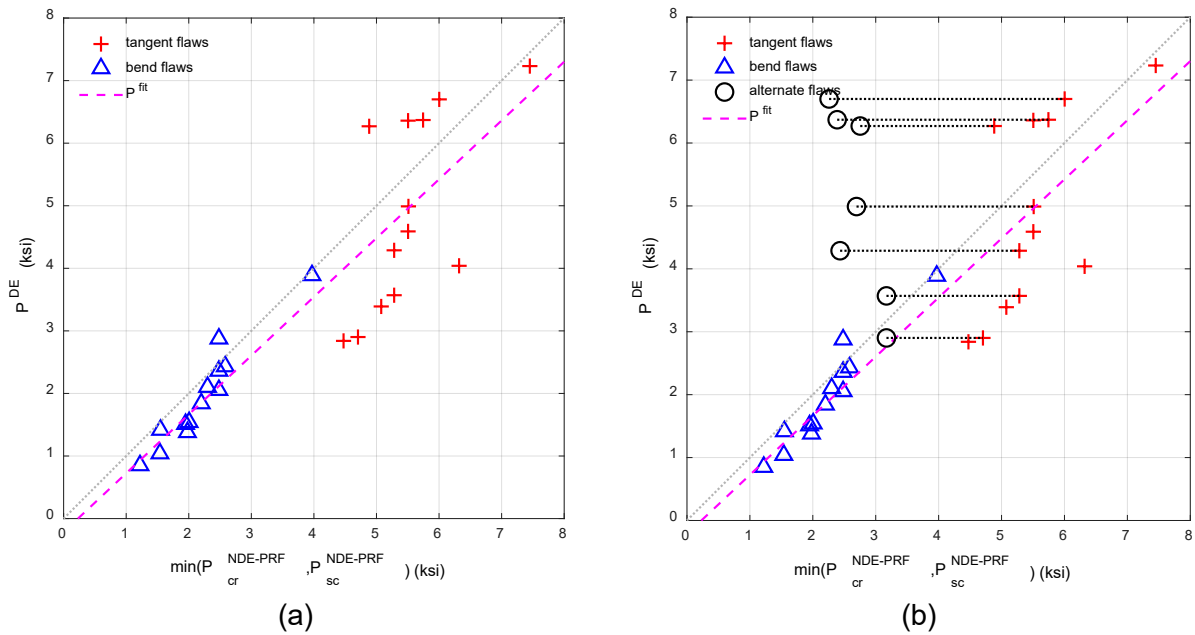


Figure 4-21. (a) Correlation plot of measured failure pressure vs. NDE-based failure pressure (lower value of ligament or rupture burst) using ERC profile and (b) the same plot as in (a) with the added points (circles) for the predicted flaw to fail based on the NDE parameter.

Table 4-1. Summary of correlation method along with the standard deviation of the fit and number of alternate selections based on the NDE parameter.

Correlation Parameter	Standard Deviation (KSI)	Alternate Selections
Amplitude	0.67020	6 (5*)
Length	0.76995	13 (7*)
Max. Depth * Length	0.77943	10 (6*)
ERC min(P_{SC} , P_{CR})	0.86627	7*
ERC Depth * ERC Length	0.94936	7*
ERC P_{SC}	0.95786	6*
Profile RA Max. Depth * ERC Length	0.97769	7*
Profile Max. Depth * ERC Length	0.99348	7*
ERC P_{CR}	1.0198	7*
Profile Cropped Max. Depth * ERC Length	1.0226	7*
ERC Length	1.0386	7*
ERC Depth	1.6127	5*
Max. Depth	1.6434	7 (3*)
Profile RA Max. Depth	1.7078	3*
Profile Cropped Max. Depth	1.8233	3*
Profile Max. Depth	1.8244	3*

* Depth profiling (ERC) was performed on larger flaws only using data collected immediately prior to pressurization tests. Other depths and lengths were obtained through conventional manual analysis for all known flaws in data collected immediately after flaw production.

Table 4-2. Summary of least squares fits to the data discussed in Sections 4-1 and 4-3.

Correlation Parameter	Fit Equation
Amplitude	$P_{fit} = -5.372 \cdot \log_{10}(V) + 4.6729$
Length	$P_{fit} = -6.0277 \cdot \log_{10}(L) + 2.7688$
Max. Depth * Length	$P_{fit} = -5.1953 \cdot \log_{10}(D_{max} \cdot L) + 12.6102$
ERC min(P_{SC} , P_{CR})	$P_{fit} = 0.93984 \cdot \min(P_{SC}, P_{CR}) + -0.21559$
ERC Depth * ERC Length	$P_{fit} = -5.3157 \cdot \log_{10}(D_{ERC} \cdot L_{ERC}) + 12.1695$
ERC P_{SC}	$P_{fit} = 0.86886 \cdot P_{SC} + -0.41083$
Profile RA Max. Depth * ERC Length	$P_{fit} = -5.5272 \cdot \log_{10}(D_{P,RA} \cdot L_{ERC}) + 12.8423$
Profile Max. Depth * ERC Length	$P_{fit} = -5.7258 \cdot \log_{10}(D_{P,max} \cdot L_{ERC}) + 13.3345$
ERC P_{CR}	$P_{fit} = 0.8944 \cdot P_{CR} + -0.24229$
Profile Cropped Max. Depth * ERC Length	$P_{fit} = -5.4739 \cdot \log_{10}(D_{P,crop} \cdot L_{ERC}) + 12.8289$
ERC Length	$P_{fit} = -5.8223 \cdot \log_{10}(L_{ERC}) + 2.156$
ERC Depth	$P_{fit} = -14.6906 \cdot \log_{10}(D_{ERC}) + 30.7865$
Max. Depth	$P_{fit} = -11.2851 \cdot \log_{10}(D_{max}) + 24.5991$
Profile RA Max. Depth	$P_{fit} = -17.4639 \cdot \log_{10}(D_{P,RA}) + 36.9793$
Profile Cropped Max. Depth	$P_{fit} = -11.3766 \cdot \log_{10}(D_{P,crop}) + 25.4414$
Profile Max. Depth	$P_{fit} = -16.8613 \cdot \log_{10}(D_{P,max}) + 36.2731$

Note: Depth profiling (D_P , ERC) was performed on larger flaws only using data collected immediately prior to pressurization tests. Other depths and lengths were obtained through conventional manual analysis for all known flaws in data collected immediately after flaw production.

5 SUMMARY AND CONCLUSIONS

In comparison with other regions of SG tube bundles, the higher levels of background interference in U-bends with small-bend radii can diminish the utility of conventional NDE techniques. Research was conducted to assess the ability of EC inspection techniques to detect and size PWSCC in small-radius U-bends. To that end, a library of tube specimens was assembled at Argonne. Representative U-bend specimens were fabricated by one of the primary SG tube manufacturers. Cracking was induced at various locations along the U-bend region of each specimen using a method developed previously by Argonne. Eddy current inspections were performed at different stages of flaw manufacturing process. Supplementary inspections were also carried out on the entire set of specimens shortly before they were submitted for DE. The NDE data were analyzed using both conventional and alternative data analysis methods. While data were collected using various EC examination techniques, assessments on NDE capability in this work were limited to inspections performed using +Pt rotating probe.

A study was initially conducted in an effort to identify the primary sources of background interference in EC rotating probe data at small-radius U-bends. Different methods for the suppression of unwanted signals in rotating probe data were also evaluated. The following observations were made based on the results of that study.

- The combined effect of tube dimensional and geometry variations, introduced by the bending process, produces a complex probe response at U-bends with small radii of curvature. This undulating probe response, commonly referred to as U-bend noise, is attributed to the change in conductivity caused by non-uniformity of tube wall thickness and variations in probe alignment and lift-off associated with tube ovalization. The U-bend noise exhibits an increasing trend in amplitude starting just above the tangents and reaching a maximum at the apex.
- The characteristic probe response at U-bend regions was found to be fairly consistent in EC data from tube specimens with the same bend radius. A comparable rotating probe response at U-bends was observed in a limited set of field data examined in this study.
- The amplitude of the background noise is largest in U-bends with the smallest bend radius and drops rapidly for bend radii greater than 152 mm. Beyond a certain bend radius (i.e., as bend radius increases), the level of background noise at U-bend regions becomes comparable to that of straight sections of SG tubing.
- The pseudo-periodic rotating probe response at U-bends can interfere both constructively and destructively with flaw signals. Thus, the ability to detect and size the same SCC signal at different locations within the U-bend region can be affected by its axial and circumferential position along that section of the tube.
- Because of the difficulty in separating potential flaw signals from the more dominant background noise, measurement of signals at U-bend regions could in effect become more subjective, thus leading to a higher degree of uncertainty in EC data analysis results.
- For historical comparison of EC data using conventional data analysis methods, the measurement window should enclose the component of signal principally associated with the flaw. In the presence of a strong background interference, inclusion of the entire composite signal (i.e., the combined probe response from background and flaw) within the

measurement window can lead to underestimation of the percent change in amplitude of the flaw signal between different inspections.

- The use of signal processing algorithms evaluated in this work has been shown to improve the detection capability for crack-like signals by suppressing the unwanted EC probe response at U-bends. However, such tools should be used with caution and in a consistent manner, because arbitrary application of filters intended for optimal suppression of unwanted signals could also result in inadvertent suppression of potentially consequential signals.

Two separate studies were subsequently conducted to assess the viability of correlations between various NDE parameters, obtained through analyses of EC inspection data, and structural parameters associated with tube integrity, obtained by DE. Only data from 57-mm-radius U-bend specimens were included in those assessments. The first study was conducted immediately after pressure testing of the tubes. It revolved around assessing the degree of indirect correlation between various NDE parameters associated with flaw size, obtained through conventional analysis of EC inspection data, and tube structural integrity, as determined by the measured failure pressure. The dataset used in those evaluations was thus limited to flaws that failed during pressure testing of the tubes. Based on the results of the first study, a subset of the NDE parameters among those examined was identified as the more viable indicators of tube structural integrity. Following the completion of destructive examinations, a second study was conducted to assess the viability of both direct and indirect correlations between NDE and DE structural parameters. The DE results obtained by fractography served as the ground truth for flaw size. The NDE estimates of flaw size used in the second study included those obtained using both conventional and alternative data analysis methods. The following observations were made based on the results of those two studies.

- Among the NDE parameters examined in this work, the maximum amplitude (voltage) of PWSCC signal in +Pt probe data provided the highest degree of correlation with tube structural integrity. This implicit relationship can be explained by the underlying principle that, for a given flaw type and in the absence of different contributing factors, the EC probe response is more closely associated with the volume than any linear dimension of the flaw.
- The crack area obtained from EC estimates of flaw size was found to be another viable indicator of tube structural integrity, exhibiting a higher degree of correlation with failure pressure than crack length and crack maximum depth alone.
- By itself, the NDE estimate of crack maximum depth provided a notably lower degree of correlation with DE structural parameters than crack length.
- In general, direct correlations between NDE and DE structural parameters produced larger standard deviations than those based on indirect correlations (i.e., tube failure pressure as a function of EC estimates of crack size).
- The use of ERC dimensions, instead of the actual crack dimensions, can reduce the scatter in correlation plots of NDE versus destructively measured structural parameters.
- From a statistical analysis standpoint, the performance indicator used in correlation analyses in this work is the regression error rather than the correlation coefficient. Therefore, the results are more indicative of viable trends in the data rather than the prediction accuracy of the correlation functions.

- In all of the cases examined, a lower standard deviation was obtained when separate regression lines were fitted to the data for cracks at tangents and cracks at other regions of the U-bend (above tangents). This result is plausibly associated with the difference in the behavior of the cracks' fracture mechanics at those locations in U-bend tubes with small-bend radii.
- Based on the results of this research, it can be generally stated that the level of confidence in engineering assessments could be increased by taking into account a larger number of NDE parameters that are considered viable indicators of SG tube structural integrity.

Finally, the following suggestions are made regarding follow-on research efforts on SG tube inspection reliability.

- The results presented in this report are limited to NDE data collected with one particular type of rotating probe. Analysis of the available EC examination data collected with other probe types could help improve SG tube inspection reliability through comparative assessments.
- Evaluation of alternative sizing methods based on analysis of the available data from U-bend specimens could help toward implementation of improved NDE techniques.
- An area of future research with a wide range of applications is the use of signal superposition to augment the existing database of PWSCC at U-bends. This approach could help to significantly reduce the cost associated with experimental evaluations.
- Evaluation of the viability of correlations between NDE and structural parameters and their applicability to other flaw types and locations in SG warrants further investigation.
- The available NDE and DE databases assembled as a result of this work could be leveraged for future research in this area.

6 REFERENCES

- [1] C.B. Bahn, S. Bakhtiari, J.Y. Park, and S. Majumdar, "Manufacturing Stress Corrosion-Cracking Tube Specimens for Eddy Current Technique Evaluation," *ASME Journal of Engineering for Gas Turbines and Power*, March 2013, Vol. 135 / 032902-1.
- [2] C.B. Bahn, S. Bakhtiari, J. Park, and S. Majumdar, "Manufacturing of Representative Axial Stress Corrosion Cracks in Tube Specimens for Eddy Current Testing," *Nuclear Engineering and Design*, Vol. 256, pp. 38–44, Mar. 2013.
- [3] T.A. Pitterle, R.F. Keating, H.O. Lagally, G.P. Pierini, S.J. Orbon, S.D. Brown, and B.W. Woodman, "Tools for Integrity Assessment Project Technical Report; Appendix B: Guidelines for NDE and Destructive Exam Data Acceptability for NDE POD and Sizing Performance Evaluations," Electric Power Research Institute, Palo Alto, CA, 1014567, 2006.
- [4] "Guidelines for PWR Steam Generator Tubing Specifications and Repair, Volume 2, Revision 1: Guidelines for Procurement of Alloy 690 Steam Generator Tubing," Electric Power Research Institute, Palo Alto, CA, Report TR-016743-V2R1, 1999.
- [5] American Society of Mechanical Engineers, "Specification for Seamless Nickel and Nickel Alloy Condenser and Heat-Exchanger Tubes: SB-163," An International Code 2010 ASME Boiler & Pressure Vessel Code, Section II Part B Nonferrous Materials Specifications, 2010, pp. 165–174.
- [6] S. Yashima, et al., "Stresses of Steam Generator U-tubes Affecting Stress Corrosion Cracking," American Society of Mechanical Engineers, ASME/ANS Nuclear Engineering Conference, 1982, Paper # 82-NE-5.
- [7] F.W. Pement, G. Economy, and R.G. Aspden, "In Situ Heat Treatment of U-Bends," Electric Power Research Institute, EPRI NP-5496, November 1987.
- [8] C.O. Ruud, "Residual and Applied Stress Analysis of an Alloy 600 Row 1 U-Bend," Electric Power Research Institute, Palo Alto, CA, EPRI NP-5282, 1987.
- [9] U.S. Nuclear Regulatory Commission, "Crack-like Indication in the U-bend Region of a Thermally Treated Alloy 600 Steam Generator Tube," NRC Information Notice 2010-21, U.S. Nuclear Regulatory Commission, Washington, D.C., 2010, ADAMS Accession No. ML102210244.
- [10] Pressurized Water Reactor Steam Generator Examination Guidelines: Revision 7, Requirements, Electric Power Research Institute, Palo Alto, CA, 2006.
- [11] S. Bakhtiari and T.W. Elmer, "Technical Letter Report on Development of Flaw Sizing Algorithms for Eddy Current Rotating Probe Examinations," U.S. Nuclear Regulatory Commission, ADAMS Accession No. ML090690837, Sept. 2008.
- [12] S. Bakhtiari, T. Elmer, C.B. Bahn, Z. Zeng, and S. Majumdar, "Assessments on Eddy Current Detection of Cracking Near Volumetric Indications in Steam Generator Tubes," NUREG/CR-7291, ANL-18/41, U.S. Nuclear Regulatory Commission, Washington, D.C., 2022.
- [13] S. Majumdar, Z. Zeng, T. Elmer, C. Bahn and S. Bakhtiari, "Technical Letter Report: Predicting Rupture Pressure and Leak Rate of Alloy 600 U-bend Tubes with PWSCC and Comparing with Test Results," U.S. Nuclear Regulatory Commission, ADAMS Accession No. ML23101A170, May 2023.

APPENDIX A – TIMELINE FOR VARIOUS RESEARCH ACTIVITIES ASSOCIATED WITH U-BEND SPECIMENS

Multiple cracks were produced sequentially in each U-bend specimen over a period of time from 2011 to 2013. This was done, in part, to maximize the utility of each costly specimen. Table A-1 displays the timeline for the manufacturing of primary water stress corrosion cracking (PWSCC) in different regions of the U-bend tubes. As noted in that table, the cracks in the apex region (90°) of 57-mm radius U-bend tubes were the first ones to be developed. That was followed by production of cracks in the 0° tangent, off-apex (45° and 135°), and 180° tangent regions of the tubes. In reference to Table A-1, production of cracks at the 0° and at the 180° tangent region overlapped at times with crack production at the apex and the off-tangent regions, respectively.

Eddy current (EC) inspections using bobbin and rotating probes were performed at various stages of the crack manufacturing process. A MIZ-30 (Zetec, Inc.) instrument was used for the acquisition of data during that stage of the work. The EC data collected afterwards were for the most part acquired using a MIZ-85 (Zetec, Inc.) instrument, which provided the additional capability to perform array probe examinations. It is worth noting that the EC data collected with the more modern MIZ-85 instrument are of higher quality than those collected earlier with the MIZ-30 instrument. The higher signal quality (i.e., higher signal-to-noise [S/N]) provided by modern EC testing instruments is due in part to the use of more advanced data acquisition systems comprised of hardware and firmware components. Table A-2 displays the timeline for various internal and collaborative research activities carried on in connection with the U-bend specimens. Some highlights of those activities include independent acquisition of EC data on all of the tubes by the Electric Power Research Institute (EPRI) in 2014; collection of a complete set of EC inspection data at Argonne National Laboratory (Argonne) prior to pressure testing of the tubes in 2015; and collection of data at Argonne on a subset of specimens for probe evaluation studies by collaborators from the Institut de Radioprotection et de Sûreté Nucléaire (IRSN), France, and from Tecnatom, Spain.

A short study was conducted to assess potential differences between EC inspection data from U-bend specimens collected at different stages of this work. The +Pt probe response associated with three PWSCCs located in the apex region of different U-bends exhibited a noticeable increase in signal amplitude in the data collected shortly before pressure testing of these tubes, as compared to the data collected earlier shortly after termination of the crack manufacturing process. Based on analysis of the earlier dataset, all three cracks were estimated to be deep and greater than 1 inch in length. In reference to Table A-1, the PWSCCs at the apex region were the first set to be manufactured in those tubes. The EC probe response is strongly dependent on the contact area across the crack faces. The crack manufacturing process involved the displacing of the U-bend legs using a clamp-type device. Thus, from the standpoint of nondestructive examination (NDE), the increase in probe response in the later dataset can be attributed to the increase in crack opening (i.e., width of a crack) as additional PWSCCs were produced in the same tube. This finding particularly holds true for large cracks located at the apex region of U-bends, which are subject to the largest forces when the legs are displaced. As discussed further below, no evidence was found indicating that the three apex cracks grew physically in size over the time period between the two measurements.

Following are some general remarks based on the results of analyses of data from the three apex cracks noted above. Despite the differences in the data analysis software environment as well as potential variabilities in re-calibration and measurement of signals, the results of the more recent analyses are generally consistent with those performed earlier in this work. In all three cases

examined, a noticeable change is observed between the PWSCC signals at the apex with and without a clamp being placed on the tube. Accordingly, the change in the amplitude of the signals from the subset of apex cracks between the data collected earlier and that collected later in this work can plausibly be attributed to the increase in crack opening caused by the crack manufacturing process as additional PWSCCs were produced in other regions of the same tube.

Table A-1. Timeline for production of PWSCC in U-bend tube specimens.

	2011-02	2011-03	2011-04	2011-10	2011-12	2012-02	2012-03	2012-06	2012-11	2013-03
Flaw production	Prelim. 6" test (62-01)	Prelim. 2.25" test (890-08, 135°)								
			2.25" Apex flaws							
			2.25" 0°-tangent flaws							
					2.25" Off-apex flaws					
					2.25" 180° flaws					
					6" Apex flaws		6" Off-apex flaws			

Table A-2. Timeline for various research activities in connection with U-bend tube specimens.

	2013-11	2013-12	2014-01	2014-03	2014-05	2014-06	2014-10	2015-01	2015-05	2015-09	2015-12	2016-02	2016-03	2017, 2018
Physical exam		Tubes sent to EPRI/SWRI				SWRI					Select tubes to EPRI for Met			
									Videoscope examination		Pressure testing (PT)			
									Fractography					
NDE Data	Round-robin set						Miz-85 data							
					X-Probe Round-robin set									
								Pre-PT EC data				Post-PT EC data		
Analysis		EPRI data					IRSN probe data			Tecnom				
		EPRI analysis												
								EC profiles on Miz-85 data				Fractography profiles		

APPENDIX B – EDDY CURRENT INSPECTION RESULTS FOR 57-MM-RADIUS U-BEND SPECIMENS

The tables provided in this appendix list the eddy current (EC) inspection results for two categories of flaws produced in the 57-mm-radius U-bend tube specimens. They include data for the predominantly axial primary water stress corrosion cracking (PWSCC) throughout the bend region and at the tangential regions. Also provided in these tables are information about the test conditions for manufacturing of each SCC and the intended location of cracks along the U-bend.

Results of EC examinations for all of the U-bend specimens with PWSCC throughout the 57-mm-radius bend region and at the tangent regions are listed in Table B-1 and Table B-2, respectively. The estimated flaw sizes are based on manual analysis of data acquired with a +Pt rotating probe, performed shortly after termination of the crack manufacturing process. Most of the specimens have multiple cracking locations. As marked on the drawing at the bottom of the table, three area indications above the tangents are used in Table B-1: 45°, 90°, and 135°. The notation 45° indicates that the PWSCC is located between “0deg” tangent and the apex. The “0deg” tangent represents a tangential area where the transition point from straight to bending is clearly defined. It should be noted that the crack is not always positioned exactly at the specified location angle. The notation 90° indicates that the crack is located near the apex extrados. The notation 135° means that the crack is located between the apex and “180deg” tangent.

Table B-1. Eddy current examination results for specimens with predominantly axial PWSCC throughout the bend region of 57-mm-radius U-bends.

Specimen ID	Total Leg Displacement (mm)	Total Test Time (h)	Crack Location	With Clamps			Without Clamps			Comments
				+Pt Max. Ampl. (v)	+Pt Max. Depth (%TW)	Crack Length (mm/in)	+Pt Max. Ampl. (v)	+Pt Max. Depth (%TW)	Crack Length (mm/in)	
890-01	5.1	175.4	90°	6.39	90	50.5/1.99	4.4	80	53.1/2.09	Mixed mode cracking: axial & circumferential
890-03	7.6	16.8	45°							
	5.1	10.3	90°	0.49	51	3.0/0.12	0.45	55	3.8/0.15	
	7.6	60.2	135°	0.24	60	3.0/0.12	0.24	60	3.0/0.12	
890-04	5.1	25.8	90°	0.23	16	25.7/1.01	0.51	51	25/1.0	
890-07	7.6	16.2	45°							Located near the apex crack
	5.1	25.2	90°	3.3	77	36.1/1.42	1.3	83	36.1/1.42	
890-08	5.1	23.3	90°	0.16	45	4.6/0.18	0.15	64	3.8/0.15	
	7.6	16.7	135°				0.43	22	15/0.6	Possibly mixed mode cracking
890-12	13.2	23.5	90°				1.38	69	47.0/1.85	Multiple parallel cracks
890-15	5.1	8 days	90°	0.2	30	5/0.2				Axial & circumferential
890-16	7.6	16.8	45°	0.24	48	8/0.3	0.21	42	8.1/0.32	
	5.1	7.2	90°	0.2	-	13/0.5	-	-	-	Mixed mode cracking: axial & circumferential
890-19	7.6	64.0	45°				0.37	39	6.6/0.26	Located near the apex crack
	5.1	9 days	90°	0.38	40	4.3/0.17	0.15	39	3.3/0.13	
890-20	5.1	7.0	90°	0.18	22	4.6/0.18	0.29	67	26.2/1.03	
920-08	7.6	17.0	45°				1.17	64	10/0.4	
	5.1	7.3	90°	1.27	77	32.3/1.27	1.2	77	34.0/1.34	
	7.6	37.3	135°	0.19	20	5/0.2	0.14	20	4.3/0.17	
920-10	7.6	4.0	45°							Located near the apex crack
	5.1	7.3	90°	1.57	83	32.8/1.29	1.26	74	32.3/1.27	
920-12	7.6	7.0	45°	0.56	58	18/0.7	0.42	55	8.1/0.32	
	5.1	4.0	90°	1.4	61	33.5/1.32	0.69	64	34.3/1.35	Multiple parallel cracks

Specimen ID	Total Leg Displacement (mm)	Total Test Time (h)	Crack Location	With Clamps			Without Clamps			Comments
				+Pt Max. Ampl. (v)	+Pt Max. Depth (%TW)	Crack Length (mm/in)	+Pt Max. Ampl. (v)	+Pt Max. Depth (%TW)	Crack Length (mm/in)	
920-15	7.6	3.5	45°	0.29	20	12/0.47	0.25	-	17/0.68	
	5.1	4.0	90°	1.45	64	25/0.98	1.07	61	27.2/1.07	
	7.6	3.3	135°	0.32	58	4.6/0.18	0.29	55	5.3/0.21	
920-19	7.6	24.5	45°	1.95	74	19/0.75	1.79	64	18/0.69	
	5.1	43.0	90°	1.59	66	31.5/1.24	1.6	70	29.7/1.17	
1100-06	7.6	18.0	45°	1.79	80	25/1	1.1	74	25/1	
	5.1	30.0	90°	-	-	-	0.2	48	23/0.92	
1100-07	5.1	63.0	90°	2.05	81	29.5/1.16	1.5	90	32.5/1.28	Mixed mode cracking: axial & circumferential
1100-08	7.6	8.0	45°	2.44	67	31.5/1.24	1.78	77	36.8/1.45	
	5.1	20.3	90°	4.78	100	48/1.9	2.08	100	52.1/2.05	
1100-14	7.6	8.0	45°	1.3	70	25/0.97	1.06	64	25/1	
	5.1	20.3	90°	4.3	85	36/1.4	2.15	95	36.1/1.42	
1100-15	7.6	7.0	45°	2.57	77	22/0.88	1.18	80	23.1/0.91	
	5.1	48.0	90°	2.77	81	41/1.6	0.95	100	41/1.6	
	7.6	26.0	135°	0.77	64	4.3/0.17	0.67	67	3.0/0.12	
1100-18	5.1	45.0	90°	4.4	85	46/1.8	2.63	90	51.1/2.01	Multiple parallel cracks
1100-19	5.1	63.0	90°	0.18	-	-	0.24	-	-	
1180-02	7.6	20.7	45°	1.99	64	27.4/1.08	1.06	70	26.7/1.05	Two parallel cracks
	5.1	64.2	90°	4.6	85	34.0/1.34	1.81	100	33/1.3	Multiple parallel cracks
	7.6	46.5	135°	0.63	51	6.1/0.24	0.54	55	8/0.3	
1180-11	7.6	20.7	45°	1.81	77	31.2/1.23	1	80	33.3/1.31	
	5.1	23.0	90°	0.47	30	33.5/1.32	0.69	67	32.8/1.29	
	5.1	24.0	135°	0.7	36	6.9/0.27	0.42	39	6.9/0.27	
1180-13	5.1	7.2	90°	1.47	77	27.7/1.09	1.2	94	29.7/1.17	
1180-14	5.1	23.0	90°	2.7	77	36/1.4	2.22	80	38.4/1.51	
1180-15	5.1	4.8	90°	0.43	30	19/0.74	0.45	36	21.1/0.83	

Specimen ID	Total Leg Displacement (mm)	Total Test Time (h)	Crack Location	With Clamps			Without Clamps			Comments
				+Pt Max. Ampl. (v)	+Pt Max. Depth (%TW)	Crack Length (mm/in)	+Pt Max. Ampl. (v)	+Pt Max. Depth (%TW)	Crack Length (mm/in)	
	7.6	49.8	135°	0.18	45	3.8/0.15	0.2	25	3.8/0.15	
1180-16	5.1	3.3	45°	0.47	48	15/0.6	0.38	55	19/0.75	
	7.6	22.7	135°	0.22	-	3/0.1	NDD	NDD	NDD	
1180-18	7.6	4.0	45°	1.45	64	12/0.48				Near the apex crack; two cracks
	5.1	23.0	90°	2.5	100	29.0/1.14	1.43	90	32.5/1.28	
1180-20	5.1	7.0	45°	0.53	55	25/0.98	0.46	48	25/1.0	
	7.6	49.8	135°	0.62	48	5.6/0.22	0.46	42	5.6/0.22	
1180-21	7.6	4.0	45°	0.55	58	19/0.75	0.5	55	19/0.75	Two axial cracks
	5.1	43.0	90°	3.27	62	43.4/1.71	1.65	80	45.5/1.79	
1180-22	7.6	5.3	45°				0.84	67	19/0.73	
	5.1	4.8	90°	1.94	67	32.8/1.29	1.01	77	34.0/1.34	
	7.6	23.0	135°	0.1	-	3.8/0.15	0.1	-	3.0/0.12	
1180-23	7.6	2.5	45°	0.15	39	19/0.75	0.17	42	19/0.73	Located near the apex crack
	5.1	7.0	90°	1.87	77	31.0/1.22	2.03	87	31.5/1.24	Multiple parallel cracks
	7.6	23.0	135°	0.36	61	4.3/0.17	0.34	55	4.3/0.17	

The position for each Location ID letter is shown on the schematic diagram.

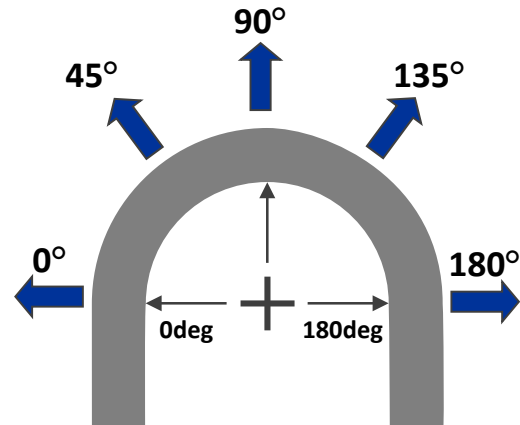


Table B-2. Eddy current examination results for specimens with predominantly axial PWSCC at tangential regions of 57-mm-radius U-bends.

Specimen ID	Total Diametric Compression (mm)	Total Test Time (h)	Crack Location		+Pt Max. Ampl. (v)	+Pt Max. Depth (%TW)	Crack Length (mm/in)	Comments
			0 or 180deg	Extrados, Intrados, or Flank				
890-01	0.15	64.0	180	Extrados	0.47	55	8.9/0.35	
890-03	0.20	65.8	0	Extrados	0.66	67	11/0.44	
	0.15	67.3	180	Extrados	0.23	45	7.4/0.29	~45° off the extrados
	0.15	67.3	180	Extrados	0.28	55	8.6/0.34	~45° off the extrados
	0.15	67.3	180	Intrados	0.32	67	4.3/0.17	
890-04	0.15	583.5	180	Extrados	0.94	90	7.6/0.3	
890-07	0.17	18.5	0	Extrados				
	0.17	24.7	180	Extrados	0.2	33	5.8/0.23	~45° off the extrados
	0.17	24.7	180	Extrados	0.21	22	4.1/0.16	~45° off the extrados
890-08	0.15	56.5	180	Extrados	0.26	36	4.3/0.17	
	0.15	56.5	180	Flank	0.12	27	5.6/0.22	
890-15	0.17	681	180	Extrados	0.29	42	3.0/0.12	~45° off the extrados
890-16	0.17	46.4	0	Extrados	0.35	60	8/0.3	
	0.17	24.7	180	Extrados	0.14	30	4.1/0.16	~45° off the extrados
890-19	0.18	46.1	0	Extrados	0.23	58	4.3/0.17	
	0.17	66.0	180	Extrados	0.56	70	7.4/0.29	~45° off the extrados
890-20	0.15	30.7	0	Extrados	0.28	58	4.3/0.17	
	0.15	30.7	0	Intrados	0.17	30	4.8/0.19	
	0.15	19.5	180	Extrados	0.28	33	8.4/0.33	
920-08	0.15	89.5	0	Intrados	1.6	48	17/0.66	Mixed mode cracking: axial & circumferential
	0.15	46.8	180	Extrados	0.3	48	6.1/0.24	~45° off the extrados
	0.15	46.8	180	Intrados	0.63	64	16/0.64	Mixed mode cracking: axial & circumferential
920-10	0.15	22.3	0	Extrados	0.23	48	3.6/0.14	
	0.15	24.7	180	Extrados				~45° off the extrados
	0.15	24.7	180	Extrados				~45° off the extrados
920-12	0.17	20.0	0	Extrados	0.82	77	8.9/0.35	
920-15	0.17	22.5	0	Extrados	0.37	70	8/0.3	
	0.15	16.5	180	Extrados	0.5	45	11/0.45	~45° off the extrados
920-19	0.15	23.2	0	Extrados	1.0	77	13/0.5	
1100-06	0.15	49.0	0	Extrados	1.53	80	16/0.64	

Specimen ID	Total Diametric Compression (mm)	Total Test Time (h)	Crack Location		+Pt Max. Ampl. (v)	+Pt Max. Depth (%TW)	Crack Length (mm/in)	Comments
			0 or 180deg	Extrados, Intrados, or Flank				
1100-07	0.17	23.0	180	Extrados	0.4	33	6.1/0.24	~45° off the extrados
	0.17	23.0	180	Extrados	0.82	61	8.6/0.34	~45° off the extrados
1100-08	0.15	19.0	0	Extrados	1.84	74	14/0.56	
	0.15	19.0	0	Intrados	0.74	50	8.9/0.35	
1100-14	0.15	22.5	0	Extrados	1.78	83	14/0.54	
1100-15	0.15	23.2	0	Extrados	1.05	70	8.4/0.33	
	0.15	23.2	0	Intrados	0.81	80	8/0.3	
	0.17	16.5	180	Extrados	0.69	30	5/0.2	~45° off the extrados
	0.17	16.5	180	Extrados	0.53	45	5/0.2	~45° off the extrados
1100-18	0.15	22.5	0	Extrados	1.73	87	15/0.6	
	0.15	22.5	0	Intrados	0.9	45	8.1/0.32	Mixed mode cracking: axial & circumferential
	0.15	17.0	180	Extrados	1.1	58	9.4/0.37	~45° off the extrados
	0.15	17.0	180	Extrados	0.72	61	9.4/0.37	~45° off the extrados
1100-19	0.15	146.3	0	Extrados	0.23	33	3.6/0.14	
	0.15	146.3	0	Intrados	1.07	77	8.4/0.33	Volumetric
	0.17	486.3	180	Flank	0.58	70	13/0.52	
1180-02	0.15	22.5	0	Extrados	1.03	70	11/0.43	
	0.17	41.5	180	Extrados				
	0.17	41.5	180	Extrados				~45° off the extrados
1180-11	0.15	21.0	0	Extrados	1.57	87	14/0.54	
	0.15	56.5	180	Extrados	0.6	61	6.4/0.25	~45° off the extrados
	0.15	56.5	180	Extrados	0.19	27	6.4/0.25	~45° off the extrados
1180-13	0.15	20.0	0	Intrados	0.36	60	80 deg	Circumferential crack
1180-14	0.15	67.7	0	Extrados	0.5	77	8.1/0.32	
	0.15	67.7	0	Intrados	1.26	100	15/0.6	Mixed mode cracking: axial & circumferential
	0.15	22.0	180	Intrados	0.26	48	3/0.1	
1180-15	0.17	67.5	0	Extrados	0.35	77	3.6/0.14	
	0.17	22.0	180	Extrados	0.23	13	3.0/0.12	~45° off the extrados
1180-16	0.18	20.2	0	Extrados	0.92	77	12/0.49	
	0.18	15.8	180	Extrados	0.24	22	3.0/0.12	
1180-18	0.17	28.5	0	Extrados	1.07	77	11/0.43	
	0.17	15.0	180	Extrados	0.34	33	5.8/0.23	~45° off the extrados
	0.17	15.0	180	Extrados	0.33	36	5.3/0.21	~45° off the extrados

Specimen ID	Total Diametric Compression (mm)	Total Test Time (h)	Crack Location		+Pt Max. Ampl. (v)	+Pt Max. Depth (%TW)	Crack Length (mm/in)	Comments
			0 or 180deg	Extrados, Intrados, or Flank				
1180-20	0.19	22.6	0	Extrados	1.68	74	17/0.66	
	0.15	15.0	180	Extrados	0.18	40	3/0.1	~45° off the extrados
1180-21	0.15	22.8	0	Extrados	1.78	87	18/0.71	
	0.17	14.2	180	Extrados	0.17	13	3.0/0.12	
	0.17	14.2	180	Extrados	0.19	51	2/0.07	
1180-22	0.20	24.0	0	Extrados	0.5	77	5.6/0.22	
	0.15	87.2	180	Extrados	0.5	51	6.6/0.26	~45° off the extrados
	0.15	87.2	180	Extrados	0.18	27	3.6/0.14	~45° off the extrados
1180-23	0.15	48.5	0	Extrados	1.27	83	12/0.46	
	0.18	87.2	180	Extrados	0.51	67	9.9/0.39	~45° off the extrados
	0.18	87.2	180	Extrados	0.76	45	9.9/0.39	~45° off the extrados

APPENDIX C – EDDY CURRENT INSPECTION RESULTS FOR 152-MM-RADIUS U-BEND SPECIMENS

The table provided in this appendix lists the eddy current (EC) inspection results for the predominantly circumferential primary water stress corrosion cracking (PWSCC) produced throughout the bend region of 152-mm-radius U-bend tube specimens. The table also provides information about the test conditions for the manufacturing of each stress corrosion crack (SCC) and the intended location of the crack along the U-bend. The estimated flaw sizes are based on manual analysis of data acquired with +Pt rotating probe, performed shortly after termination of the crack manufacturing process. Most of the specimens listed in Table C-1 have multiple cracking locations. As marked on the drawing at the bottom of the table, seven location identifications (A through G) are used in Table C-1. It should be noted that the crack is not always positioned exactly at the specified Location identification (ID). Finally, percent degraded area (PDA) is provided in Appendix B, Table B-1 for a subset of circumferential cracks on which destructive examination (DE) was performed.

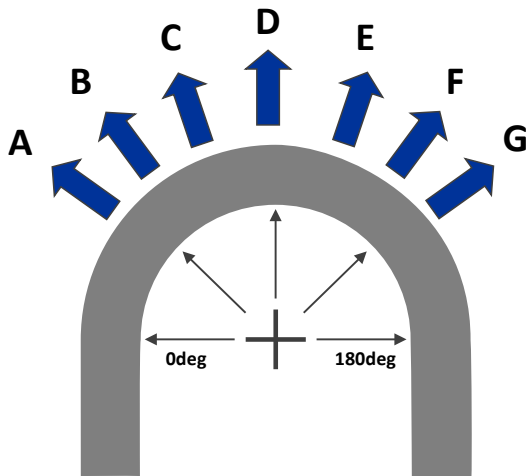
Table C-1. Eddy current examination results for specimens with predominantly circumferential PWSCC throughout the bend region of 152-mm-radius U-bends.

Specimen ID	Total Leg Displacement ^a (mm)	Total Test Time (h)	Crack Location		+Pt Max. Amplitude (v)	+Pt Max. Depth (%TW)	Crack Extent (deg)	DE PDA (%)	Comments
			Location ID ^b	Extrados, Intrados or Flank					
07-01	10	20.0	D	Extrados	4.31	94	106		Multiple parallel circ. cracks
07-02	10	22.2	B	Flank-extrados	2.72	100	53		Axially extended circ. cracks
	10	5.8	F	Flank-extrados	0.43	40	34		Possibly mixed mode: circ. & axial cracks
07-03	10	22.2	B	Flank-extrados	2.89	100	61		Axially extended circ. cracks
	10	19.0	F	Extrados	0.63	47	30		
	10	19.0	F	Flank-extrados	1.25	90	41	13.5	
07-04	25	72.0	D	Extrados	19.48	100	246		
14-01	10	3.0	B	Flank-extrados	1.13	44	30		Axially extended circ. cracks
	-13	7.0	E	Intrados	3.96	56	163	22.1	
	10	16.4	F	Extrados	0.64	58	74		Possibly mixed mode
	10	16.4	F	Intrados	0.44	30			7-mm-long axial crack
	-13	4.5	G						
15-02	10	3.0	B	Flank-extrados	0.64	50	34		Axially extended circ. cracks
	10	6.8	E	Flank-extrados	0.39	52	26		Possibly mixed mode
	-13	7.3	E	Flank-intrados	0.13	49	19		
	-13	6.9	F	Intrados	0.26	46	23	0.99	
	-13	8.3	G	Flank-extrados	0.33	11			4-mm-long axial crack
20-01	10	14.0	B	Flank-extrados	0.86	40	30		Axially extended circ. cracks
	-13	7.0	C	Intrados	4.14	62	182		
	-13	4.5	D	Intrados	0.3	37	27	28.6	
	-13	4.0	E	Flank-intrados	0.27	42			5-mm-long axial crack
	10	7.7	F	Flank-extrados	0.6	41	33		
	-13	3.7	G						
21-01	-25	22.2	D	Flank	3.4	100			49-mm-long axial crack
	-25	22.2	D	Intrados	0.46	62	23		
	-25	61.7	F	All around	19.75	100	200		
22-01	-13	23.3	-						25 mm above 0deg tangent
	-13	8.0	-						51 mm above 0deg tangent
	-13	24.2	-	Flank				3.95	25 mm above 180deg tangent; possibly mixed mode

Specimen ID	Total Leg Displacement ^a (mm)	Total Test Time (h)	Crack Location		+Pt Max. Amplitude (v)	+Pt Max. Depth (%TW)	Crack Extent (deg)	DE PDA (%)	Comments
			Location ID ^b	Extrados, Intrados or Flank					
	-13	17.7	-	Flank					51 mm above 180deg tangent
23-01	-13	8.3	A	Flank-intrados	0.136	37	23	0.86	
	-13	6.9	B	Flank-intrados	1.43	62	56		Possibly mixed mode
	-13	7.3	C	Flank-intrados	0.68	32	31		Possibly mixed mode
	-13	6.5	D	Flank-intrados	2.04	65	160		
	10	8.0	F	Flank-extrados	0.79	61	93		Multiple parallel circ. cracks
	10	8.0	F	Intrados	0.52	36			7-mm-long axial crack
25-01	-8	24.7	A	Intrados				27.2	
	-8	6.0	B	Flank					Possibly mixed mode
	-8	5.3	C	Flank					Possibly mixed mode
	-8	7.7	D	Flank-intrados					Possibly mixed mode
	-	-	D	Extrados	0.34	36			Preexisting 18-mm-long axial flaw-like indication
	-8	5.2	E	Flank-intrados					
	-8	5.2	F	Flank-intrados					
	-8	6.0	G	Flank					Possibly mixed mode
29-01	-13	7.8	A	Intrados	0.38	46	27		Possibly mixed mode
	-13	7.3	B	Flank-extrados	0.63	50	45		Volumetric flaw
	-13	6.5	C	Flank-intrados	0.98	28	50		Possibly mixed mode
	-13	6.3	D	Flank	0.54	43	42		
	-13	6.3	D	Near flank	0.65 0.41	55 67			6- or 5-mm-long axial cracks
31-01	-13	7.8	A	Flank-intrados	0.57	50	53		Possibly mixed mode
	-13	7.3	B	Flank-intrados	0.35	50	27		Possibly mixed mode
	-13	6.5	C	Flank-intrados	0.8	31	45		Possibly mixed mode
	-13	6.3	D	Flank-intrados	0.63	43	34		Volumetric flaw
37-01	-13	6.7	A	Flank	0.17	27			4-mm-long axial crack
	-13	7.7	B	Intrados	0.45	59	27		Possibly mixed mode
	-13	5.2	C	Flank-intrados	0.52	62	27		
	-13	12.0	D	Intrados	1.06	76	34		Possibly mixed mode
	-13	7.3	E	Flank-intrados	0.42	46	30		

Specimen ID	Total Leg Displacement ^a (mm)	Total Test Time (h)	Crack Location		+Pt Max. Amplitude (v)	+Pt Max. Depth (%TW)	Crack Extent (deg)	DE PDA (%)	Comments
			Location ID ^b	Extrados, Intrados or Flank					
	-13	8.2	F	Flank-intrados	0.35	40	31		Possibly mixed mode
	-13	7.3	G	Flank-intrados	0.85	69	53		
52-01	-8	24.7	A	Intrados	20	82	235		
	-8	6.0	B	Flank-intrados	0.62	56	53	1.6	
	-8	5.3	C	Flank	0.26	11			8-mm-long axial crack
	-8	7.7	D	Flank-intrados	0.33	37	27		Possibly mixed mode
	-8	5.2	E	Flank	0.37	36			Volumetric flaw
	-8	5.2	F	Flank	0.25	45			Volumetric flaw
	-8	6.0	G	Flank	0.25	42			8-mm-long axial crack
59-01	10	8.0	F	Extrados	18.95	90	122		
62-01	25	24.0	D	Extrados	14.63	91	129		
63-03	-13	75.5	D	All around	16.34	90	180		
	-13	16.2	F	Flank-intrados	1.01	72	49		Possibly mixed mode
	-13	16.2	F	Flank	0.34	33			4-mm-long axial crack
63-04	-13	6.7	A	Flank-intrados	0.58	52	38		
	-13	12.8	B	Flank-intrados	0.44	65	23		Volumetric flaw
	-13	12.8	C	Flank	0.13	27			4-mm-long axial crack; volumetric flaw
	-13	7.8	D	Flank-intrados	0.99	46	54		
	-13	7.0	E	Flank-intrados	1.15	40	91		
	-13	12.0	F	Flank-intrados	0.42	49	27		Possibly mixed mode
	-13	7.3	G	Flank-intrados	0.19	43	23		

^a Positive and negative values mean inward and outward leg displacement, respectively.
^b The position for each Location ID letter is shown on the schematic diagram.

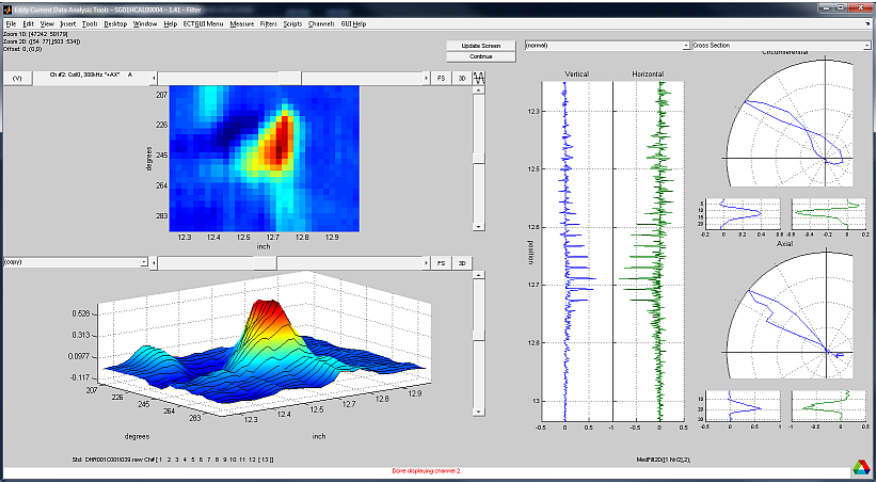
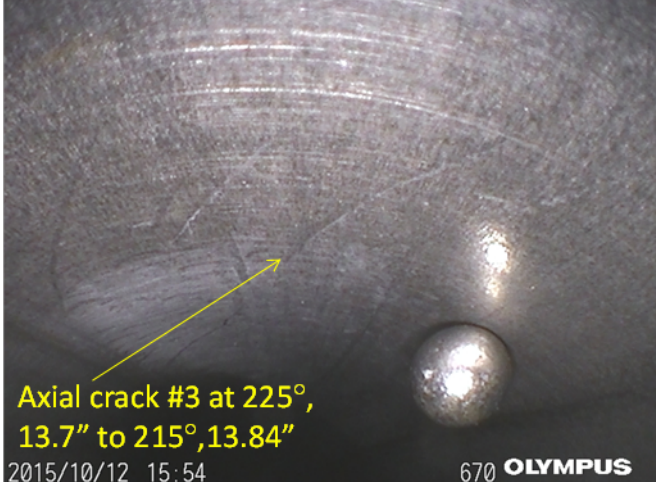
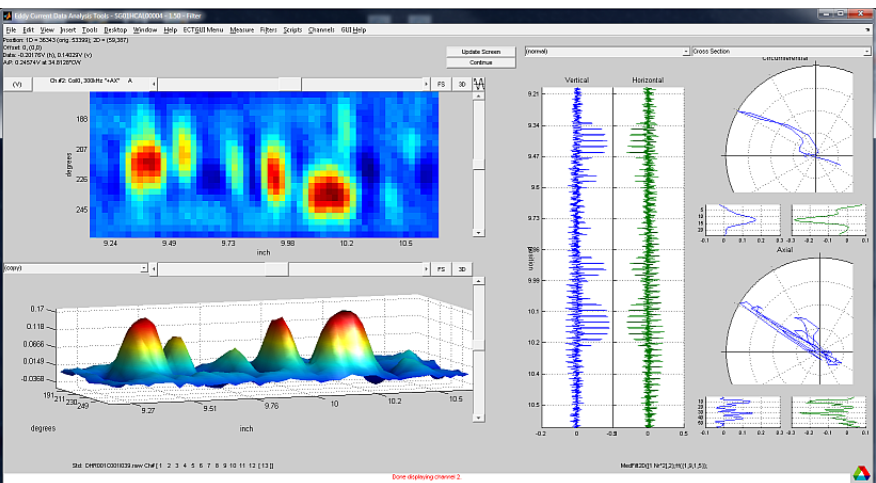
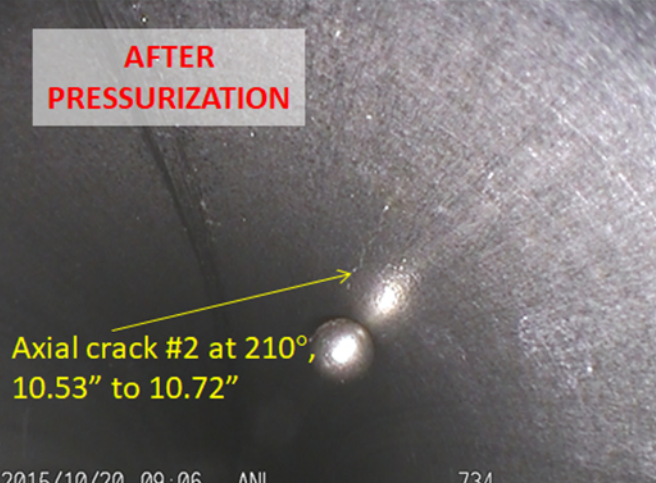


APPENDIX D – EDDY CURRENT AND VISUAL INSPECTION DATA FOR 57-MM-RADIUS U-BEND SPECIMENS

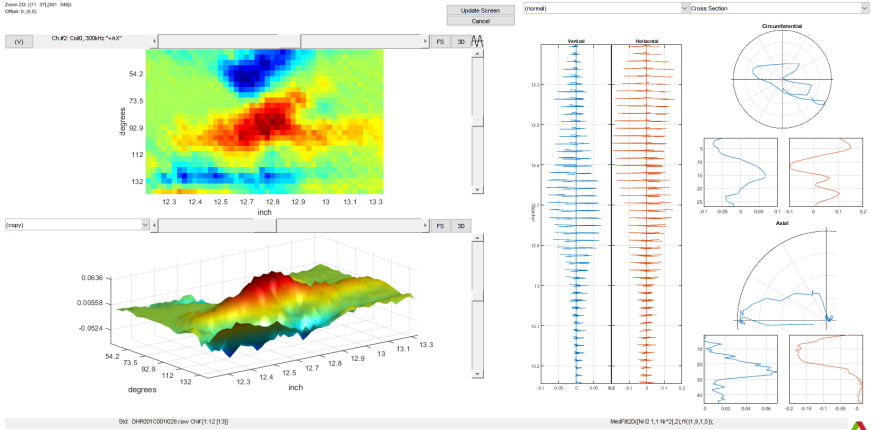
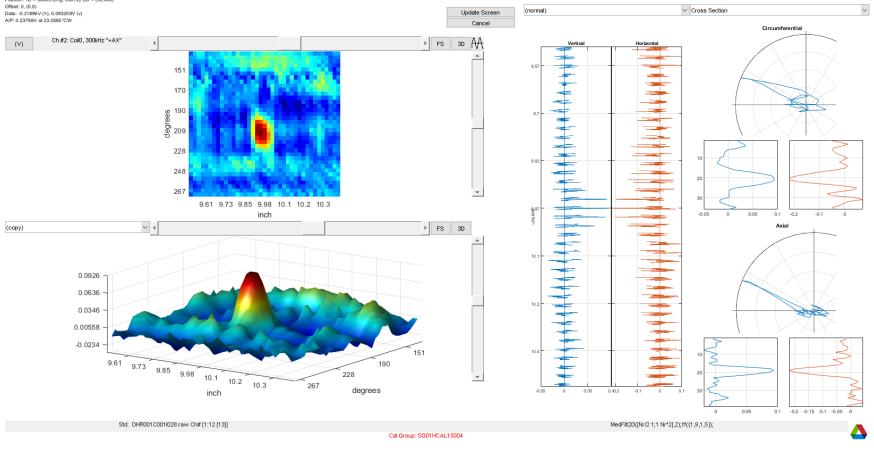
Videoscope images are provided in Table D-1 below for all the primary water stress corrosion cracks (PWSCCs) in 57-mm-radius U-bend tube specimens that were later examined destructively. The nondestructive examination (NDE) data were collected on all the tubes shortly prior to pressure testing of the U-bend specimens. Associated with each video image in the table is a screen capture of the processed eddy current (EC) data. Analysis of EC data was performed using the computer-aided data analysis tool implemented at Argonne National Laboratory (Argonne). The screen captures of the rotating +Pt probe data provided in these tables are associated with different stages of the data analysis process, displaying the data in the main analysis user interface. Along with the specimen identification (ID) number in the first column, information is provided about the approximate location of the crack signal in the U-bend. The PWSCCs with a detectable EC signal but with no discernible visual data are denoted as not detectable (ND) in the first column. Data on pre- and post-pressure-test NDE and destructive examination (DE) for PWSCCs in 57-mm-radius U-bend tube specimens are provided in Table D-2.

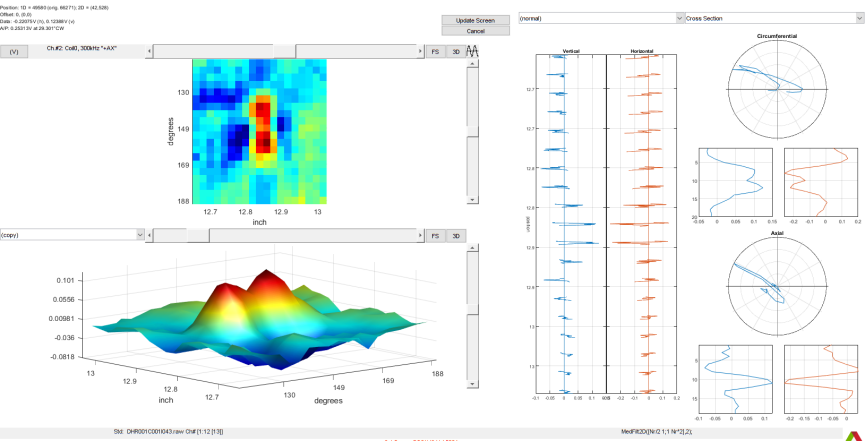
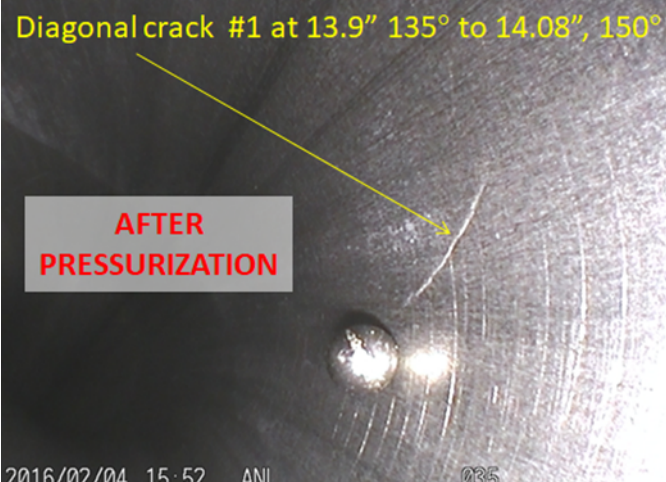
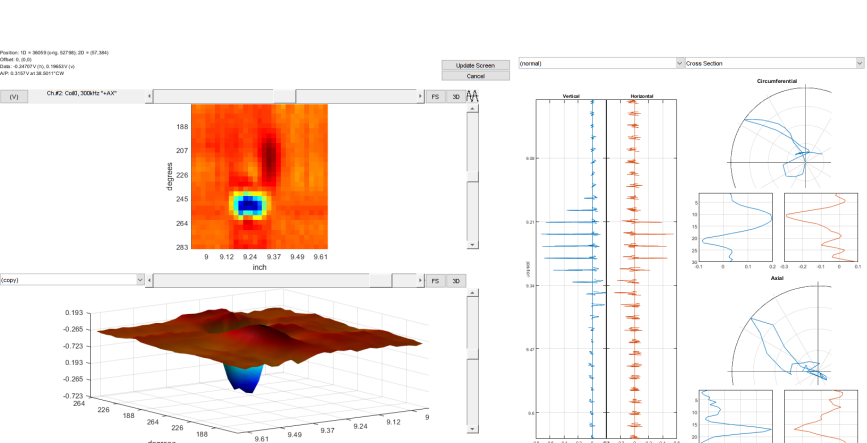
Table D-1. Eddy current and visual (videoscope) data for PWSCCs in 57-mm-radius U-bend tube specimens.

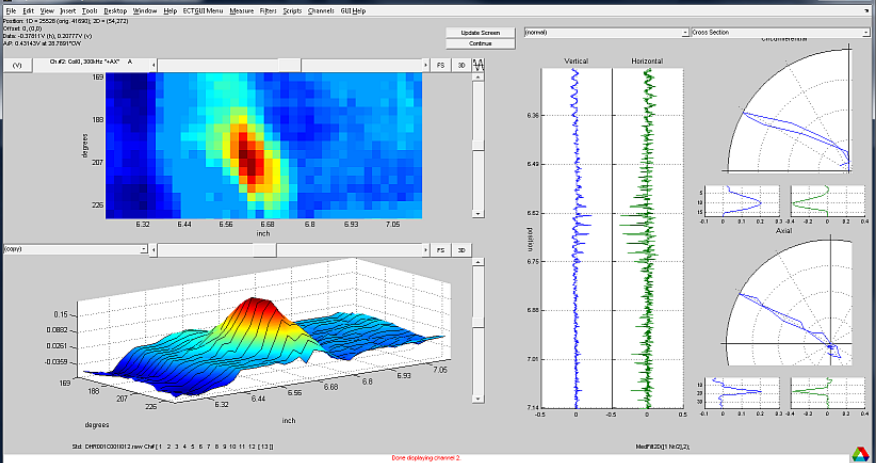
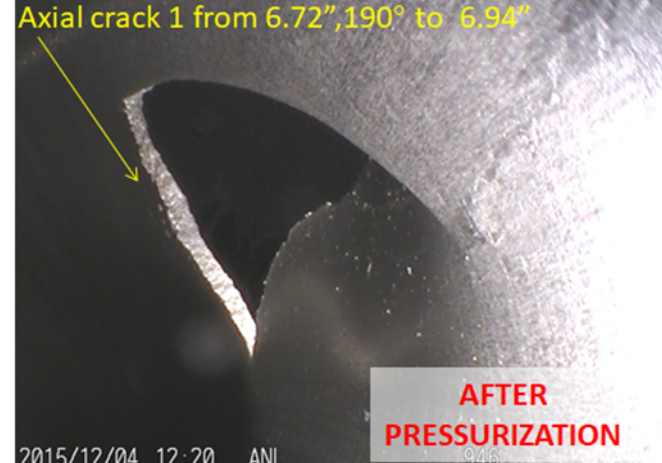
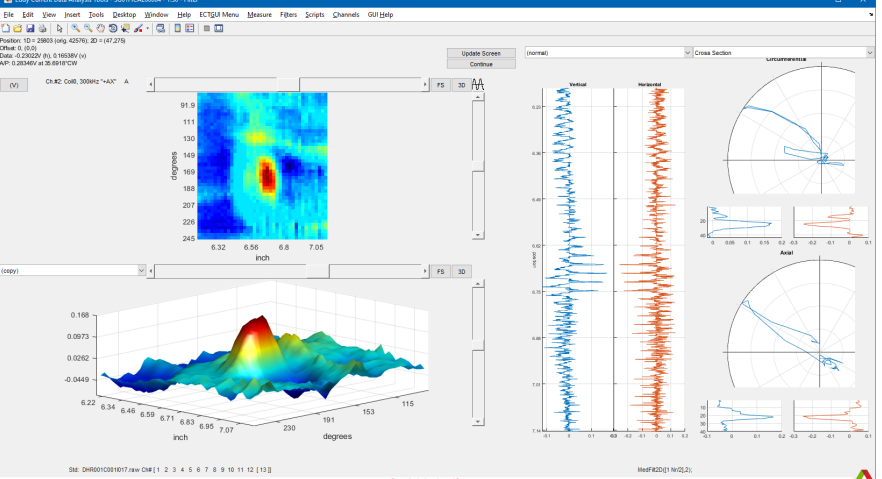
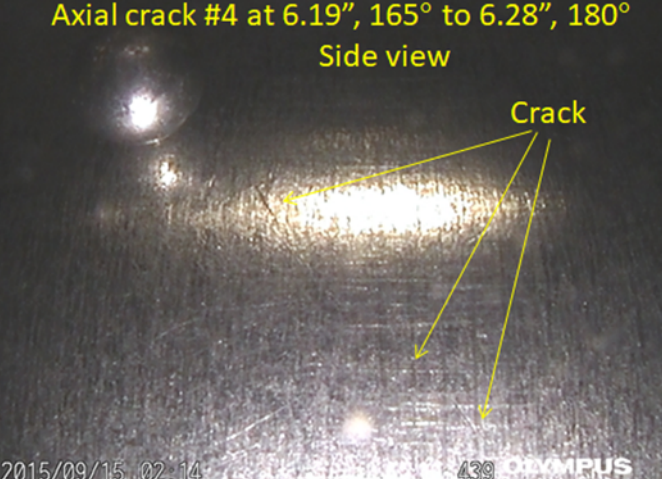
U-bend ID*	Pre-test ECT*	Pre-pressurization Visual
<p>890-01 (90°, Ex) (#1a)</p>		
<p>890-03 (0°, Ex) (#1)</p>		

U-bend ID*	Pre-test ECT*	Pre-pressurization Visual
<p>890-04 (180°, Ex) (#3)</p>		
<p>890-04 (90°, Ex) (#3)</p>		

U-bend ID*	Pre-test ECT*	Pre-pressurization Visual
<p>890-07 (90°, Ex) (#6)</p>		
<p>890-08 (180°, Ex) (ND)</p>		

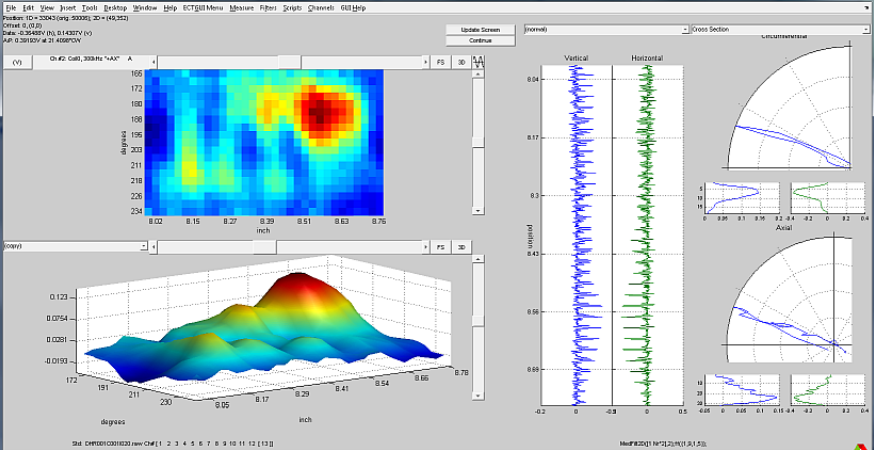
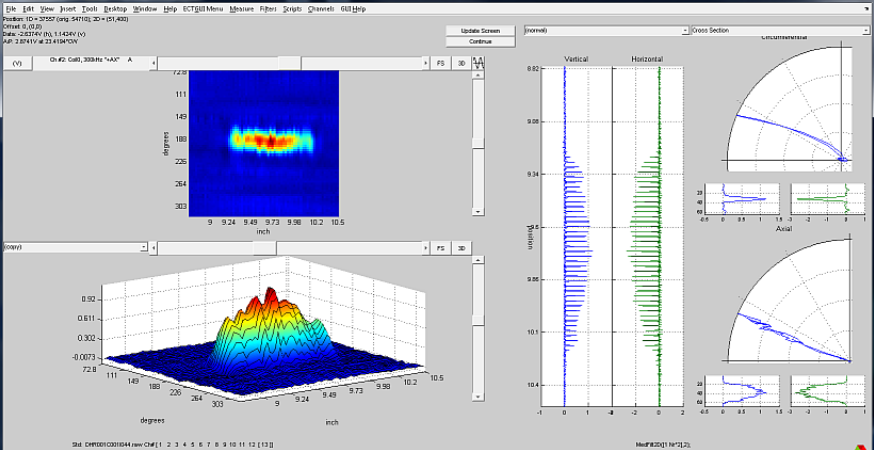
U-bend ID*	Pre-test ECT*	Pre-pressurization Visual
<p>890-08 (180°, FI) (ND)</p>		<p>[No image]</p>
<p>890-08 (90°, Ex) (ND)</p>		<p>[No image]</p>

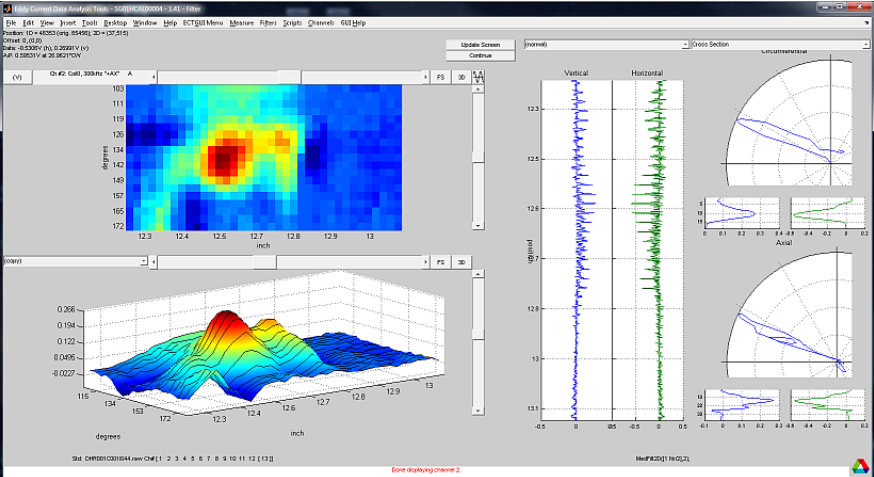
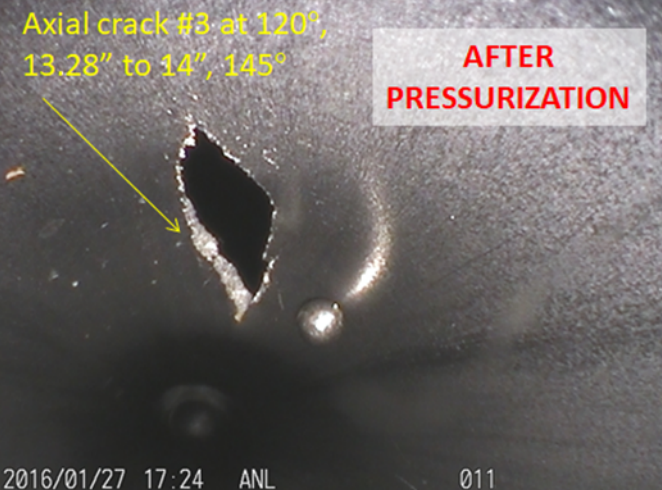
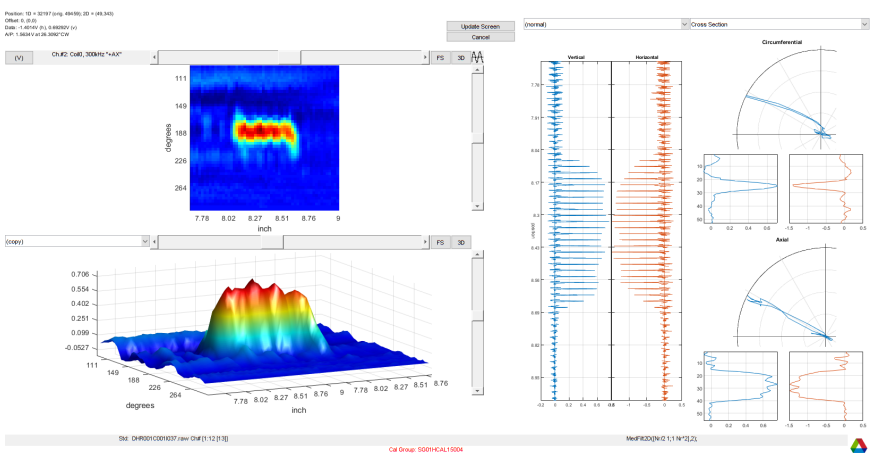
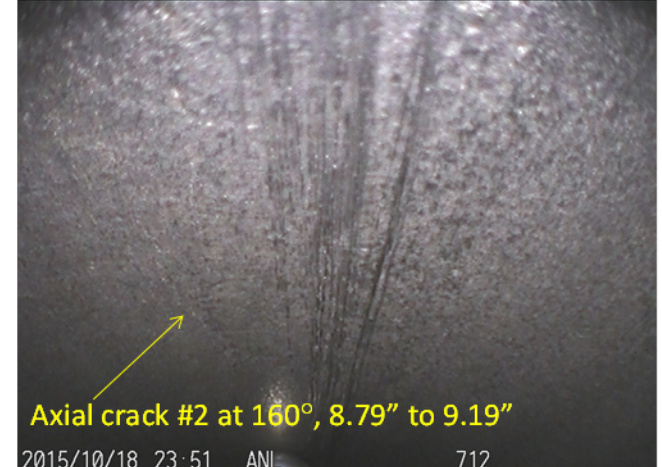
U-bend ID*	Pre-test ECT*	Pre-pressurization Visual
<p>890-15 (180°, 45°-off Ex) (ND)</p>		<p>Diagonal crack #1 at 13.9" 135° to 14.08", 150°</p> 
<p>890-15 (90°, Ex) (#5)</p>		 <p>C-shape crack #5 from 9.47", 185° to 9.52 165° To 9.56" , 185°</p>

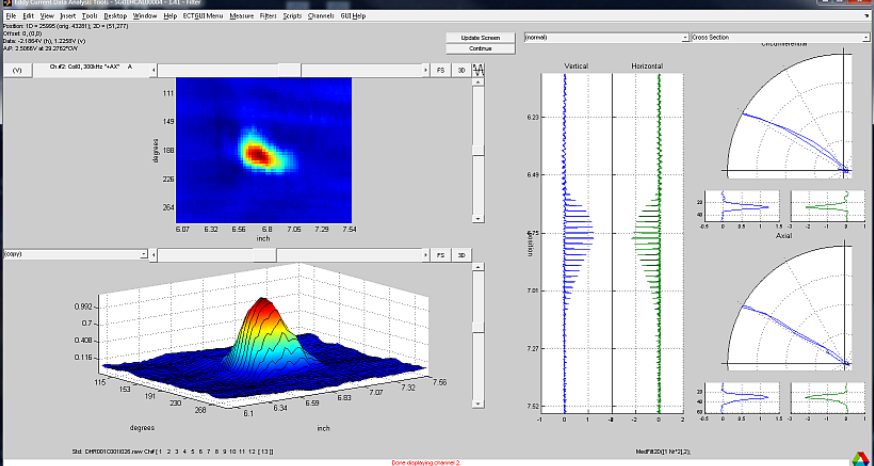
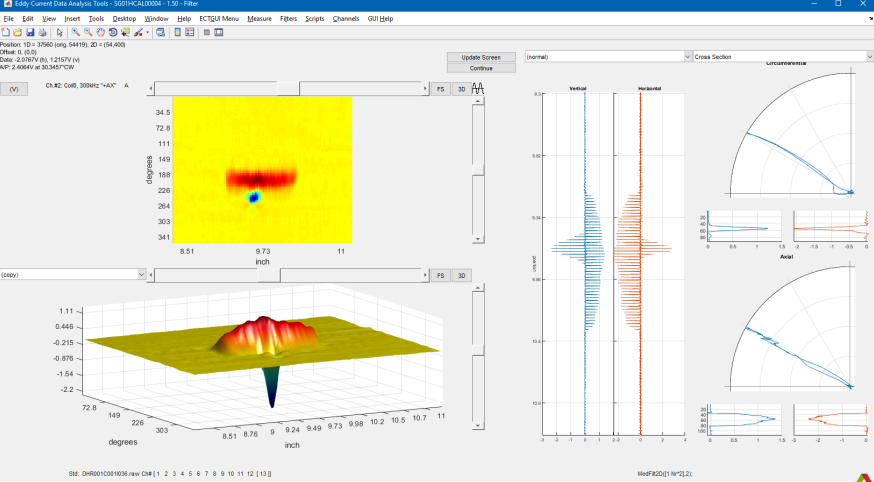
U-bend ID*	Pre-test ECT*	Pre-pressurization Visual
<p>890-16 (0°, Ex) (ND)</p>		
<p>890-20 (0°, Ex) (#4)</p>		

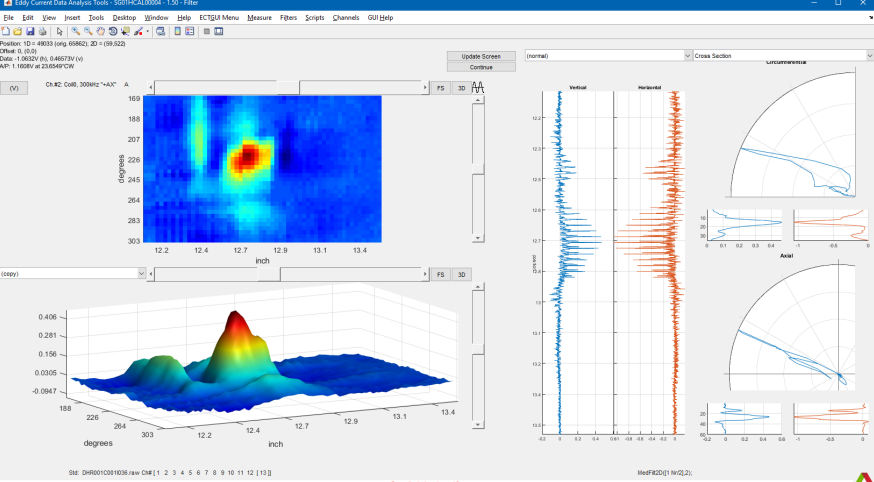
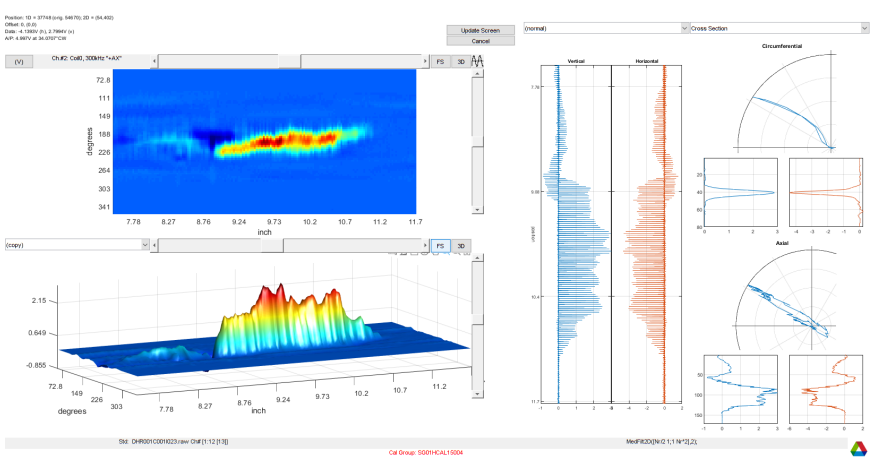
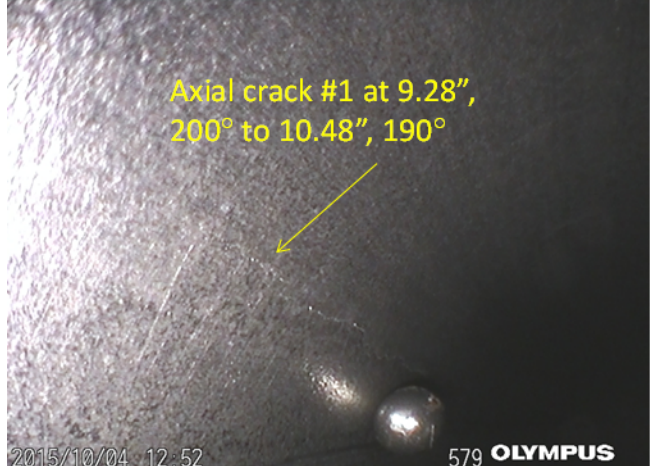
U-bend ID*	Pre-test ECT*	Pre-pressurization Visual
<p>920-08 (0°, In) (#2)</p>		
<p>920-09 (180°) (ND)</p>		

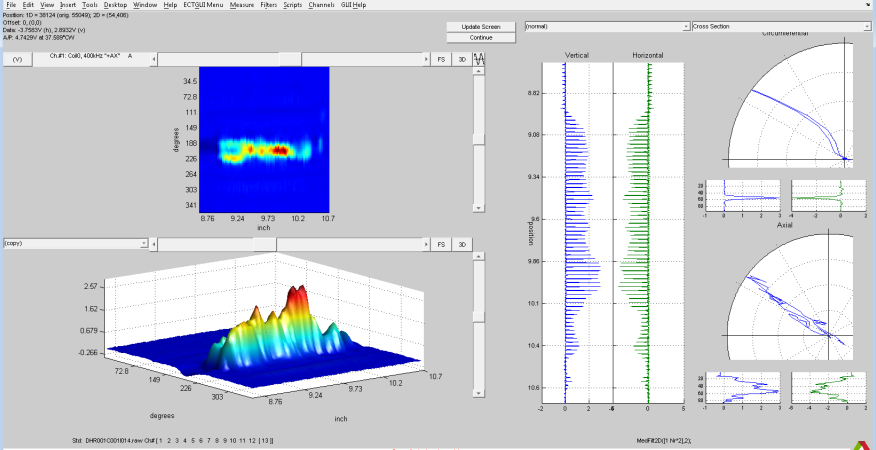
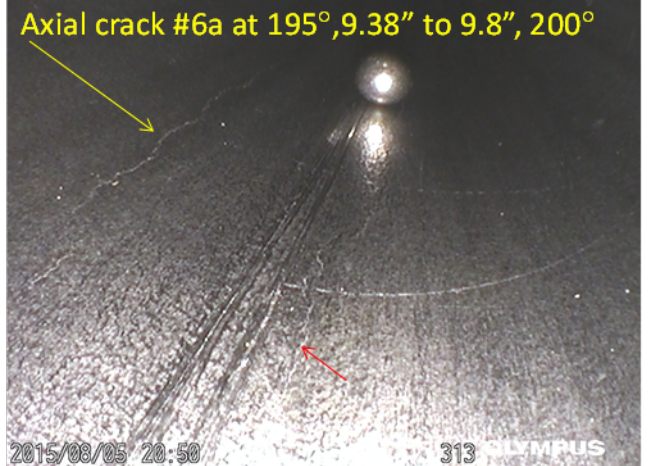
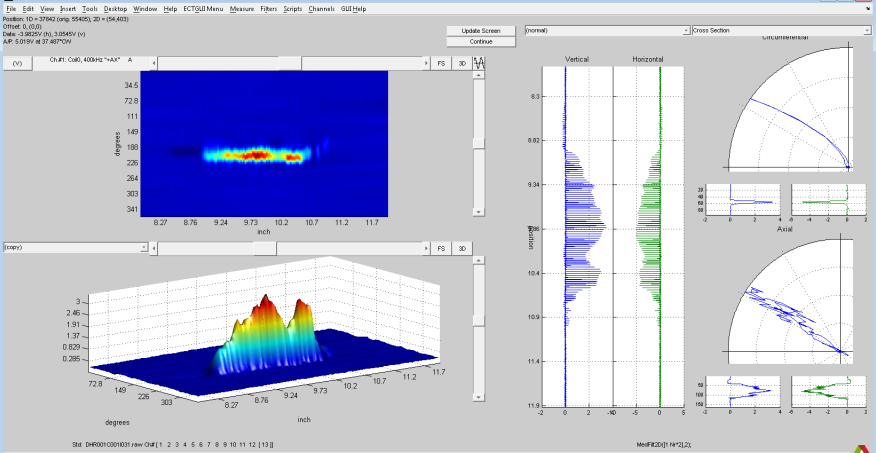
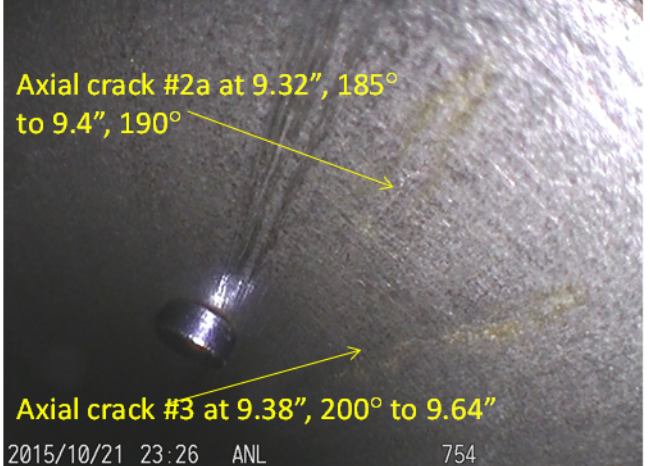
U-bend ID*	Pre-test ECT*	Pre-pressurization Visual
<p>920-10 (90°, Ex) (#2a, #2b, #2c1)</p>		
<p>920-12 (0°, Ex) (#2)</p>		

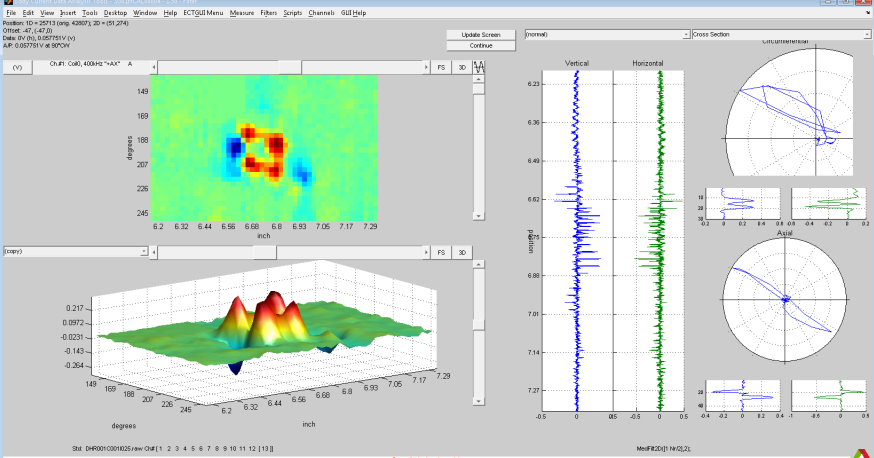
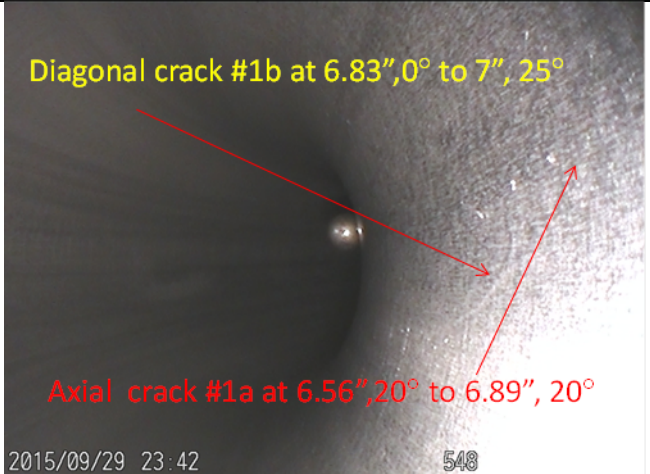
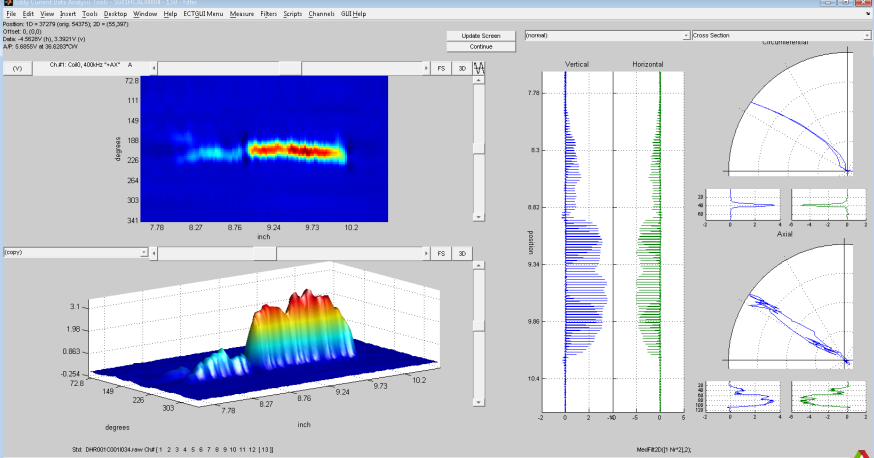
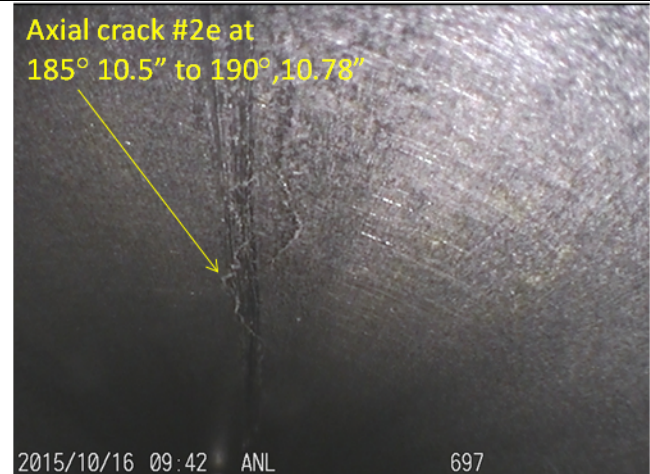
U-bend ID*	Pre-test ECT*	Pre-pressurization Visual
<p>920-12 (65°, Ex) (ND)</p>		<p>[No image]</p>
<p>920-15 (90°, Ex) (#2)</p>		 <p>2015/10/07 15:09 633 OLYMPUS</p>

U-bend ID*	Pre-test ECT*	Pre-pressurization Visual
<p>920-15 (180°, 45°- off Ex) (ND)</p>		<p>Axial crack #3 at 120°, 13.28" to 14", 145°</p> <p>AFTER PRESSURIZATION</p>  <p>2016/01/27 17:24 ANL 011</p>
<p>920-19 (45°, Ex) (#2)</p>		<p>Axial crack #2 at 160°, 8.79" to 9.19"</p>  <p>2015/10/18 23:51 ANL 712</p>

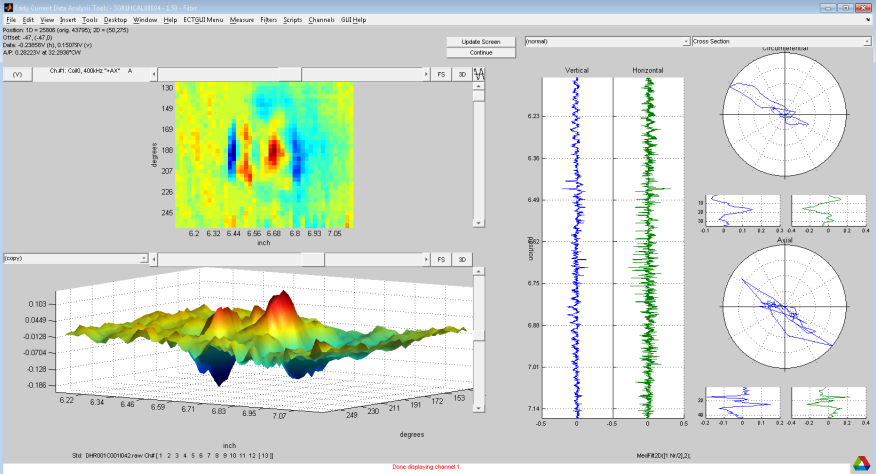
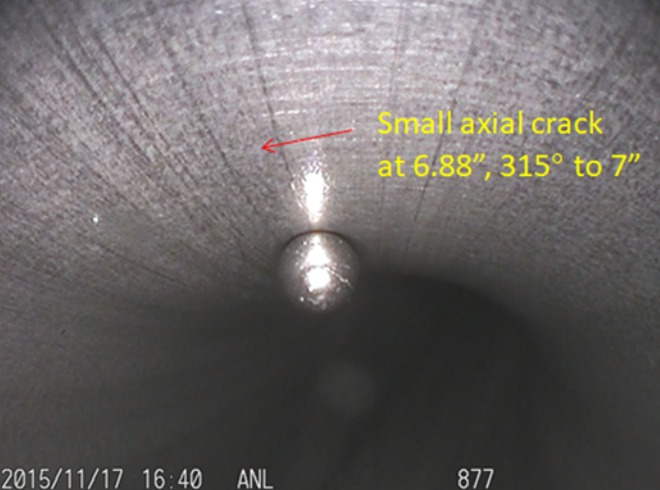
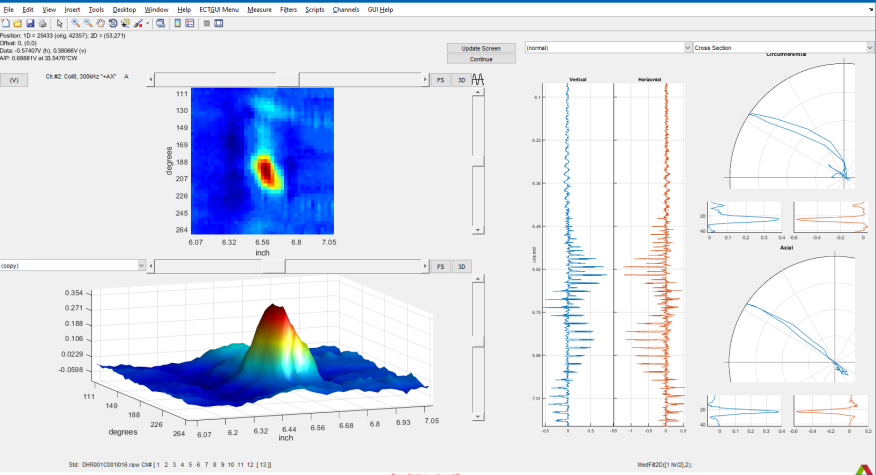
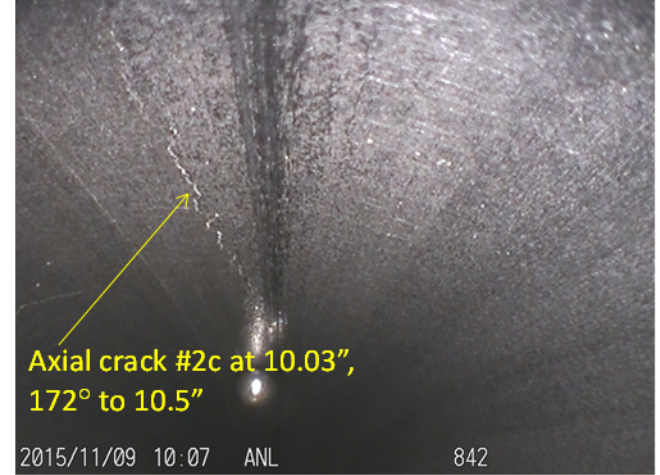
U-bend ID*	Pre-test ECT*	Pre-pressurization Visual
<p>1100-06 (0°, Ex) (#1)</p>		
<p>1100-07 (90°, Ex) (#6)</p>		

U-bend ID*	Pre-test ECT*	Pre-pressurization Visual
<p>1100-07 (180°, 45°- off Ex) (#7)</p>		 <p>Axial crack #7 from 13.69", 230° to 13.91", 220°</p> <p>Axial crack #7</p> <p>2015/08/08 21:24 355 OLYMPUS</p>
<p>1100-08 (90°, Ex) (#1)</p>		 <p>Axial crack #1 at 9.28", 200° to 10.48", 190°</p> <p>2015/10/04 12:52 579 OLYMPUS</p>

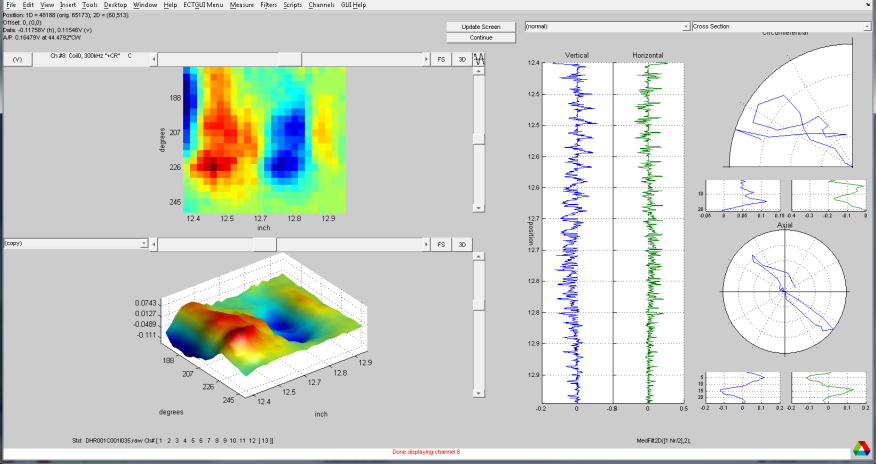
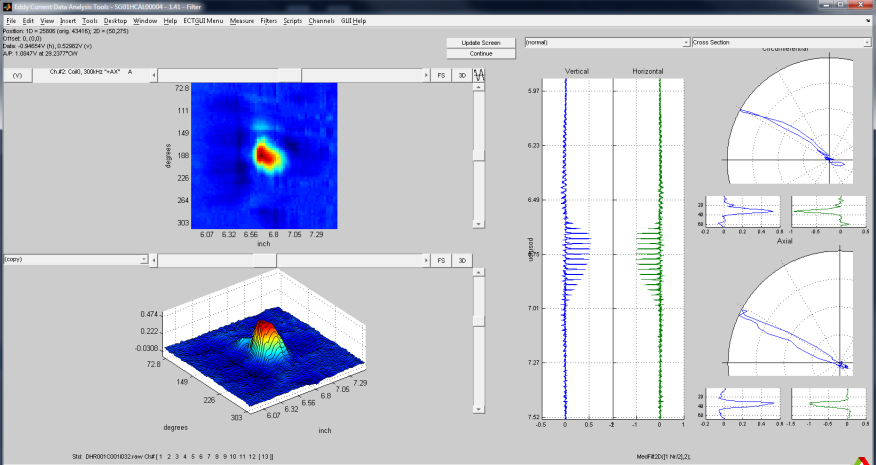
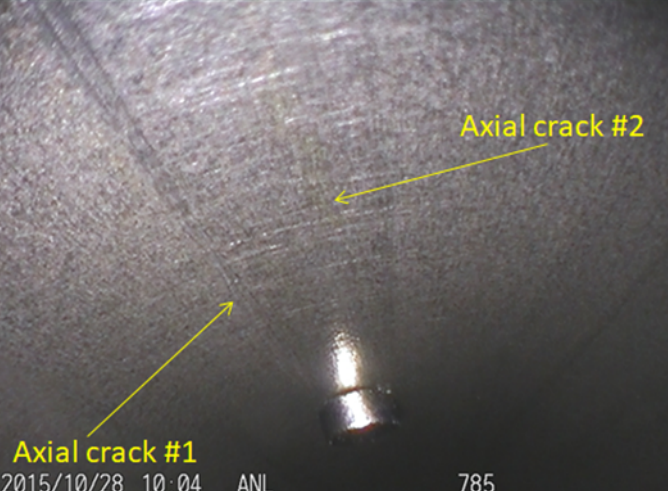
U-bend ID*	Pre-test ECT*	Pre-pressurization Visual
<p>1100-15 (90°, Ex) (#6a)</p>		
<p>1100-18 (90°, Ex) (#2a, #3)</p>		

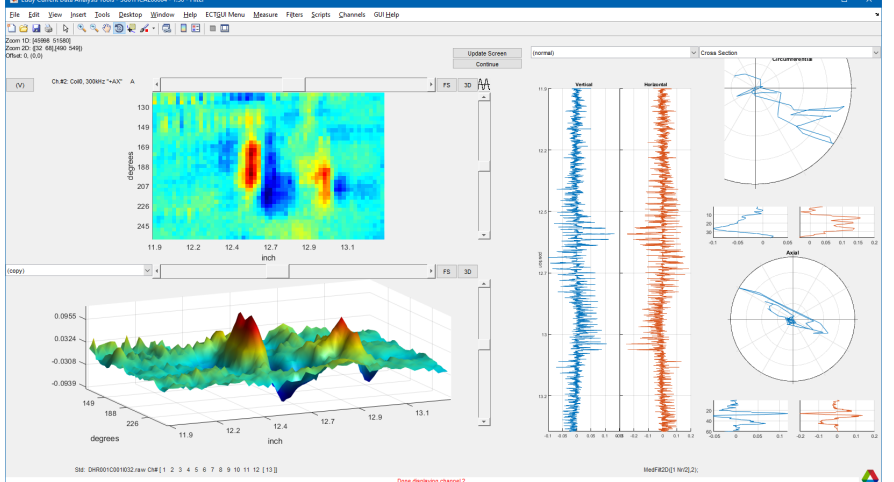
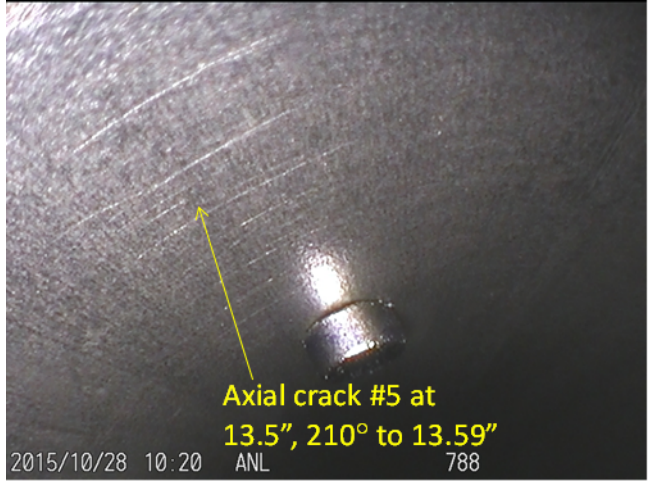
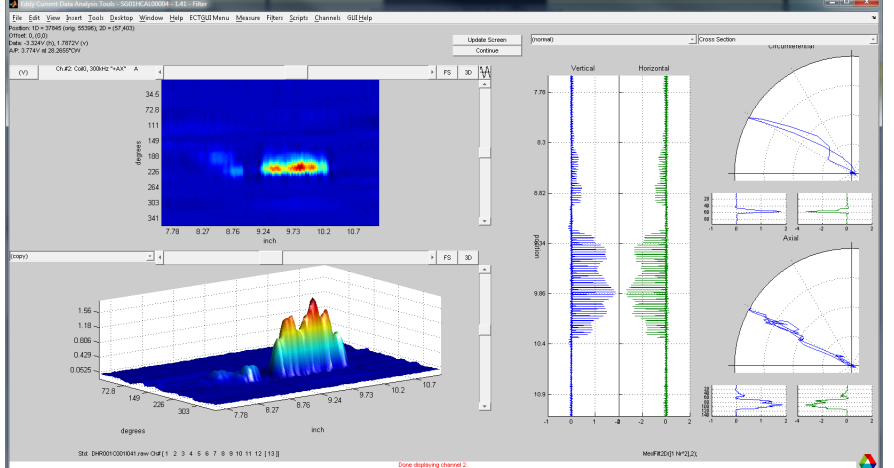
U-bend ID*	Pre-test ECT*	Pre-pressurization Visual
<p>1100-19 (0°, In) (#1b)</p>		 <p>Diagonal crack #1b at 6.83", 0° to 7", 25°</p> <p>Axial crack #1a at 6.56", 20° to 6.89", 20°</p> <p>2015/09/29 23:42 548</p>
<p>1180-02 (90°, Ex) (#2e)</p>		 <p>Axial crack #2e at 185° 10.5" to 190°, 10.78"</p> <p>2015/10/16 09:42 ANL 697</p>

U-bend ID*	Pre-test ECT*	Pre-pressurization Visual
<p>1180-11 (0°, Ex) (#2)</p>		<p>2015/09/21 15:59 468 OLYMPUS</p>
<p>1180-11 (45°, Ex) (#3)</p>		<p>2015/09/21 16:09 469 OLYMPUS</p>

U-bend ID*	Pre-test ECT*	Pre-pressurization Visual
<p>1180-13 (0°, In) (ND)</p>		 <p>2015/11/17 16:40 ANL 877</p>
<p>1180-14 (0°, Ex) (#2c)</p>		 <p>2015/11/09 10:07 ANL 842</p>

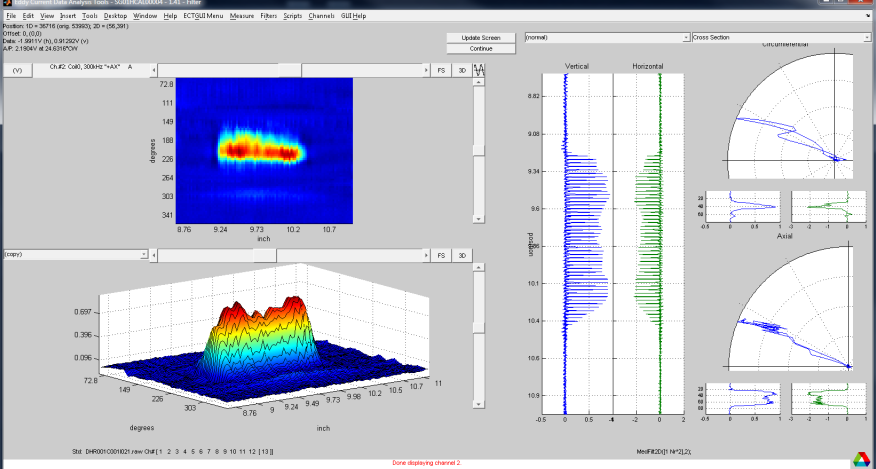
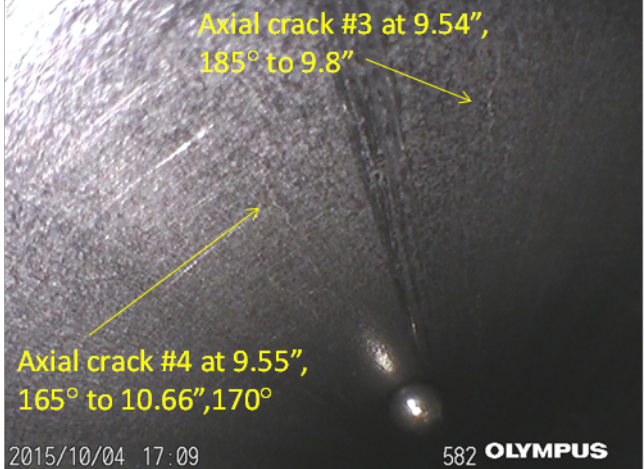
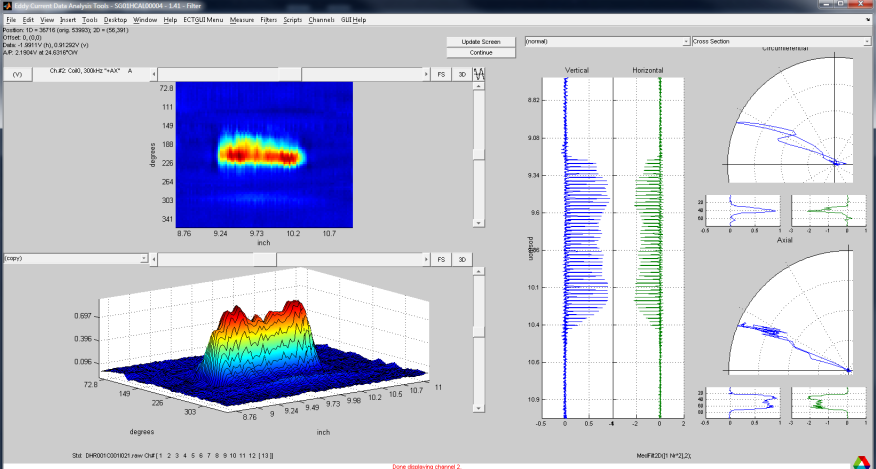
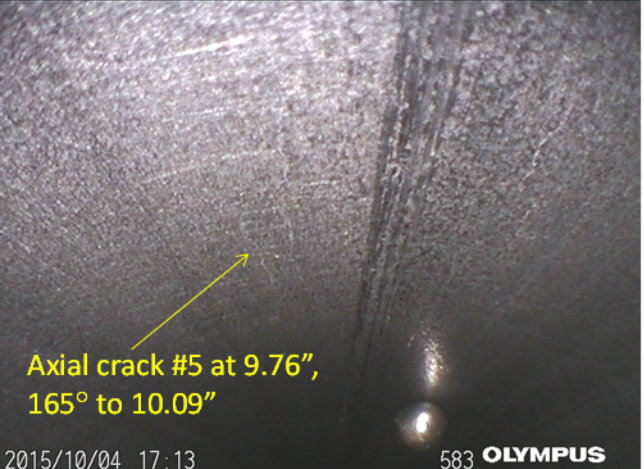
U-bend ID*	Pre-test ECT*	Pre-pressurization Visual
<p>1180-15 (90°, Ex) (#2)</p>		
<p>1180-15 (180°, Ex) (ND)</p>		

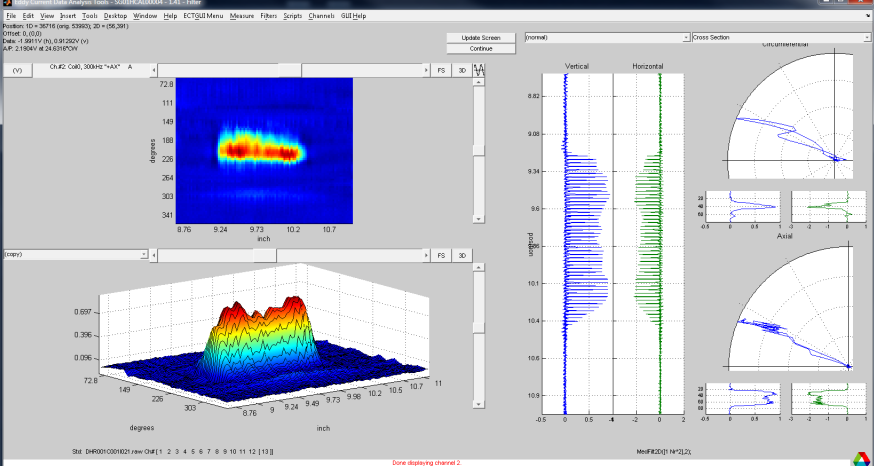
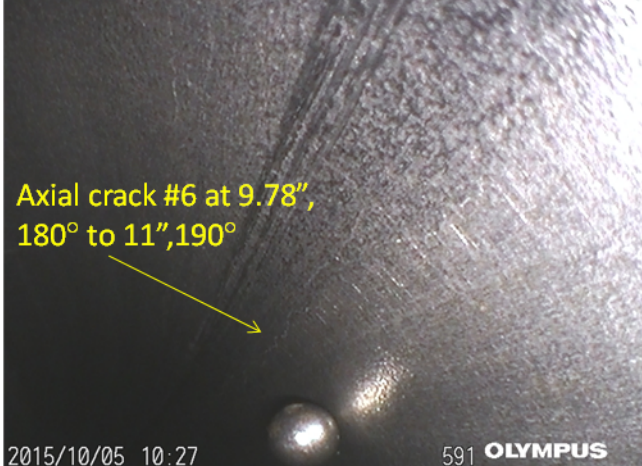
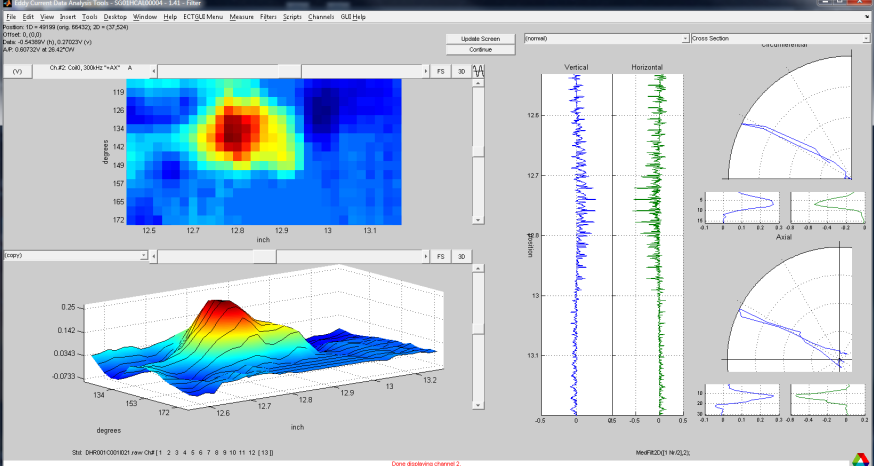
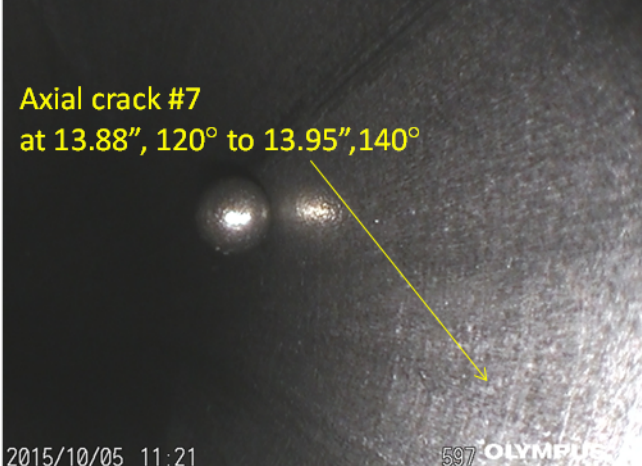
U-bend ID*	Pre-test ECT*	Pre-pressurization Visual
	 <p style="text-align: center;">[circ]</p>	
<p>1180-16 (0°, Ex) (ND)</p>		 <p style="text-align: right;">Axial crack #2</p> <p style="text-align: right;">Axial crack #1</p> <p style="text-align: right;">2015/10/28 10.04 ANL</p> <p style="text-align: right;">785</p>

U-bend ID*	Pre-test ECT*	Pre-pressurization Visual
<p>1180-16 (180°, Ex) (#5)</p>		
<p>1180-18 (90°, Ex) (#3c)</p>		

U-bend ID*	Pre-test ECT*	Pre-pressurization Visual
<p>1180-18 (180°, 45°- off Ex) (ND)</p>		<p>[No image]</p>
<p>1180-20 (0°, Ex) (#2)</p>		

U-bend ID*	Pre-test ECT*	Pre-pressurization Visual
<p>1180-20 (45°, Ex) (#4)</p>		
<p>1180-21 (90°, Ex) (#1a)</p>		

U-bend ID*	Pre-test ECT*	Pre-pressurization Visual
<p>1180-22 (90°, Ex) (#4)</p>		
<p>1180-22 (90°, Ex) (#5)</p>		

U-bend ID*	Pre-test ECT*	Pre-pressurization Visual
<p>1180-22 (90°, Ex) (#6)</p>		
<p>1180-22 (180°, 45°- off Ex) (#7)</p>		

U-bend ID*	Pre-test ECT*	Pre-pressurization Visual
<p>1180-23 (0°, Ex) (ND)</p>		
<p>1180-23 (90°, Ex) (#6a, #6b)</p>		

* Ex = Extrados; ECT = eddy current testing; FI = Flank; ID = identification; In = Intrados; ND = not detectable.

Table D-2. Pre- and post-pressure test NDE and DE data for PWSCCs in 57-mm-radius U-bend tube specimens.

Tube ID	Pre-test +Pt ECT (with clamps)					Pre-pressurization Visual					Post-Test SEM ^c		Pressure test	
	Location		Amplitude (v)	Length (in.)	Depth (%TW)	Crack #	Position before pressure test				Crack Length (in.)	Max. Depth (%TW)	Rupture Position	Rupture Pressure (KSI)
	ϕ (°)	Θ^*					Start position D (in.)	θ (°)	End position D (in.)	θ (°)				
890-01	90°	Ex	6.39	1.99	90	1	9.36	180°	11.34	195°	2.68"	98	Apex	1.04
890-03	0°	Ex	0.66	0.44	67	1	7.20	175°	7.42	175°	0.63"	96	0° Tangent	4.59
890-04	180°	Ex	0.94	0.3	90	2					0.63"	81	180° Tangent	4.99
	90°	Ex	0.23	1.01	16	3	13.70	225°	13.84	215°	0.43"	97		
890-07	90°	Ex	3.30	1.42	77	6	9.72	200°	10.45	175°	1.11"	92	Apex	2.43
890-08	180°	Ex	0.26	0.17	36	B1					0.07"	34	No rupture	
	180°	Fl ^b	0.12	0.22	27									
	90°	Ex	0.16	0.18	45	C					0.18"	57		
890-15	180°	45° off Ex	0.29	0.12	42	1					0.19"	58	No rupture	
	90°	Ex	0.20	0.20	30	90C					0.11"	61		
890-16	0°	Ex	0.35	0.3	60	1					0.31"	89	0° Tangent	7.2(burst)
890-20	0°	Ex	0.28	0.17	58	1					0.19"	75	No rupture	No rupture
920-08	0°	In ^c	1.6	0.66	48	2	6.90	5°	7.19	5°	0.60"	96	0° Tangent	2.9
						3					0.25"	84		
920-09	180°				NDD	C1					0.48"	18	No rupture	
	180°				NDD	D1					0.22"	16		
920-10	90°	Ex	1.57	1.29	83	2	9.70	185°	10.89	190°	1.41"	96	Apex	2.7
920-12	0°	Ex	0.82	0.36	77	2	6.63	185°	7.19	185°	0.46"	93	0° Tangent	6.37(burst)
	65°	Ex	0.56	0.70	58	B					0.55"	52.6		

Tube ID	Pre-test +Pt ECT (with clamps)					Pre-pressurization Visual					Post-Test SEM ^c		Pressure test	
	Location		Amplitude (v)	Length (in.)	Depth (%TW)	Crack #	Position before pressure test				Crack Length (in.)	Max. Depth (%TW)	Rupture Position	Rupture Pressure (KSI)
	ϕ (°)	Θ^*					Start position D (in.)		End position D (in.)					
920-15	90°	Ex	1.45	0.98	64	2	9.76	170°	10.09	170°	1.19"	73	180° Tangent	6.27(burst)
	180°	45° off Ex	0.50	0.45	45	3					0.61"	88		
920-19	45°	Ex	1.95	0.75	74	2	8.79	160°	9.19	160°	0.80"	88	~60°	3.89
1100-06	0°	Ex	1.53	0.64	80	1	6.72	190°	7.19	190°	0.66"	96	0° Tangent	2.84
						2					0.14"	71		
1100-07	90°	Ex	2.05	1.16	81	3,6	9.55	165°	10.81	170°	1.51"	91	Apex	2.09
	180°	45° off Ex	0.82	0.34	61	7	13.69	230°	13.91	220°	0.65"	84		
1100-08	90°	Ex	4.78	1.9	100	1	9.28	200°	10.84	195°	2.33"	99	Apex	0.85
1100-14	90°	Ex	4.30	1.4	85	3	9.59	165°	10.11	165°	0.51"	95	Apex	1.84
						4	9.97	185°	10.98	185°	1.23"	98		
1100-15	90°	Ex	2.77	1.6	81	6	9.38	195°	10.14	185°	1.68"	99	Apex	1.51
1100-18	90°	Ex	4.40	1.8	85	2	9.32	185°	11.17	185°	2.31"	98	Apex	1.4
1100-19	0°	In	1.07	0.33	77	1a	6.15	20°	6.89	20°	0.31"	99	0° Tangent	4.04
						1b	6.83	0°	7.00	25°	0.23"			
1180-02	90°	Ex	4.60	1.34	85	2	8.50	195°	10.78	190°	2.74"	98	Apex	1.38
1180-11	0°	Ex	1.57	0.54	87	1					0.24"	95	0° Tangent	3.57
						2	6.86	200°	7.23	200°	0.64"	97		
	45°	Ex	1.81	1.23	77	3	8.41	190°	10.05	185°	1.41"	88		
1180-13	0°	In	0.36	80	60	2					0.41"	88	Apex	[--]
1180-14	0°	Ex	2.70	1.4	77	2	9.61	175°	10.50	172°	1.81"	97	Apex	2.1

Tube ID	Pre-test +Pt ECT (with clamps)					Pre-pressurization Visual					Post-Test SEM ^c		Pressure test	
	Location		Amplitude (v)	Length (in.)	Depth (%TW)	Crack #	Position before pressure test				Crack Length (in.)	Max. Depth (%TW)	Rupture Position	Rupture Pressure (KSI)
	ϕ (°)	Θ^*					Start position D (in.)		End position D (in.)					
1180-15	90°	Ex	0.43	0.74	30	2	9.92	175°	10.28	175°	0.93"	54	No rupture	
	180°	Ex	0.23	0.12	13	3					0.24"	64		
						4					0.17"	65		
1180-16	0°	Ex	0.92	0.49	77	1					0.60"	91	0° Tangent	6.3 (burst)
	180°	Ex	0.24	0.12	22	5					0.33"	52		
1180-18	90°	Ex	2.50	1.14	100	3	9.63	195°	10.50	188°	1.45"	97	Apex	2.36
	180°	45° off Ex	0.33	0.21	36	180B					0.32"	59		
1180-20	0°	Ex	1.68	0.66	74	1					0.14"		0° Tangent	3.39
						2	6.89	185°	7.17	185°	0.65"	91		
	45°	Ex	0.53	0.98	55	4	8.72	200°	9.13	200°	1.16"	62		
1180-21	90°	Ex	3.27	1.71	62	1	9.39	195°	11.17	190°	2.15"	99	Apex	1.54
1180-22	90°	Ex	1.94	1.29	67	4	9.55	165°	10.66	170°	1.39"	73	180° Tangent	6.7 (burst)
						5	9.76	165°	10.09	165°				
						6	9.78	180°	11.00	190°				
	180°	45° off Ex	0.50	0.26	51	7	13.88	120°	13.95	140°	0.44"	92		
1180-23	0°	Ex	1.27	0.46	83	1					0.64"	99	Tangent	4.3
	90°	Ex	1.87	1.22	77	6	10.14	205°	11.02	205°	0.87"	82		

^a Location angle along the U-bend.

^b Location angle around tube circumference: Ex=Extrados; Fl=Flank; In=Intrados.

^c SEM =scanning electron microscopy.

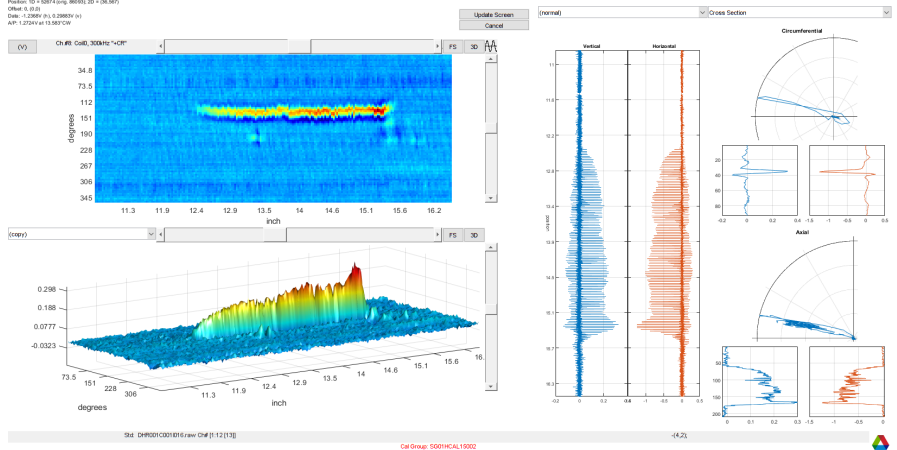
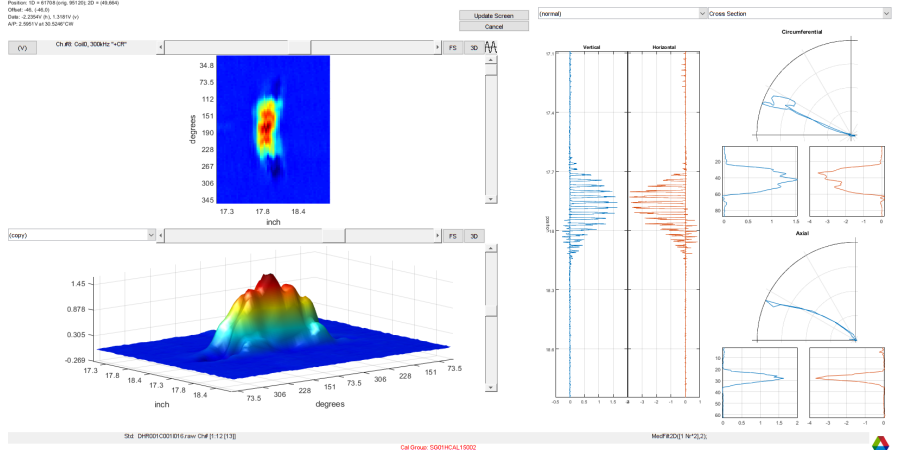
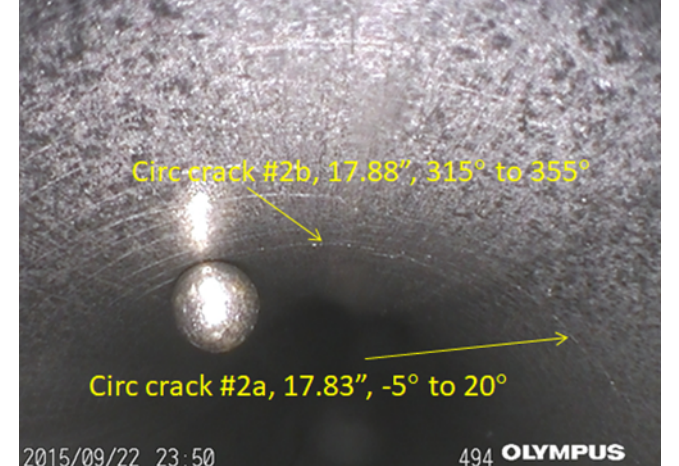
APPENDIX E – EDDY CURRENT AND VISUAL INSPECTION DATA FOR 152-MM-RADIUS U-BEND SPECIMENS

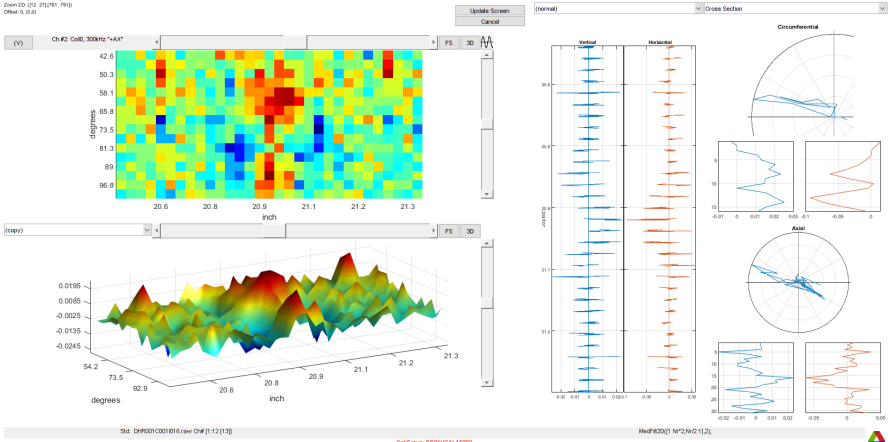
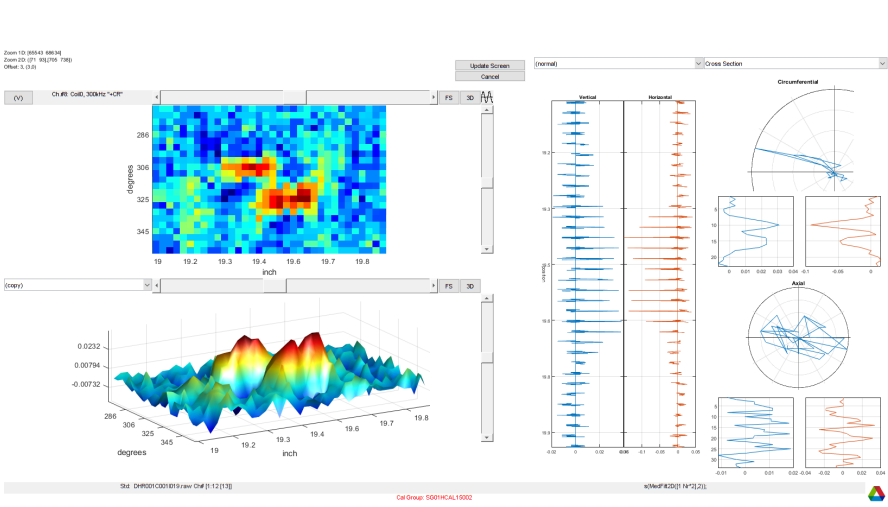
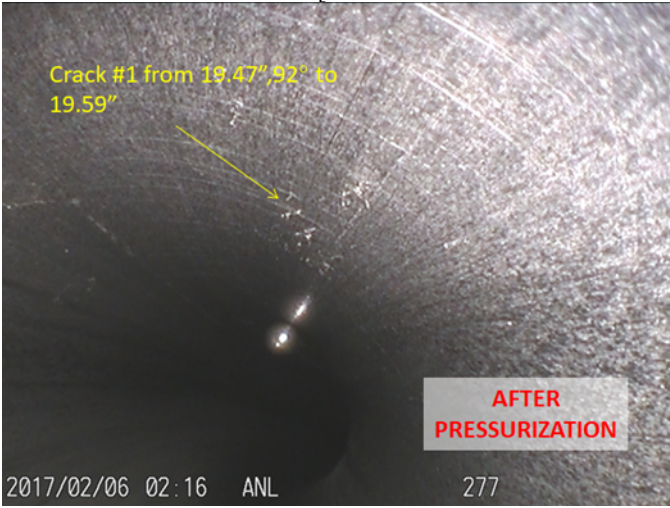
Videoscope images are provided in Table E-1 for all the primary water stress corrosion cracking (PWSCCs) in 152-mm-radius U-bend tube specimens, a subset of which were later examined destructively. The nondestructive examination (NDE) data were collected on all of the tubes shortly prior to pressure testing of the U-bend specimens. Associated with each video image in the table is a screen capture of the processed eddy current (EC) data. Analysis of EC data was performed using the computer-aided data analysis tool implemented at Argonne National Laboratory (Argonne). The screen captures of the rotating +Pt probe data provided in these tables are associated with different stages of the data analysis process, displaying the data in the main analysis user interface. Along with the specimen identification (ID) number in the first column, information is provided about the approximate location of the crack signal in the U-bend. The PWSCCs with a detectable EC signal but with no discernible visual data are denoted as not detectable (ND) in the first column. Table E-2 provides data on pre- and post-pressure test NDE and destructive examination (DE) for PWSCCs in 152-mm-radius U-bend tube specimens.

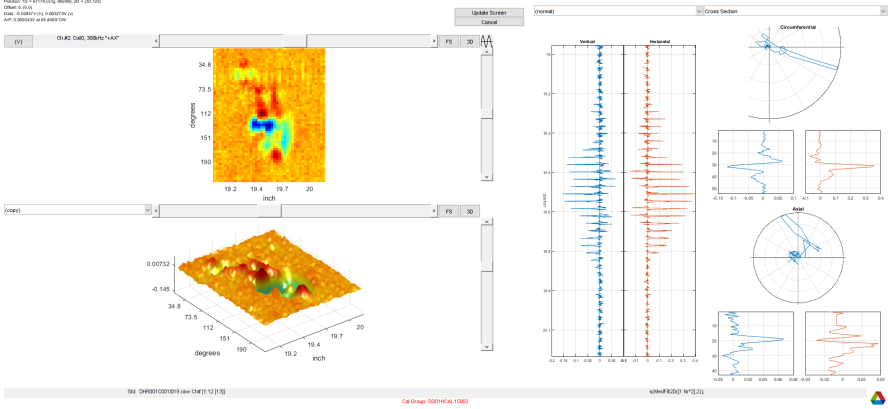
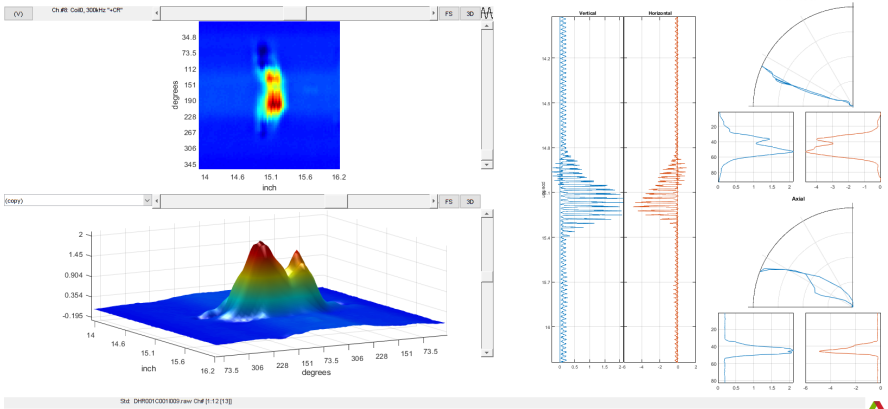
Table E-1. Eddy current and visual (videoscope) data for PWSCCs in 152-mm-radius U-bend tube specimens.

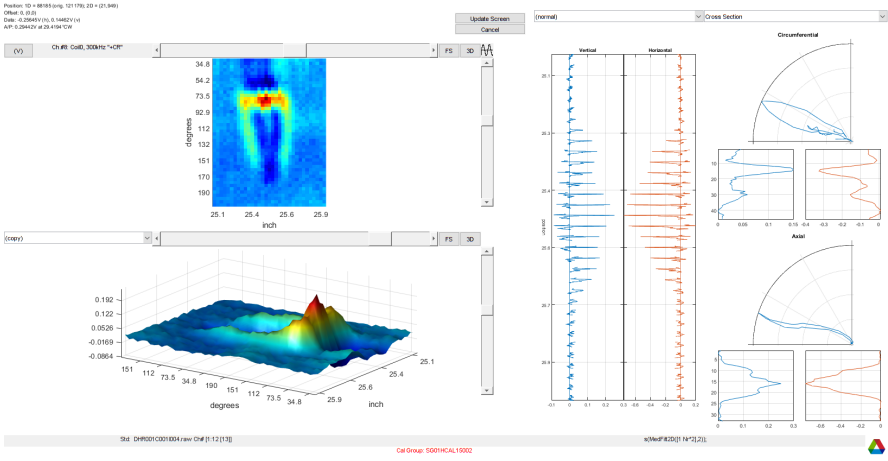
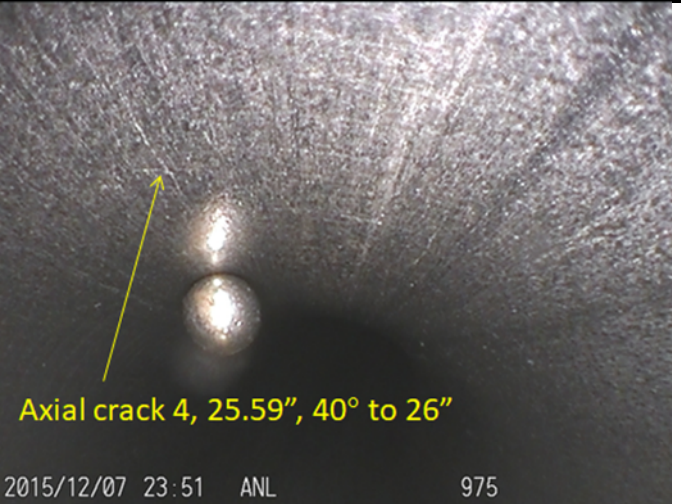
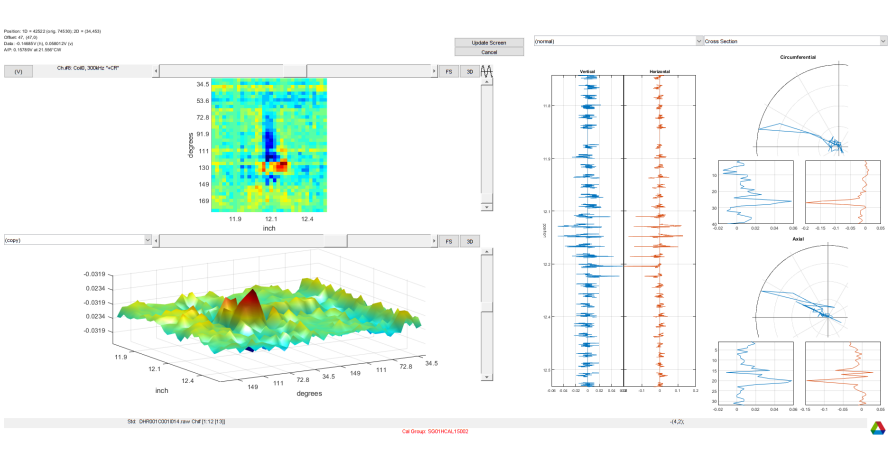
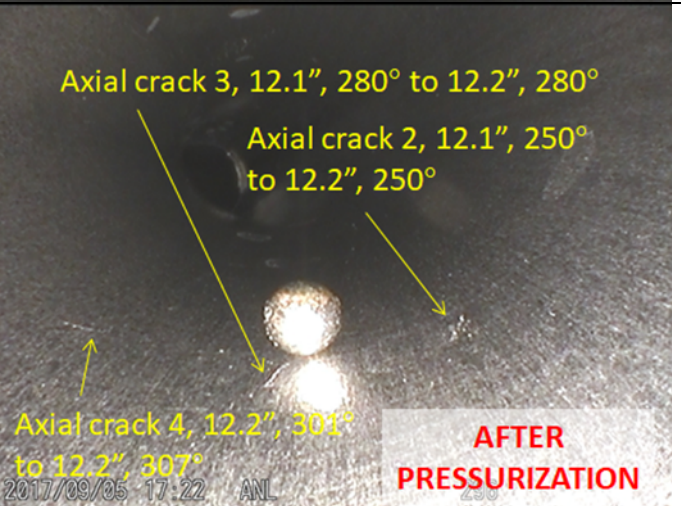
U-bend ID*	Pre-test ECT*	Pre-pressurization Visual
<p>07-02 (60°, Ex-FI) (#7, etc.)</p>		
<p>07-02 (120°, Ex-FI) (ND)</p>		<p>[No image]</p>

U-bend ID*	Pre-test ECT*	Pre-pressurization Visual
<p>07-03 (70°, Ex-FI) (#4)</p>		
<p>07-03 (105°, Ex) (109°, Ex) (#10)</p>		

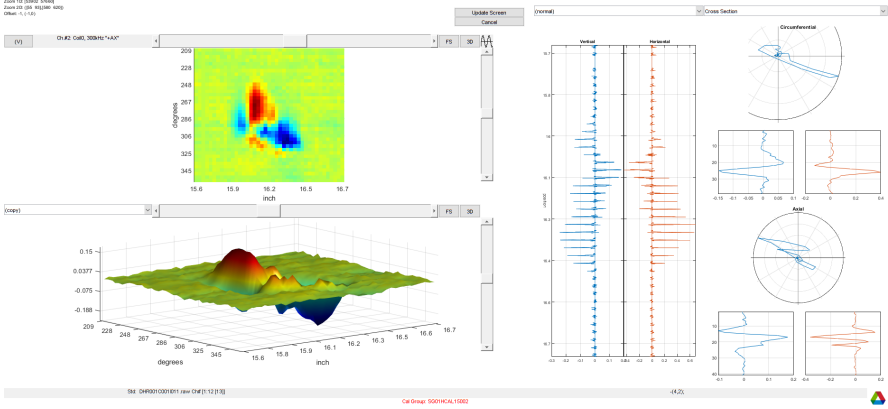
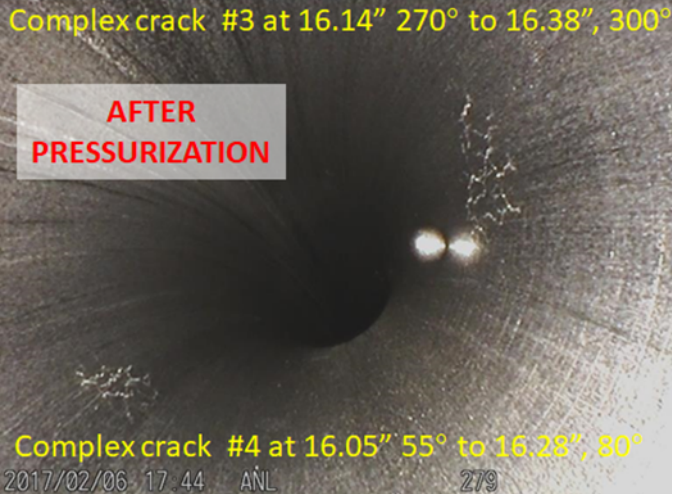
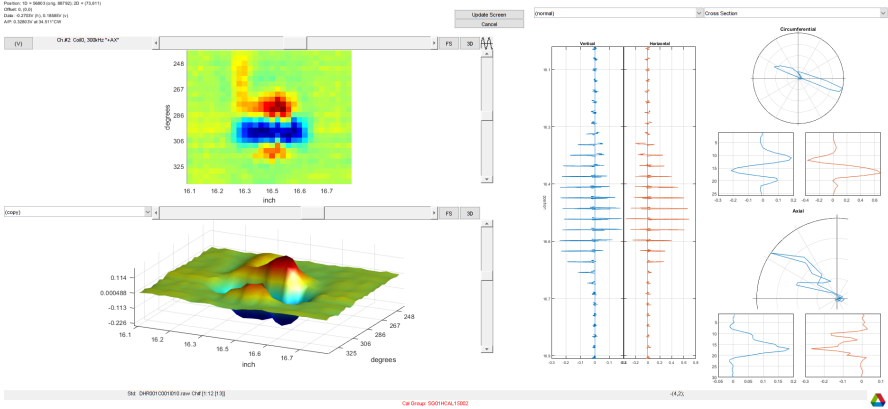
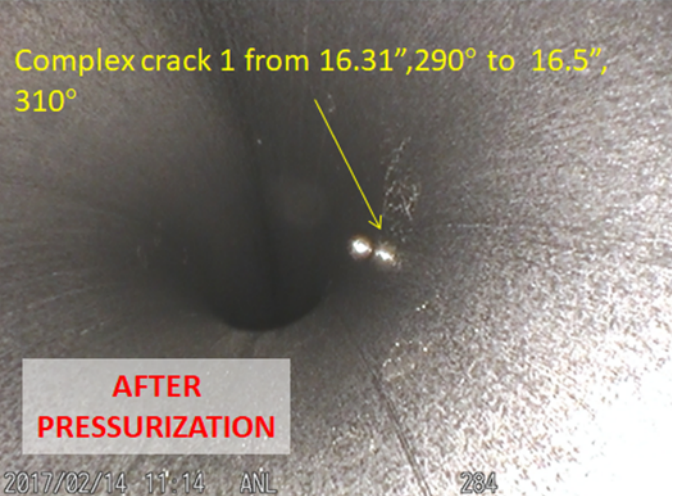
U-bend ID*	Pre-test ECT*	Pre-pressurization Visual
<p>14-01 (75°, Ex-FI) (#1)</p>		
<p>14-01 (105°, In) (#2)</p>		

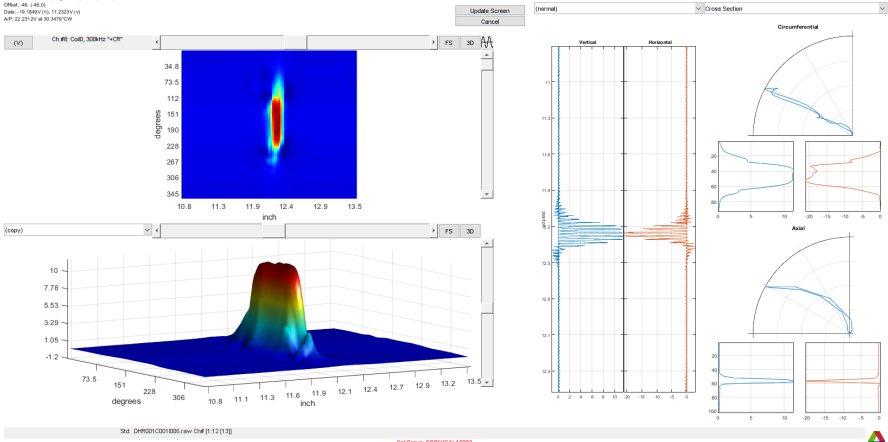
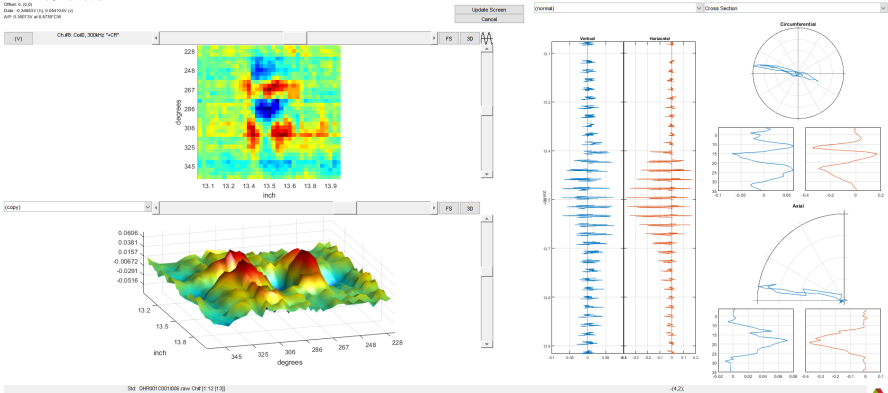
U-bend ID*	Pre-test ECT*	Pre-pressurization Visual
<p>14-01 (135°, In-Fl) (ND)</p>		<p>[No image]</p>
<p>15-02 (105°, In-Fl) (ND)</p>		<p>[No</p>  <p>image]</p>

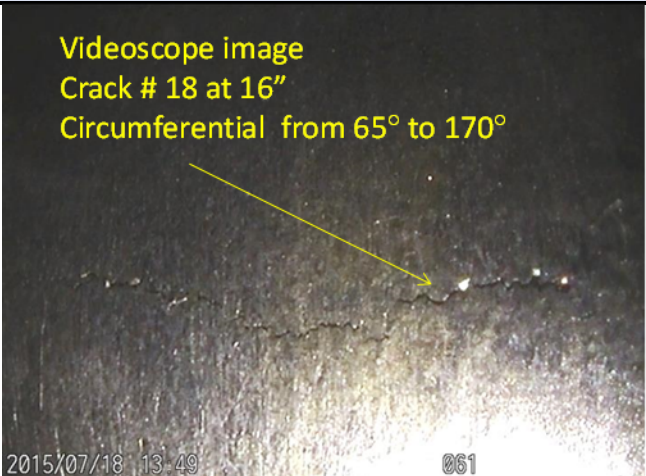
U-bend ID*	Pre-test ECT*	Pre-pressurization Visual
<p>15-02 (120°, Ex-FI) (ND)</p>		<p>AFTER CUT</p> 
<p>20-01 (90°, In) (#1)</p>		

U-bend ID*	Pre-test ECT*	Pre-pressurization Visual
<p>22-01 (180°, FI) (#4)</p>		 <p>Axial crack 4, 25.59", 40° to 26"</p> <p>2015/12/07 23:51 ANL 975</p>
<p>23-01 (45°, In-FI) (ND)</p>		 <p>Axial crack 3, 12.1", 280° to 12.2", 280°</p> <p>Axial crack 2, 12.1", 250° to 12.2", 250°</p> <p>Axial crack 4, 12.2", 301° to 12.2", 307°</p> <p>2017/09/05 17:22 ANL</p> <p>AFTER PRESSURIZATION</p>

U-bend ID*	Pre-test ECT*	Pre-pressurization Visual
<p>23-01 (90°, In-FI) (ND)</p>		<p>AFTER PRESSURIZATION</p> <p>Complex crack 8, 16.17", 60° to 16.25", 105°</p> <p>Complex crack 9, 16.19", -110° to 16.44", 20°</p> <p>2017/02/14 16:03 ANL 289</p>
<p>25-01 (45°, In) (#1)</p>		<p>Circ crack 1, 12.09", 30° to 55°</p> <p>Circ crack 1a, 12.12", -20° to 35°</p> <p>Circ crack 1c, 12.16", 300° to 345°</p> <p>2015/12/08 00:20 ANL 976</p>

U-bend ID*	Pre-test ECT*	Pre-pressurization Visual
<p>29-01 (90°, In-FI) (ND)</p>		<p>Complex crack #3 at 16.14" 270° to 16.38", 300°</p>  <p>Complex crack #4 at 16.05" 55° to 16.28", 80° 2017/02/06 17:44 ANL 279</p>
<p>31-01 (90°, In-FI) (ND)</p>		<p>Complex crack 1 from 16.31",290° to 16.5", 310°</p>  <p>Complex crack 1 from 16.31",290° to 16.5", 310° 2017/02/14 11:14 ANL 284</p>

U-bend ID*	Pre-test ECT*	Pre-pressurization Visual
<p>52-01 (45°, In) (ND)</p>	 <p>The image displays ECT data for U-bend 52-01. It includes a 2D heatmap of the bend area, a 3D surface plot showing a localized peak, and several cross-sectional graphs (Vertical, Horizontal, Circumferential, Axial) showing signal variations across the bend.</p>	<p>[No image]</p>
<p>52-01 (60°, In-FI) (ND)</p>	 <p>The image displays ECT data for U-bend 52-01. It includes a 2D heatmap showing a more complex signal pattern, a 3D surface plot with multiple peaks, and several cross-sectional graphs (Vertical, Horizontal, Circumferential, Axial) showing signal variations.</p>	<p>[No image]</p>

U-bend ID*	Pre-test ECT*	Pre-pressurization Visual
1260-06 (test) (#18)	[Test specimen; No NDE data]	<p data-bbox="1394 280 1843 391">Videoscope image Crack # 18 at 16" Circumferential from 65° to 170°</p>  <p data-bbox="1339 695 1535 721">2015/07/18 13:49</p> <p data-bbox="1776 695 1814 721">061</p>

*ECT=eddy current testing; Ex = Extrados; FI = Flank;In = Intrados; ND = not detectable.

Table E-2. Pre- and Post-pressure test NDE and DE data for PWSCCs in 152-mm-radius U-bend tube specimens.

Tube ID	Pre-test +Pt ECT (with clamps)					Pre-pressurization Visual					Post-Test SEM		Pressure Test	
	Location		Amplitude (v)	Length (in or °)	Max Depth (%TW)	Crack #	Position before pressure test				Crack Length (in or °)	Max Depth (%TW)	Rupture Location	Rupture Pressure (KSI)
	φ^a (°)	Θ^b					Start position		End position					
						D (in)	θ (°)	D (in)	θ (°)					
07-02	60°	Ex – Fl	2.72	53°	100	1					2.76"	90	~45°	6.06
	120°	Ex – Fl	0.43	34°	40	9					0.10"	45		
07-03	70°	Ex – Fl	2.89	61°	100	4	14.91	100°	14.91	145°	60.5°	95	Apex	[---]
	105°	Ex	0.63	30°	47	11					0.10"	26		
14-01	75°	Ex – Fl	1.13	30°	44	1					3.16"	41	No rupture	
	105°	I	3.96	163°	56	2	17.83	-5°	17.88	315°	138.5°	79		
	135°	In – Fl	0.17	<i>0.22"</i>	40	C1					0.12"	25		
15-02	105°	In – Fl	0.13	19°	49	1					0.17"	39	No rupture	
	120°	Ex – Fl	0.26	23°	46	3					8°	51		
20-01	90°	In	0.30	27°	37	1	15.09	5°	15.09	40°	197°	88	No rupture	
22-01	180°	Fl	1.38	<i>0.48"</i>	40	4					40°	65	No rupture	
23-01	45°	In – Fl	0.136	23°	37	4					0.31"	43	No rupture	
	90°	In – Fl	2.04	160°	65	9					0.29"	51		
25-01	45°	In	[---]	[---]	100	1	12.16	-60°	12.02	55°	119°	99	~45°	6.8
29-01	90°	In – Fl	0.65	<i>0.24"</i>	55	3					0.26"	41	No rupture	
31-01	90°	In – Fl	0.63	34°	43	1					0.28"	32	No rupture	
52-01	45°	In	20	235°	82	(Too large, no interest in fractography)						45°	[----]	
	60°	In – Fl	0.62	53°	56	4					37.8°			36
1260-06	(test sample, no NDE data)					18	16.00	65°	16.00	170°	3.88"	95	Apex	4.6

^a location angle along the U-bend

^b location angle around tube circumference: Ex=Extrados; Fl=Flank; In=Intrados.

Length in blue italics for axial

APPENDIX F – NDE DEPTH PROFILES FOR CRACKS IN 57-MM-RADIUS U-BEND SPECIMENS

Depth profiles of primary water stress corrosion cracks (PWSCCs) in 57-mm-radius U-bend tube specimens are presented in Figures F-1 through F-40. The eddy current (EC) sizing results are based on the analysis of rotating +Pt probe data at 300 kHz. The estimates of nondestructive examination (NDE) depth, based on EC signal phase angle information, were obtained using the computer-aided data analysis tool implemented at Argonne National Laboratory (Argonne). Also drawn on each plot is the depth profile calculated based on the Argonne-developed equivalent rectangular crack (ERC) model — also referred to as burst-effective length and depth. The depth profiles, in %TW, are plotted as negative values, which by convention is used to display inside diameter (ID)-originated flaws (i.e., outside diameter [OD]-originated flaws are plotted as positive values). The ERC algorithm is embedded within the Argonne data analysis software, and the results are generated by using the NDE depth profiles. It should be noted that the mechanical properties of Alloy 600 tubes, such as yield and ultimate strength, used for calculation of the tube failure pressures — ligament rupture pressure (P_{SC}) and burst pressure (P_{CR}) — may not represent the actual values for the specific heat of tubing used in this work. The ERC model for U-bends is discussed in a separate report [13] in connection with tube integrity studies conducted under the International Steam Generator Tube Integrity Program (ISG-TIP).

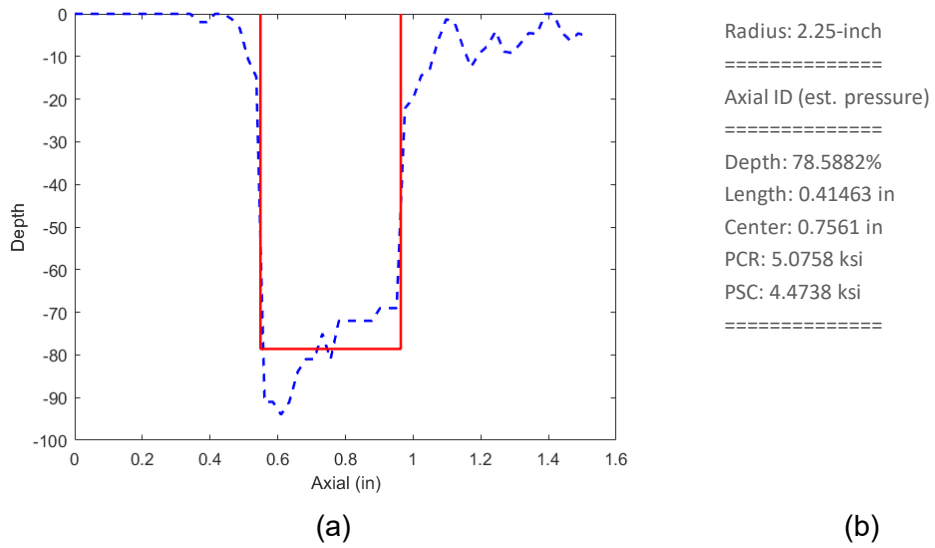


Figure F-1. Data analysis results for an axial PWSCC in specimen 1100-06 showing (a) EC (dashed line) and ERC (solid line) depth profiles and (b) output of the ERC tool using the Argonne data analysis software.

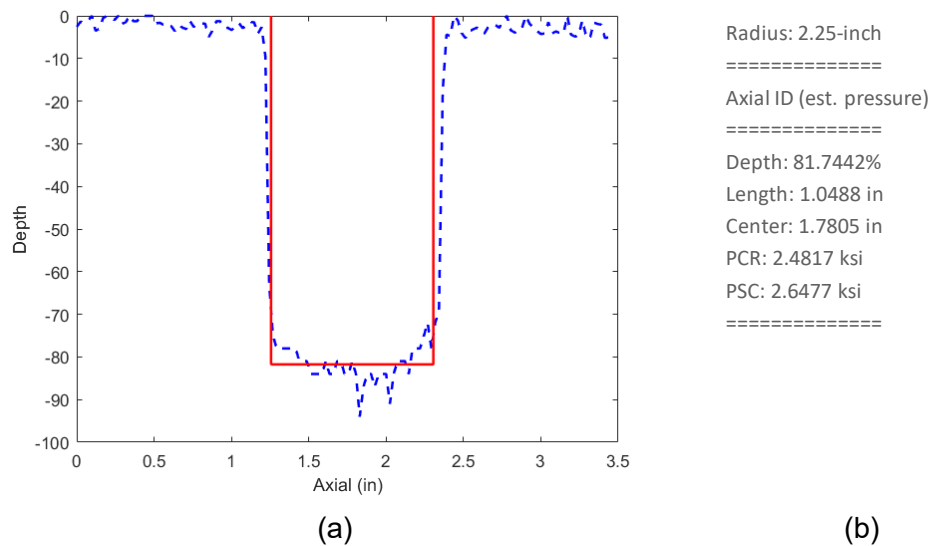


Figure F-2. Data analysis results for an axial PWSCC in specimen 1100-07 showing (a) EC (dashed line) and ERC (solid line) depth profiles and (b) output of the ERC tool using the Argonne data analysis software.

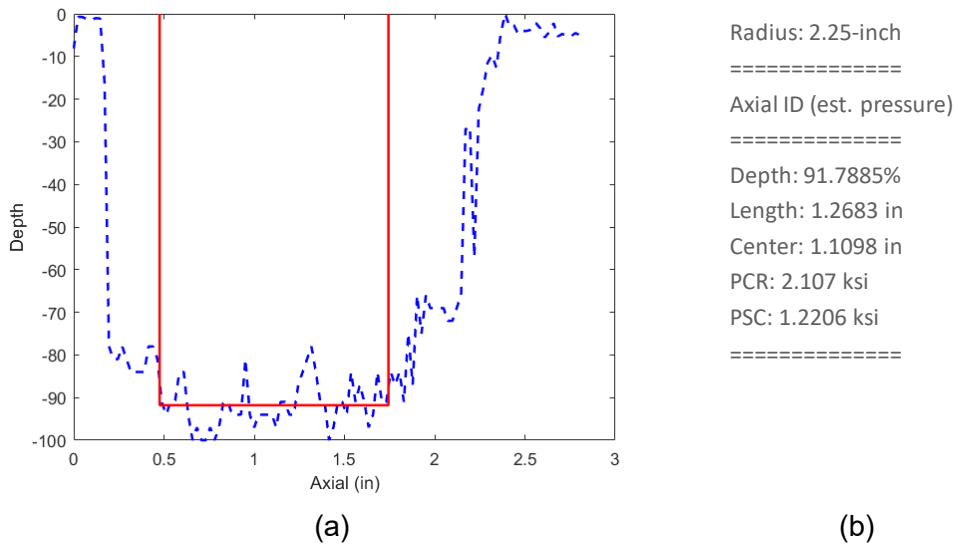


Figure F-3. Data analysis results for an axial PWSCC at 90° in specimen 1100-08 showing (a) EC (dashed line) and ERC (solid line) depth profiles and (b) output of the ERC tool using the Argonne data analysis software.

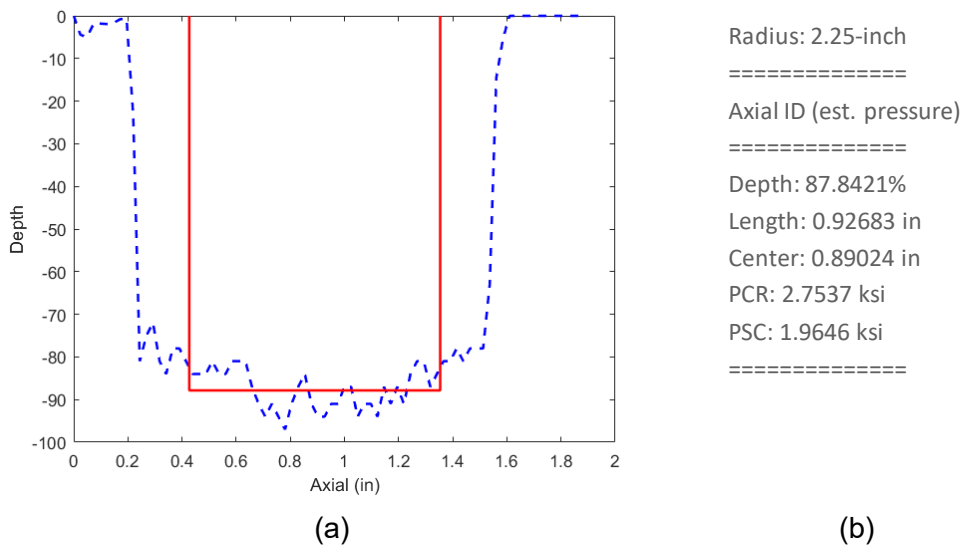


Figure F-4. Data analysis results for an axial PWSCC at 90° in specimen 1100-14 showing (a) EC (dashed line) and ERC (solid line) depth profiles and (b) output of the ERC tool using the Argonne data analysis software.

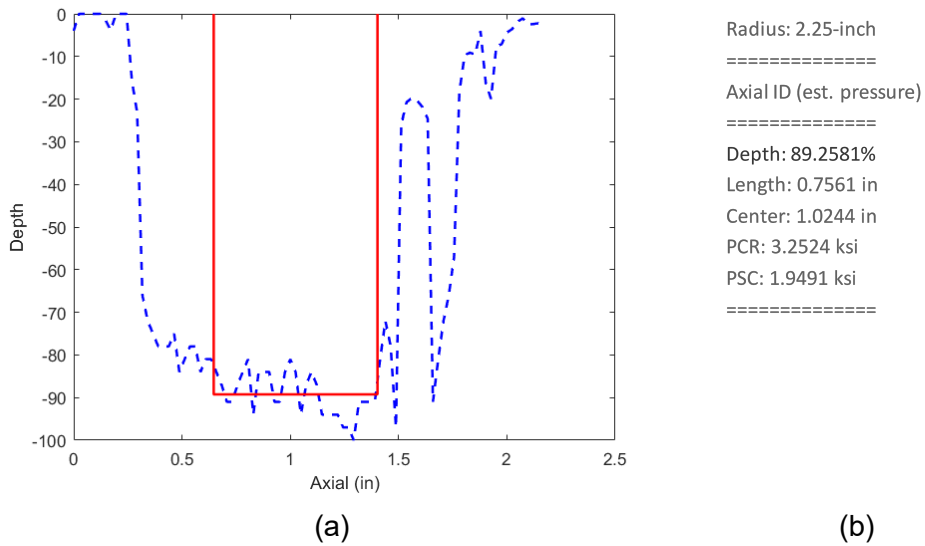


Figure F-5. Data analysis results for an axial PWSCC at 90° in specimen 1100-15 showing (a) EC (dashed line) and ERC (solid line) depth profiles and (b) output of the ERC tool using the Argonne data analysis software.

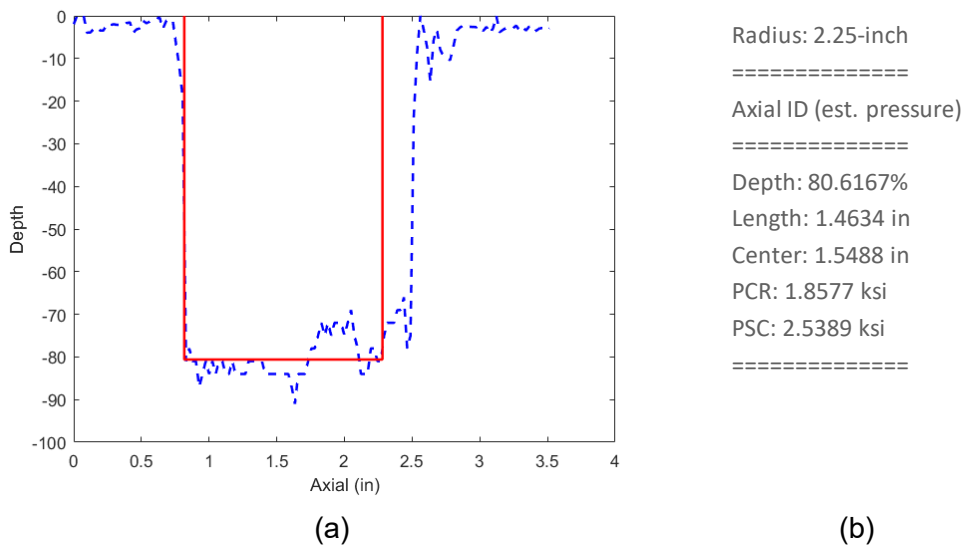


Figure F-6. Data analysis results for an axial PWSCC at 90° in specimen 1100-18 showing (a) EC (dashed line) and ERC (solid line) depth profiles and (b) output of the ERC tool using the Argonne data analysis software.

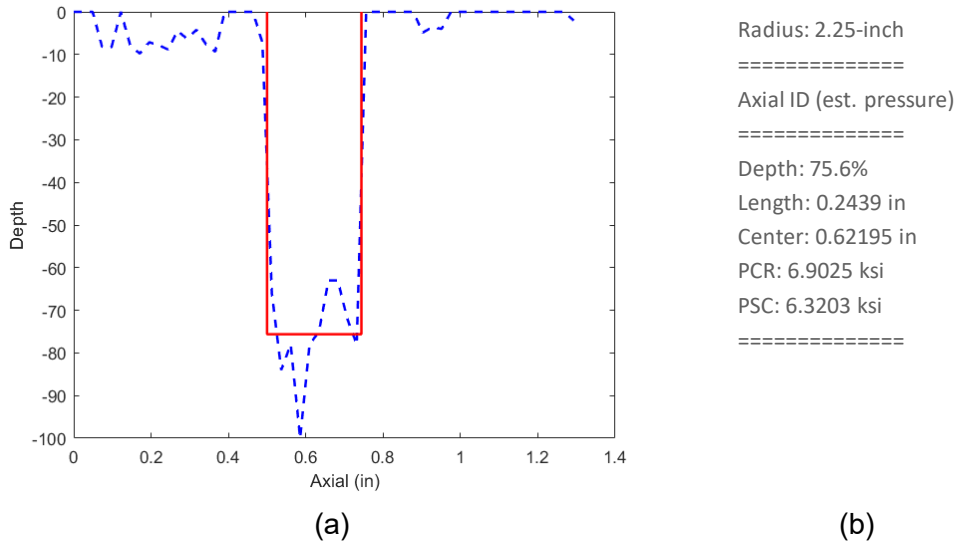


Figure F-7. Data analysis results for an axial PWSCC at 0° intrados in specimen 1100-19 showing (a) EC (dashed line) and ERC (solid line) depth profiles and (b) output of the ERC tool using the Argonne data analysis software.

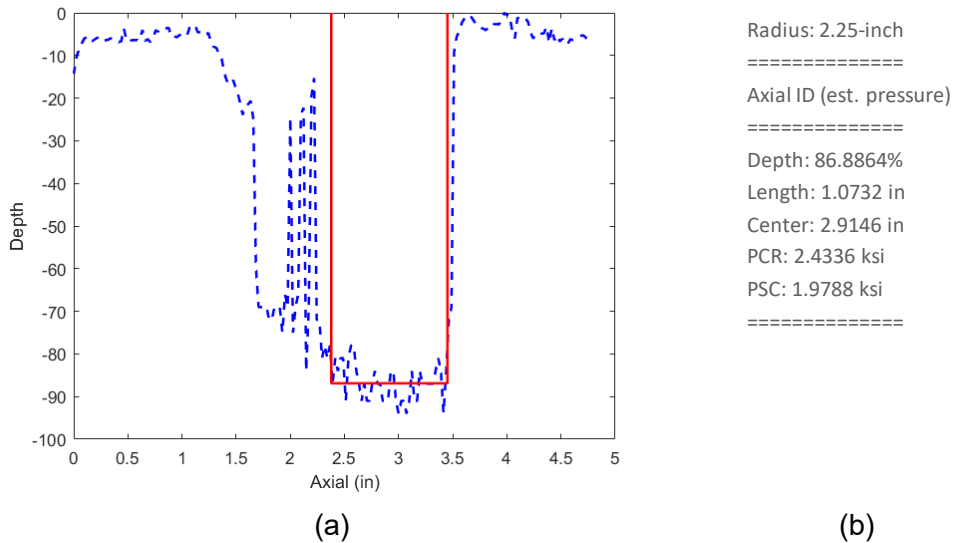


Figure F-8. Data analysis results for an axial PWSCC at 90° in specimen 1180-02 showing (a) EC (dashed line) and ERC (solid line) depth profiles and (b) output of the ERC tool using the Argonne data analysis software.

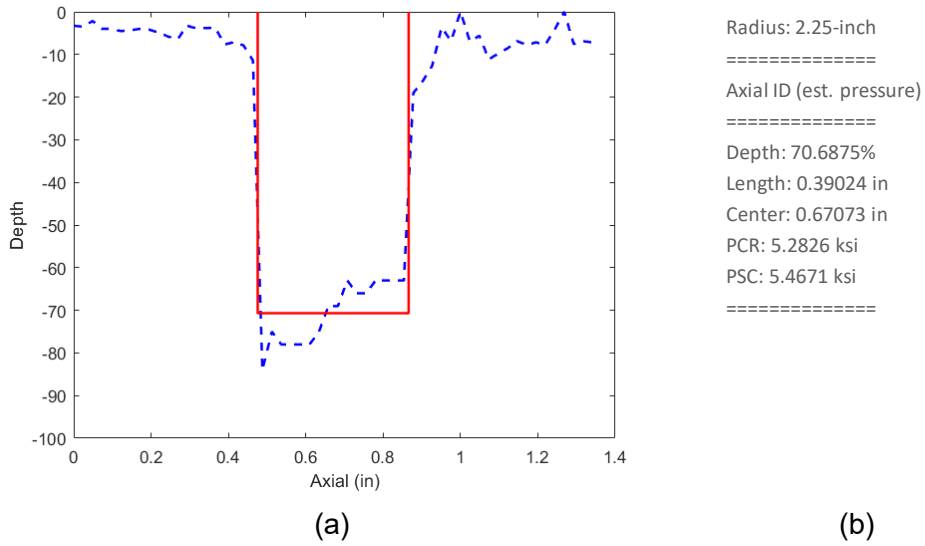


Figure F-9. Data analysis results for an axial PWSCC at 0° extrados in specimen 1180-11 showing (a) EC (dashed line) and ERC (solid line) depth profiles and (b) output of the ERC tool using the Argonne data analysis software.

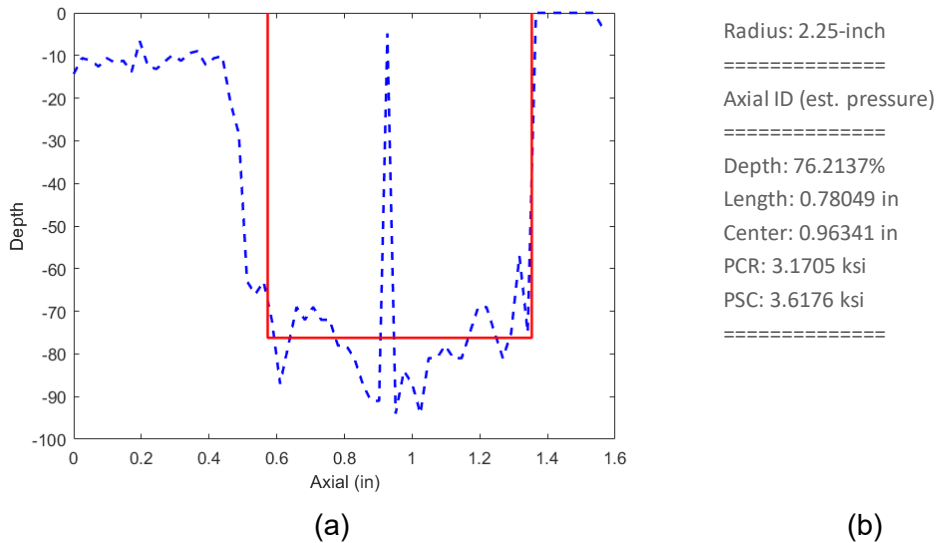


Figure F-10. Data analysis results for an axial PWSCC at 45° in specimen 1180-11 showing (a) EC (dashed line) and ERC (solid line) depth profiles and (b) output of the ERC tool using the Argonne data analysis software.

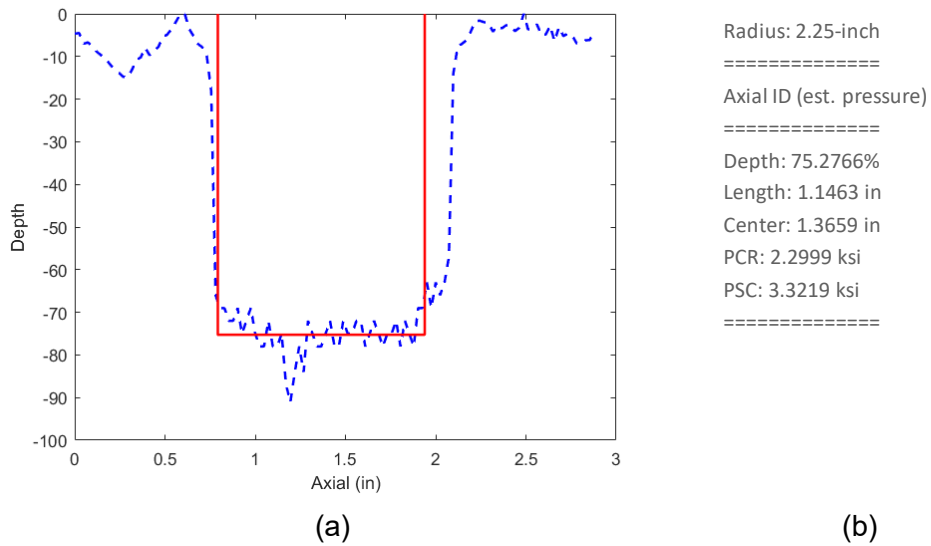


Figure F-11. Data analysis results for an axial PWSCC at 90° in specimen 1180-14 showing (a) EC (dashed line) and ERC (solid line) depth profiles and (b) output of the ERC tool using the Argonne data analysis software.

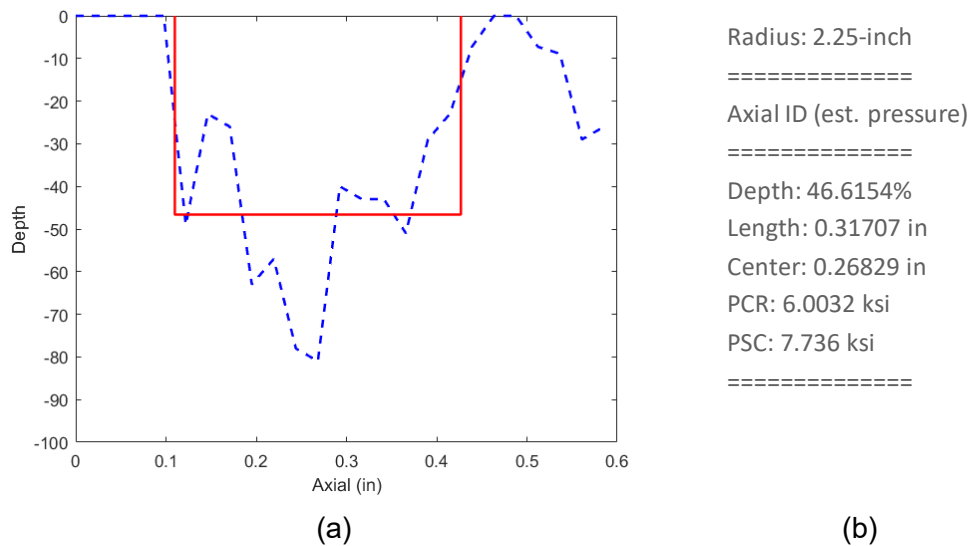


Figure F-12. Data analysis results for an axial PWSCC at 180° extrados in specimen 1180-15 showing (a) EC (dashed line) and ERC (solid line) depth profiles and (b) output of the ERC tool using the Argonne data analysis software.

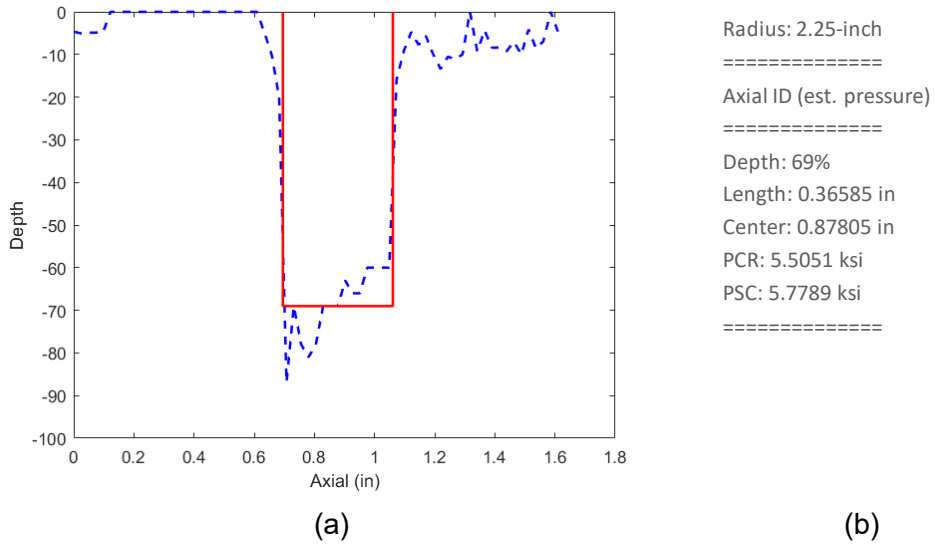


Figure F-13. Data analysis results for an axial PWSCC at 0° extrados in specimen 1180-16 showing (a) EC (dashed line) and ERC (solid line) depth profiles and (b) output of the ERC tool using the Argonne data analysis software.

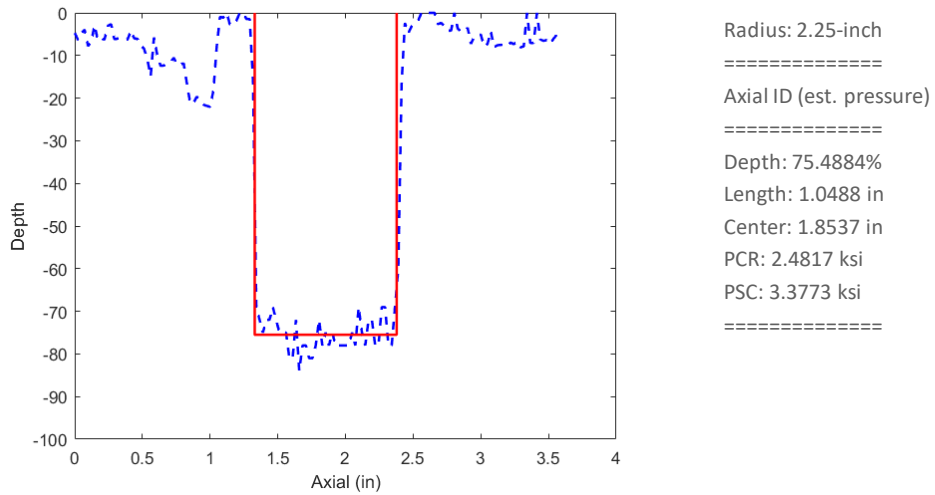


Figure F-14. Data analysis results for an axial PWSCC at 90° in specimen 1180-18 showing (a) EC (dashed line) and ERC (solid line) depth profiles and (b) output of the ERC tool using the Argonne data analysis software.

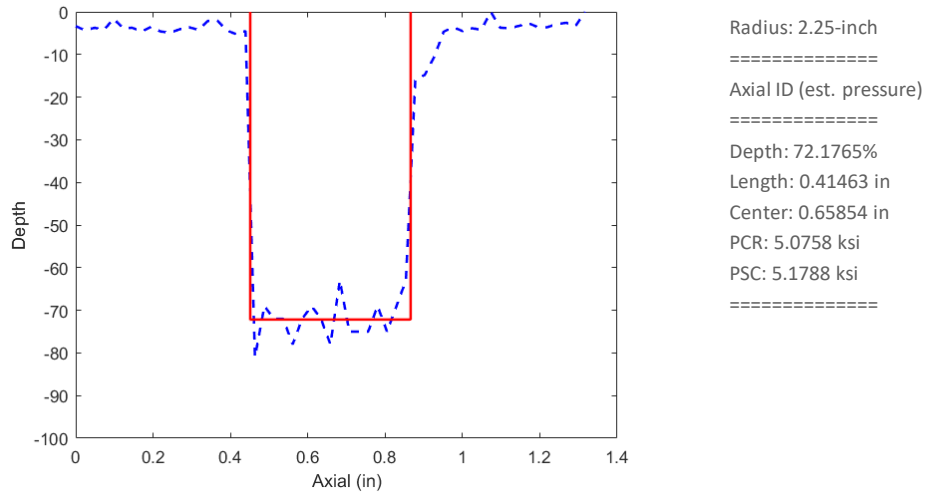


Figure F-15. Data analysis results for an axial PWSCC at 0° extrados in specimen 1180-20 showing (a) EC (dashed line) and ERC (solid line) depth profiles and (b) output of the ERC tool using the Argonne data analysis software.

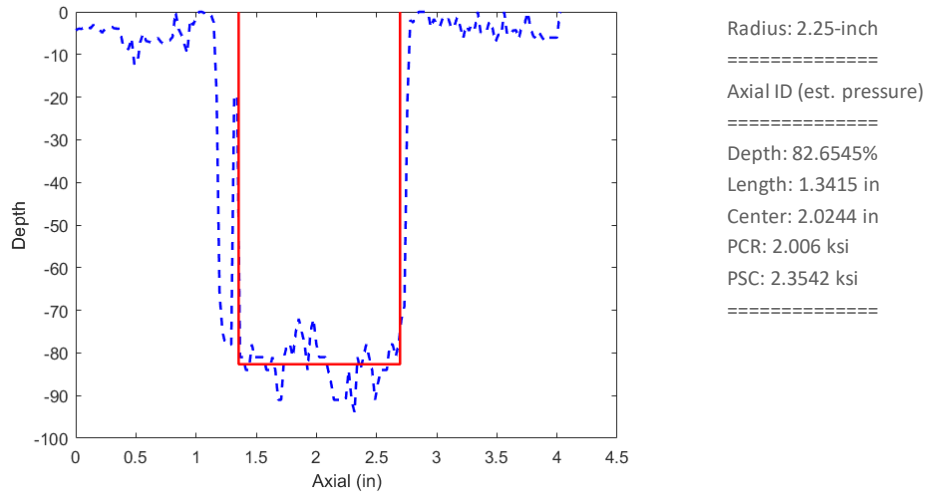


Figure F-16. Data analysis results for an axial PWSCC at 90° in specimen 1180-21 showing (a) EC (dashed line) and ERC (solid line) depth profiles and (b) output of the ERC tool using the Argonne data analysis software.

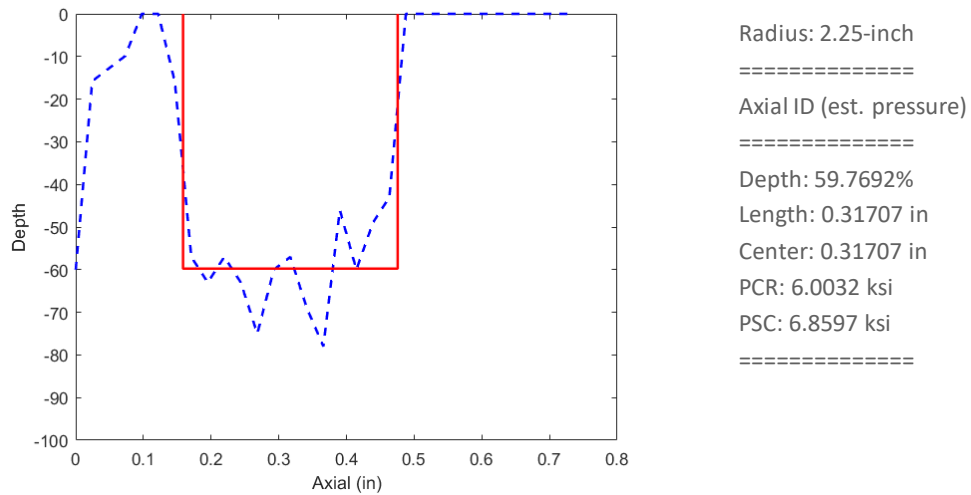


Figure F-17. Data analysis results for an axial PWSCC at 180° extrados in specimen 1180-22 showing (a) EC (dashed line) and ERC (solid line) depth profiles and (b) output of the ERC tool using the Argonne data analysis software.

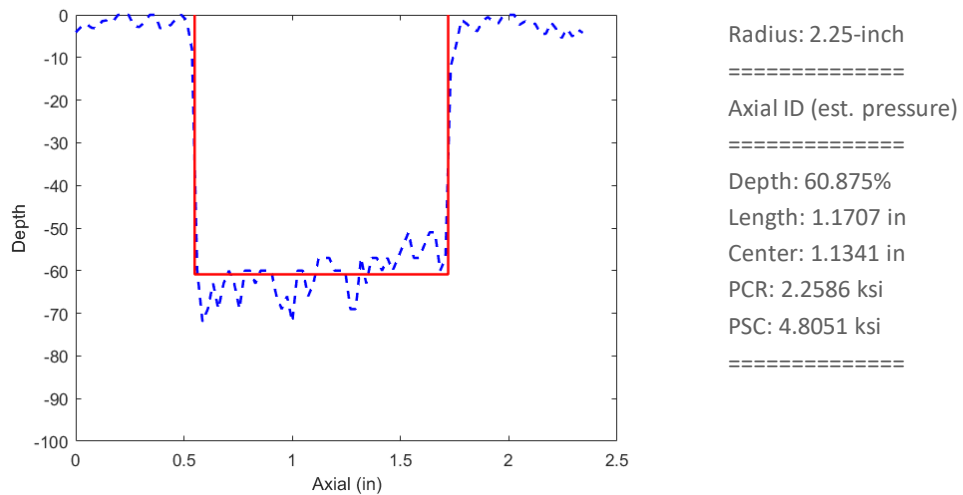


Figure F-18. Data analysis results for an axial PWSCC at 90° extrados in specimen 1180-22 showing (a) EC (dashed line) and ERC (solid line) depth profiles and (b) output of the ERC tool using the Argonne data analysis software.

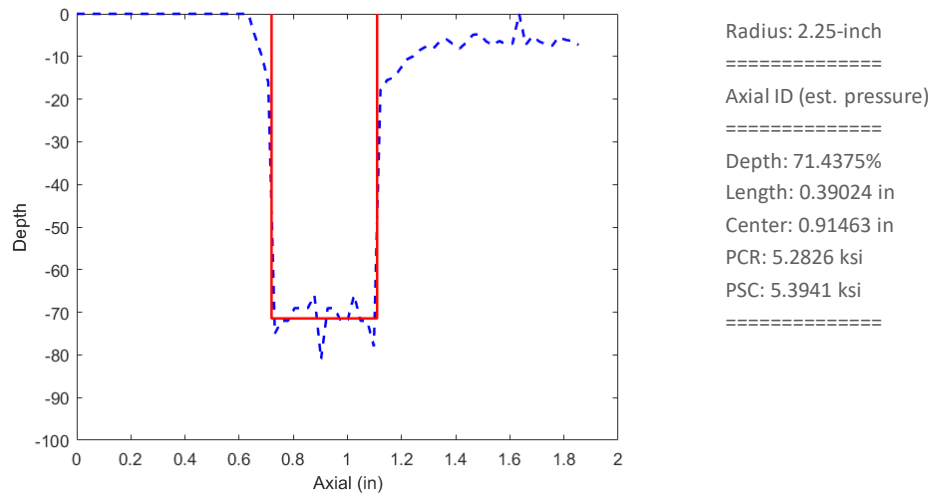


Figure F-19. Data analysis results for an axial PWSCC at 0° extrados in specimen 1180-23 showing (a) EC (dashed line) and ERC (solid line) depth profiles and (b) output of the ERC tool using the Argonne data analysis software.

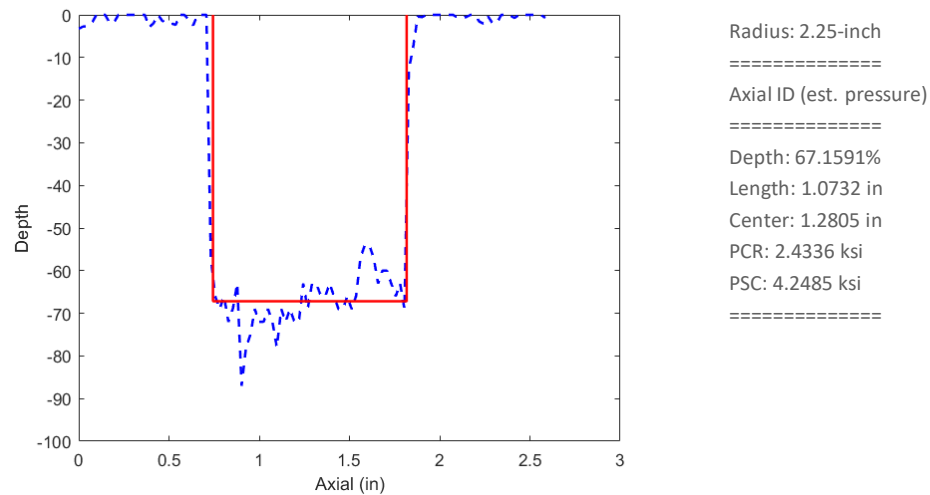


Figure F-20. Data analysis results for an axial PWSCC at 90° extrados in specimen 1180-23 showing (a) EC (dashed line) and ERC (solid line) depth profiles and (b) output of the ERC tool using the Argonne data analysis software.

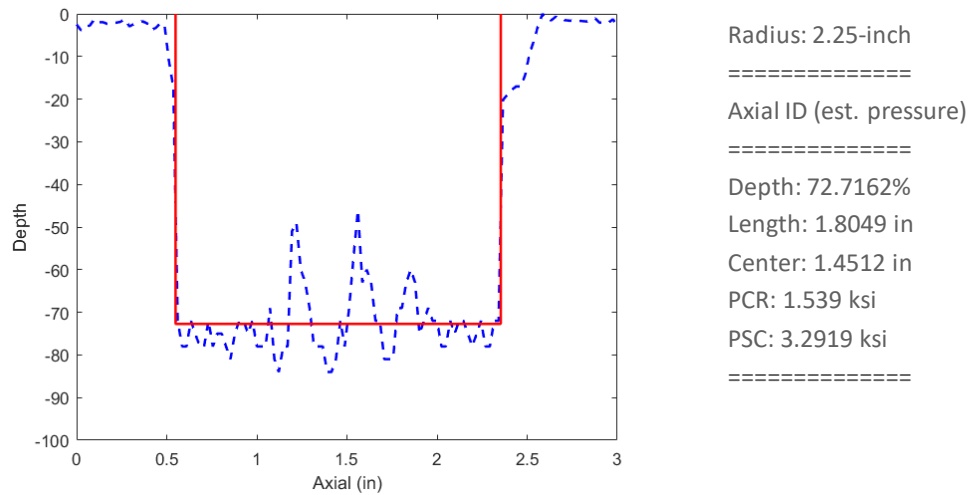


Figure F-21. Data analysis results for an axial PWSCC at 90° in specimen 890-01 showing (a) EC (dashed line) and ERC (solid line) depth profiles and (b) output of the ERC tool using the Argonne data analysis software.

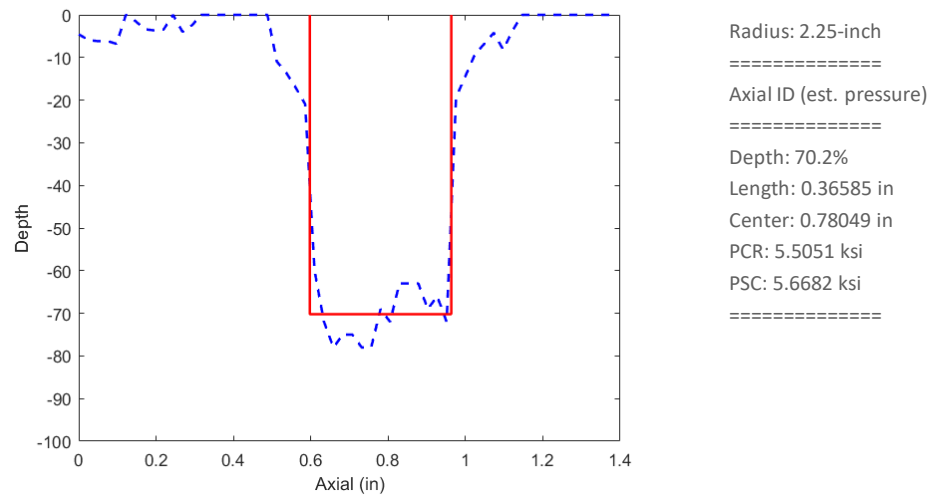


Figure F-22. Data analysis results for an axial PWSCC at 0° extrados in specimen 890-03 showing (a) EC (dashed line) and ERC (solid line) depth profiles and (b) output of the ERC tool using the Argonne data analysis software.

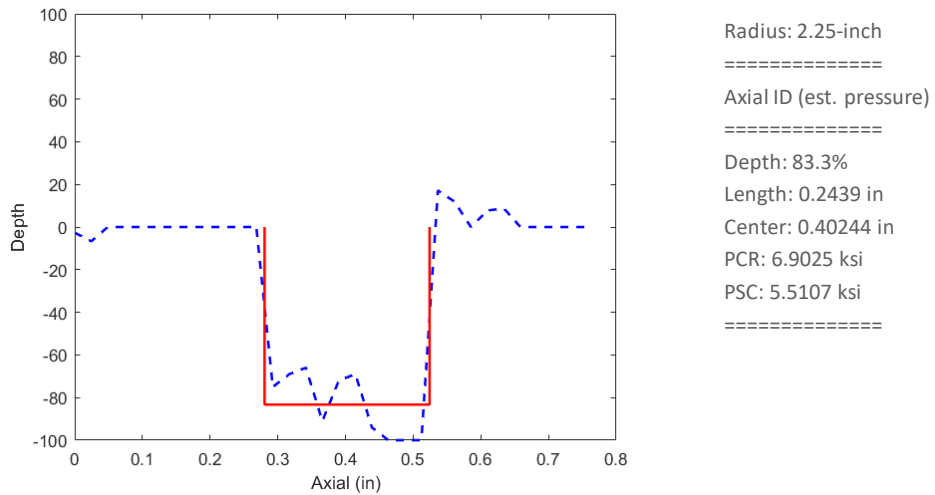


Figure F-23. Data analysis results for an axial PWSCC at 180° flank in specimen 890-04 showing (a) EC (dashed line) and ERC (solid line) depth profiles and (b) output of the ERC tool using the Argonne data analysis software.

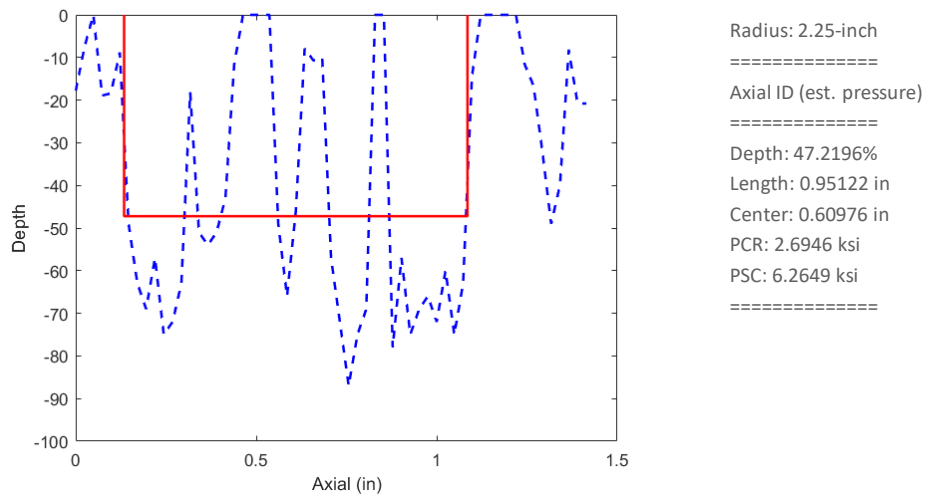


Figure F-24. Data analysis results for an axial PWSCC at 90° in specimen 890-04 showing (a) EC (dashed line) and ERC (solid line) depth profiles and (b) output of the ERC tool using the Argonne data analysis software.

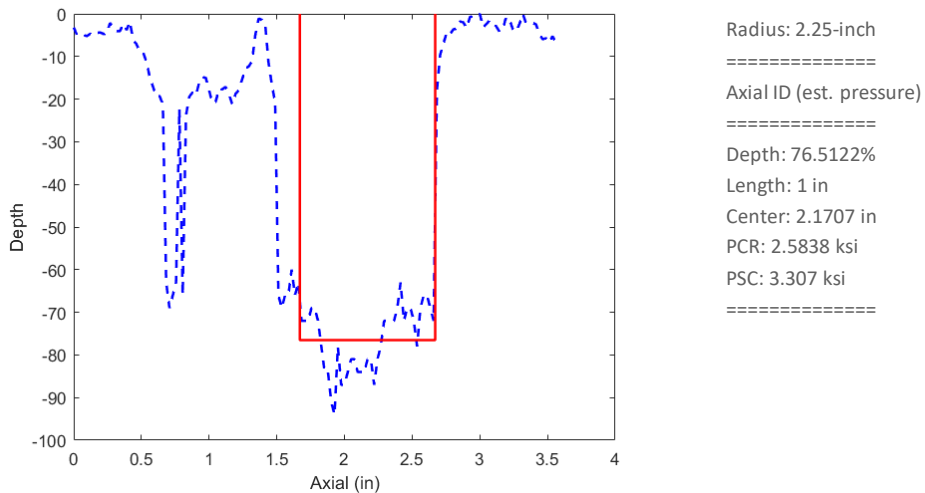


Figure F-25. Data analysis results for an axial PWSCC in specimen 890-07 showing (a) EC (dashed line) and ERC (solid line) depth profiles and (b) output of the ERC tool using the Argonne data analysis software.

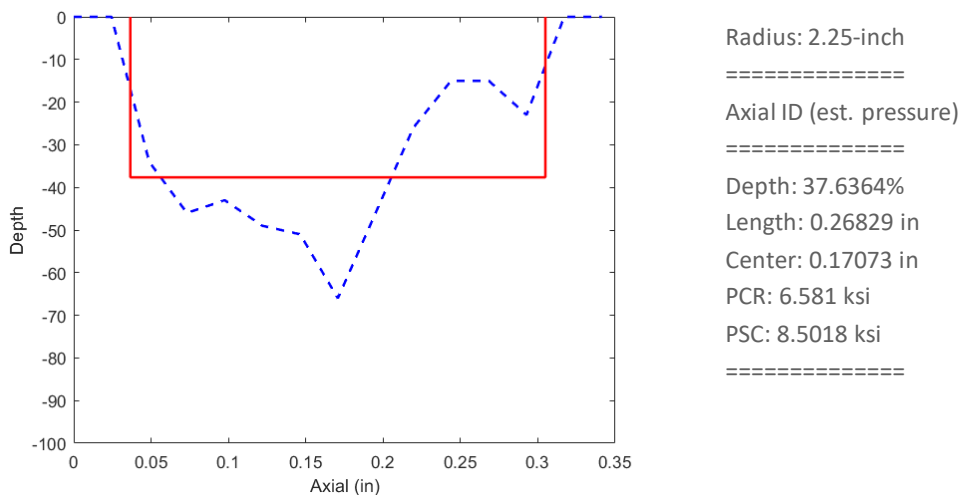


Figure F-26. Data analysis results for an axial PWSCC at 180° (flaw #3) in specimen 890-08 showing (a) EC (dashed line) and ERC (solid line) depth profiles and (b) output of the ERC tool using the Argonne data analysis software.

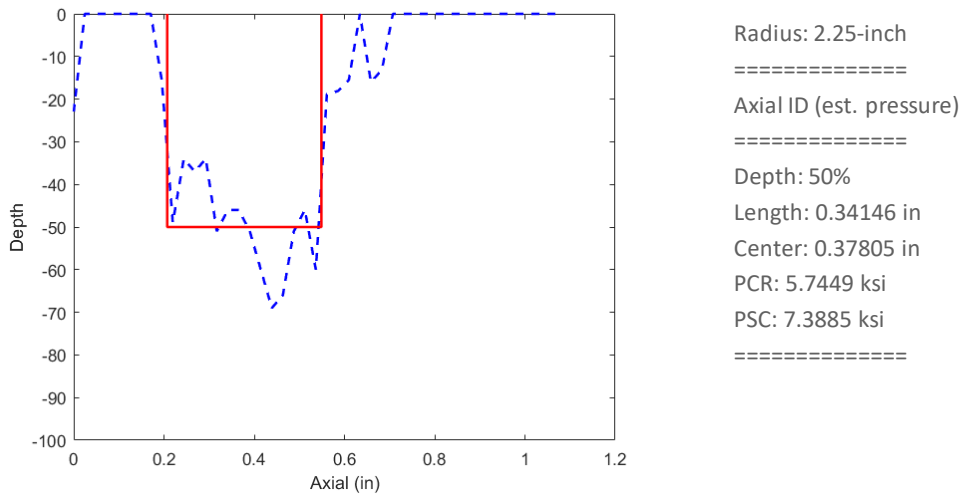


Figure F-27. Data analysis results for an axial PWSCC at 180° (B1) in specimen 890-08 showing (a) EC (dashed line) and ERC (solid line) depth profiles and (b) output of the ERC tool using the Argonne data analysis software.

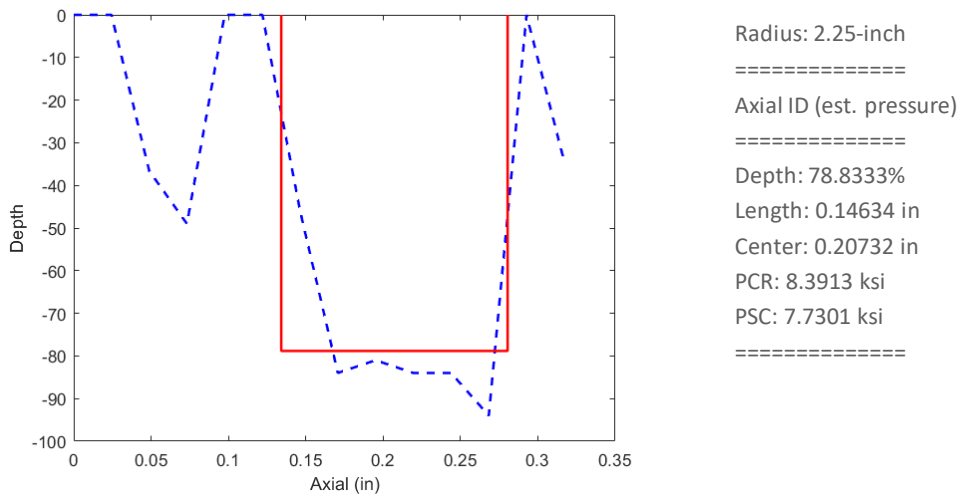


Figure F-28. Data analysis results for an axial PWSCC at 180° in specimen 890-08 showing (a) EC (dashed line) and ERC (solid line) depth profiles and (b) output of the ERC tool using the Argonne data analysis software.

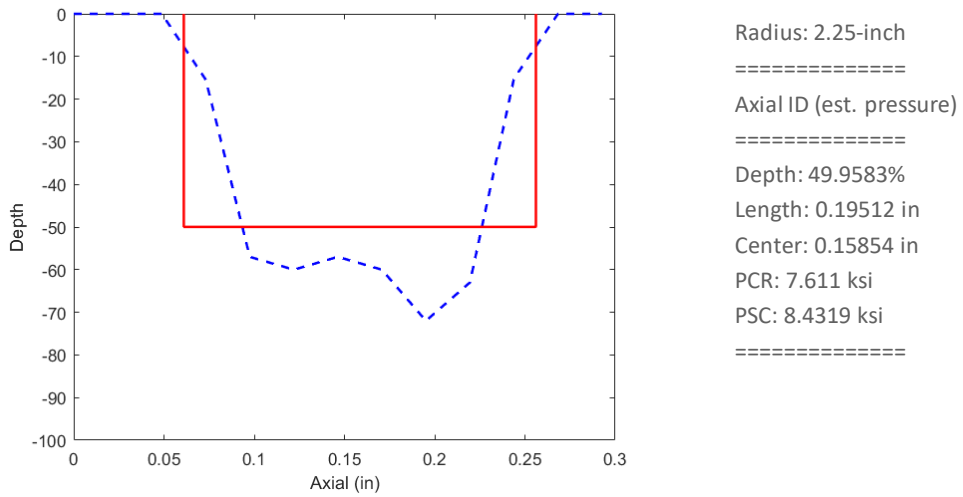


Figure F-29. Data analysis results for an axial PWSCC at 90° in specimen 890-08 showing (a) EC (dashed line) and ERC (solid line) depth profiles and (b) output of the ERC tool using the Argonne data analysis software.

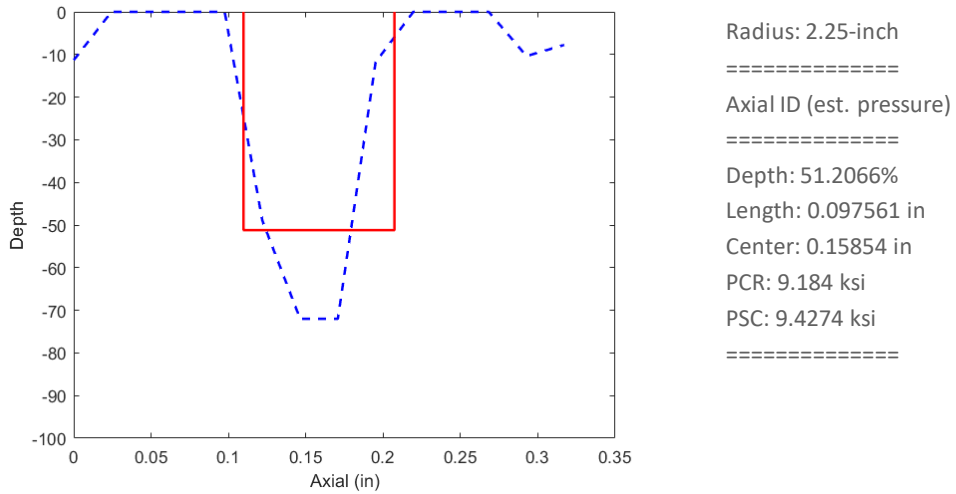


Figure F-30. Data analysis results for an axial PWSCC at 180° in specimen 890-15 showing (a) EC (dashed line) and ERC (solid line) depth profiles and (b) output of the ERC tool using the Argonne data analysis software.

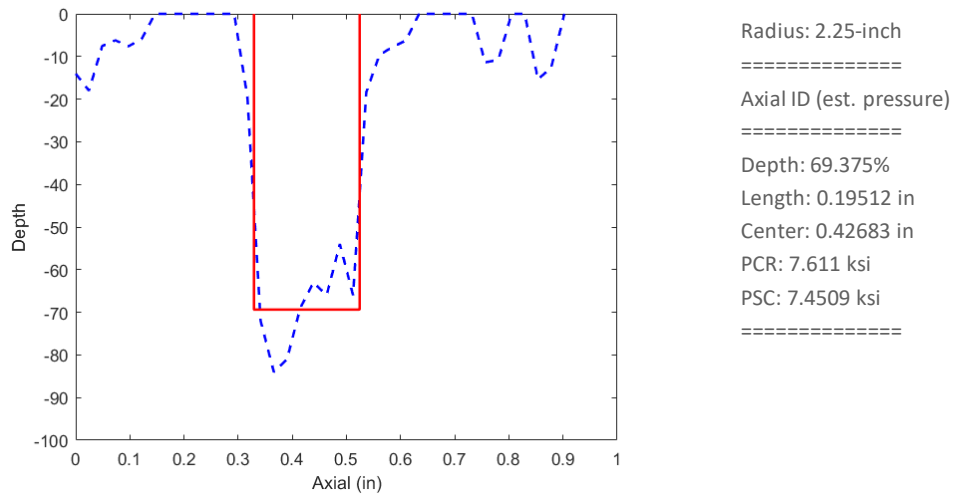


Figure F-31. Data analysis results for an axial PWSCC at 0° extrados in specimen 890-16 showing (a) EC (dashed line) and ERC (solid line) depth profiles and (b) output of the ERC tool using the Argonne data analysis software.

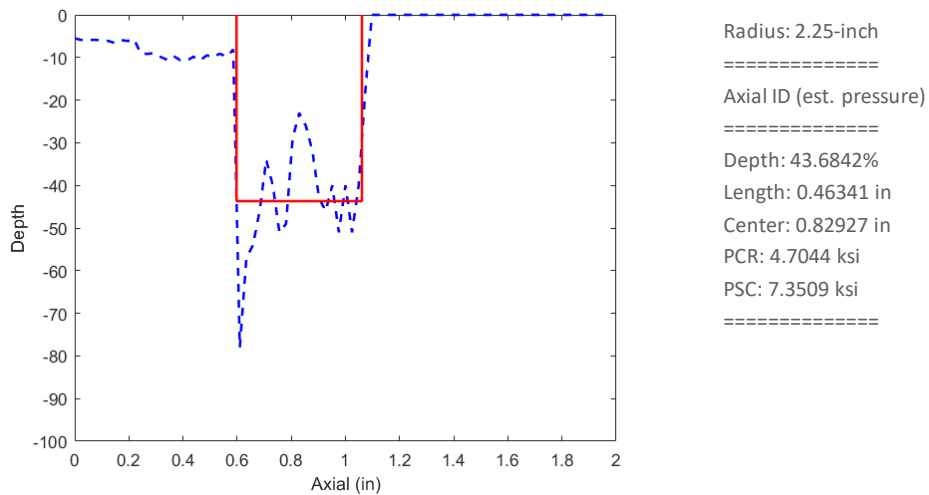


Figure F-32. Data analysis results for an axial PWSCC at 0° intrados in specimen 920-08 showing (a) EC (dashed line) and ERC (solid line) depth profiles and (b) output of the ERC tool using the Argonne data analysis software.

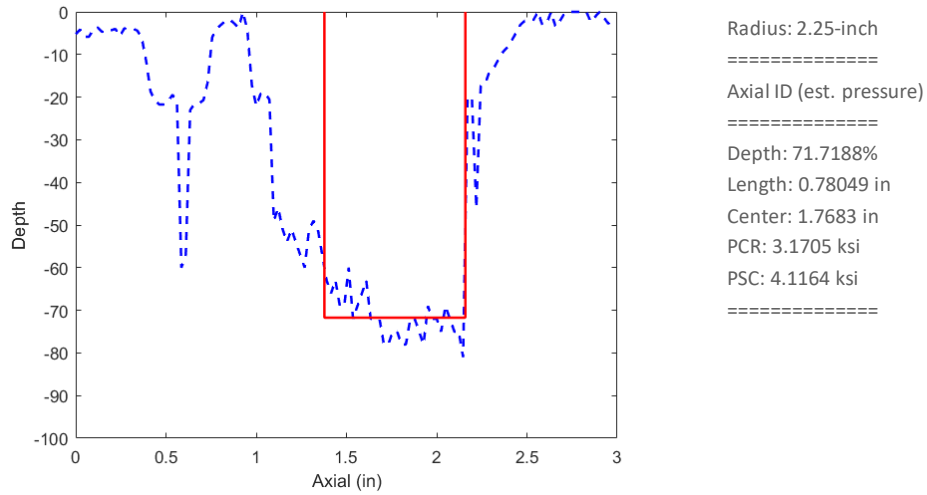


Figure F-33. Data analysis results for an axial PWSCC at 90° extrados in specimen 920-08 showing (a) EC (dashed line) and ERC (solid line) depth profiles and (b) output of the ERC tool using the Argonne data analysis software.

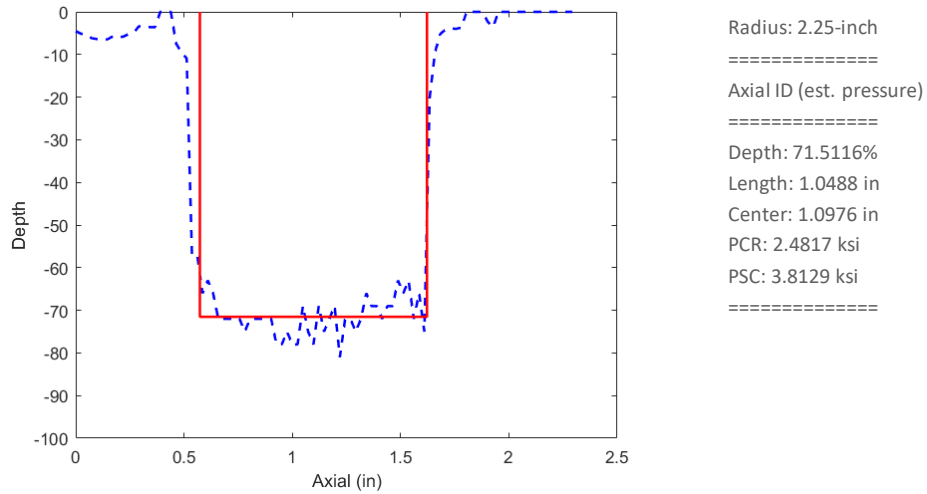


Figure F-34. Data analysis results for an axial PWSCC in specimen 920-10 showing (a) EC (dashed line) and ERC (solid line) depth profiles and (b) output of the ERC tool using the Argonne data analysis software.

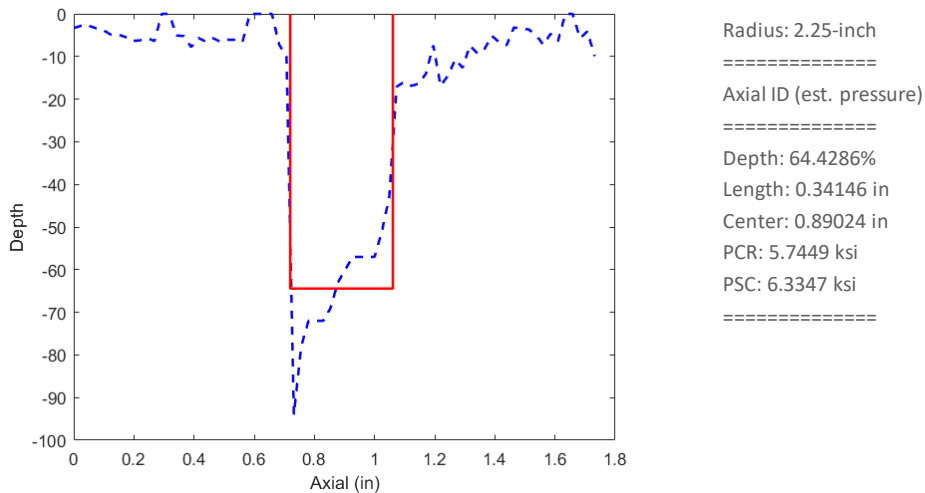


Figure F-35. Data analysis results for an axial PWSCC at 0° extrados in specimen 920-12 showing (a) EC (dashed line) and ERC (solid line) depth profiles and (b) output of the ERC tool using the Argonne data analysis software.

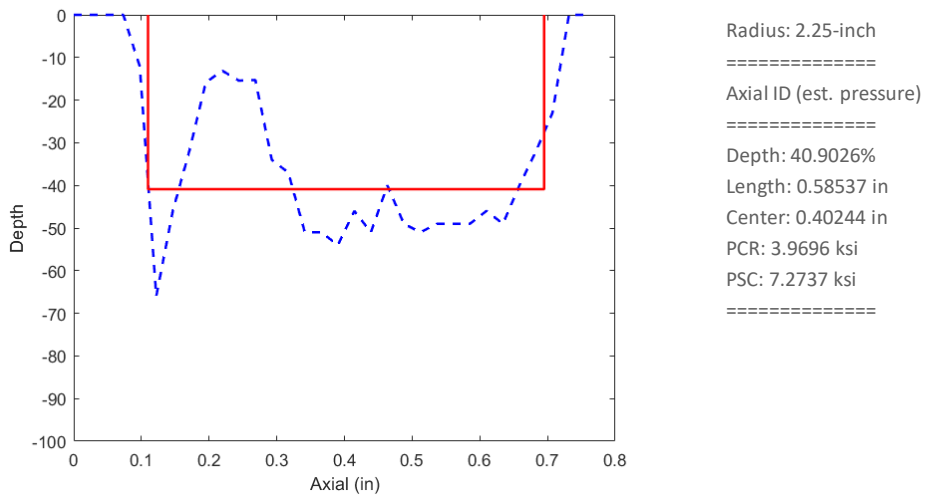


Figure F-36. Data analysis results for an axial PWSCC at 80° extrados in specimen 920-12 showing (a) EC (dashed line) and ERC (solid line) depth profiles and (b) output of the ERC tool using the Argonne data analysis software.

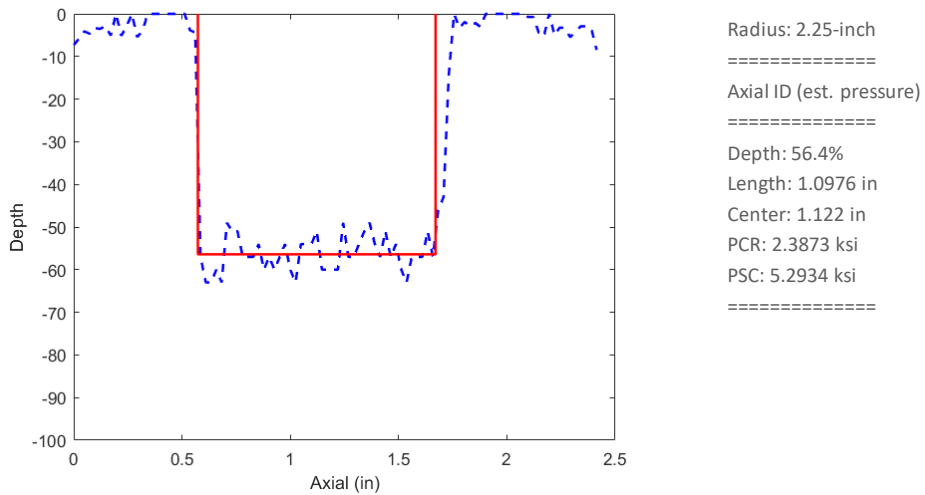


Figure F-37. Data analysis results for an axial PWSCC at 90° extrados in specimen 920-12 showing (a) EC (dashed line) and ERC (solid line) depth profiles and (b) output of the ERC tool using the Argonne data analysis software.

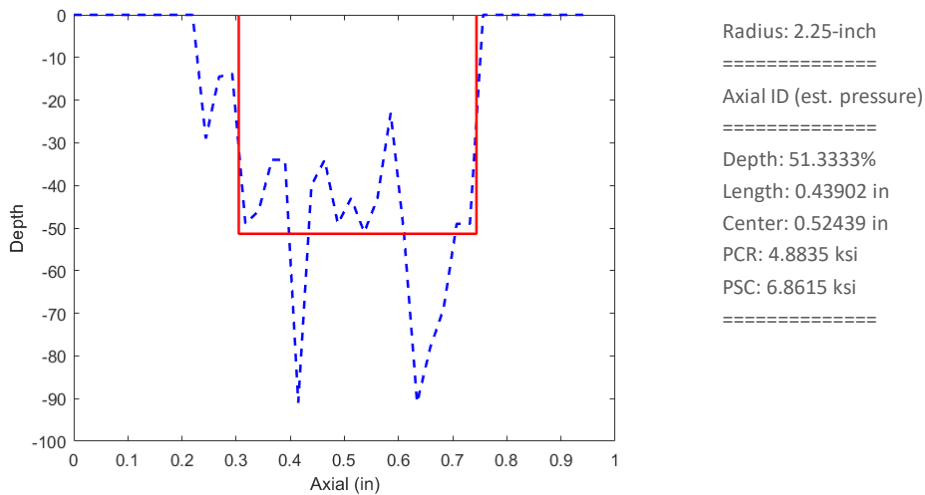


Figure F-38. Data analysis results for an axial PWSCC at 180° extrados in specimen 920-15 showing (a) EC (dashed line) and ERC (solid line) depth profiles and (b) output of the ERC tool using the Argonne data analysis software.

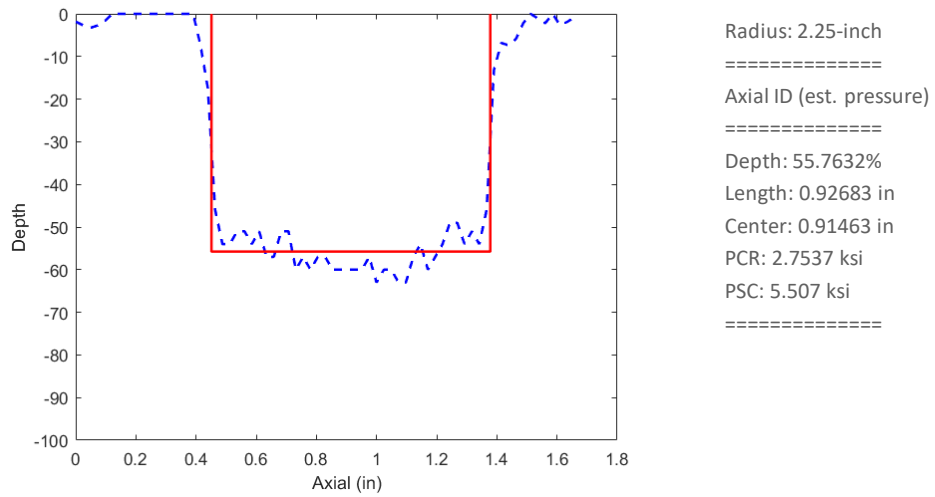


Figure F-39. Data analysis results for an axial PWSCC at 90° extrados in specimen 920-15 showing (a) EC (dashed line) and ERC (solid line) depth profiles and (b) output of the ERC tool using the Argonne data analysis software.

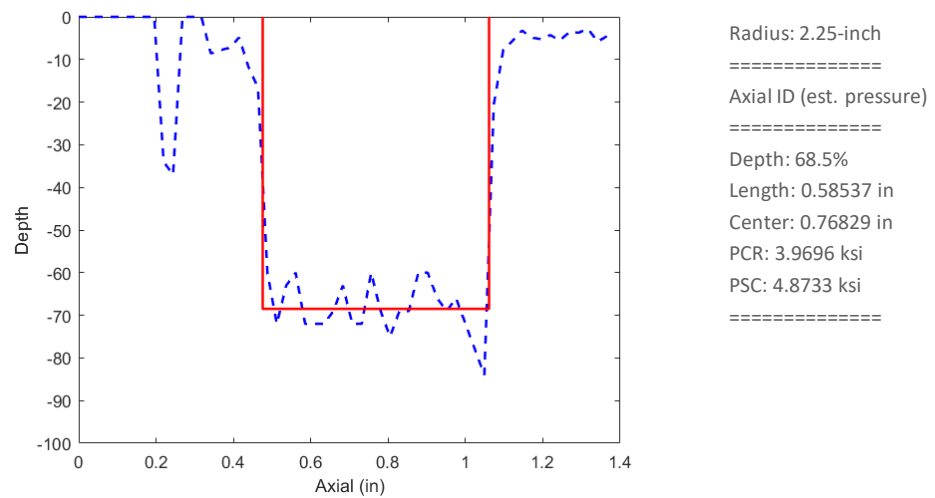
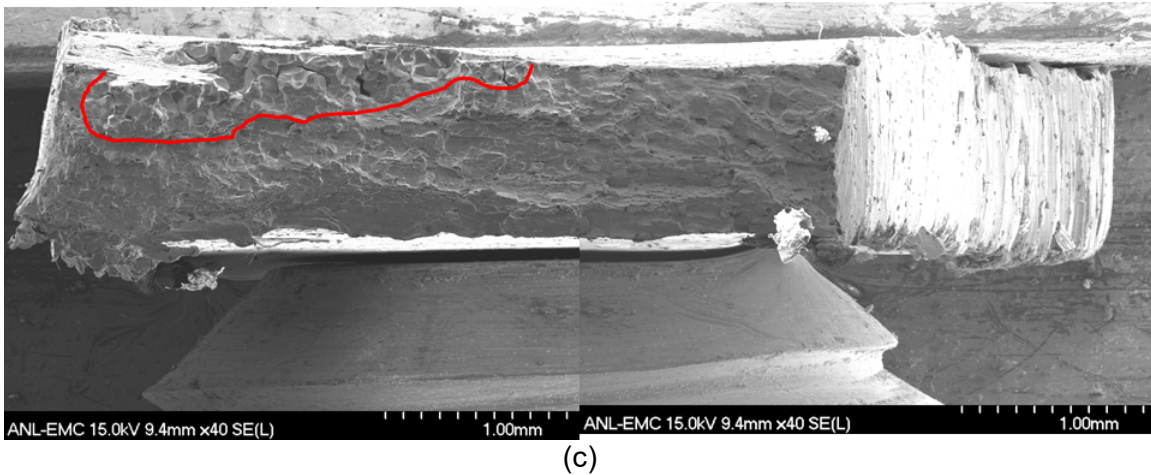
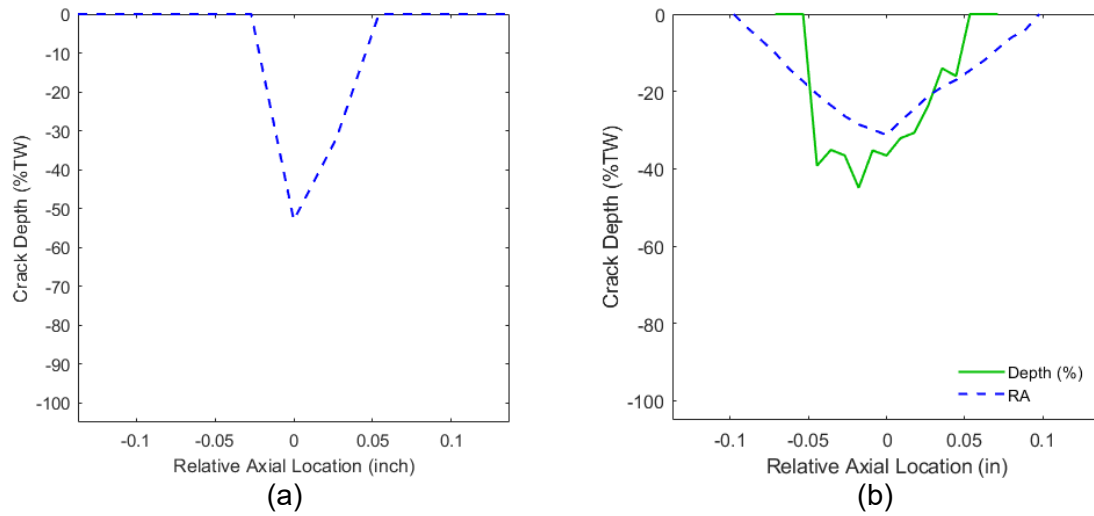


Figure F-40. Data analysis results for an axial PWSCC at 45° in specimen 920-15 showing (a) EC (dashed line) and ERC (solid line) depth profiles and (b) output of the ERC tool using the Argonne data analysis software.

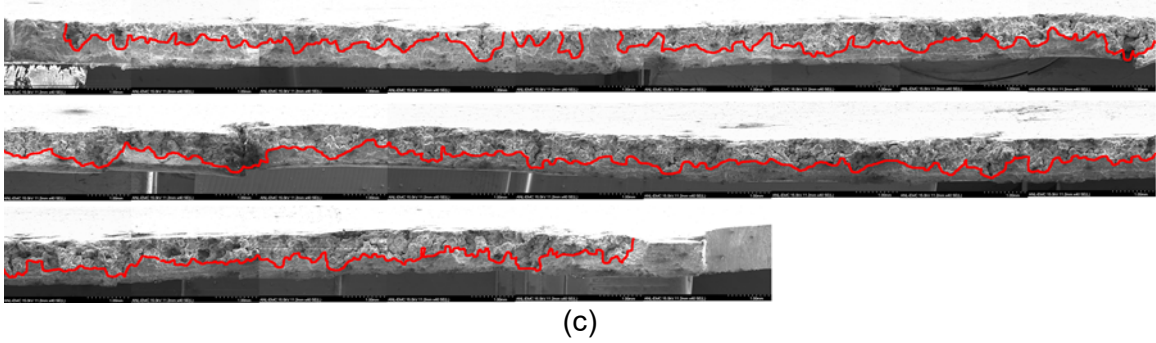
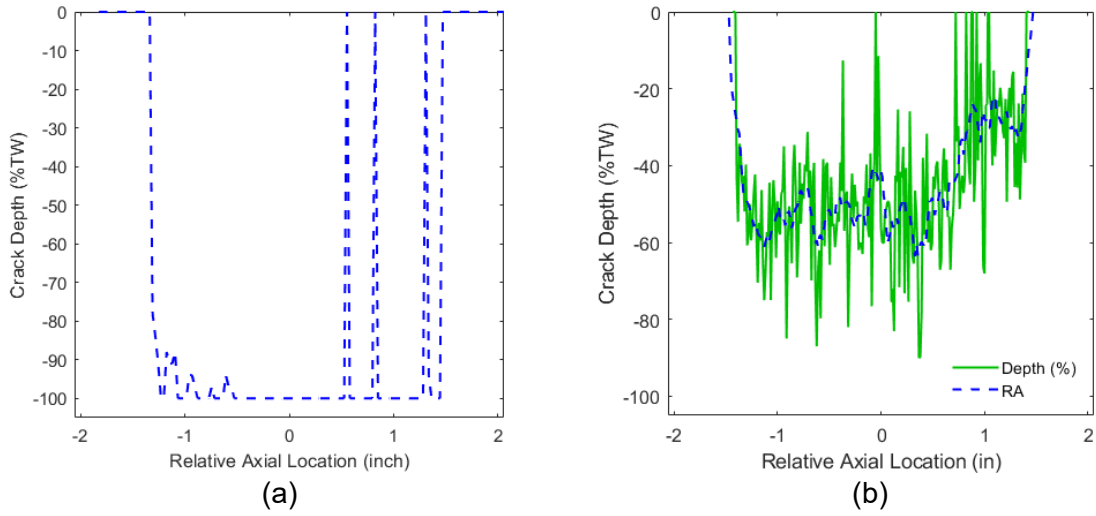
APPENDIX G – NDE AND DE DEPTH PROFILES FOR PWSCC IN 152-MM-RADIUS U-BEND SPECIMENS

Depth profiles for a subset of primary water stress corrosion cracks (PWSCCs) in 152-mm-radius U-bend tube specimens on which destructive examination (DE) was performed are presented in Figures G-1 through G-17. The eddy current (EC) sizing results are based on the analysis of rotating +Pt probe data at 300 kHz. The nondestructive examination (NDE) depth estimates, based on EC signal phase angle information, were obtained using the computer-aided data analysis tool implemented at Argonne National Laboratory (Argonne). Also shown in each figure is the corresponding DE depth profile, obtained by fractography, and the scanning electron microscopy (SEM) image of the crack surface. The depth profiles, in %TW, are plotted as negative values, which by convention is used to display inside diameter (ID)-originated flaws (i.e., outside diameter [OD]-originated flaws are plotted as positive values). The DE depth profile is plotted with and without the application of a running average (RA) filter. An outline of the crack surface is drawn on each SEM image.



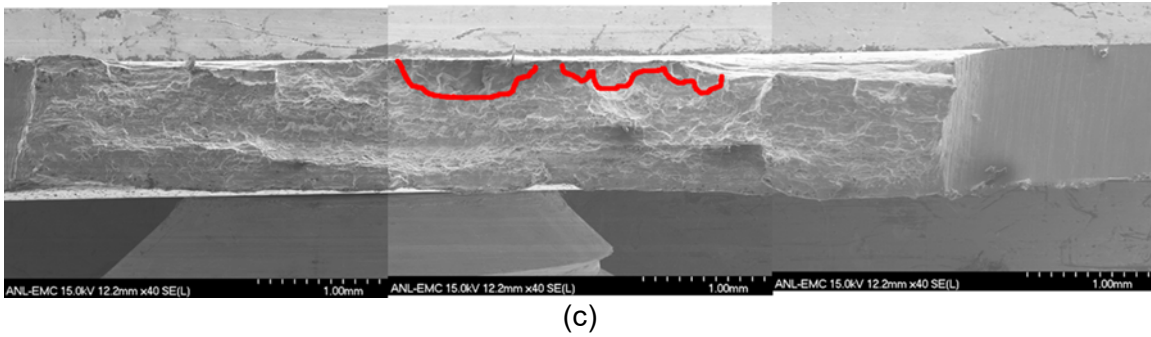
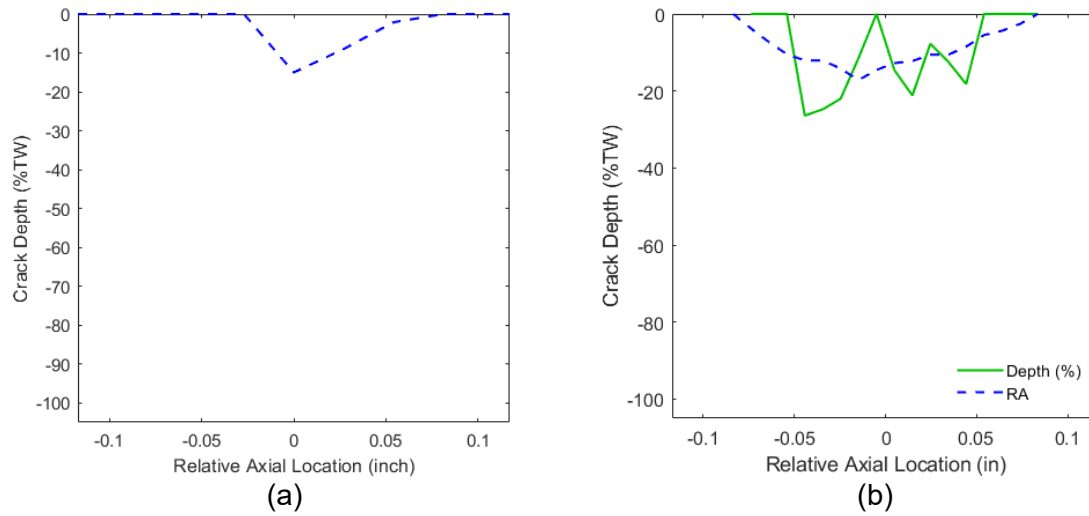
Note: This axial PWSCC was found at location F, between flank and extrados, of U-bend specimen 07-02.

Figure G-1. NDE and DE results for a PWSCC at location F in specimen 07-02. Shown here are (a) the estimated EC depth profile based on +Pt data at 300 kHz, (b) DE depth profile with and without RA filter, and (c) SEM image of crack surface.



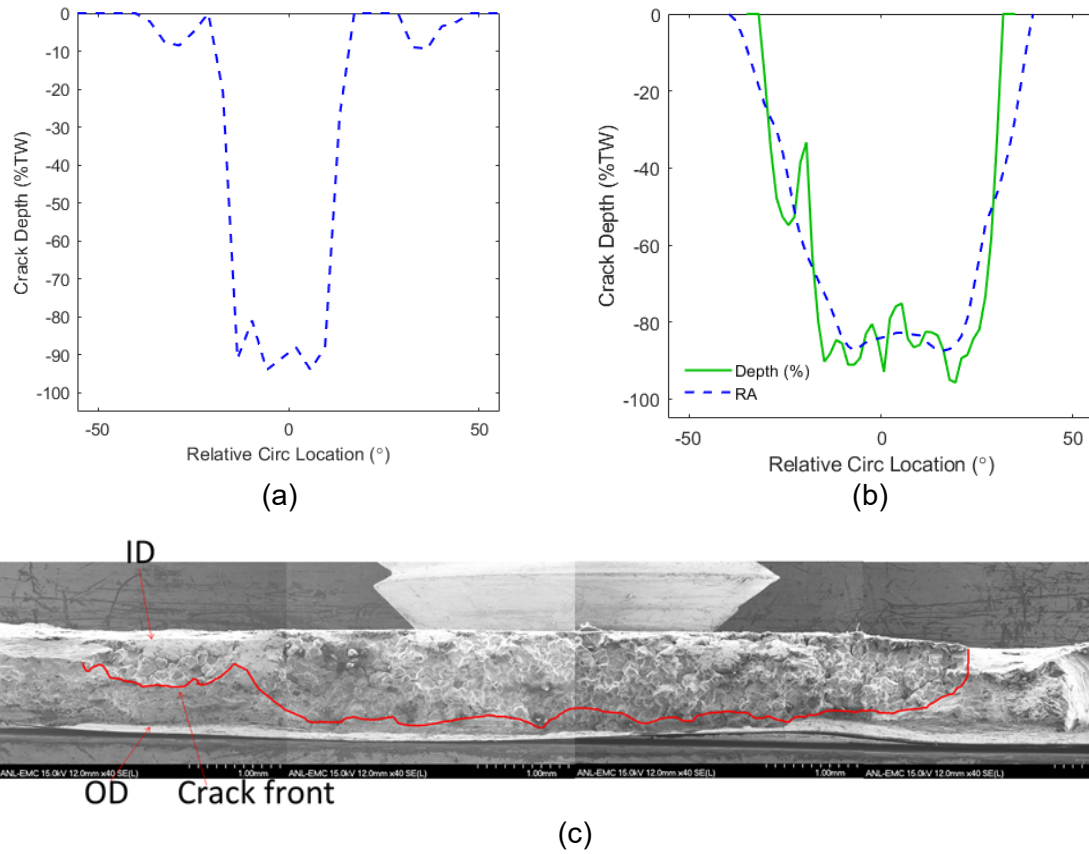
Note: This PWSCC was found at location B, between flank and extrados, of U-bend specimen 07-02. Video examination indicated the presence of an axially extended series of closely spaced short circumferential cracks.

Figure G-2. NDE and DE results for the PWSCC at location B in specimen 07-02. Shown here are (a) the estimated EC depth profile based on +Pt data at 300 kHz, (b) DE depth profile with and without RA filter, and (c) SEM image of crack surface.



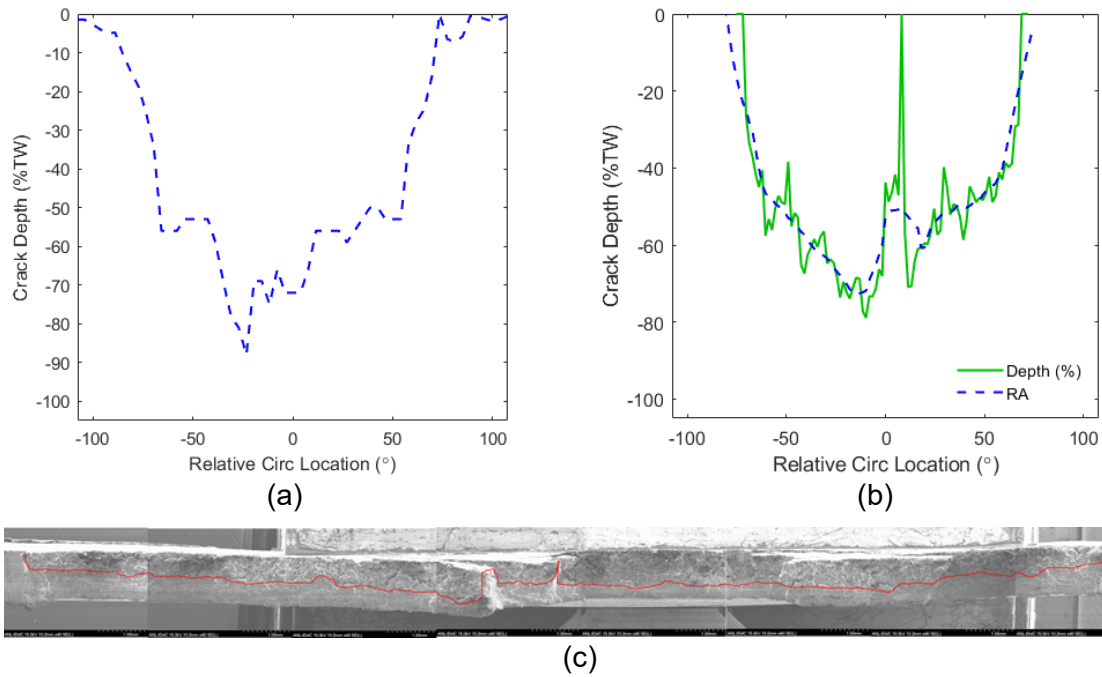
Note: This axial PWSCC was found at location E, between flank and extrados, of U-bend specimen 07-03.

Figure G-3. NDE and DE results for a PWSCC at location E in specimen 07-03. Shown here are (a) the estimated EC depth profile based on +Pt data at 300 kHz, (b) DE depth profile with and without RA filter, and (c) SEM image of crack surface.



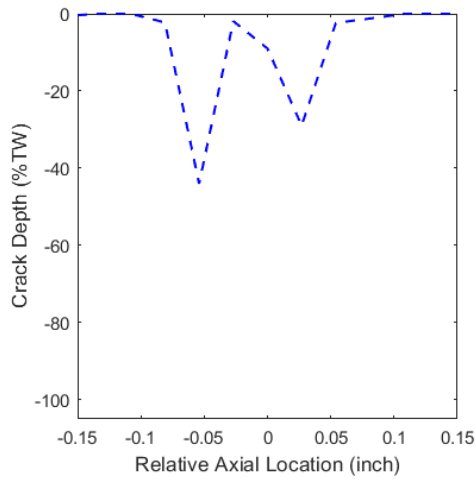
Note: This circumferential PWSCC was found at location F, between flank and extrados, of U-bend specimen 07-03.

Figure G-4. NDE and DE results for a PWSCC at location F in specimen 07-03. Shown here are (a) the estimated EC depth profile based on +Pt data at 300 kHz, (b) DE depth profile with and without RA filter, and (c) SEM image of crack surface.

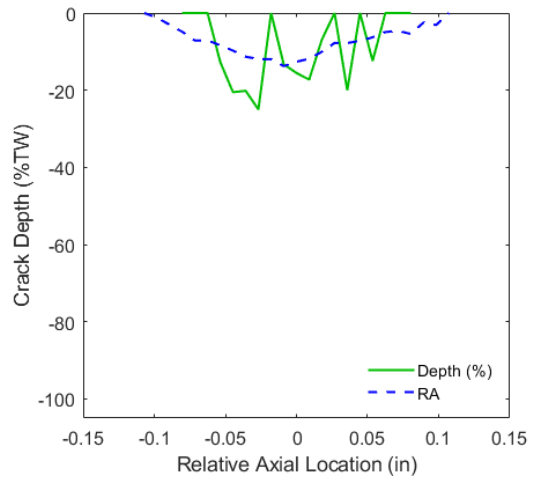


Note: This circumferential PWSCC was found at location E, intrados region, of U-bend specimen 14-01.

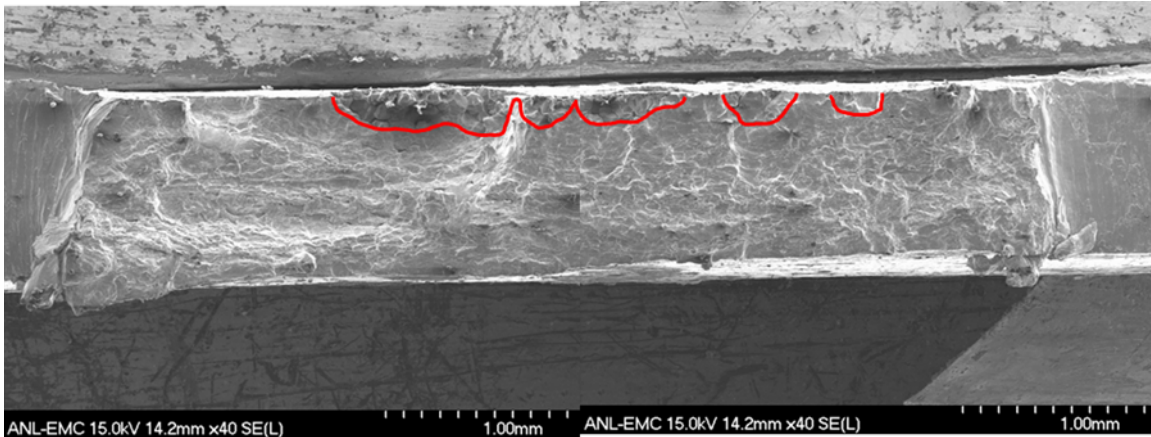
Figure G-5. NDE and DE results for a PWSCC at location E in specimen 14-01. Shown here are (a) the estimated EC depth profile based on +Pt data at 300 kHz, (b) DE depth profile with and without RA filter, and (c) SEM image of crack surface.



(a)



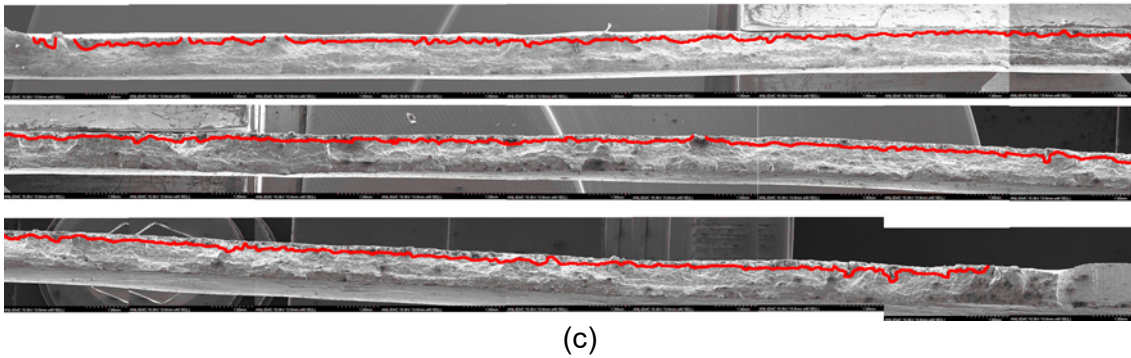
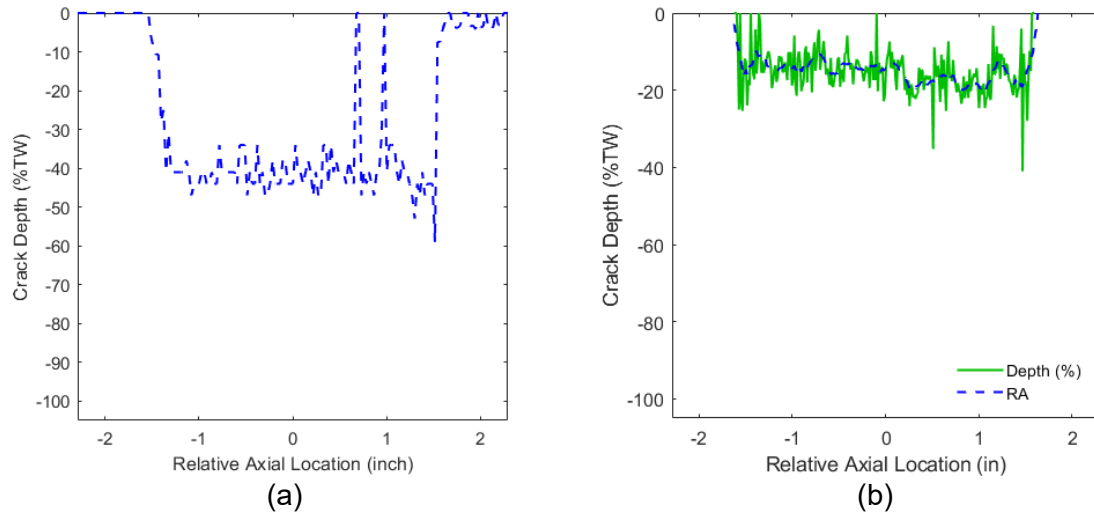
(b)



(c)

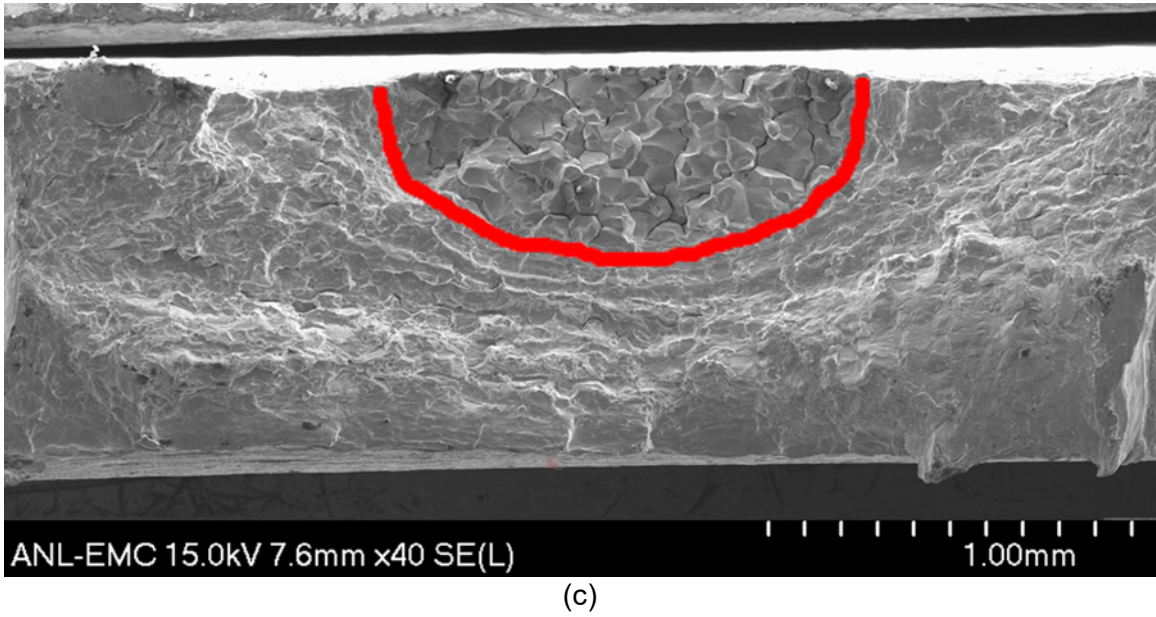
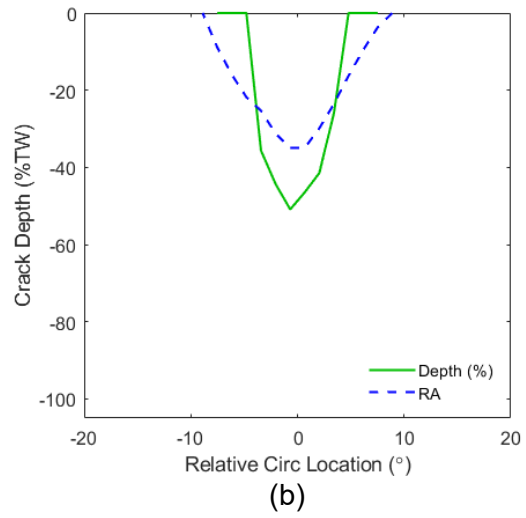
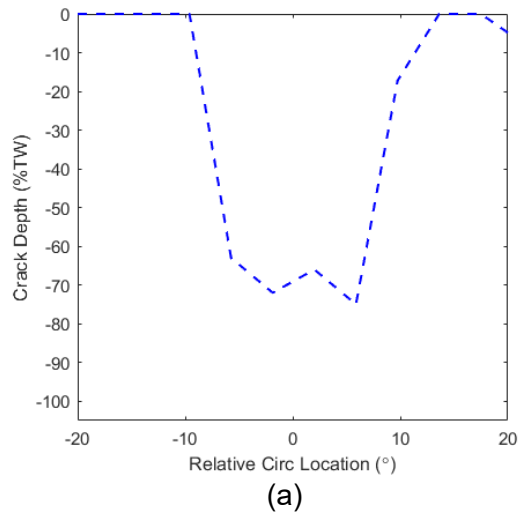
Note: This axial PWSCC was found at location G, between flank and intrados, of U-bend specimen 14-01.

Figure G-6. NDE and DE results for a PWSCC at location G in specimen 14-01. Shown here are (a) the estimated EC depth profile based on +Pt data at 300 kHz, (b) DE depth profile with and without RA filter, and (c) SEM image of crack surface.



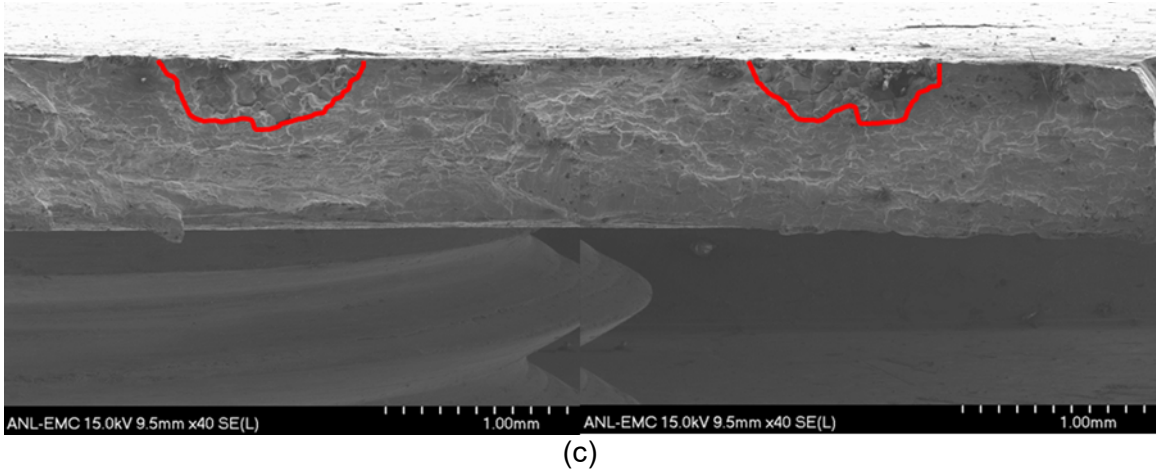
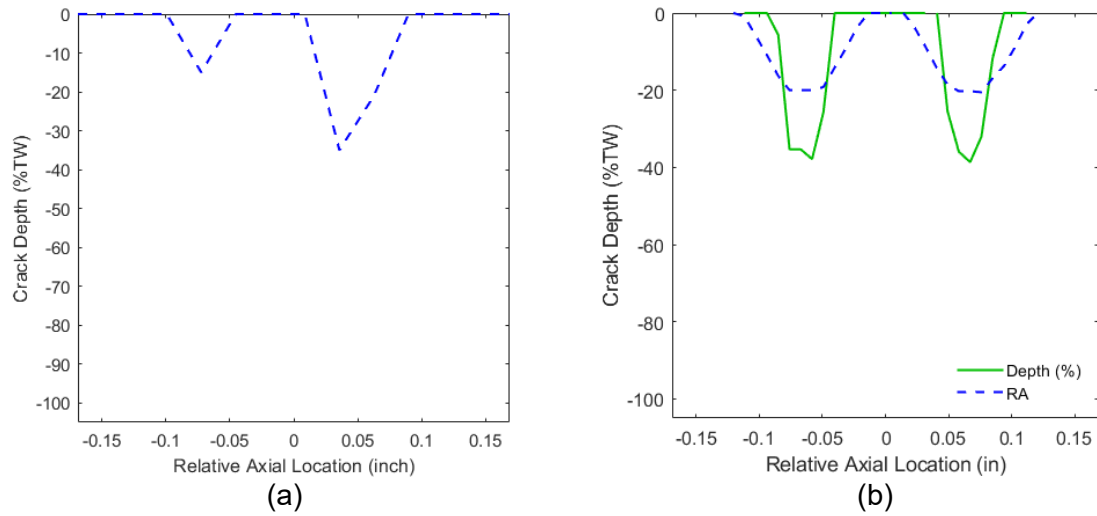
Note: This PWSCC was found at location B, between flank and extrados, of U-bend specimen 14-01. Video examination indicated the presence of an axially extended series of closely spaced short circumferential cracks.

Figure G-7. NDE and DE results for a PWSCC at location B in specimen 14-01. Shown here are (a) the estimated EC depth profile based on +Pt data at 300 kHz, (b) DE depth profile with and without RA filter, and (c) SEM image of crack surface.



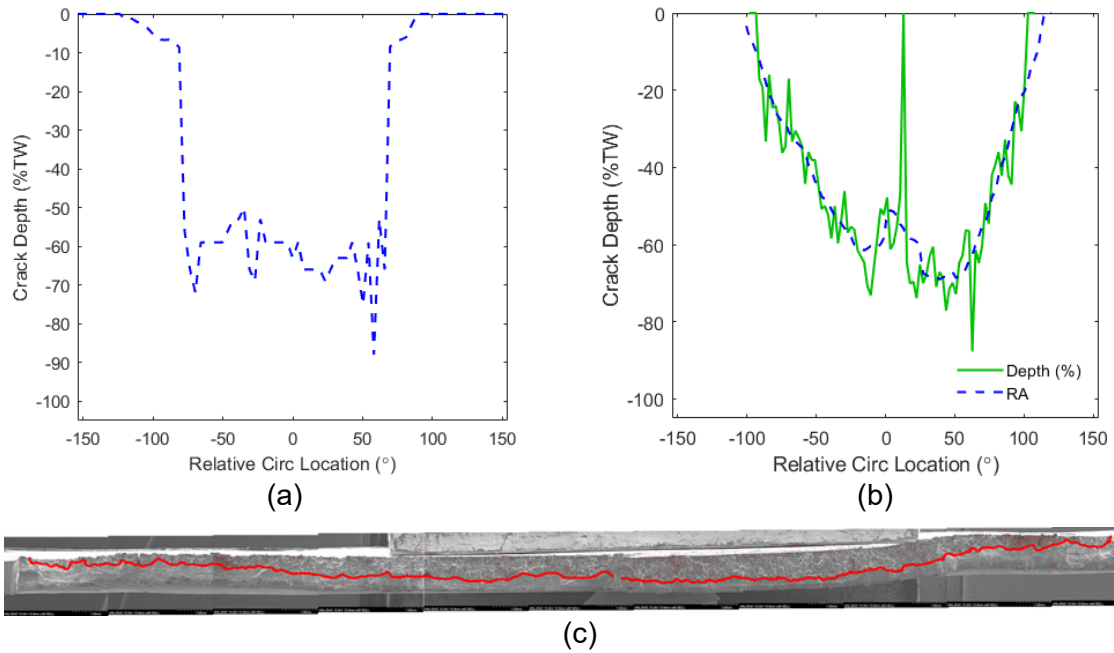
Note: This circumferential PWSCC was found at location F, between flank and extrados, of U-bend specimen 15-02.

Figure G-8. NDE and DE results for a PWSCC at location F in specimen 15-02. Shown here are (a) the estimated EC depth profile based on +Pt data at 300 kHz, (b) DE depth profile with and without RA filter, and (c) SEM image of crack surface.



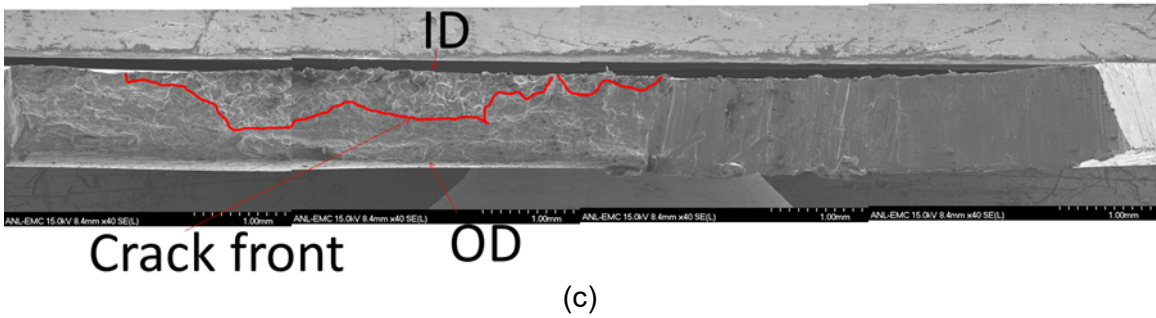
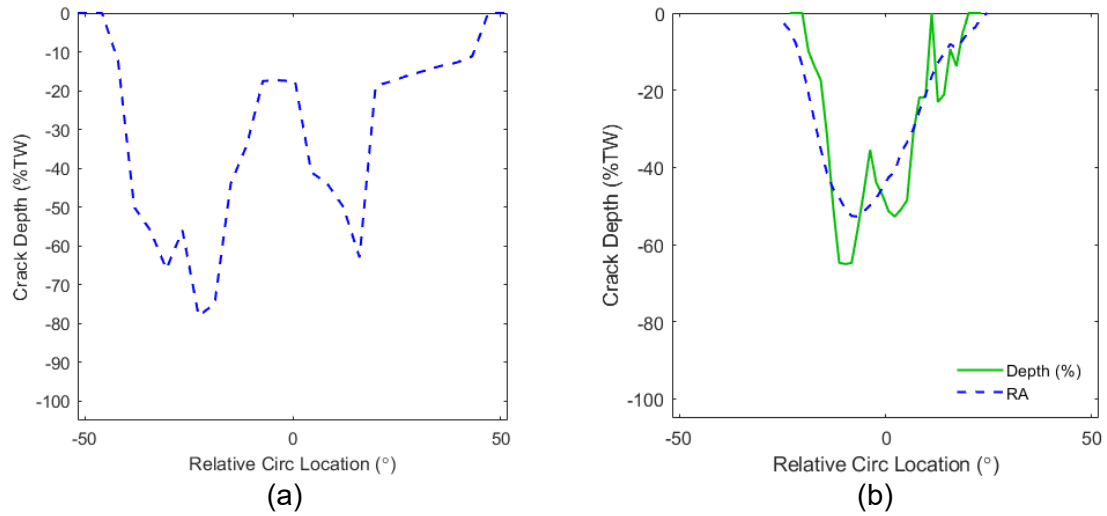
Note: These axial PWSCCs were found at location F, between flank and extrados, of U-bend specimen 15-02.

Figure G-9. NDE and DE results for two PWSCCs at location F in specimen 15-02. Shown here are (a) the estimated EC depth profile based on +Pt data at 300 kHz, (b) DE depth profile with and without RA filter, and (c) SEM image of crack surface.



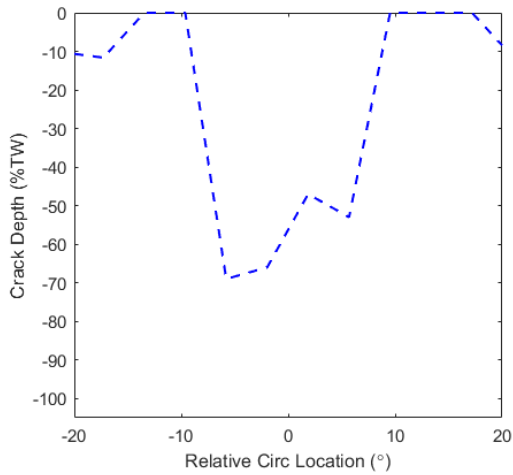
Note: This circumferential PWSCC was found at location D, intrados region, of U-bend specimen 20-01.

Figure G-10. NDE and DE results for a PWSCC at location D in specimen 20-01. Shown here are (a) the estimated EC depth profile based on +Pt data at 300 kHz, (b) DE depth profile with and without RA filter, and (c) SEM image of crack surface.

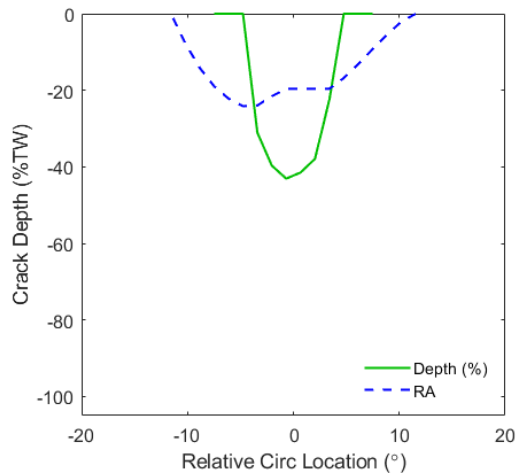


Note: This circumferential PWSCC was found 1.0-in. above the 180° tangent, in the flank region, of U-bend specimen 22-01.

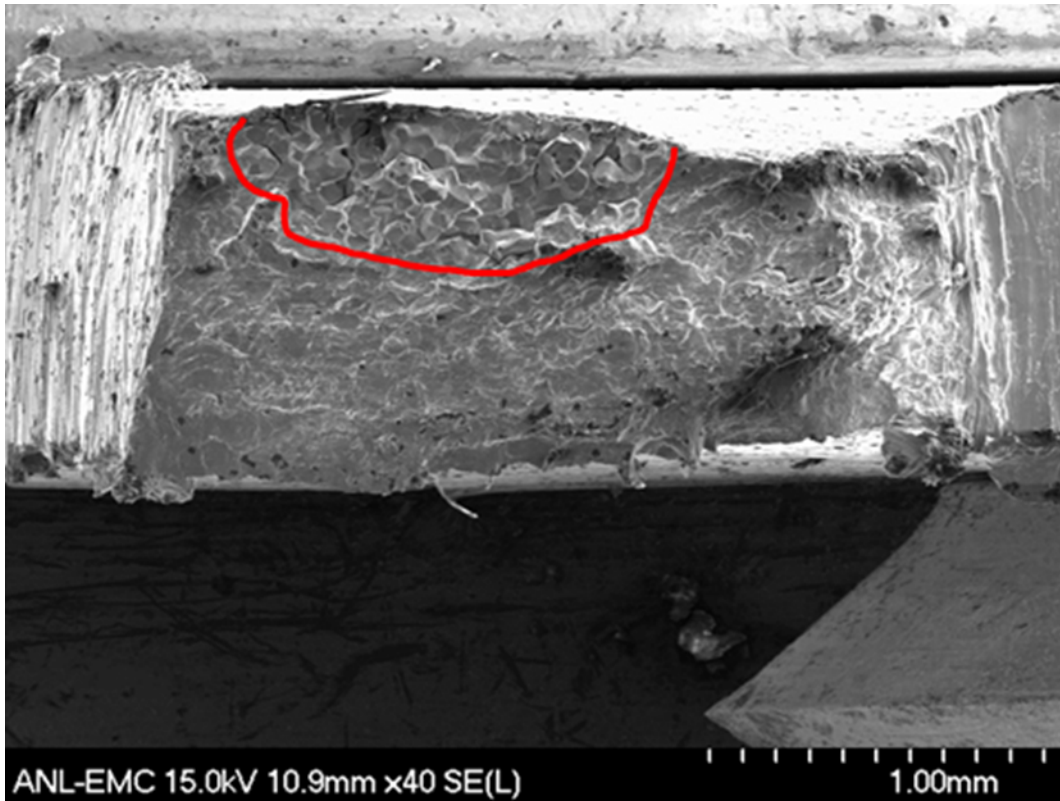
Figure G-11. NDE and DE results for a PWSCC above the 180° tangent in specimen 22-01. Shown here are (a) the estimated EC depth profile based on +Pt data at 300 kHz, (b) DE depth profile with and without RA filter, and (c) SEM image of crack surface.



(a)



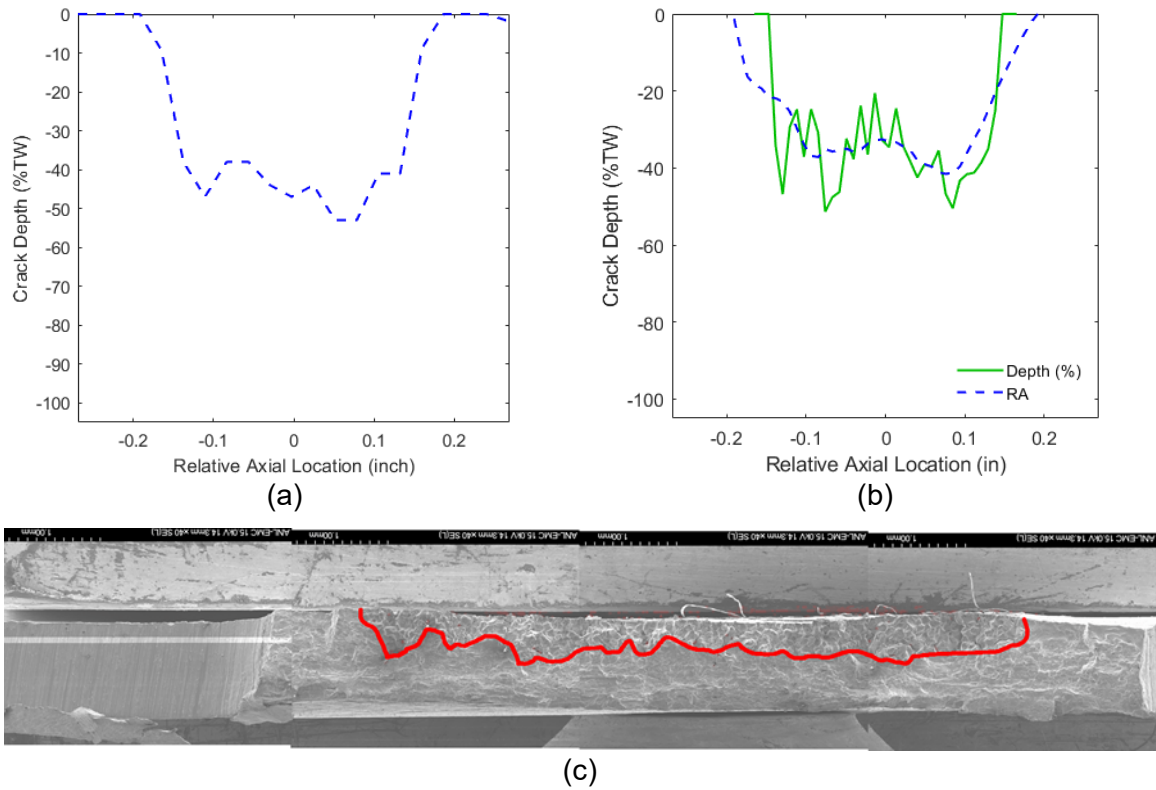
(b)



(c)

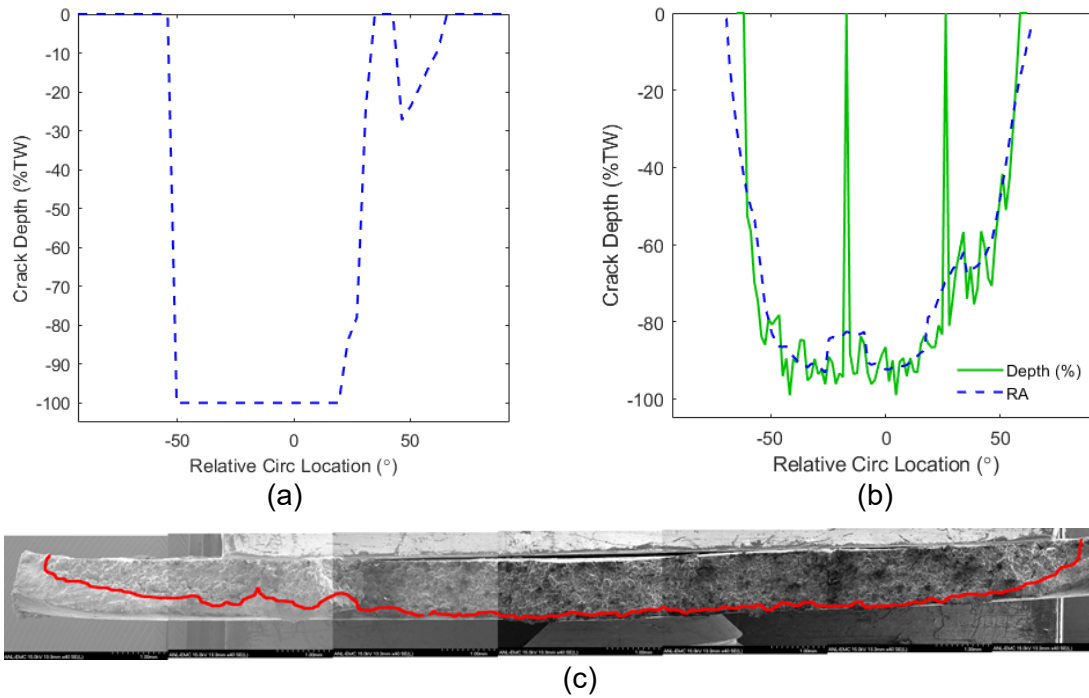
Note: This circumferential PWSCC was found at location A, between flank and intrados, of U-bend specimen 23-01.

Figure G-12. NDE and DE results for a PWSCC at location A in specimen 23-01. Shown here are (a) the estimated EC depth profile based on +Pt data at 300 kHz, (b) DE depth profile with and without RA filter, and (c) SEM image of crack surface.



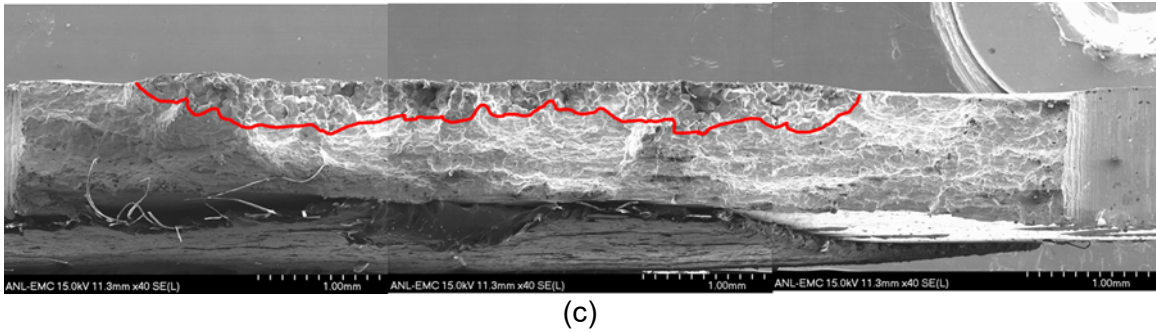
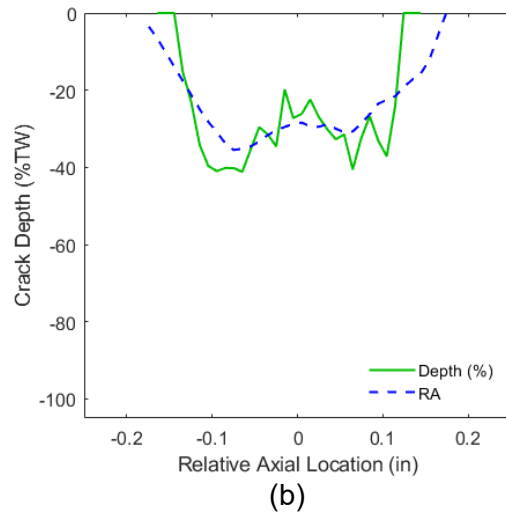
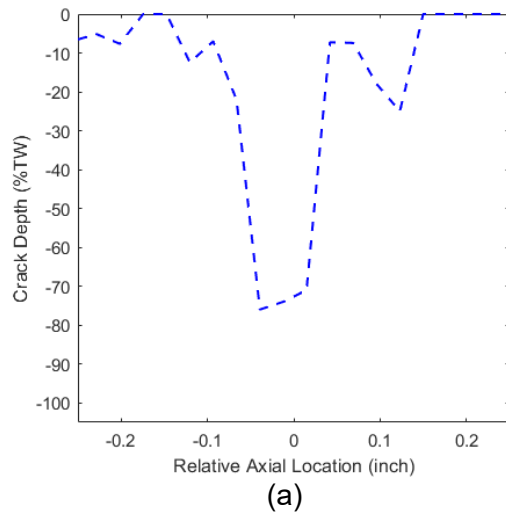
Note: This axial PWSCC was found at location D, between flank and intrados, of U-bend specimen 23-01. Video examination indicated the presence of a circumferentially extended network of axial cracks.

Figure G-13. NDE and DE results for a PWSCC at location D in specimen 23-01. Shown here are (a) the estimated EC depth profile based on +Pt data at 300 kHz, (b) DE depth profile with and without RA filter, and (c) SEM image of crack surface.



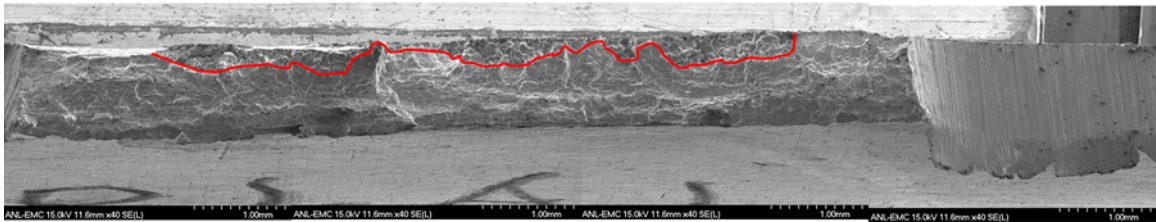
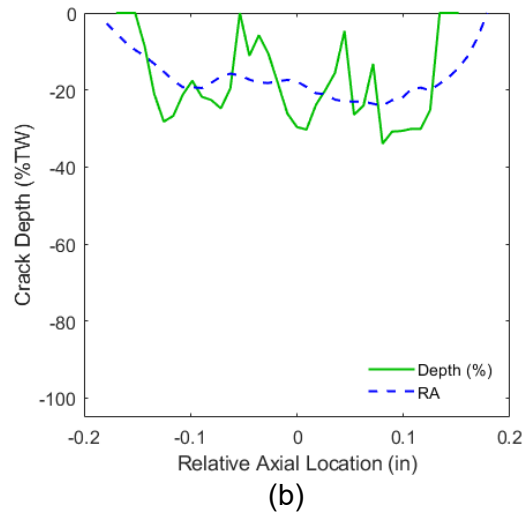
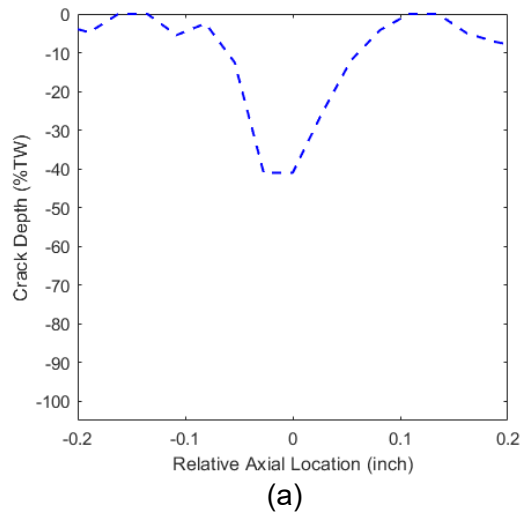
Note: This circumferential PWSCC was found at location A, intrados region, of U-bend specimen 25-01.

Figure G-14. NDE and DE results for a PWSCC at location D in specimen 25-01. Shown here are (a) the estimated EC depth profile based on +Pt data at 300 kHz, (b) DE depth profile with and without RA filter, and (c) SEM image of crack surface.



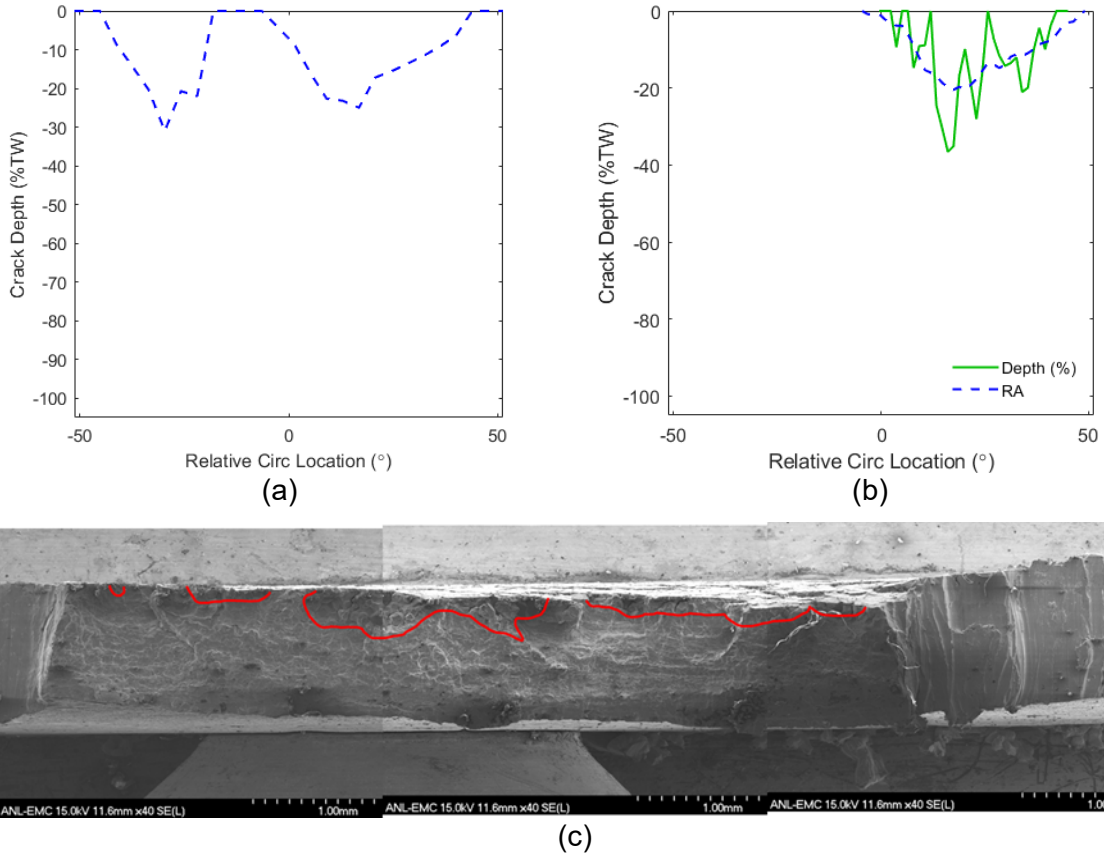
Note: This axial PWSCC was found at location D, between flank and intrados, of U-bend specimen 29-01.

Figure G-15. NDE and DE results for a PWSCC at location D in specimen 29-01. Shown here are (a) the estimated EC depth profile based on +Pt data at 300 kHz, (b) DE depth profile with and without RA filter, and (c) SEM image of crack surface.



Note: This axial PWSCC was found at location D, between flank and intrados, of U-bend specimen 31-01.

Figure G-16. NDE and DE results for a PWSCC at location D in specimen 31-01. Shown here are (a) the estimated EC depth profile based on +Pt data at 300 kHz, (b) DE depth profile with and without RA filter, and (c) SEM image of crack surface.



Note: This circumferential PWSCC was found at location B, between flank and intrados, of U-bend specimen 52-01.

Figure G-17. NDE and DE results for a PWSCC at location D in specimen 52-01. Shown here are (a) the estimated EC depth profile based on +Pt data at 300 kHz, (b) DE depth profile with and without RA filter, and (c) SEM image of crack surface.